Generalized relationships between the ionic radii of octahedral cations and the b crystallographic parameter of clay and related minerals

S. Petit, A. Decarreau, B. Grégoire, E. Ferrage

Generalized relationships between the ionic radii of octahedral cations and the *b* crystallographic parameter of clay and related minerals

S. Petit *, A. Decarreau, B. Grégoire, E. Ferrage

Institut de Chimie des Milieux et Matériaux de Poitiers (IC2MP), CNRS, Université de Poitiers, F-86073 Poitiers, France

Running head: Relationships between the ionic radii of octahedral cations and *b*

*corresponding author: sabine.petit@univ-poitiers.fr

ABSTRACT: Over several decades, a wealth of literature has been devoted to correlations between the chemistries of phyllosilicates and their crystallographic unit-cell parameter values. The *c* parameter is currently used because of its relation to the layer-to-layer distance, characteristic of the different families of phyllosilicates. The *b* parameter is also of interest because it allows measurements of the layer lateral dimensions and inherent structural adjustments. This unit-cell distance can be extracted from X-ray diffraction patterns from the (06ℓ;33ℓ) diffraction region, and by attributing the main diffraction peak observed to a 060 reflection leading to the relationship $b = 6.d(060)$. The aim of this paper is to revisit the relationships between the *b* value (or equivalent) of the phyllosilicate (*i.e.*, TO, TOT, and TOTO) or hydroxide (*i.e.*, hydroxide, oxyhydroxide, and layered double hydroxide) families and the layer chemistry based on a mean ionic radius *R* of octahedral cations calculated as: $R = \sum_{i=1}^{n}(r_i . x_i)$, where r_i is the ionic radius of the octahedral cation i and x_i is its molar fraction over n types of octahedral cations ($\sum_{i=1}^{n}(x_i) = 1$). The data were

This is a 'preproof' accepted article for Clay Minerals. This version may be subject to change during the production process.
DOI: 10.1180/clm.2023.20

collected from the literature and involved both natural and synthetic samples with both dioctahedral and trioctahedral structures of the octahedral sheet.

The results showed that *b* values can clearly be linked to *R*, leading to suitable linear regressions for all the studied structures. All correlations were found to be applicable irrespective of the di- or trioctahedral nature of the octahedral sheet and were discussed in light of (i) the lateral dimension of the octahedral sheet as well as (ii) the dimensional misfit between the tetrahedral and octahedral sheet. For hydroxide families, all data can be gathered on a single *b vs*. *R* correlation line, and the dimensional properties of the octahedral sheet can be interpreted simply based on an oxygen-cation-oxygen mean distance. For TO structures, two general *b vs*. *R* correlation trends were reported and assigned to two adjustment mechanisms corresponding to distinct types of tetrahedral and octahedral distortions. For the mica TOT family, two main trends were also reported, whereas interestingly, the use of the synthetic mica series allowed us to demonstrate that the obtained scattering of data was mainly driven by the presence of multiple limited solid solutions. Such chemical complexity was also noted for smectites, especially regarding the tetrahedral composition and associated variability in layer charge. This variability made it difficult to propose a general regression correlating *b* to *R* values for smectites, although the regression obtained for neutral TOT layers can apply as a first-order relation. Finally, a single general *b vs*. *R* correlation was obtained for chlorites, and the observed slope of the regression was interpreted by the role played by the isolated hydroxide sheet on the evolution of the lateral dimension of the structures.

Keywords: *b* parameter, ionic radius, hydroxide, serpentine, mica, chlorite, smectite, phyllosilicate.

https://doi.org/10.1180/clm.2023.20 Published online by Cambridge University Press

INTRODUCTION

Phyllosilicates are layer silicates whose layer unit is comprised of an octahedral sheet (O) (closed packing array of anions) linked to one or two tetrahedral sheets (T) (near hexagonal rings of tetrahedra). Three basic structures of layers are generally found, i.e., the so-called TO (1:1), TOT (2:1), and TOTO (2:1 + interlayer octahedral sheet) layers (Fig. 1A). Adjacent layers are linked by hydrogen bonds, e.g., TO minerals, by van de Waals forces, e.g., talc and pyrophyllite, or by various interlayer materials (hydrated cations, e.g., smectite; cations, e.g., mica; metal-hydroxyl octahedral sheet, e.g., chlorite). The assemblage of a layer plus interlayer is a unit structure and must be electrostatically neutral overall (e.g., Bailey, 1981, Brigatti *et al*., 2011). In the T sheet, the most common cations are Si, Al and Fe^{3+}, whereas in the O sheet, cations are Al, Mg, Fe^{3+}, and Fe^{2+}. Numerous other substitutions occur in natural and synthetic phyllosilicates (e.g., Kloprogge, 2017). When the octahedral cations are divalent, all octahedral sites are occupied and the structure is trioctahedral, whereas if octahedral cations are trivalent, only 2/3 of octahedral sites are occupied and the structure is dioctahedral (Fig. 1B). The position of (OH) in the dioctahedral sheet determines *trans* and *cis* octahedra (Fig. 1C). The plane layer cell is classically described by an (*a,b*) ortho-hexagonal cell in which the *b* parameter value (simply noted "*b*" in the following) is equal to three times the distance between two adjacent octahedral cations. The structures of the O sheets are similar to those of hydroxide structures.

To form a layer, similar lateral dimensions are required between the O and T sheets. In general, the lateral dimensions of the T sheet are larger than those of the O sheet, and a dimensional misfit occurs between these sheets. The T and O sheets can better form layers by contraction of T sheets by rotation of adjacent tetrahedra as measured by the α angle (Fig. 1D) (e.g. Radoslovich & Norrish, 1962; Bailey, 1991a). An expansion of the lateral dimensions of the O sheet by flattening can better accommodate the linkage to the T sheet (e.g. Brigatti *et al*., 2013). Other structural adjustments depending on the amount of strain at the sheet junction and the flexibility of the component O and T sheets can occur (e.g., Guggenheim & Eggleton 1986). The degree of stress on the plane of the junction between O and T sheets greatly influences the resultant crystal size, morphology, and structure of phyllosilicates (Bailey, 1981).

Numerous authors studied correlations between the compositions of phyllosilicates and unit-cell parameters. The *c* parameter is particularly useful for phyllosilicates because in monoclinic unit cells, the $c.\sin(\beta) = c^* = d(001)$ corresponds to the "basal spacing", or the layer-to-layer distance (Fig. 1A). The periodicity along c* can vary, depending on polytypic arrangement because of the different number of layers involved in the stacking sequence (e.g.,

https://doi.org/10.1180/clm.2023.20 Published online by Cambridge University Press

Brigatti *et al*., 2011). The *b* parameter is also of interest because it describes the O sheet lateral dimensions (Fig. 1B). Its value is obtained from X-ray diffraction (XRD) patterns of the (06ℓ;33ℓ) reflections with the (060) giving $b = 6.d(060)$. The $d(060)$ value is commonly used to distinguish dioctahedral from trioctahedral phyllosilicates, the former ranging from 1.49 to 1.52 Å and the latter from 1.52 to 1.53 Å, respectively (e.g., Środoń, 2013). Nontronite, a Fe^{3+}-rich smectite, is an exception, with *b* superposed over the trioctahedral range (e.g., Petit *et al*., 2017). *b* is sensitive to the octahedral site composition of phyllosilicates, and many correlations are available in the literature. For example, the $d(060)$ has been used to identify octahedral substitutions in kaolinite (e.g., Petit *et al*., 1990). Brigatti (1983) correlated the octahedral site content of Fe and *b* of smectites (discussed below).

Most results were presented as linear relationships (e.g., Russell & Clark, 1978; Brigatti, 1983; Petit *et al*., 2017) between the *b* and octahedral site (and sometimes tetrahedral site) content. Many authors (e.g. Radoslovich, 1962; Rieder *et al*., 1971; Wiewiora & Wilamowski, 1996) used multiple regression equations:

$$b = b_0 + \sum_{i=1}^{n}(a_i.c_i) \qquad (1)$$

where b_0 is the *b* cell parameter of the end-member mineral with a_i as the required regression coefficient for substituting cation i, and c_i is the atomic content of cation i in the structural formulae containing n types of substituting cations. These relations are restricted to a given family of phyllosilicates and do not allow generalized relationships. Hazen & Wones (1972) established a clear correlation between the *b* of trioctahedral micas and the ionic radius of M^{2+} octahedral-site cations. Similarly, Brindley & Kao (1984) correlated the *a* and *c* unit-cell parameters of $M(OH)_2$ hydroxides and M-O distances. Gerth (1990) observed that the unit-cell *b* dimension varied with the ratio of metal-substituted goethite and was related to the ionic radii of incorporated metals. Bentabol & Ruiz Cruz (2013) examined the unit-cell values of lizardites with the ionic radius of the dominant M cations. However, for several M cations, the unit-cell values depend on the contribution of all octahedral cations (relative proportions and distribution). The current paper explores in the light of the dimensional misfit between T and O sheets, the connection between the *b* of clay minerals and some related minerals with the mean ionic radius *R* of octahedral cations calculated as:

$$R = \sum_{i=1}^{n}(r_i.x_i) \qquad (2)$$

where r_i is the ionic radius of octahedral cation i and x_i its molar fraction over n types of octahedral cations ($\sum_{i=1}^{n}(x_i) = 1$). Each family of minerals has a dedicated section that can be read separately.

METHODS

https://doi.org/10.1180/clm.2023.20 Published online by Cambridge University Press

Data for natural and synthetic samples were obtained from the literature. Most of the available b values were calculated from d(060) value measured by XRD unoriented powder patterns, according to the relation $b = 6.d(060)$. The diffraction band at (060) is observed at 1.49–1.54 Å for clay minerals and represents several overlapping (06ℓ;33ℓ) reflections with small differences in d spacing. Accordingly, differences between actual *vs* extracted b values is expected and must be considered for comparing data between measurement methods.

The d(hkl) values (in Å) derived from XRD experiments are generally given to ±0.005 Å, whereas the spot sizes in the figures represent the estimated uncertainties in the unit-cell parameters of samples. The mean ionic radius R of octahedral cations is calculated following Eq. 2.. Ionic radii are from Shannon (1976) (Table 1) and are given with ±0.01 Å uncertainty. Structural formulas (SFs) are from the literature or were calculated from chemical compositions. The uncertainty of R values cannot be generalized or estimated with accuracy. The data were selected carefully. For example, samples with SF appearing obviously erroneous were disregarded.

The b dimension of a theoretical "free" T sheet (i.e., with hexagonal symmetry and no tetrahedral rotations) is: $b_{tet.} = (4\sqrt{2})*(\text{Si-O}) \approx 9.15$ Å with an average bond length for Si-O = 1.618 ± 0.01 Å (Bailey, 1981; Bailey, 1984b) (Fig. 1D), and substitutions of larger cations for Si increase this value following this equation:

$$b_{tet.} = ax + 9.15 \qquad (3)$$

where x is the number of tetrahedral atoms substituted for Si ($Si_{1-x}{}^{IV}T_x$). Accordingly, parameter a takes the value of 0.74, 1.26, and 1.15 for Al, Fe^{3+}, and Ga, respectively. Be is treated as an equivalent to Si in calculating $b_{tet.}$, as the Be-O bond length is close to that of Si-O (1.62 *vs.* 1.618 Å, respectively). The equation (4) can be used to calculate α the tetrahedral rotation angle also termed ditrigonal rotation:

$$\alpha = arccos(b/b_{tet.}) \qquad (4)$$

This unique relationship assumes that contraction occurs solely by tetrahedral rotation (e.g., Radoslovich & Norrish, 1962), and is not very accurate compared to structure refinement X-ray diffraction single crystal data (Brigatti & Guggenheim, 2002). Clearly, for $b/b_{tet.}$ values >1, tetrahedral rotations do not apply because (i) existing uncertainties in the bond lengths (e.g., the Si-O and ^{IV}Al-O bond lengths used are from Bailey (1984b) and greater than those of Shanon (1976)), (ii) various other mechanisms are involved to adjust T and O sheet lateral dimensions, and (iii) tetrahedral angles may vary. Accordingly, $b/b_{tet.}$ that also provides a measure of misfit (McCauley & Newnham, 1971), was used here over the α value to compare samples. Moreover, Peterson *et al.* (1979) estimated by semi-

https://doi.org/10.1180/clm.2023.20 Published online by Cambridge University Press

empirical molecular-orbital cluster calculations, that a 6-fold ring of a "free" ideal T sheet has a minimum energy at α = 16° and not at α = 0°, suggesting the ring has an intrinsic ditrigonal character irrespective of octahedral articulation. Finally, the M-O bond lengths were calculated using *R* (Eq. 2) as the average of the ionic radii in six-fold coordination (Table 1). For octahedral oxygen ions, coordination is (i) in four-fold for trioctahedral configuration, i.e., each oxygen ion bonded to three M^{2+} cations and one H^{+} ion, or (ii) in three-fold for dioctahedral configuration, i.e., each oxygen ion bonded to two M^{3+} cations and one H^{+} ion. The *b* dimension of a theoretical "free" O sheet i.e. with regular octahedra is:

$b_{oct.} = 3.\sqrt{2}$.M-O (e.g. Guggenheim & Eggleton, 1987), and thus :

$$b_{oct.} = 3.\sqrt{2}.(R+1.38) \quad (5)$$

The percent of octahedral enlargement corresponding to the difference between the calculated $b_{oct.}$ and observed *b* is:

$$\% \text{ O enlargement} = ((b/b_{oct.}) - 1).100) \quad (6)$$

The % O enlargement reflects variations in O sheet lateral dimensions and is related to octahedral flattening and to O sheet thickness as described for micas by Toraya (1981). An increase of % O enlargement is related to an increase in octahedral flattening and a decrease of O sheet thickness. The % O enlargement vs. *R* plot is another graphic representation of the *R* vs. *b* plot that can be useful to discuss the variations in O sheet dimension (Guggenheim & Eggleton, 1987) and O sheet thickness.

https://doi.org/10.1180/clm.2023.20 Published online by Cambridge University Press

RESULTS AND DISCUSSION

Hydroxides, oxyhydroxides, and layered double hydroxides

Hydroxides, oxyhydroxides and layered double hydroxides (Fig. 2) require cell parameters must be transformed for comparison to phyllosilicates. Thus, to be equivalent to the *b* parameter of phyllosilicates, the hexagonal *a* of $M(OH)_2$ hydroxides, the orthorhombic *c* of diaspore, the orthorhombic *b* cell parameters of other oxyhydroxides and the *a* of layered double hydroxides were each tripled. Table 2 provides data used, which are plotted in Fig. 3 as a function of *R*.

The plots for synthetic $M^{2+}(OH)_2$ brucite-like hydroxide structures (Fig. 2) with M=Mg, Ni, Co, Fe, Mn, Cd, and Ca are in excellent agreement with *b vs*. *R* correlation (Fig. 3A). The relation, $b = 4.4878.R + 6.2462$, is consistent with Brindley & Kao (1984). Moreover, the $M^{2+}(OH)_2$ minerals plus gibbsite fall on the same correlation line with a very good R^2 (0.996). Thus, the *b* conforms to the mean ionic radius of either di- or trivalent actual octahedral cations. In other words, the contribution of the vacant site is integrated in *R*. Actually, each octahedron is distorted, and the size of the vacant site is the largest (Saalfeld & Wedde, 1974).

For MO(OH) oxyhydroxides (Figs. 2, 3B), a unique regression was derived for the group except for $M=Mn^{3+}$ (see below), yielding the relation $b = 4.6673.R + 6.0546$. Diaspore (Al), goethite (Fe^{3+}), synthetic GaO(OH) end-members, and synthetic goethite substituted by heterovalent (divalent, tetravalent) cations, are in good agreement with the regression. Except for Ga^{3+}, cation substitution is very limited in goethite (Table 2). For example, Stiers & Schwertmann (1985) failed to synthesize the complete Fe^{3+}-Mn^{3+} goethite solid solution and achieved ≤ 15% Mn^{3+} (Table 2). Groutite (α-MnOOH), which is isostructural with goethite has an orthorhombic *b* of ~2.87 Å but ~3.02 Å for goethite (Table 2), although $r(Mn^{3+})$ is identical to $r(Fe^{3+})$ (Table 1). Because of Jahn Teller effects (Shannon *et al.*, 1975), octahedra are strongly distorted in groutite, with four short Mn-O distances (two of 1.895 Å and two of 1.965 Å) and two long Mn-O distances (2.174 and 2.338 Å), with a mean Mn-O distance of 2.039 Å (Kohler & Armbruster, 1997). Assuming this mean Mn-O distance and $r(O^{2-}) = 1.36$ Å, the mean $r(Mn^{3+})$ would be 0.679 Å that cannot account for the large difference in the equivalent *b* between groutite and goethite. When using the regression obtained for MO(OH) structures (Fig. 3B), the *b* for groutite corresponds to an "effective" $r(Mn^{3+}) = 0.548$ Å. Using this "effective" $r(Mn^{3+})$, the synthetic Mn-goethites (Stiers & Schwertmann, 1985) follow the regression well (Fig.

https://doi.org/10.1180/clm.2023.20 Published online by Cambridge University Press

3B), and the R^2 of the regression was slightly better when the Mn^{3+} data were included (0.9845 *vs.* 0.9818). This suggests that in the groutite structure, *b* is mainly dependent on the shortest Mn-O distances.

The layered double hydroxide (LDH) structure is based on brucite $Mg(OH)_2$ with octahedral coordination around the metal ions (Fig. 2). Substitutions of divalent cations M^{2+} by trivalent cations M^{3+} produce many isostructural materials with the general formula $M^{2+}_{1-x}M^{3+}_x(OH)_2\ A^{n-}_{x/n}, yH_2O$ (Table 2). These layered materials are readily synthesized (e.g., Forano *et al.*, 2013), and have numerous applications (e.g., Costantino et *al.*, 2009; Choi *et al.*, 2008). Studying natural as well as synthetic hydroxy-carbonates, Brindley & Kikkawa (1979) observed a very good correlation between the *a* parameter and the extent of Al/M^{2+} substitution, but considered the Mg-Al and Ni-Al systems separately. Using the mean ionic radius *R* of octahedral cations, the cell parameters can be compared, regardless of the elemental composition of the LDHs, and leads to the relation $b = 4.2043.R + 6.3758$ (Fig. 3C). The lower goodness of the regression coefficient for the LDH minerals compared to the other hydroxides, may be related to uncertainties in their more complex chemical composition. Indeed, because LDHs are synthesized under pH conditions in which cations can precipitate, bulk chemical analyses would give elemental compositions consistent with the elemental composition of the starting solution. However, the coprecipitation of amorphous or nanocrystalline phases cannot be excluded and may hardly be detected by conventional analytical methods so that the true elemental composition of LDH phases may be different from the expected composition. Chemical analyses obtained from transmission electron microscopy coupled to an energy dispersive X-ray detector would thus give more reliable results since the elemental composition and its dispersion through the sample is a good indicator of the purity of the studied samples. As an example, for the shigaite natural sample, which is relatively far from the range (Fig. 3C), the calculated value for the M^{2+}/M^{3+} ratio using the correlation equation would be 2.57 instead of 2.00, i.e., 2.16 for number of Mn^{2+} atoms instead of 2.

The regressions between the O sheet dimensions and *R* for the three types of hydroxide families have similar slopes (Fig. 3D), despite different crystallographic structures, implying that the O sheet dimension depends essentially on the shape and size of neighboring octahedra. The effect of the octahedral composition on the distance between two octahedral cations located in two adjacent octahedra is similar for $M^{n+}(OH)_n$, MO(OH), and LDH, regardless of the di- or tri-octahedral character of minerals. For the same *R*, the octahedral dimension of $M^{n+}(OH)_n$ hydroxide minerals is slightly higher (0.08 ±0.005 Å) than those of the two other structures that are more constrained due to their higher complexity (Fig. 3D). Interestingly, the impact of the structure is similar for oxy-hydroxides and LDH in the existing compositional range.

https://doi.org/10.1180/clm.2023.20 Published online by Cambridge University Press

Brindley & Kao (1984) showed that the octahedral sheets in trioctahedral brucite-like structures are all flattened to the same extent with a mean flattening angle τ = O-M-O with O in the same plane varying slightly from 97.1° to 98.1° (average 97.4°). The unique linear regression observed here between gibbsite and trioctahedral hydroxides suggests that τ is similar for gibbsite and for all $M^{n+}(OH)_n$ hydroxides. Accordingly, from refined structures the value of the flattening angle τ was found to be 98.5° and 98.3°, for gibbsite (Saalfeld & Wedde, 1974) and brucite (Parise *et al.*, 1994), respectively.

The structure of $M^{n+}(OH)_n$ hydroxides approximates a hexagonally close-packed arrangement of anions with M^{n+} ions in octahedrally coordinated positions between alternate pairs of anion planes. The b used here is given by $b = 6.(M\text{-}O).\sin(\tau/2)$ with the (M-O) distance being the sum of the effective ionic radii for cations (M) in six-fold coordination and oxygen ions (O) in four-fold coordination ($r(^{IV}O^{2-}) = 1.38$ Å, Table 1) (Brindley & Kao, 1984). Using the mean ionic radius of octahedral cations R, this relation can be easily rewritten as: $b = 6.(R+1.38).\sin(\tau/2)$.

Following a structurally based interpretation, a relation $b = A.R + C$ can be obtained for each family of hydroxides studied here using a simple model with $A = 6.\sin(\tau/2)$ and $C = A.1.38$ (in Å). The A (and thus τ and C) were determined by fitting with the experimental regressions (Fig. 3D).

For $M^{n+}(OH)_n$ hydroxides, A and C are 4.51 and 6.22, respectively (Fig. 3D), close to the experimental values derived from the correlation line shown in Fig. 3A (4.49 and 6.25, respectively). The corresponding $\tau = 97.3°$ agrees well with literature (see above). The corresponding percent of octahedral enlargement (or octahedral flattening) is ~6.3%.

The proposed model for $M^{n+}(OH)_n$ hydroxides is also suitable for MO(OH) and LDH, as seen in Fig. 3D, where A are very close for MO(OH) and LDH: 4.47 and 4.48, respectively. The octahedra are slightly less flattened in MO(OH) and LDH compared to $M^{n+}(OH)_n$ hydroxides, with $\tau = 96.3°$ (~5.4% octahedral enlargement) for MO(OH) and $\tau = 96.6°$ (5.6% octahedral enlargement) for LDH.

The structurally based model of the hexagonally close-packed arrangement of anions with M^{n+} ions in octahedrally coordinated positions shows very good efficiency in reconciling structural and chemical data for all families of studied hydroxides as well as for both di- and tri-octahedral minerals (Fig. 3D), and the relation between the equivalent b and the mean ionic radius of octahedral cations R for each mineral, allows to measure the flattening of octahedra which is similar for all the families and does not vary significantly within each family.

TO phyllosilicates

https://doi.org/10.1180/clm.2023.20 Published online by Cambridge University Press

TO phyllosilicates are composed of the superimposition of a T sheet of pseudo-hexagonal ring of $(SiO_4)^{4-}$ units on an O sheet of edge-sharing octahedra leading to an electrostatically neutral layer (Fig. 1A). The general SF is $(Si_aR^{3+}{}_b)_2\ (R^{3+}{}_cR^{2+}{}_d\square_e)_3\ O_5(OH)_4$, with R^{3+} being mainly Al and Fe^{3+}, R^{2+} being mainly Mg (but could be very varied with other divalent cations, such as Ni and Fe^{2+}), and □ being a vacant site. Anions other than OH^-, such as F^- or Cl^-, are rarely reported to occur and will not be discussed here. Kaolins and serpentines constitute the dioctahedral and trioctahedral families, respectively. Kaolin group minerals include kaolinite, dickite, nacrite, and halloysite and have a general composition of $Al_2Si_2O_5(OH)_4$ ($+nH_2O$ for halloysite), with similar *b* (Giese, 1991) and very few substitutions. Consequently, only kaolinite was considered in the following as a representative of the whole kaolin group.

Contrary to kaolins representing Al end-members with no tetrahedral substitutions and a very simple chemical composition, serpentines display a wide range of chemical compositions leading to many end-members depending on (i) the extent of tetrahedral substitutions and (ii) the nature of the dominant octahedral cations. For instance, lizardite (Mg) and nepouite (Ni) (a~2 and d~3), berthierine (b~0.5, c~0.5, and d~2.5), brindleyite (b~0.5, c~1, d~1.75, and e~0.25), and amesite (Al-Mg) and cronstedtite (Fe^{3+}, Fe^{2+}) (b~1, c~1, and d~2) represent different minerals of these serpentine families (Wiewiora, 1990). Three structural groups of serpentines based on particle shape are also distinguished, i.e., flat layers as for lizardite (Fig. 4A), cylindrical layers as for chrysotile (Fig. 4B), and corrugated layers as for antigorite (Fig. 4C) (e.g., Wicks & Whittaker, 1975), and many morphologies have been reported (e.g., Andreani *et al.*, 2008).

Kaolinite and lizardite. Kaolinite and lizardite are the Al-dioctahedral and Mg-trioctahedral end-members, respectively, for TO phyllosilicates having the $Si_2(R^{3+}{}_cR^{2+}{}_d)O_5(OH)_4$ general SF. For the kaolinite dioctahedral end-member, c and d are 2 and 0, respectively, and R^{3+} is Al, while for the lizardite trioctahedral end-member, c and d are 0 and 3, respectively, and R^{2+} is Mg. No or limited octahedral substitutions (mainly Fe^{3+}-for-Al^{3+}) occur in natural kaolinite. By using the synthesis method, the Fe^{3+} substitution amount can be slightly increased, and other octahedral cations can be introduced in the structure (Table 3). Among the large set of published data available for pure natural Al-end-member kaolinite, the Keokuk kaolinite studied by Rietveld refinement (Bish & Von Dreele, 1989) was selected as representative for this study. According to the general SF above, lizardite *sensus stricto* does not have tetrahedral substitutions. Consequently, in this study, lizardite with > 0.1 ^{IV}Al was considered in the Al-serpentine series rather than in the lizardite series.

https://doi.org/10.1180/clm.2023.20 Published online by Cambridge University Press

As shown in Fig. 5A, the *b vs. R* plot for all TO samples display a relatively scattered pattern. Two different regressions, i.e., kaolinite-lizardite (*K-L*) and greenalite-caryopilite (*G-C*) lines, can be distinguished, however, with a wide cloud of dots at their intersection (Fig. 5A).

Interestingly, natural kaolinite, synthetic Al-Fe^{3+}-kaolinite series, and synthetic Ni-Mg lizardite series appear quasi-aligned (*(K-L)* line) (Fig. 5A and 5B). The (K-L) line was first calculated with the synthetic series of Fe^{3+}-kaolinites (Petit *et al.*, 1990; Iriarte *et al.*, 2005) and Ni-Mg lizardites (Baron *et al.*, 2016a) (Figs. 5A and 5B). Including the natural kaolinite in these two synthetic series slightly increases the correlation coefficient (0.9987 instead of 0.9985) without significantly modifying the regression ($b = 1.5092.R + 8.1371$ instead of $b = 1.5097.R + 8.1368$). The (*K-L*) regression including the natural kaolinite was kept in the following. Because aluminum is the octahedral cation with the smallest ionic radius (0.535 Å, Table 1) to form a TO clay structure, *b* of the pure Al end-member exhibits the smallest value observed for TO phyllosilicates. Accordingly, the natural Keokuk pure kaolinite is located at the origin of the regression line with a *R* of 0.535 Å and a *b* of 8.945 Å, according to Bish & Von Dreele (1989). Few *b* for synthetic Fe^{3+}- and Ga^{3+}-substituted kaolinites of Bentabol *et al.* (2009) are lower than 8.945 Å (Table 3, Fig. 5B), suggesting an underestimation of these *b*. The data for the kaolinite synthesized with the highest Cr^{3+} content also deviate slightly from the correlation lines (Fig. 5B). Except for the samples described in Bentabol *et al.* (2009), the dataset for other synthetic diversely substituted kaolinites is located on or close to the regression line (Fig. 5B). Up to approximately 0.1 octahedral Fe^{3+} pfu is observed in natural kaolinites, whereas up to 0.6 substituted Fe^{3+} pfu can be measured in synthetic kaolinites (Table 3). For the theoretical Fe^{3+}-kaolinite end-member ($Si_2Fe^{3+}{}_2O_5(OH)_4$), *b* extrapolated using the experimental data from Iriarte *et al.* (2005), is located close to the (*K-L*) regression line, arguing for the suitability of the dataset for a large range of compositions (Fig. 5B). Moreover, as concluded by some authors (Petit *et al.*, 1988; Petit & Decarreau, 1990; Iriarte *et al.*, 2005), the Al-Fe^{3+} kaolinite synthetic series behaves like a solid solution within the compositional range explored, and no evidence exists to date that the maximum value experimentally obtained (0.6 pfu) corresponds to a steric limit of Fe^{3+} substitution in kaolinite.

In contrast to kaolinite, different end-members of lizardite are encountered, and Mg cations are commonly at least partially replaced by other divalent cations (Table 3). As shown in Fig. 5B, the synthetic Mg-Ni-lizardites are remarkably aligned on the (*K-L*) line, The Co-lizardite does not fit well the regression. The two different *b* were measured for the same sample, as Bayliss (1981) indeed calculated a significantly higher *b* than measured by Dalmon & Martin (1968) (Fig. 5B). The deviation from the (*K-L*) regression line and the *b* fluctuations likely suggest a problem with these data. In a review work dedicated to serpentine group minerals, Bayliss *et al.* (1980) observed some

https://doi.org/10.1180/clm.2023.20 Published online by Cambridge University Press

significant fluctuations in reported *b*, with apparently the same chemistry, suggesting possible different ways or inaccuracies in measuring this parameter. Fluctuations are noticed for synthetic Mg end-members with *b* ranging from 9.204 to 9.241 Å (Table 3). Fluctuations are also observed for natural lizardites whose single-crystal XRD refinement of two different crystals from a same sample with an assumed homogeneous chemical composition, resulted in two different *b*, as illustrated by the Gew-graze lizardite-1*T* (Mellini *et al.* (2010) and the Monte Fico lizardite-1*T* (Mellini & Viti, 1994) (Table 3). More consistent with the results observed here, Mellini & Zanazzi (1987) measured a slight variation in *b* coupled with a slight variation in the chemical composition between two polytypes of the Coli lizardite sampled within a same vein (Table 3). These examples illustrate how the established correlation lines can help to identify if deviation originated from structural features or difficulties in accurately measuring *b*.

Lizardite, chrysotile, and antigorite are three polymorphs with flat, curved, and corrugated wavy layer structures, respectively. In fact, antigorite corresponds to a polysomatic series with T sheets regularly inversed in polysomes (Fig. 4). A more correct general formula for antigorite would then be $(Mg)_{3m-3}Si_{2m}O_{5m}(OH)_{4m-6}$, where m represents the number of tetrahedra within a full wavelength, and m=17 has been proposed as the most common value (Capitani & Mellini, 2004). The set of data do not allow the identification of possible differences between the polymorphs. As far as synthetic Mg- and Ni- lizardites (Baron *et al.*, 2016a) and chrysotiles (Jasmund *et al.*, 1975) are concerned, *b* measured for chrysotiles appear slightly lower than those of lizardites (Table 3). Because the two sets of samples were measured with different techniques, it would be uncertain to conclude that *b* for chrysotile are lower than for lizardite.

Al- and Fe^{3+}- serpentines. Al- and Fe^{3+}- serpentines whose general SF are respectively $(Si_{2-x}Al_x)(Mg_{3-x}Al_x)O_5(OH)_4$ and $(Si_{2-x}Fe^{3+}{}_x)(Fe^{3+}{}_xFe^{2+}{}_{3-x})O_5(OH)_4$, most often exhibit high tetrahedral substitution contents, up to 1 Al or Fe^{3+} per $O_5(OH)_4$, to neutralize the positive octahedral layer charge generated by the heterovalent octahedral substitutions of divalent cations (mainly Mg and Fe^{2+}) by trivalent cations (mainly Fe^{3+} and Al). The dataset for Al- and Fe^{3+}- serpentines is strongly scattered (Fig. 5A), and this scattering is more pronounced for natural samples than for synthetic Al- serpentines, which lay close to the (*K-L*) regression line (Fig. 5B). The natural Al- and Fe^{3+}- serpentines exhibit a wide range of tetrahedral substitutions and several polytypes, but no specific trend can be observed between these two characteristics and *b* (Fig. 5C).

https://doi.org/10.1180/clm.2023.20 Published online by Cambridge University Press

Greenalite and caryopilite. Greenalite and caryopilite are respectively Fe^{2+}- and Mn-rich TO phyllosilicates with corrugated structure and with the following general SF: $Si_2\ (M)_{(2.5\text{-}3)}O_5\ (OH)_4$, with M = Fe, Mn, Mg, and Al as the main octahedral cations. Partial oxidation of octahedral Fe and Mn often occurs, and some octahedral sites may be vacant. The regression parameters for the (*G*-*C*) line (Fig. 5A) and the structural interpretation are discussed in detail below. The slope of the (*G*-*C*) regression line is approximately 4.5 times higher than that of the (*K*-*L*) line. Jasmund *et al.* (1975) reported that the greenalite synthesized as the Fe^{2+} end-member was structurally nonequivalent to the Ni-, Mg-, and Co-lizardites. The observed scattering of samples around the (*G*-*C*) line (Fig. 5A) can be tentatively assigned to uncertainties in the data and/or to the various modulated local substructures. Indeed, greenalite and caryopilite exhibit domed island-like structures due to tilting of tetrahedra with periodic inversions of three- and four-fold rings (Guggenheim & Eggleton, 1998). This structural adjustment is a way to enlarge the T sheet dimensions to allow congruence with the large O sheet dimensions due to the occurrence of significant amounts of octahedral cations having large ionic radii, such as Mn^{2+} and Fe^{2+} (Table 1).

Influence of tetrahedral composition. If no relation can be observed between tetrahedral content and *b* as shown above (Fig. 5C), it is clear however, from a simple comparison for example between Mn-rich serpentines *i.e.* kellyite (^{IV}Al-serpentine), guidottite ($^{IV}Fe^{3+}$-serpentine), and caryopilite (negligible tetrahedral substitution and corrugated structure), that the tetrahedral composition plays a role in the dimensional misfit between T and O sheets. All these Mn-rich serpentines have high *R* (from ~0.73 to ~0.80 Å) and *b* (from ~9.4 to ~9.8 Å) due to their high Mn content. The tetrahedral substitutions in kellyite and guidottite allow to increase the lateral dimension of the T sheet making the fit between T and O sheets possible without corrugation of the layer.

The $b/b_{tet.}$ values were calculated for all TO phyllosilicates and plotted as a function of *R* (Fig. 6A). Three general trends are observed. The (*K*-*L*)' correlation line (Fig. 6A) corresponds to the (*K*-*L*) line (Fig. 5A), and the regression was calculated using the same data. These samples have no tetrahedral substitutions and thus the correction by the $b_{tet.}$ value does not influence the data alignment (Fig. 6A). Note that the synthetic R^{2+}-Al-serpentine samples (Bentabol *et al.*, 2013) that were above the (*K*-*L*) line (Fig. 5A and 5B) are now closer to the (*K*-*L*)' line (Fig. 6A). The odinite data systematically deviate from the trend (Fig. 5A and 6A), and possible impurities and redox variation make their SF unsure. Interestingly, compared to the *b vs. R* plot (Fig. 5A), the cloud of dots associated with the Al-serpentine disappeared in Fig. 6A. Less predictable is that the corrugated Fe^{2+}-Mn-serpentines roughly follow the same high slope (*G*-*C*)' line as most of the Al-serpentines (Fig. 6A). For this (*G*-*C*)' line, the regression was calculated

https://doi.org/10.1180/clm.2023.20 Published online by Cambridge University Press

using antigorites, greenalites and caryopilites, and Al-serpentines that are on (or close to) the (*G-C*)' line. Furthermore, the Fe^{3+}-serpentines, except the pecoraite sample which lies on the (*G-C*)' line, follow fairly well a different linear trend *(Fe^{3+}-Serp)'* with the same slope as the (*G-C*)' line (Fig. 6A).

For Al- and Fe^{3+}- serpentines, a general relationship of *b vs. R*, introducing the tetrahedral composition can be formulated from each (*K-L*)', (*G-C*)', and *(Fe^{3+}-Serp*)' regression lines (Fig. 6A)

$$b = R\,(a.T + c) + d.T + e \qquad (7)$$

For Al-serpentines following the *(K-L)*' line (Fig. 6A):

$$b = R\,(0.061.T + 1.509) + 0.327.T + 8.137$$

For Al- (and Fe^{3+} *i.e.* pecoraite) following the *(G-C)'* line (Fig. 6A):

$$b = R\,(0.275.T + 6.854) + 0.173.T + 4.302$$

For Fe^{3+}-serpentines following the *(Fe^{3+}-Serp)'* line (Fig. 6A):

$$b = R\,(0.470.T + 6.854) + 0.27.T + 3.932$$

T being the number of ^{IV}Al or $^{IV}Fe^{3+}$ phfu.

The intersect coordinates for the two (*K-L*)' and (*G-C*)' lines are $R = 0.717$ and $b = 9.220$ Å, approximately corresponding to the Mg-lizardite end-member. The corresponding $b/b_{tet.}$ value is 1.007, thus indicating a tetrahedral rotation angle α close to 0°. Accordingly, the theoretical modeling using the distance least-squares method indicates that the O and T sheets fit together without any major distortions in the Mg-lizardite structure (Bish, 1981; Wicks & Hawthorne, 1986; Wicks & O'Hanley, 1991), and α measured by structure refinement is close to 0° (~-1.5(1)°) for natural Mg end-member lizardite (Guggenheim & Zhan, 1998; Mellini *et al*., 2010).

Based on all the results above, three main distinct mechanisms of adjustment between O and T sheet lateral dimensions to compensate the misfit for kaolinite - lizardite, Al- and Fe^{3+}- serpentines, and phyllosilicates with corrugated structure, are proposed below.

Focus on the structural adjustment mechanism for kaolinite-lizardite family. Samples on the (*K-L*)' line (Fig. 6A), are those for which *b* is driven by *R* according to the good regression observed for the (*K-L*) line (Fig. 5A). For pure kaolinite (Al end-member that exhibits the lowest *R*), T sheets are relatively large compared to O sheets and have to reduce their lateral dimensions to adjust to the O sheets. Moving to lizardite, and thus increasing *R*, makes the dimensional misfit decrease. The (*K-L*)' trend (Fig. 6A) gives evidence of a progressive decrease of the angle of tetrahedral rotation α with increasing *R*. Accordingly, the rotation of tetrahedra to ditrigonal symmetry (Fig. 1D) is the

https://doi.org/10.1180/clm.2023.20 Published online by Cambridge University Press

principal process to overcome the misfit when $b_{oct.} < b_{tet.}$ in TO phyllosilicates by reducing the lateral dimension of T sheet (e.g., Radoslovich, 1963; Bailey, 1966; Wicks, 1975; Guggenheim & Eggleton, 1987). However, this process is not the only one to achieve congruency between the T and O sheets dimension. Indeed, the O sheet enlargement (Eq. 6) increases progressively with a decrease of *R* (Fig. 6B). The O sheet enlargement corresponds to a lateral expansion of the sheet by thinning (Bailey, 1984b). The $b_{oct.}$ value corresponding to an unconstrained O sheet, was taken for hydroxides as determined above ($b_{oct.} = 4.51.R + 6.22$ (Fig. 3D)). Consequently, positive % O enlargement corresponds to an O sheet flattening (or thinning) compared to hydroxides, whereas negative % O enlargement corresponds to a thickening of O sheet compared to hydroxides, a null value being obtained for $R = 0.642$. Ionic radius of Fe^{3+} being 0.645 Å (Table 1), the theoretical Fe^{3+}-kaolinite end-member would have similar dimension than the corresponding hydroxide. The $Fe(OH)_3$ mineral, bernalite, actually exists but it has a pseudo cubic structure of perovskite type (Birch *et al.*, 1993) that cannot be compared. Kaolinite exhibits the highest enlargement: 3.6% as compared to hydroxides (10.1% as compared to undistorted O sheet) agreeing well with the value measured by structure refinement (10.1%, Bish & Von Dreele, 1989). Co-lizardite with the lowest octahedral enlargement (- 3.7% and 2.3% compared to hydroxide and to undistorted O sheet, respectively) has the thickest O sheet of the family. The linear regression observed between kaolinite and lizardite (Fig. 6B and *(K-L)* line Fig. 5A) suggests an increase of the size of the vacant site with an increase of *R* for dioctahedral samples.

The few Al- and Fe^{3+}- serpentines with a rather low rate of tetrahedral substitutions that lay on (or close to) the (*K-L*)' line, *i.e.* brindleyite, pecoraite, and synthetic R^{2+}-Al- serpentines (Fig. 6A) behave similarly to the kaolinite and lizardite family. These Al-serpentines exhibit a high number of octahedral vacant sites, possibly increasing the plasticity of the octahedral sheet compared to the other serpentines.

Focus on the Al- and Fe^{3+}- serpentines family. The samples that are scattered between the (*K-L*) and (*G-C*) lines exhibit a high misfit due to relatively small O sheet lateral dimensions (small *R*) compared to large T sheet lateral dimensions due to tetrahedral substitutions. The T sheet dimensions have to decrease significantly to adjust to the O sheet. As for kaolinite and lizardite, this reduction of T sheet dimension with decreasing *R* is made by a progressive increase of the tetrahedral rotation angle α as evidenced by the *(G-C)'* and *(Fe^{3+}-serp)'* regressions (Fig. 6A). However, contrary to the kaolinite-lizardite series, the O sheet enlargement does not vary linearly with *R* and is relatively more pronounced than for kaolinite-lizardite (Fig. 6B). This explains the higher *b* relative to *R* observed for Al- and Fe^{3+}- serpentines compared to the kaolinite-lizardite series (Fig. 5A). In fact, in Al- and Fe^{3+}- serpentines, the

https://doi.org/10.1180/clm.2023.20 Published online by Cambridge University Press

O sheet enlargement is directly linked to the tetrahedral substitutions as shown by the plot of the O sheet enlargement *vs.* b_{tet} (Fig. 6C). Each of the two observed regressions (calculated using natural samples only) concerns mainly Al-serpentines or Fe^{3+}- serpentines and corresponds to the *(G-C)'* or *(Fe^{3+}- Serp)'* lines, respectively (Fig. 6A). The two regressions intersect for $b_{tet.}$ ~9.13 Å and % O enlargement ~-2.7 (~3.4% compared to a free O sheet). This $b_{tet.}$ value is close to the theoretical 9.15 Å value calculated for a free T sheet (e.g., Bailey (1981), Eq. 3). The % O enlargement is negative or close to 0 for amesite, meaning that O sheets are always thicker /never thinner in Al- and Fe^{3+}-serpentines than in their corresponding hydroxides (*i.e.* hydroxide with same *R*). For amesite, the ~0 % O enlargement compared to hydroxides means than the flattening of O sheet is as for hydroxides: ~6.3% compared to free O sheet, agreeing well with the structure refinement of amesite (Wiewiora et *al.*, 1991; Zheng & Bailey, 1997a).

In serpentine, when Tschermak substitutions (coupled tetrahedral R^{3+}/Si^{4+} to octahedral R^{3+}/R^{2+} substitutions) occur, there is a cumulative antagonistic effect of R^{3+}. Note, however, that in the case where Tschermak substitutions occur with coupled tetrahedral Al^{3+}/Si^{4+} to $^{VI}M^{3+}/Mg^{2+}$ substitutions, with $r(^{VI}M^{3+}) > r(^{VI}Al^{3+})$ such as for $^{VI}M^{3+} = {}^{VI}Fe^{3+}$, the antagonistic effect can be neutralized. The antagonistic effect of Al is well illustrated with the synthetic series $((Si_{2-x}Al_x)(Mg_{3-x}Al_x)O_5(OH)_4$ with $0 \leq x \leq 1$) of Chernosky (1975) (Table 3)). For this series, $b_{tet.}$ and $b_{oct.}$ are anticorrelated, making the misfit dramatically increase when *R* decreases (Fig. 6A). The lateral dimensions of O and T sheets are identical for $b_{tet.} = b_{oct.} = 9.33$ Å corresponding to $R = 0.690$, to x = 0.49, and to $b \sim 9.2$ Å. This x value has been widely discussed in the past, and an Al content corresponding to $x \approx 0.3$ (corresponding to $R \sim 0.702$) was proposed (Bates, 1959; Radoslovich, 1963; Chernosky, 1975; Caruso & Chernosky 1979). The difference between these two x values comes mainly from the values taken for M-O bond lengths calculations of $b_{tet.}$ and $b_{oct.}$.

Due to the antagonistic effect of Al, tetrahedral substitutions are not expected to release the misfit between T and O sheets in aluminous serpentines but will promote it further. Consequently, strong constraints are expected to occur for the Al-richest samples as a result of T and O sheet lateral dimension accommodation. Furthermore, for the Al-richest serpentine with an end-member amesite-like composition, T sheets contract significantly ($b/b_{tet.}$= 0.961 (Fig. 6A)), all the more so as O sheets enlargement is relatively limited (Fig. 6B). This contraction corresponds to an angle of tetrahedral rotations $\alpha \approx 16°$, a value that agrees well with $\alpha \approx 14$-$15°$ measured by structure refinement of natural amesite (Bailey, 1991b, Wiewiora *et al.*, 1991; Zheng & Bailey, 1997a). With increasing heterovalent substitutions, an increasing linkage by H bonding from layer to layer occur and the interlayer thickness decreases when the ditrigonalization of the T sheet increases (Mellini & Viti, 1994). Structural refinement of natural amesites also has indicated various cation ordering patterns. This cation ordering in addition to the electrostatic attraction between

https://doi.org/10.1180/clm.2023.20 Published online by Cambridge University Press

layers due to substantial tetrahedral substitutions, is believed to have a positive effect on the regularity of the stacking of layers in amesite (Bailey, 1991b). This may explain its platy morphology even though a curled morphology could be expected due to misfit constraints. This may also explain the existence of multilayer polytypes in serpentine with significant amount of trivalent cations. Accordingly, Chernosky (1975) observed 1 layer ortho cell structure for $0.05 \leq x \leq 0.375$ and 6 1ayer ortho cell structure for $x > 0.375$.

Focus on the phyllosilicates with corrugated structure. These samples follow the *(G-C)* and *(G-C)'* lines (Fig. 5A and 6A) and the high misfit is due to O sheet lateral dimensions higher than T sheet lateral dimensions. In greenalite and caryopilite, high $b_{oct.}$ are due to large octahedral cations such as Fe^{2+} and Mn^{2+}, whereas $b_{tet.}$ are relatively low compared to Al- and Fe^{3+}- serpentines due to negligible tetrahedral substitutions. The stretching of the T sheet attains its limits constraining the O sheet to curl and the T sheet to be discontinuous, forming modulated layers. It is worth noticing that for these TO phyllosilicates the %O enlargement is similar to those of equivalent hydroxides (Fig. 6B). Detailed description of the various n-ring arrangements to accommodate misfit in modulated 1:1 layer silicates can be found in literature (Guggenheim & Eggleton, 1991, 1998) and will not be discussed here.

Impact of misfit on layer curling and morphology. Layer curling arises because of the complex interplay between chemical composition and structural adjustments required to achieve articulation between the O and T sheets. From the above results, it is hypothesized that samples close to the $b/b_{tet.}$ line = 1 correspond mostly to samples with flat morphology. The misfit between the O and T sheets dimensions are mainly accommodated by tetrahedra rotation to reduce T sheet dimension. The existence of vacant sites also probably increases the plasticity of O sheet facilitating its lateral dimension increase. Exceptions must be made as for chrysotiles (Fig. 6A) which exhibit non-flat morphology (cylindrical morphology, Fig. 4B). Only three data were available, and samples are synthetic and may not be representative. However, the curling observed in chrysotile is not due to misfit between T and O sheet dimensions but rather to reaction kinetics, with chrysotile occurring as a metastable form of a serpentine (Evans, 2004; Andréani *et al.*, 2008). Accordingly, Jasmund & Sylla (1971) observed that tubes of synthetic Mg- and Ni-chrysotiles transformed to platy Mg- and Ni-antigorites with increasing reaction time. An analogy, previously highlighted by Bates (1959), can be made with halloysite (which is not represented in this study, *b* and *R* being similar to kaolinite). Halloysite probably curled for the same reason as chrysotile. Indeed, the morphology of halloysite, which can be tubular, spheroidal, onion-like, crumpled lamellar and so on, but also platy, is related to crystallization conditions and

https://doi.org/10.1180/clm.2023.20 Published online by Cambridge University Press

geological occurrences (Joussein *et al.*, 2005). Notably, synthetic kaolinites can also exhibit spherical metastable particles precipitating from solution with a high degree of supersaturation (e.g. Fiore *et al.*, 1995).

For samples with $b/b_{tet.}$ <1 (Fig. 6A), the T sheet is compressed, constraining the O sheet to increase its lateral dimensions by flattening the octahedra, as described above. If layers curl, the O sheets are always on the convex side of the layer. However, in Al- and Fe^{3+}- serpentine, the increase of heterovalent substitutions induces the increase of electrostatic attraction between layers, and an ordering of cations distribution, favoring flat morphology.

It is tempting to further discuss the morphology of serpentines as a function of misfit, as examined earlier by many authors (e.g., Pauling, 1930; Bates, 1959; Radoslovich, 1963; Bailey, 1966). However, the simple approach developed here cannot replace detailed structural studies to determine the actual structure and morphology of TO layer silicates. For example, some serpentines, such as polygonal serpentines, may appear as fibers but are composed of 1:1 flat layers (Baronnet *et al.*, 1994; Mellini, 2013), and reversely, structural modulation can account for apparently plate-like particles (Guggenheim & Eggleton, 1991). Moreover, mixtures of several morphologies are often reported in synthetic series (Chernosky, 1975; Bentabol *et al.*, 2013) as well as in natural samples (Capitani *et al.*, 2021).

TOT phyllosilicates

Pyrophyllite - talc. Pyrophyllite and talc are TOT layer silicates composed of electro-neutral stacked 2:1 layers formed by two T sheets sandwiching one O sheet (Fig. 7A). These two minerals correspond to the Al-dioctahedral and Mg-trioctahedral end-members, respectively, having the general SF of Si_4 (R^{3+}, R^{2+}, □)$_3$ $O_{10}(OH,F)_2$, with R^{3+} being mainly Al, R^{2+} being mainly Mg but could be very different, and □ being a vacant site. In the present study, kerolites were also included in this group because these clay minerals are considered hydrated (but disordered) talc-like minerals (Brindley *et al.*, 1977). Available data found in the literature for this group of minerals cover a small chemical variability (Table 4). For dioctahedral minerals, only pyrophyllite, with limited Fe^{3+} substitutions, and ferripyrophyllite, are reported to occur, with ferripyrophyllite exhibiting the highest R and b. For trioctahedral phyllosilicates, Ni-talc exhibits the lowest R and b. Natural talcs with significant amounts of Fe and Ni are not rare. The Mg-Ni solid solution is complete in talc (talc-willemseite sequence) and kerolite (kerolite-pimelite sequence), whereas the Fe^{2+}-Mg solid solution is limited to ((Fe^{2+}/(Fe^{2+}+Mg)) values near 0.4 for natural as well as synthetic minerals (Corona *et al.*, 2015). Minnesotaite, a chemically Fe^{2+} talc-like end-member is reported here but it displays a modulated structure (Guggenheim & Bailey, 1982; Guggenheim & Eggleton, 1986, 1987). Synthetic talcs with other

https://doi.org/10.1180/clm.2023.20 Published online by Cambridge University Press

divalent octahedral cations, such as Co (complete solid-solution), Zn, and Cu (limited solid-solution), can be synthesized (e.g., Wilkins & Ito, 1967). Unfortunately, detailed XRD data are not available for these minerals. Except minnesotaites and some natural kerolites, data for natural and synthetic samples appear quasi-aligned on a line joining dioctahedral (*i.e.* pyrophyllite) and trioctahedral (*i.e.* talc) end-members on the *b* vs. *R* plot (Fig. 8A). This agrees with the work of McEwan (1961), who deduced a coefficient proportional to the ionic radius of Mg and Al from the pyrophyllite-talc pair that can be used to calculate *b* by multiple regression. The *b vs. R* regression for the pyrophyllite-talc (*P-T*) line, calculated using pyrophyllite and the three natural talc samples (Mg, Antwerp Fe^{2+}-substituted talc, and Ni^{2+}- substituted talc *i.e.* willemseite - Table 4) is excellent, and leads to the relation $b = 1.1162.R + 8.3691$ (Fig. 8A).

Another regression was calculated using the synthetic Fe^{2+}-Mg talc (Forbes, 1965) and Ni-Mg kerolite series (Baron, 2016a) only, and the equation is similar to the former one (Fig. 8A), the slight difference being possibly due to the lower crystallinity of samples.

Ferripyrophyllites follow the general trend (Fig. 8A), but data selected here appear prone to bias given that the three available SFs exhibit a deficit of layer charge, probably due to impurities (Table 4). Accordingly, Chukhrov *et al.* (1979a) identified approximately 5% smectite in their ferripyrophyllite sample, justifying the Ca presence in the SF to balance the layer charge. Coey *et al.* (1984) studied the same sample by Mössbauer spectroscopy and revisited its SF, attributing more Fe^{3+} to T sheet (Table 4). However, in light of recent studies, (i) the partition coefficient of Al^{3+} and Fe^{3+} between tetrahedral sites in dioctahedral smectites indicated a strong preference of Al^{3+} to substitute for Si in T sheet (Decarreau & Petit, 2014), and (ii) Mössbauer spectroscopy was shown to be inadequate for quantifying tetrahedral Fe^{3+} in smectite if its content was unknown (Baron *et al.*, 2017). Consequently, it appears that the SF given by Chukhrov *et al.* (1979a) is probably more suitable than the SF revisited by Coey *et al.* (1984).

Some natural kerolites deviate from the general trend (Fig. 8A). As mentioned above, kerolite differs from talc by their water content, possibly due to a small charge occurrence due to octahedral vacant sites resulting in some swelling properties. Some natural kerolite samples were also characterized as talc-stevensite mixed-layer minerals (Maksimovic, 1966; Brindley *et al.*, 1977; Eberl *et al.*, 1982; Pozo & Casas, 1999). In fact, their deviation from the pyrophyllite-talc regression line may reflect the degree of their "smectitic" character. Accordingly, the P-7 kerolite (Eberl *et al.*, 1982; Table 4), possessing the highest charge of the kerolite group of this study, and in which the authors identified 30% expandable layers, is the farthest above the *(P-T)* line. These results suggest that the occurrence of a negative octahedral charge in trioctahedral TOT clay minerals tends to induce a decrease in *b*.

https://doi.org/10.1180/clm.2023.20 Published online by Cambridge University Press

Minnesotaites are dramatically out of trend and exhibit higher *b* than expected from *R* (Fig. 8A). This can be seen as reminiscent of the roles played by structure and morphology on crystal parameters, similarly to TO phyllosilicates with corrugated structures (see below).

Calculated with the same data than for the (*P-T*) line, the regression for the (*P-T*)' line is $b/b_{tet.} = 0.122.R + 0.9144$ (Fig. 8B). The similarity between Fig. 8A and Fig. 8B is obviously related to the negligible amounts of tetrahedral substitutions for the pyrophyllite-talc family. The lower $b/b_{tet.}$ is 0.984 for pyrophyllite. The calculated tetrahedral rotation angle $\alpha \approx 11.6°$, in agreement with that determined by structure refinement ($\alpha \approx 10°$) (Evans & Guggenheim, 1991), allows the lateral dimensions of T sheets to be reduced to adjust to the smaller O sheets. When *R* increases, $b/b_{tet.}$ linearly increases to a value slightly higher than 1, thus indicating that the mismatch between the T and O sheet lateral dimensions progressively decreases, as discussed above for TO phyllosilicates. Accordingly, the angle of tetrahedral rotations α is low, ~3.6° in talc (Perdikatsis & Burzlaff, 1981). The synthetic Fe^{2+}-richest talc (with octahedral composition: $Mg_{2.4}Fe^{2+}_{0.6}$) exhibits the highest $b/b_{tet.}$ (1.008). Note that the natural Antwerp talc contains a similar Fe^{2+} amount, but the presence of octahedral Al and Fe^{3+} tends to lower *R* (Table 4). The continuous increase in $b/b_{tet.}$ with *R* implies a progressive decrease in tetrahedral rotation angle approaching 0° with T sheets maximally stretched for the highest *R* (*i.e.* Fe^{2+}-rich talc). Although a miscibility gap between Fe^{2+}-rich talc and minnesotaite, if one exists, has not been determined, between the limit *R* value ~ 0.74 (Fe^{2+}-rich talc) and ~0,76 (minnesotaite), the misfit between the T and O sheets is too high (high $b/b_{tet.}$ Fig. 8B), and the constraints are released by structural modulations inducing the development of a superlattice for minnesotaite (Guggenheim & Eggleton, 1986). Minnesotaite has a continuous O sheet with adjacent Si tetrahedra on each side. Tetrahedral strip widths are narrow, namely, three and four tetrahedra wide, compared to the seven tetrahedra found across the island in greenalite (Guggenheim & Eggleton, 1986). This is consistent with the smaller $b/b_{tet.}$ measured for minnesotaite (~1.03) compared to greenalite TO phyllosilicate (~1.05).

The excellent linear relation, according to the *(P-T)* line, observed between O sheet enlargement (Eq. 6) with *R* for all samples, except minnesotaites and the out of trend kerolite P-7 (Fig. 8C), indicates that O sheet thinning (and thicking compared to hydroxides) acts together with tetrahedral rotation angle to attain congruency between T and O sheets dimension, as observed for the kaolinite-lizardite family (Fig. 6B). The O sheet enlargement increases progressively with a decrease of *R* from -3.6% to 3.8% compared to hydroxides (2.5% and 10.3% compared to an ideal unconstrained O sheet, respectively) (Fig. 8C), a null value being obtained for $R = 0.635$, corresponding well to ferripyrophyllite. According to the results above, the crystal structure refinement of a Mg-talc has indicated that the O

https://doi.org/10.1180/clm.2023.20 Published online by Cambridge University Press

sheet was thinner than the ideal dimensions, and that O sheet flattening occurs before the T sheet is maximally stretched (α ~3.6°) (Perdikatsis & Burzlaff, 1981).

Two compositional gaps are observed between the pyrophyllite and talc end-members for R from ≈ 0.54 to ≈ 0.65 and from ≈ 0.65 to ≈ 0.69 (Fig. 8A, B, C). For the former range, all values of R could be taken by varying the Al^{3+}/Fe^{3+} ratio, suggesting that the pyrophyllite-ferripyrophyllite solid solution is limited due to the respective contrasted geological occurrence of the two end-members: mainly low grade Al-rich metamorphic rocks for pyrophyllite (Deer *et al.*, 2009), and precipitation from low temperature Fe-rich hydrothermal fluids for ferripyrophyllite (Badaut *et al.*, 1992, Chukhrov *et al.*, 1979b).

The second range of R values corresponds to the "di-trioctahedral region", with the highest value for the dioctahedral end-member being $R = 0.645$ (for $r(^{VI}Fe^{3+})$ and the lowest value for trioctahedral end-members being 0.69 ($r(Ni^{2+})$ (Table 1). Neutral di-trioctahedral structures would then require Tschermak substitutions and/or extra octahedral vacant sites to neutralize the charge due to heterovalent substitutions. Tschermak substitution would create stress within the structure due to the antagonistic effect of the trivalent cations on the misfit, as discussed above for TO phyllosilicates. However, in contrast to TO structures, excessive out-of-plane tilting of tetrahedra in TOT phyllosilicates cannot occur because the identical sheets on opposite sides of a neighboring O sheet hold it flat under tension (Guggenheim & Eggleton, 1986). To our knowledge, no neutral di-trioctahedral TOT layer silicates have been reported to occur up to now.

Smectites. Smectites are TOT clay minerals with a negative layer charge generally ranging between 0.2 and 0.6 pfu due to isomorphous octahedral and/or tetrahedral heterovalent substitutions. This charge is balanced by the presence of cations located in the interlayer space, whereas hydration of the cations leads to the intercalation of zero to several water sheets (Fig. 7B) (e.g., Ferrage, 2016). The general SF takes the form of $(Si_{4-x}R^{3+}_x)(R^{3+}_aR^{2+}_bR^{+}_c\square_d)O_{10}(OH)_2\ M_y$, where a+b+c+d = 3 and y = x-3a-2b-c+6 if the interlayer cation M is monovalent. Smectites present a high variability in chemical compositions, density and location of layer charge, giving rise to numerous end-members with dedicated terminology (e.g. Brigatti *et al.*, 2013).

The dataset used is representative of the large compositional range encountered for both natural and synthetic smectites (Table 5). Vermiculite, though generally composed of macroscopic particles (e.g. de la Calle & Suquet, 1991) was added in this category because it has the same SF than smectite with y>0.6, and cannot be distinguished from high charge saponite in its swelling properties (Suquet *et al.*, 1977).

https://doi.org/10.1180/clm.2023.20 Published online by Cambridge University Press

Especially for smectites that are typically finely divided clay minerals, *b* and *R* are probably less reliable than for the other phyllosilicates. No single crystal structure refinements have been carried out on smectites and *b* was mostly measured from the direct measurement of the (06ℓ;33ℓ) band. Using a Rietveld simulation of XRD traces of smectites synthesized by Andrieux *et al.* (2010), Heuser *et al.* (2013) found *b* significantly higher than those obtained from the (06ℓ;33ℓ) band (Petit *et al.*, 2015) (Table 5). The nature of the interlayer cation and the hydration state were also shown to induce variation in *b* up to 0.03 Å (Suquet *et al.*, 1981). SF must also be viewed cautiously due to:

- (i) difficulty in obtaining pure smectite, admixtures affecting its chemical composition.
- (ii) chemical heterogeneity within a given sample. Several populations of smectites may occur in the same sample, and the resulting *R* and *b* measured thus represent mean values. For example, Ferrage *et al.* (2007) identified two populations of beidellites in a dioctahedral smectite, while the Ölberg iron-rich smectite first studied by Köster *et al.* (1999) was shown to be heterogeneous, being constituted by Fe^{3+}-montmorillonite and smectite with some tetrahedral charge and with less Mg and more Al than Fe^{3+}-montmorillonite (Petit *et al.*, 2002).
- (iii) chemical heterogeneity between samples from a given site. As an illustration, the SF of the Manito nontronite revealed 0.21 ^{VI}Al and 0.1 $^{VI}Fe^{2+}$ in Köster *et al.* (1999), while no $^{VI}Fe^{2+}$ and only 0.03 ^{VI}Al was proposed by Radoslovich (1962), both leading to different but coherent values (0.642 and 0.644 for *R* and 9.125 and 9.155 for *b,* respectively) (Table 5). Similar observations can be made for some other smectites (Otay montmorillonite, Black Jack mine beidellite, Garfield nontronite).
- (iv) difficulty in evaluating the actual rate of tetrahedral substitutions.
- (v) redox state.

Despite these limitations, the plot of the *b vs. R* reveals that the samples generally follow the pyrophyllite-talc (*P-T*) trend (Fig. 9A). The scattering of data may be mostly related to layer charge occurrence in smectite. For example, for the synthetic Fe^{3+}-nontronite series $(Si_{4-x}\,Fe^{3+}_{x})\,Fe^{3+}_{2}O_{10}(OH)_2Na_x$ (with $0.43 \leq x \leq 1.54$), where tetrahedral iron was the only variable parameter, *R* is constant, while *b* increases with the tetrahedral iron content (Fig. 10A), leading to vertical dot alignment on the *b vs. R* plot (green triangles in Fig. 9A). A similar observation is made for natural and synthetic saponites (respectively light green squares and triangles in Fig. 9A). For the synthetic saponite series with the general SF $(Si_{4-x}Al_x)(Mg_{(3-y)}Al_y)Na_{x-y}$ with $0.33 \leq x \leq 1$ and y=0 and 0.2, giving *R* of 0.720 and 0.708, respectively, Suquet *et al.* (1981) established the following relationship: $b = 9.174 + 0.079\,^{IV}Al - 0.07\,^{VI}Al$. Tetrahedral Al increases *b*, while octahedral Al decreases *b*. For y=0, x corresponds to the layer charge and to the ^{IV}Al content, and *b* increases linearly with it (Fig. 10B). For y=0.2, the variation appears to be non-rigorously linear (Fig. 10B).

https://doi.org/10.1180/clm.2023.20 Published online by Cambridge University Press

Unfortunately, without having strong confidence in the accurate ^{IV}Al and ^{VI}Al contents (Suquet *et al.*, 1977), no farther discussion can be made.

The vertical dot alignments are also observed on the $b/b_{tet.}$ *vs*. R plot (Fig. 9B). Most of the samples lay below the *(P-T)'* line. Those which are the most above the line are synthetic samples that display $b/b_{tet.}$ higher than 1 and are suspected to be problematic. Small underestimation of the tetrahedral charge may induce a deviation from the (*P-T*)' line. For example, modifying the ^{IV}Al content from 0.46 to approximately 0.62 for sample A of Chemtob *et al.* (2014), which exhibits the highest deviation, would place it on the (*P-T*)' line.

The specific influence of the tetrahedral composition when R varies, even in a simple system, is difficult to measure. For the synthetic Al–Fe^{3+} smectitic series $(Si, Al)_4$ $(Fe^{3+}_{(2-x)}Al_x)$, with 0 to 1.66 Al and 0.34 to 2 Fe^{3+} (Petit *et al.*, 2016; Table 5), b increases with R (*i.e.*, with increasing octahedral Fe^{3+}) with a higher slope compared to the (*P-T*) line (Fig. 9A). For this series, Petit *et al.* (2016) observed that tetrahedral substitutions were dominated by Al except when total Fe exceeded 1.8 pfu and that tetrahedral and octahedral Fe^{3+} had a similar (and inseparable) effect on b. The specific role of tetrahedral Al could not be quantitatively measured (see the review of Petit *et al.* (2017)). A similar observation can be made for the Ga–Fe^{3+} smectitic series (Table 5), whose dots are aligned too on a slope higher than that of the regression (*P-T*) line (Fig. 9A) and whose b was correlated to total Fe^{3+} (Petit *et al.* 2016). For these Ga–Fe^{3+} smectites, the high $b/b_{tet.}$ slope (Fig. 9B) is due to the combined effect of the increase in $b_{oct.}$ due to the relative increase in octahedral Fe^{3+} and the decrease in $b_{tet.}$ due to the decrease in tetrahedral Ga^{3+}. Various relations linking b with iron content are available in the literature for iron-rich natural smectites (e.g., Heuser *et al.*, 2012) and generally work well, at least when Fe^{3+} is the dominant cation. Brigatti (1983) observed a linear correlation between total iron and b but for $Fe^{3+} > 0.5$ pfu only.

For the natural beidellite sample series from Post *et al.* (1997), b does not follow the general (*P-T*) trend. Indeed, b decreases as R increases (dark blue circles, Fig. 9A), related to the fact that the R and Al contents of beidellites vary inversely. b increases linearly with increasing tetrahedral Al (Fig. 10C), resulting in a $b/b_{tet.}$ that is exactly the same for the four samples (0.9716 ±0.0001) (Fig. 9B). Such a $b/b_{tet.}$ corresponds to an angle of tetrahedra rotation $\alpha \approx 13.7°$ that is in the same range as that measured in aluminous dioctahedral TOT phyllosilicates (pyrophyllite and micas). By analogy with the afore-mentioned other phyllosilicates structures, it is hypothesized that T sheets adjust their lateral dimensions by tetrahedral rotation to match those of the O sheet, and all the more so as they are further below the (*P-T*)' line (Fig. 9B).

https://doi.org/10.1180/clm.2023.20 Published online by Cambridge University Press

The %O enlargement *vs. R* plot reveals an excellent alignment of samples along the line determined for neutral TOT structures (Fig. 11), indicating that smectite samples follow well the same trend than for pyrophyllite-talc. However, it can be observed that samples that are above the line are mainly with dominant tetrahedral charge (e.g., beidellites, nontronites, saponites, sauconites, vermiculites) (Table 5). These samples are those located above the *(P-T)* line (Fig. 9A), *i.e.* with b higher than they should be in regard to R. The thinning of O sheets by octahedral flattening is relatively higher than for neutral phyllosilicates to facilitate dimensional congruency between T and O sheets, $b_{tet.}$ having higher values due to tetrahedral substitutions.

In a lesser manner, smectites with dominant octahedral layer charge (e.g., montmorillonites, stevensites, hectorites), are rather below or on the pyrophyllite-talc line (Fig. 11), as the intermediary Fe^{3+}-Mg natural smectitic series (Gaudin *et al.*, 2004) and the Fe^{3+}-Mg synthetic series (Grauby *et al.*, 1995) that possess an almost constant layer charge from an octahedral origin. For samples located below the (*P-T*) line (Fig. 9A), b are lower than they should be in regard to R, and it can be hypothesized that the flattening of octahedra is less compared to neutral TOT phyllosilicates.

When considering the whole series of samples, R covers the entire compositional range from dioctahedral to trioctahedral smectites and, contrary to neutral TOT phyllosilicates, no compositional gaps could be observed (Fig. 9 and 11). The possibility of having various tetrahedral compositions and balancing the negative layer charge by interlayer cations allows to sweep a very large range of compositions, including di-trioctahedral smectites. The variability of chemistry and type of layer charge compensation, associated with the difficulty of accounting for the wide range of tetrahedral charge through the $b/b_{tet.}$, make it inappropriate to propose a general regression correlating the b to R for smectites. One may thus assume that (*P-T*) correlation line can apply as a first-order relation, but with a higher degree of uncertainty compared to other mineral families. To go a step further, one could derive, however, specific sub-correlations as done for beidellites or saponites (Fig. 10B and 10C).

Micas.

Micas are 2:1 phyllosilicates having general SF similar to that of smectites but with a negative layer charge ~1 pfu (true micas) or ~2 pfu (brittle micas), balanced by anhydrous monovalent interlayer cations (mostly K^+) in true micas and divalent interlayer cations (such as Ca^{2+} and Ba^{2+}) in brittle micas (Fig. 7). Illite, phengite, glauconite, and in a lesser extent celadonite, are non-expanding interlayer deficient mica-like minerals. Isomorphic substitutions in O and T sheets and interlayer spaces vary and are used to define the complex nomenclature of micas and mica-like minerals (Bailey, 1984a; Brigatti *et al.*, 2013). Note that the substitution of OH^- by F^- is also common and complicates the

https://doi.org/10.1180/clm.2023.20 Published online by Cambridge University Press

system even more. Many names and varieties have been previously used, as seen for the sample series of Radoslovich & Norrish (1962) (Table 6), sometimes erroneously (Bailey, 1984b; Rieder *et al.*, 1998). Several synthetic and natural sample series, which cover a very wide range of compositions, were considered in the present study (Table 6). The Al end-member muscovite used here was issued from an average of 12 end-member synthetic muscovites (Guidotti *et al.*, 1992).

A global trend correlating *b* with increasing *R* was observed with a strong scattering of data. The two main sub-correlations were plotted for more clarity (Fig. 12A): (i) The muscovite-phlogopite line (*M-Ph*) ($K(Si_3Al_1)(Al_{2-x}Mg_{3x/2})O_{10}(OH)_2$), with the relation $b = 1.1478.\ R + 8.3794$, calculated using the synthetic muscovite and phlogopite end-member data (x=0 and 2, respectively), and the phlogopite-annite line (*Ph-A*) ($K(Si_3Al_1)(Mg_{3-x}Fe^{2+}_x)O_{10}(OH)_2$, with the relation $b = 2.3942.\ R + 7.4821$, calculated using the synthetic phlogopite and annite end-member data (x=0 and 3, respectively, Table 7). Accordingly, the true micas with tetrahedral Al and K contents with the 0.8 to 1.2 pfu compositional window are located on or not so far to these lines. The synthetic Mn-mica end-member exhibits the highest *R* and *b* and is relatively close to the (*M-Ph*) line. Contrarily, interlayer deficient micas (^{IV}Al-poorest micaceous samples), Na-micas, brittle micas, and synthetic ferri-annites and Ge-micas are generally significantly located far from the (*M-Ph*) and (*Ph-A*) lines (Fig. 12A).

Dots for Li-bearing micas are strongly scattered (Fig. 12A). However, a deeper analysis of the data shows that *b* globally decrease with increasing Li content (Fig. 13A) but increase with increasing ^{IV}Al content (Fig. 13B), with Li and tetrahedral Al being well negatively correlated (Fig. 13C). These correlations decidedly illustrate (i) the impact of Li content on *b*, and (ii) that the chosen value for $r(^{VI}Li^+)$ used in the calculation of *R* is critical for these samples. Indeed, the choice of a $r(^{VI}Li^+)$ close to that of other octahedral cations (e.g., Mg or Fe^{2+}) can reduce the range of obtained *R*, whereas an enhanced contrast between $r(^{VI}Li^+)$ and that of other cations can lead to a spreading of calculated *R*. In the present case (Fig. 13D), the *b vs*. *R* dataset appears rather shrunken, likely asserting an overestimation of the chosen $r(^{VI}Li^+)$ at 0.76 Å (Table 1; Shannon, 1976). The ionic sizes for Li cation in other coordination numbers, such as $r(^{IV}Li^+)$ and $r(^{V}Li^+)$, are 0.59 Å (Shannon, 1976) and 0.69 Å, respectively (Brown & Shannon, 1973). This could help to enlarge the *R* window, but structure refinement of the studied micas excludes their occurrence (Brigatti *et al.*, 2000, 2001, 2007). As discussed above for Mn in groutite, Li octahedra are probably considerably distorted in Li-rich micas. However, the maximum distortion for octahedra in M-O bonds is limited to ≈ 10^{-3} Å (Brown & Shannon, 1973) and alone cannot account for the potential decrease in the $r(^{VI}Li^+)$ size. For Li-micas, the substitution of OH^- by F^- is common, and the value of $r(^{VI}Li^+) = 0.685$ Å, as in LiF, was tested and

https://doi.org/10.1180/clm.2023.20 Published online by Cambridge University Press

improves the correlation between b and R (Fig. 13E). Lowering the values of $r(^{VI}Li^{+})$ gradually down to $r(^{VI}Li^{+})$ = 0.535 Å further improves the regression coefficient (Fig. 13D-F). Radoslovich (1962) observed that for Li-micas, Li behaves similar to Al with regard to the variation in b with composition, and he used a $r(^{VI}Li^{+})$ = 0.60 Å. A low $r(^{VI}Li^{+})$ is found in the Li_3AlF_6 perovskite-like structure, where ^{VI}Li–F bond lengths of 1.95 Å were measured (Jain *et al.*, 2013), leading to $r(^{VI}Li^{+})$ = 0.62 Å (with $r(F^{-})$ = 1.33 Å). In contrast, Weiss *et al.* (1985) found good agreement between the mean fictive ionic radii calculated from 66 refined crystal structures of micas, including Li-bearing ones, and the crystal radii of Shannon (1976). However, Bailey (1984b) observed that the relative ratio of large octahedra (especially Li^{+} with the crystal radii of Shannon (1976)) over small octahedra measured by structure refinement is not always in agreement with the ratio of large to small octahedral cations present. In such a case, the ordering pattern with Li occurring both in small and large sites has been described in lepidolites, agreeing well with the suitability of a lower $r(^{VI}Li^{+})$ than that proposed by Shannon (1976). Regarding the correlative approach used in the present study, an estimated $r(^{VI}Li^{+})$ at ~0.6 Å is suggested to be adequate. Accordingly, the whole b *vs.* R dataset shown in Fig. 12A can be replotted considering $r(^{VI}Li^{+})$ = 0.6 Å (Fig. 12B), and the dots for Li-micas are logically less scattered and closer to the global trend. In addition, the compositional gap situated at $0.610 < R < 0.650$ for $r(^{VI}Li^{+})$ = 0.76 Å (Fig. 12A) now disappears (Fig. 12B). The scattering of Li-micas dots is also significantly reduced comparing the $b/b_{tet.}$ *vs.* R and the %O enlargement *vs.* R plots for the two values of $r(^{VI}Li^{+})$ (not shown for $r(^{VI}Li^{+})$ = 0.76 Å), arguing for the suitability of a $r(^{VI}Li^{+})$ close to 0.6 Å, agreeing well with Radoslovich (1962).

As discussed above, the apparent dependence of the rate of tetrahedral substitutions on b observed for Li-micas (Fig. 13B), actually issued from Li, Li being negatively correlated to tetrahedral Al (Fig. 13C), and cannot be generalized for the entire mica group. Indeed, true micas display similar tetrahedral trisilicic compositions but contrasted b, as obviously illustrated by b of muscovite (~8.99 Å) and phlogopite (~9.20Å) (Table 6). However, the various tetrahedral substitution rates are certainly responsible for some data scattering (as for smectites), as revealed through the comparison between b and $b/b_{tet.}$ *vs.* R plot (Figs. 12B and 14A, respectively). Two main trends between $b/b_{tet.}$ and R are revealed (Fig. 14A). One trend follows the (*Ph-A*)' line, which was simply calculated using the same data as that for (*Ph-A*) and the trisilicic composition for the $b_{tet.}$ value and is mostly concerned with trioctahedral micas in a limited R range ($0.670 < R < 0.780$). The second trend follows a curve that continuously links dioctahedral to trioctahedral K-micas and involves micas with various compositions, including Li-micas, and micaceous samples. Two main trends are also observed in the %O enlargement *vs.* R plot (Fig. 14B). One trend follows the (*M-Ph*)° line, plotted using the muscovite and phlogopite end-members, and mostly concerns micas with full interlayer, no matter of

https://doi.org/10.1180/clm.2023.20 Published online by Cambridge University Press

their dioctahedral or trioctahedral nature. The second trend, with a higher slope, mostly concerns the interlayer depleted micas *i.e* glauconites, celadonites, illites, and phengites, and indicating that the O sheets are thicker for a same *R* in these micaceous samples. The three *b vs. R* (Fig. 12B), $b/b_{tet.}$*vs. R* (Fig. 14A), and %O enlargement *vs. R* (Fig. 14B) plots indicate that for most of micas, the octahedral flattening is mainly controlled by *R* and that it gradually decreases with decreasing misfit between the T and O sheets, as suggested by Toraya (1981).

Some samples do not follow these general trends: mainly Na-micas, most of brittle micas, and synthetic Ge micas and ferri-annites.

In the Al side ($0.535 \leq R \leq 0.560$), Na-micas *i.e*. paragonite and ephesite (a trioctahedral mica with ideal SF of $(Si_2Al_2)(LiAl_2)(OH)_2Na$), and brittle Ca-micas, *i.e.* margarite and bityite (a trioctahedral mica with ideal SF of $(Si_2AlBe)_4(LiAl_2)(OH)_2Ca$)), exhibit lower *b*, $b/b_{tet.}$and %O enlargement values than muscovite. This indicates a significant influence of the nature of the interlayer cation on *b* and a more limited accommodation of the O sheets to increase their lateral dimensions compared to their K-counterpart. Accordingly, small interlayer cations such as Na and Ca allow larger tetrahedral rotations than K^+ that appears to induce a stretching of the O sheets (Bailey, 1984b). Muscovite exhibits a $b/b_{tet.}$ of ~0.96 (α ~15°) whereas margarite, bityite, and ephesite exhibit the lowest $b/b_{tet.}$, corresponding to α as high as 20-23°; these values have been confirmed by structure refinements (Guggenheim, 1984; Brigatti & Guggenheim, 2002).

In brittle micas, the T sheets are much larger than the O sheets due to the high rate of tetrahedral substitutions (~2Al pfu., Table 6), and the large tetrahedral rotations reduce the T sheet dimensions. Paragonite also has a relatively large α (~17°) due to the small size of the interlayer Na (Guggenheim, 1984). Note that nanpingite (ideally, the muscovite Cs- counterpart) follows well the *(M-Ph)* trends (Fig. 12B, 14A, 14B).

On the trioctahedral side, the Na-mica (preiswerkite) and Ca-micas (clintonite, also previously named xanthophyllite, Table 6), exhibit lower *b*, $b/b_{tet.}$and %O enlargement values than their K counterparts, as observed for the Na- and Ca- Al-rich micas. Accordingly, preiswerkite and clintonite exhibit $b/b_{tet.}$ corresponding to large α, respectively ~17°, and ~21°, agreeing pretty well with the values determined by structure refinement, respectively ~20° and 23-25° (Brigatti & Guggenheim, 2002).

Brittle Ba-micas *i.e.* kinoshitaites and anandites exhibit different behaviors. Kinoshitaites globally follow the trend of the K-micas with similar *R*, according to similar size of Ba and K interlayer cations (Shannon, 1976). On the other hand, anandites exhibit higher *b* (Fig. 12B) and %O enlargement (Fig.14B) than their K counterparts. This is mainly due to their high content of tetrahedral iron that induces a large T sheets dimension. Consequently, the O sheet has to

https://doi.org/10.1180/clm.2023.20 Published online by Cambridge University Press

enlarge comparatively more than the Al micas to reduce the dimensional misfit. The same observation is made for the synthetic tetra-ferri-annites (ideally $(Si_{3.0}\ Fe^{3+}_{1.0})\ (Fe^{2+}_{3.0})\ O_{10}\ OH_2\ K$), whose Cs-form has the largest unit-cell volume reported to date for 1M micas (Brigatti & Guggenheim, 2002).

For synthetic Ge-micas, due to the respective ionic radii of Ge^{4+} and Si^{4+} (0.39 Å and 0.26 Å, respectively, Table 1), *b* are higher than their silicate counterparts (Figs. 12 and 15A), whereas $b/b_{tet.}$ being lower (Figs. 14A and 15B). Accordingly, Martin *et al.* (1992) observed an increase in the angle α for synthetic Mg- Ni- and Co- SiGe talcs tetrahedral solid-solutions when the germanium content increases. As expected to adjust the O sheet dimension to the larger T sheets, the %O enlargement is higher for Ge-micas than for Si-micas for a same *R* (Figs. 14B and 15C).

In an effort to assess the origin of the observed trends, a focus is made on synthetic micas because their chemical composition is less complex than that in natural systems and because chemical joins are available (Fig. 15A). The dataset of synthetic mica samples reveals general trends similar to those of natural mica samples (Figs. 12 and 14). The $b/b_{tet.}$ versus *R* plot for all the synthetic samples reveals two main distinct but parallel trends for dioctahedral (muscovite-aluminoceladonite) and trioctahedral micas (phlogopite-annite) (Fig. 15B). However, data for synthetic micas are lacking, especially for the compositional range corresponding to $R \approx 0.650$. In natural micas, this compositional gap is filled by Li-micas and by celadonites and glauconites (Fig. 12B and 14B).

Except for the Ni-mica, which is on the (*M-Ph*) and (*M-Ph*)' lines, all the trioctahedral trisilicic micas, including the rather "exotic" Cu^{2+}- and Co^{2+}- micas (Hazen & Wones, 1972), are on or close to the (*Ph-A*) correlation line (Fig. 15A) and are also located near the (*Ph-A*)' line owing to their similar tetrahedral Al content (Fig. 15B).

The synthetic Mn-mica roughly follows the muscovite-phlogopite trend in the *b*, $b/b_{tet.}$, and %O enlargement *vs R* plots (Fig. 15A-C). The %O enlargement is the smallest of all the dataset (-6% compared to hydroxides) and correspond to the thickest O sheet very close to the dimension of an unconstrained O sheet. As for the synthetic Fe^{2+} (annite) end-member, $b/b_{tet.}$ *i*s higher than 1 (Fig. 15B). Unfortunately, the status of Mn is not sufficiently detailed (Frondel & Ito, 1966) to be confident of the highest *R* and $b_{tet.}$. As Mn was assumed to be octahedral and divalent, some octahedral Mn^{3+} would have made *R,* and thus the O sheet lateral dimensions, decrease, while tetrahedral Mn^{2+} would increase $b_{tet.}$ (Table 1).

Three synthetic mica series representing chemical joins will be studied in more detailed below.

The first synthetic mica series corresponds to the dioctahedral mica series along the join muscovite - aluminoceladonite $(K(Si_{3+x}Al_{1-x})(Al_{2-x}Mg_x)O_{10}(OH)_2$ with $x \leq 1$) of Schmidt *et al.* (2001), which was also later studied and compared to natural samples by Zviagina & Drits (2019) (Table 6). With increasing *R*, the dataset for these micas

https://doi.org/10.1180/clm.2023.20 Published online by Cambridge University Press

shifted away from the (*M-Ph*) line (Fig. 15A). Accordingly, Schmidt *et al.* (2001) and Zviagina & Drits (2019) reported a "difficult to understand" reduction of *b* for the highest Mg- content. Schmidt *et al.* (2001) hypothesized that this reduction could be associated with a partial trioctahedral character, with some Mg possibly filling some M1 octahedral sites (which are theoretically larger than the M2 octahedra and are empty in ideally dioctahedral structures). Zviagina & Drits (2019) did not confirm this interpretation because their analysis of the M1 octahedral site occupancies was negligible. Rather, these authors hypothesized that the change in the trend for *b* was associated with a decrease in mutual repulsion of octahedral cations with increasing contents of divalent cations, resulting in a less flattening of O sheets for the Mg-richest synthetic micas. This interpretation is confirmed by % O enlargement *vs. R* plot where the dots progressively deviate from the *(M-Ph)*° line with increasing *R* (Fig. 15C). Moreover, the increase in octahedral charge related to the increase in the Al/Mg substitution rate in this sample series implies a concomitant decrease in tetrahedral charge to keep the layer charge at 1. The coupled increase in Mg and decrease in tetrahedral Al has a direct effect on the dimensional misfit reduction between the T and O sheets. A higher octahedral Mg content (and thus *R*), as hypothesized by Schmidt *et al.* (2001), would not make $b/b_{tet.}$ decreases, as observed in Fig. 15B. The second synthetic mica series corresponds to Al-Mg micas $K(Si_{3-x+2y}Al_{1+x-2y})(Mg_{3-x-y}Al_x\square_y)O_{10}(OH)_2$ from the sample series of Robert (1976). These samples also lay on (or very close to) the (*M-Ph*) line, except sample 29 with the tetrasilicic composition $Si_4Mg_{2.5}$ (Fig. 15A). This sample series displays a large range of compositions with significant variation in the amounts of tetrahedral and octahedral Al, as well as octahedral Mg or vacant sites, whereas the octahedral occupancy ranging from 2.75 to 3 indicates a partial di-trioctahedral character. Robert (1976) observed a linear decrease in *b* with increasing octahedral Al content, but only for nine selected samples with a low number of vacant sites. As shown in Fig. 16A, *b* for all the di-trioctahedral Al-Mg micas (except sample 29) plotted as a function of R follow a linear regression, despite noticeable compositional changes in the T sheet composition, as ^{IV}Al contents range from 1 to 1.6 (Table 7). However, the regression coefficient is relatively low (R^2=0.95, Fig. 16A) and even decreases for the $b/b_{tet.}$ correlation (R^2=0.79, Fig. 16B), whereas it is very good for the %O enlargement (R^2=0.99, Fig. 16C). In fact, several linear regressions can be observed between b and R depending on the parameter chosen (Table 7). For instance, if samples with the same y value in the SF are compared (*i.e.*, samples having the same octahedral occupancy (Figs. 17A and B)), then nice correlations can be obtained using b or $b/b_{tet.}$ *vs.* R graphs, respectively. As expected, the decrease in octahedral occupancy (increase in dioctahedral character) globally provokes a gradual decrease in the *b* dimension. For most y values, regressions with similar slopes can be drawn for at least the $b/b_{tet.}$ *vs.* R graph (Fig. 17B, Table 7). Because this synthetic mica series can be described with x and y only, as seen

https://doi.org/10.1180/clm.2023.20 Published online by Cambridge University Press

in the general SF (in other words, Al, Mg, Si, and vacant site amounts are interdependent), precise b or $b/b_{tet.}$ *vs.* R graphs are also observed for each y=f(x) series (Figs. 17C and D, respectively, Table 7). As a consequence, the scattering of data that is higher in the $b/b_{tet.}$ *vs.* R plot compared to the b *vs.* R plot (Fig. 16B and 16A, respectively) results from the superimposition of accurate sub-relationships. In fact, the general relationship $b = 1.1509.R + 8.3841$ is likely to satisfactorily (± 0.006) predict b from R for this synthetic mica series (except sample 29) but corresponds to a general trend, only. Sample 29 is a tetrasilicic mica and behaves differently from the other samples of the series. For a same R, it exhibits lower b and %O enlargement and a higher $b/b_{tet.}$ (Fig. 16A, 16B, and 16C) than the other samples. On the other hand, the synthetic tetrasilicic micas *i.e.* the synthetic F- counterpart of sample 29 (sample 108, tetrasilicic fluorophlogopite), polylithionite and tainiolite (with Li_2Al and Mg_2Li octahedral composition, respectively) (Brigatti & Guggenheim (2002), Table 6) follow trends including sample 29 (Fig. 15A, 15B, and 15C). Indeed, the dots of the four samples are roughly aligned on a line approximately parallel to the muscovite-phlogopite line whatever the plots (Fig. 15A, 15B, and 15C). Moreover, when adding the few natural tetrasilicic micas, *i.e.* some celadonites, a polylithionite (sample 45 (Rieder *et al.*, 1970), Table 6), a fairly good regression is observed (Fig. 18A). Note that the samples of the muscovite - aluminoceladonite synthetic series of Schmidt *et al.* (2001) presented above ($K(Si_{3+x}Al_{1-x})(Al_{2-x}Mg_x)O_{10}(OH)_2$) move to the tetrasilicic micas "*(Si_4)*" regression line and follow the trends when approaching a tetrasilicic composition (Fig. 15A, 15B, and 15C). Even if the *(Si_4)* regression cannot be considered as robust due to the fact that few samples were available only, and that the proposed revised $r(Li^+)$ of 0.6 Å used for calculating R for tainiolite and tetraferriphlogopite is only approximate, it indirectly argues for the suitability of a $r(Li^+)$ ~0.6 Å. Using the $r(Li^+)$ of 0.76 Å (Shannon, 1976), would lead to scattered dots (Fig. 18B).

Note that norrishite ($KSi_4(LiMn^{3+}_2)$-mica, sample 111 (Brigatti & Guggenheim, 2002), Table 6), is systematically out of all the trends (Figs. 12-14, and 18). Accordingly, Brigatti & Guggenheim (2002) also observed an anomalous behavior of this norrishite sample compared to the other micas, they related to octahedral distortions induced by the Jahn-Teller effect.

As a conclusion, the impact of R on the b is similar between tetrasilicic and trisilicic micas, and the lower b observed for tetrasilicic micas is related to a less flattening of O sheets compared to trisilicic ones.

The third and last synthetic mica series that will be studied corresponds to the trioctahedral micas ($Si_{3-z}Al_{1+z}$)($Mg_xFe^{2+}_yAl_z$)K (Hewitt & Wones, 1975; Redhammer & Roth, 2002; Mercier *et al.*, 2005) that appear slightly above the (*Ph-A*) and (*M-Ph*) lines in the b *vs.* R and %O enlargement *vs.* R plots (Fig. 15A and 15C, respectively) and on or below the (*Ph-A*)' line in the $b/b_{tet.}$ *vs.* R plot (Fig. 15B). A less scattering of data is noticed in the $b/b_{tet.}$ *vs.* R

https://doi.org/10.1180/clm.2023.20 Published online by Cambridge University Press

plot as illustrated by the respective regression coefficients (calculated using the Hewitt & Wones, (1975) series only, R^2=0.82, 0.97, and 0.89, Figs. 19A, 19B, and 19C, respectively). As for the previous synthetic mica series, several sub-relationships can be noticed and correspond to specific solid solutions. As an illustration, for constant values of z (Al content), linear regressions corresponding to the respective Mg-Fe^{2+} solid solutions are observed (Fig. 20A). In such solid solutions, *b* systematically decreases with the Fe^{2+}/Mg ratio, as expected considering the respective ionic radii of Mg and Fe^{2+} (Table 1). The slope of these regression lines increases slightly from approximately 2.4 to 2.9 with increasing z (Table 7). For z=0, the equation is very similar to that of the (*Ph-A*) line. The small difference is assigned to the fact that both regressions were calculated in a different way, using the end-members data for (*Ph-A*) regression, whereas using the solid solution for z=0. The slopes for each Mg-Fe^{2+} solid-solution linear regression are more than twice as high as those for $(Si_{3-z}Al_{1+z})(Mg_{3-z}Al_z)K$ and $(Si_{3-z}Al_{1+z})(Fe^{2+}{}_{3-z}Al_z)K$, which exhibit similar slopes (Table 7). The regression for the $(Si_{3-z}Al_{1+z})(Mg_{3-z}Al_z)K$ solid solution is close to that of the (*M-Ph*) line, and the small difference is due to the strictly trioctahedral character involved by Tschermak substitutions in the sample series of Hewitt & Wones (1975) compared to the di-trioctahedral muscovite-phlogopite solid solution. The $b/b_{tet.}$ *vs*. *R* plot reveals that regressions also exist for each solid solution (Fig. 20B). The misfit between T and O sheets increases with decreasing *R i.e*. with decreasing amounts of Fe^{2+} relative to Mg and more severely with increasing Al content due to Tschermak substitutions and the antagonistic effect of Al, as discussed above for Al-serpentines. For the trisilicic Fe^{2+} end-member, $b/b_{tet.}$ slightly exceeds 1 (Fig. 20B), suggesting a T sheet fully extended with a symmetry close to hexagonal to fit the O sheet large lateral dimension. Accordingly, the O sheet is the thickest of the series (Fig. 20C). The increase of tetrahedral Al content induces an increase in T sheet lateral dimensions and the thinning of O sheets by octahedral flattening to reduce the misfit (Fig. 20C). For a same Al content, the octahedral flattening also increases with increasing Mg/Fe^{2+} substitution, to contribute with the tetrahedral rotation to reduce the misfit. The cumulative effect is evidenced here by the increase in the slope of the regressions with increasing Al content, i.e. increasing z (Fig. 20, Table 7). As for the sample series of Robert (1976), the scattering of data observed for the series of Hewitt & Wones (1975) is assigned to the superimposition of accurate sub-relationships corresponding to limited solid solutions.

In light of the results obtained for synthetic micas, the observed scattering of data (Figs. 12 and 14) for all the dataset is mainly due to the chemical complexity of the samples, and multiple limited solid solutions probably exist between a multitude of end-members.

https://doi.org/10.1180/clm.2023.20 Published online by Cambridge University Press

Chlorites

Chlorites are phyllosilicates composed of 2:1 layers whose negative charge, arising mainly from heterovalent tetrahedral substitutions, is most often balanced by the presence of a positively charged O sheet in the interlayer space (Fig. 1A) (e.g., Bailey, 1991c). The structure of chlorite is then globally electrostatically neutral with a general SF as $(Si_{4-x}Al_x)\ (R^{3+}_yR^{2+}_z\square_V)\ O_{10}(OH)_8$, where □ is a vacant site and y+z+v = 6. The composition of the layer is $(Si_{4-x}Al_x)$ $(R^{3+}, R^{2+}, \square)_3\ O_{10}(OH)_2$ and that of the interlayer octahedral sheet $(R^{3+}, R^{2+}, \square)_3\ (OH)_6$. It is difficult to determine the composition of each of them accurately (e.g., Zazzi *et al.*, 2006), especially since the chemical composition of chlorites is very variable (see for example the review of Wiewiora & Weiss (1990)). Trioctahedral chlorites (trioctahedral in both the layer and the interlayer) are the most common in nature, and several families exist, such as for example, clinochlore, chamosite, and penninite, with respectively Mg Fe^{2+}, and Mn^{2+} as the dominant octahedral cation.

Owing to the complex chemical composition of chlorite, numerous studies have been devoted to the relations between *b* and the amounts of octahedral and tetrahedral cations. Several equations with the form of $b = b_0 + \sum_{i=1}^{n}(a_i.x_i)$ can be found in the literature for a long time (von Engelhardt, 1942; Radoslovich 1962), especially for trioctahedral chlorites, as exemplified by Lee *et al.* (2007) who observed a robust linear relationship between *b* and Mg/Mg+Fe for natural chlorite samples from Al-saturated metamorphic assemblages. Wiewora & Wilamowski (1996) formulated two distinct regression equations for trioctahedral chlorites (Eq. 7), and di-tri- and di-dioctahedral chlorites (Eq. 8) as:

$$b_{tri.} = 9.225+0.027^{IV}Al+0.0386^{VI}Al+0.0376Fe^{2+}+0.0376Cr^{3+}+0.0665Mn^{2+} \quad (8)$$

$$b_{di\text{-}tri./di\text{-}di.} = 8.860+0.112^{IV}Al+0.0524Mg^{2+}+0.0752Fe^{2+}+0.06Fe^{3+}-0.0523Li^{+} \quad (9)$$

The dataset used in the present study is taken mainly from the review work of Wiewora & Wilamowski (1996) where several *b* were measured by structure refinement. To avoid any potential bias from using a unique data source and to enlarge the range of chemical compositions investigated for chlorite, the compiled data from Radoslovich (1962) were added as well as a few other samples, i.e., two samples whose single crystal structure has been refined: one ordered triclinic clinochlore (Smyth *et al.*, 1997) and one cookeite (Zheng & Bailey, 1997b), and four uncommon chlorites, namely, V^{3+}-rich chlorites (Whitney & Northrop, 1986) and Fe^{3+}-sudoites (Billault *et al.*, 2002) (Table 8). The evolution of *b* as a function of *R* for all samples reveals fairly good data alignment for all compositions ranging from dioctahedral to trioctahedral chlorites (Fig. 21A). In contrast to Wiewora & Wilamowski (1996), the *b vs. R* regression is suitable for the entire range of chemical compositions. *R* for di-tri and trioctahedral chlorites even

https://doi.org/10.1180/clm.2023.20 Published online by Cambridge University Press

overlap in the intermediary range (for $0.64 < R < 0.70$). This is probably because trioctahedral occupancy with cations of different valences, such as ($R^{3+}_{x}R^{2+}_{3-x}$) and ($R^{3+}_{x}R^{+}_{3-x}$), is expected to occur in chlorites, at least in the interlayer O sheets, to counterbalance the negative tetrahedral charge. The clinochlore and cookeite samples with single crystal refined fall on, or close to, the correlation line. The uncommon vanadium-rich chlorites (Whitney & Northrop, 1966), assuming Fe and V as trivalent cations, as well as Fe^{3+}-sudoites (Billault *et al.*, 2002), do not reveal any specific behavior (Fig. 21A). Some samples such as samples 8, 28, and 30 (Table 8), deviate significantly from the regression line (Fig. 21A). For sample 28, *R* is suspected to be underestimated due to a problem of redox as the Fe^{2+}/Fe^{3+} ratio was reversed in a previous study (Steinfink, 1958). As sample 8 was classified in the trioctahedral group, the Fe^{2+} and Fe^{3+} contents have probably been mistakenly switched (Table 8), and the dot moved close to the regression line after switching back both contents (Fig. 21A). Other typographical errors cannot be excluded, as another one could be identified for sample 82 (Table 8). Unfortunately, data for sample 30 are unpublished author's data and could not be checked.

Some chlorites of the di-tri- and di-di- octahedral series are Li-rich. The Al_2Li configuration is likely to occur in the interlayer hydroxide sheet to create a positive charge balancing the tetrahedral negative charge (Zheng & Bailey, 1997b). The revised $r(Li^{+})$ of 0.60 Å (instead of 0.76 Å) determined for Li-rich micas (see above) was used alternatively (Fig. 21B). The general regression was slightly modified to $b = 2.30.R + 7.67$ and the regression coefficient was slightly improved ($R^2 = 0.865$ *vs.* 0.884), likely arguing for the suitability of a lower $r(Li^{+})$. Contrary to Wiewora & Wilamowski (1996), who included tetrahedral Al in their equations with a higher coefficient for di-tri- and di-dioctahedral chlorites than for trioctahedral chlorites (Eq. 7 and 8), the unique linear regression (Fig. 21B) indicates that *b* is mainly driven by *R* and that the tetrahedral Al is not a first-order parameter. Accordingly, a unique main trend is also observed for the the $b/b_{tet.}$ *vs R* regression, though its coefficient is lower than for the *b vs. R* one (0.78 (Fig. 22A) and 0.88 (Fig. 21B), respectively). The observed dispersion of dots may be partly due to the scattering of tetrahedral charge ranging from 0.45 to 1.80 (Table 8), but without being strongly confident in their accuracy for the entire dataset.

$b/b_{tet.}$ vary from 0.952 (dioctahedral chlorites) to 1.009 (trioctahedral chlorites), which correspond to angles of tetrahedral rotation $\alpha \approx 18°$ and 0°, respectively, matching relatively well with α measured by structure refinement: ≈ 14° for dioctahedral donbassite and ≈ 5-7° for trioctahedral chlorites (Bailey, 1991c). Focussing on some samples whose single crystal structure was refined (Table 9), an excellent relationship is observed between α_{ref} the tetrahedral rotation angle measured by structure refinement, and α_{calc} the tetrahedral rotation angle calculated from $b/b_{tet.}$ (Eq.4)

https://doi.org/10.1180/clm.2023.20 Published online by Cambridge University Press

(Fig. 22C). Surprisingly, the regression coefficient is better when using Si-O and Al-O bond length of respectively 1.618Å and 1.748Å following Bailey (1984a), than when using the T-O mean bond length determined by structure refinement (Fig. 22B). The Si-O and Al-O bond lengths were calculated to match the α_{ref}, and very coherent values were obtained (Table 9). This study also shows that using adequate bond lengths, Eq. 4 allows to calculate the angle of tetrahedral rotation α accurately, at least for most of the common samples.

Going from dioctahedral chlorites to trioctahedral ones, *i.e.* with R increasing, the the tetrahedral rotation angle α progressively decreases, as shown by the $b/b_{tet.}$ plot (Fig. 22A) while the flattening of O sheets concomitantly decreases (Fig. 22B). For di- and ditri- octahedral chlorites, O sheets are thinner than the hydroxides with same R, while they are thicker for trioctahedral chlorites.

In chlorite, the element partitioning between both O sheets will not significantly affect R, which is a mean value, but such a partitioning is likely to impact the misfit between the T and O sheets. As for the other phyllosilicates families, the misfit between T and O sheets increases when R decreases, and both the shortening of T sheets by tetrahedral rotation and flattening of O sheets are expected to occur. Most trioctahedral chlorites show $b/b_{tet.}$ close to 1, revealing an easy accommodation of the T and O sheets. Samples with the highest $b/b_{tet.}$ and R are Mn-rich and have a high tetrahedral Al content (cf. samples 1, 2, and 3 of the trioctahedral series of Wiewiora & Wilamowski, 1996) and sample “pennantite” (Radoslovich, 1962) (Table 8). For these samples, both T and O sheets have large lateral dimensions, and misfit compensation is likely to be facilitated. It is worth noticing that the clinochlore and cookeite samples with single crystal refined fall very close to the b, $b/b_{tet.}$, and %O enlargement vs. R. correlation lines (Figs. 21-22). In this regard, the data scattering shown in Fig. 21 is likely related to the structural complexity of chlorites associated with multiple possibilities of misfit accommodation, variable composition and charge balance between T and O sheets, coupled to chemical uncertainties.

DISCUSSION

For the samples studied, *i.e.*, hydroxides, oxyhydroxides, layered double hydroxides, TO phyllosilicates (kaolinite-lizardite or modulated series), neutral TOT phyllosilicates (pyrophyllite-talc series), smectites (same as the neutral TOT phyllosilicates), micas (muscovite-phlogopite, phlogopite-annite, tetrasilicic micas series), and chlorites, the following relation can be applied as a first order:

https://doi.org/10.1180/clm.2023.20 Published online by Cambridge University Press

$$b = A.R + B \quad (10)$$

The A and B parameters for the different families are reported in Table 10. The ionic radii dataset taken from Shannon (1976) allows to obtain suitable *R*, except for Mn^{3+}, as discussed for groutite (layer double hydroxides section) and Li^{+} as discussed for micas and chlorites, for which a smaller size appears to be more suitable. As a matter of fact, the equations of the regressions for these minerals were reported (Table 10) with *R* calculated with $r(Li^{+}) = 0.60$ Å rather than the 0.76 Å value from Shannon (1976).

The *b* vs. *R* correlation lines determined for all the studied minerals families were reported on a same plot (Fig. 23A). Note that the development of correlation lines does not necessarily imply the existence of a complete isomorphous series between end-members, that is obviously dependent on their physicochemical conditions of formation and thermodynamic stability. Samples that are not represented on this figure because no *b vs. R* linear relation could be observed will be discussed later. *b* of a calculated theoretical "free" T Si-O sheet (=$b_{tet.}$) is ~ 9.15 Å and increases with tetrahedral substitutions (Eq. 3) ($b_{tet.}$~ 9.34 Å for $Si_{0.75}{}^{IV}Al_{0.25}$). The determined *b* vs. *R* regression for $M^{n+}(OH)_n$ hydroxide structures can be considered as representing the "free" O sheets, *i.e.*, without any constraint from the T sheets. The T sheet and O sheet (hydroxides) lines intercept at *R* ~ 0.65 Å, and at *R*~ 0.69 Å when ¼ of Si is substituted by Al (Fig. 23A).

The slope of the regression line (*i.e.*, the A parameter in Eq. 10) is found to be significantly higher for hydroxides than for phyllosilicates, except for the TO phyllosilicates with modulated structure (Fig. 23A; Table 10). Such a contrast clearly demonstrates the prominent role played on *b* by the misfit accommodation between lateral dimension of O and T sheets. This finding was used to derive a structurally based interpretation of *b* evolution with *R* in terms of process of misfit accommodation.

In a global way, at the lattice scale, the *b vs. R* linear relations (Fig. 23A) were interpreted mainly as resulted from the misfit accommodation by coupling more or less pronounced tetrahedral rotation and O sheet flattening whatever *R*. These two processes are often presented as being the main ones to accommodate misfit in micas (e.g. Radoslovich, 1962; Donnay *et al.* 1964; Toraya, 1981). From dioctahedral to trioctahedral phyllosilicates, a decrease of the tetrahedral rotation angle α allows to reduce the T sheet lateral dimension, while a thickening of O sheet allows to decrease their lateral dimension. The $b/b_{tet.}$ and %O enlargement *vs. R* plots (Fig. 23B and 23C, respectively) are complementary representations of the *b vs. R* one (Fig. 23A), allowing to distinguish better the respective role of T and O sheets.

https://doi.org/10.1180/clm.2023.20 Published online by Cambridge University Press

For TO phyllosilicates (excluding ^{IV}Al- and $^{IV}Fe^{3+}$- serpentines and modulated phyllosilicates), TOT neutral structures, micas (excluding those with small interlayer cations (Na and Ca) and with interlayer depleted (micaceous samples)), and chlorites, the O sheet dimension, and thus *R*, mainly drives *b*. The different slopes observed (Fig. 23A) for the different families are then related to the relative importance of the adjustments of T and O sheets in the misfit accommodation. This agrees well with Bailey (1984b) who stated that "the T sheets appear sufficiently flexible to conform to the lateral dimensions dictated by smaller O sheets, and T and O lateral dimensions are similar enough that articulation of T with O sheets can be accomplished readily by tetrahedral rotation and additional thinning or thickening of O sheets". The thinning or thickening of phyllosilicates O sheets is compared here to the thickness of their hydroxide counterparts (*i.e.*, hydroxides with the same *R* as the considered phyllosilicates).

It is worth noticing that O sheet thickening occur (%O enlargement < 0 in Fig. 23C) when the O sheet remains smaller than the T sheet ($b/b_{tet.}$<1 in Fig. 23B).

For tetrasilicic micas and muscovite-phlogopite micas series, $b<b_{tet.}$ whatever *R* (Fig. 23B), whereas the octahedral flattening varies continuously, the thickness of O sheets being similar to that of their hydroxides counterparts for *R* ~ 0.62 and 0.65 Å, respectively (Fig. 23C). Interestingly, the slopes of the tetrasilicic micas *(Si$_4$)*° and trisilicic micas*(M-Ph)*° regression lines are similar. For a same *R*, *b* and flattening of O sheet are higher for trisilicic micas than for tetrasilicic micas (Fig. 23C), agreeing well with the O sheet thickness measured by structure refinement (Table 11). Only one refined data for talc was available for comparison with neutral TOT structure without interlayer cation, as the *(P-T)*° line has also similar slope than the tetrasilicic *(Si$_4$)*° and trisilicic *(M-Ph)*° micas lines.

For talc, the octahedral flattening is comparatively more pronounced than for tetrasilicic micas and less pronounced than for trisilicic micas (Fig. 23C) agreeing well with the O sheet thickness (Table 11). On the other hand, the calculated values of the tetrahedral rotation angle α are adequately lower for tetrasilicic micas compared to trisilicic ones, but they are inappropriate (Table 11). For tetrasilicic, the tetrahedral rotations have probably to be limited to enssure an enough large size hole for K, and the contribution of the O sheet has to be more pronounced to allow congruency between O and T sheets dimensions.

For lizardites and talcs, $b>b_{tet}$ from *R* >~0.67 and ~0.70 Å, respectively (Fig. 23A), but as for the tetrasilicic and muscovite-phlogopite micas, the octahedral flattening varies continuously whatever *R* too.

For chlorites and phlogopite-annite, O sheet becomes higher than T sheet for high *R* and high tetrahedral substitutions rates and the thickening of O sheets occurs more strongly than for the other phyllosilicates (Fig. 23C).

https://doi.org/10.1180/clm.2023.20 Published online by Cambridge University Press

These results agree well with previous works (e.g., Toraya 1981; Lin & Guggenheim 1983; Weiss *et al.* 1985, 1992), and especially with Hazen & Wones (1972) who suggested that octahedral flattening is controlled by the octahedral cation radius.

The afore-mentioned structurally based interpretation is likely at the origin of the roughly similar regression lines received for the (*K-L*), (*P-T*), *(Si)*$_4$ and (*M-Ph*) sample series (Fig. 23A) and pleading for the tetrahedral rotations and O sheet flattening as the primary crystallographic distortions allowing the T and O sheets accommodation. The role of the presence of a T sheet on *b* can also be evidenced by analyzing the evolution of the *b vs. R* regression line of trioctahedral micas and chlorites. Indeed, the high *b* obtained for these minerals for high *R* compared to other phyllosilicates (Fig. 23A; Table 10), can be due to the presence of trioctahedral O sheets coupled to large T sheet lateral dimensions. The above two features likely enhance the decrease of tetrahedral rotations (Fig. 23B) and relatively limit the O sheet flattening (Fig. 23C) in trioctahedral micas and chlorites compared to the other phyllosilicates.

The (*G-C*) line exhibits a higher slope than the correlation obtained for chlorites or even for the hydroxides (Fig. 23A). This likely indicates a strong influence of the O sheet (which are similar to hydroxides sheets (Fig. 6B)) over the T sheet for the (*G-C*) sample series and may explain the origin of the observed corrugated structures as a way to accommodate the dimensional misfit for these minerals. Such a mechanism is less likely to occur for TOT structures due to the constraints applied by the two sandwiching T sheets. Interestingly, the (*G-C*) line intersects the correlation line for chlorites when the dimensional misfit between T and O sheets is minimal (Fig. 23A). Note that even if the slope of the (*G-C*) line is higher than that received for the hydroxides, *b* his type of TO phyllosilicates never intersect the latter (Fig. 23A), likely providing evidence of a structural limit to the misfit accommodation. The similarity of *b* between chlorites and serpentines for the same octahedral composition may explain their intimate relationships in geological processes (e.g., Ryan & Hillier, 2002; Zhang *et al*. 2021).

For ^{IV}Al- and Fe^{3+}-serpentines, excellent regressions were obtained for $b/b_{tet.}$ *vs R* (Fig. 6A) and the results obtained with Eq. 10, were improved by integrating the tetrahedral sheet composition following this equation:

$$b/b_{tet.} = \mathrm{C}.R + \mathrm{D} \qquad (11)$$

with $b_{tet.}$ calculated according to Eq. 3..

As expected, micas with small interlayer cations (Na and Ca), or which are not silicic are out of the trends and specific processes to assure congruency between sheets cannot be reached by this simplistic approach.

https://doi.org/10.1180/clm.2023.20 Published online by Cambridge University Press

Obviously, the schematized structurally-based interpretation of the control of *b* by *R* in hydroxides and various phyllosilicates represents the principal processes but is not unique. As evidenced for the synthetic mica series, the presence of sub-relationships related to limited solid solutions is also responsible for variations in the regression lines. Moreover, this study shows for smectites and micas as expected, that the layer charge, especially arising from tetrahedral substitution, may likely also impact the received *b*.

CONCLUSION

According to an abundant literature, the octahedral chemical composition of phyllosilicates is related to *b*. Using the mean ionic radius of octahedral cations *R* allows generalizing the different correlations that can be found in literature between *b* and the octahedral chemistry of phyllosilicates and hydroxides which are most often restricted to a limited type of sample series in terms of chemical composition or dioctahedral *vs.* trioctahedral character. Integrating the tetrahedral sheet composition using $b_{tet.}$ for phyllosilicates that possess tetrahedral substitutions improves the relation between *b* and *R*.

A nanomechanistic interpretation based on the misfit accommodation by coupling more or less pronounced tetrahedral rotation and O sheet flattening, explains globally well the results, and potentially impacts the processes of formation and transformation of phyllosilicates.

Refining the proposed model to account for the structural peculiarities could represent a logical perspective to this work.

ACKNOWLEDGMENTS

The authors are much indebted to anonymous reviwers for their extremely careful and constructive reviews which improved the quality of the paper significantly. The authors are also very grateful to Milan Rieder, who kindly provided us a valuable table with mica data he measured half a century ago, and to Alain Meunier for his valuable comments on a preliminary version. The authors are grateful to the European Joint Program EURAD (WP "Future" - grant ID 847593), the French government program "Investissements d'Avenir" (EUR INTREE, reference ANR-18-EURE-0010), and the European Union (ERDF) and "Région Nouvelle Aquitaine" for providing financial support for this study.

https://doi.org/10.1180/clm.2023.20 Published online by Cambridge University Press

REFERENCES

Allmann R. (1968) The crystal structure of pyroaurite. *Acta Crystallographica*, **B24**, 972-977.

Anderson C. S. & Bailey S. W. (1981) A new cation ordering pattern in amesite-2H_2. *American Mineralogist*, **66**, 185-195.

Andreani M., Grauby O., Barronnet A. & Munoz M. (2008) Occurrence, composition and growth of polyhedral serpentine. *European Journal of Mineralogy*, **20**, 159-171.

Andrieux P. & Petit S. (2010) Hydrothermal synthesis of dioctahedral smectites: the Al-Fe^{3+} chemical series. Part I: Influence of experimental conditions. *Applied Clay Science,* **48**, 5-17.

Arima M., Fleet M. E. & Barnett R. L. (1985) Titanian berthierine: a Ti-rich serpentine-group mineral from the Picton ultramafic dyke, Ontario. *The Canadian Mineralogist*, **23***,* 213-220.

Badaut D., Decarreau A. & Besson G. (1992) Ferripyrophyllite and related Fe^{3+} rich 2:1 clays in recent deposits of Atlantis II deep Read Sea. *Clay Minerals*, **27**, 227-244.

Bailey S.W. (1966) The status of clay minerals structures. Pp. 1-23 in: *Proceedings of the Fourteenth national conference on clays and clay minerals*. Berkeley, California (S.W. Bailey, editor).

Bailey S.W. (1969) Polytypism of trioctahedral 1:1 layer silicates. *Clays and Clay Minerals*, **17**, 355-371.

Bailey S.W. (1981) Structures of layer silicates. Pp. 1-124 in: *Crystal structures of clay minerals and their X-Ray identification* (G.W. Brindley & G. Brown, editors). Mineralogical Society, London, UK.

Bailey S.W. (1984a) Classification and structures of the micas. Pp. 1-12 in: *Micas, Reviews in Mineralogy, Volume 13* (S.W. Bailey, editor). Mineralogical Society of America, Washington D.C., USA.

Bailey S.W. (1984b) Crystal chemistry of the true micas. Pp. 13-60 in: *Micas* (*Reviews in Mineralogy, Volume 13)* (S.W. Bailey, editor). Mineralogical Society of America, Washington D.C., USA.

Bailey S.W. (1988) Odinite, a new dioctahedral- trioctahedral 1:1 Fe^{3+}- rich clay mineral. *Clay Minerals*, **23**, 237-247.

Bailey S.W. (1991a) Introduction. Pp 1-8 in: *Hydrous phyllosilicates (Reviews in Mineralogy, Volume 19)* (S.W. Bailey editor). Mineralogical Society of America, Washington D.C., USA.

Bailey S.W. (1991b) Structures and compositions of other trioctahedral 1:1 phyllosilicates. Pp 169-188 in: *Hydrous phyllosilicates (Reviews in Mineralogy, Volume 19)* (S.W. Bailey editor). Mineralogical Society of America, Washington D.C., USA.

Bailey S.W. (1991c) Chlorites: Structures and crystal-chemistry. Pp. 347-453 in: *Hydrous phyllosilicates (Reviews in Mineralogy, Volume 19)* (S.W. Bailey editor). Mineralogical Society of America, Washington D.C., USA.

Baron F., Pushparaj S.S.C., Fontaine C., Sivaiah M.V., Decarreau A. & Petit S. (2016a) Microwave-Assisted Hydrothermal Synthesis of Ni-Mg Layered Silicate Clays. *Current Microwave Chemistry*, **3**, 85-89.

Baron F., Petit S., Tertre E. & Decarreau A. (2016b) Influence of aqueous Si and Fe(III) speciation on tetrahedral Fe(III) substitutionin nontronites: a clay synthesis approach. *Clays and Clay Minerals*, **64**, 189-203.

Baron F., Petit S., Pentrack M., Decarreau A. & Stucki J. (2017) Revisiting the nontronite Mössbauer spectra. *American Mineralogist*, **102**, 1501-1515.

Bayliss P. (1981) Unit cell data of serpentine group minerals. *Mineralogical Magazine*, **44**, 153-156.

Bayliss P., Berry L. G., Mrose M. E. & Smith D. K. (1980) Mineral Powder Diffraction File, JCPDS, Swarthmore Pa.

https://doi.org/10.1180/clm.2023.20 Published online by Cambridge University Press

Bellotto M., Rebours B., Clause O., Lynch J., Bazin D. & Elkaïm E. (1996) A reexamination of hydrotalcite crystal chemistry. *Journal of Physical Chemistry*, **100**, 8527-8534.

Bentabol M., Ruiz Cruz M. D. & Huertas F.J. (2009) Isomorphous substitution vs. defect density in hydrothermally synthesized (200 °C) Fe^{3+}, Ga^{3+} and Cr^{3+} -substituted kaolinites. *Applied Clay Science*, **45**, 36-43.

Bentabol M., Ruiz Cruz M.D. & Sobrados I. (2010) Chemistry, morphology and structural characteristics of synthetic Al-lizardite. *Clay Minerals*, **45**, 131–143.

Bentabol M. & Ruiz Cruz M. D. (2013) Chemistry, morphology and structural characteristics of synthetic Al–Ni and Al–Co-lizardites. *Applied Clay Science*, **77**, 68-78.

Billault V., Beaufort D., Patrier P. & Petit S. (2002) Crystal-chemistry of Fe-sudoites from Mac Arthur River U-deposits (Saskatchewan, Canada). *Clays and Clay Minerals*, **50**, 70-81.

Birch W.D., Pring A., Reller A. & Schmalle H.W. (1993) Bernalite, $Fe(OH)_3$, a new mineral from Broken Hill, New South Wales: Description and structure. *American Mineralogist*, **78**, 827-834.

Bish D.L. (1981) Distortions in the lizardite structure: A distance leastsquares study. *EOS*, **62**, 417.

Bish D.L. & Brindley G. W. (1977) A reinvestigation of takovite, a nickel aluminum hydroxy- carbonate of the pyroaurite group. *American Mineralogist*, **62**, 458-464.

Bish D.L. &Von Dreele R.B. (1989) Rietveld refinement of non-hydrogen atomic positions in kaolinite. *Clays and Clay Minerals*, **37**, 289-296.

Braithwaite R.S.W., Dunn P.J., Pritchard R.G. & Paar W.H. (1994) Uowaite, a reinvestigation. *Mineralogical Magazine*, **58**, 79-85.

Brigatti M. F. (1983) Relationships between composition and structure in Fe-rich smectites. *Clay Minerals*, **18**, 177-186.

Brigatti M.F., Frigeri P. & Poppi L. (1998) Crystal chemistry of Mg-Fe- bearing muscovites-$2M_1$. *American Mineralogist*, **83**, 775-785.

Brigatti M.F., Lugli C., Poppi M., Foord E.E. & Kile D.E. (2000) Crystal chemical variations in Li- and Fe-rich micas from Pikes Peak batholith (central Colorado). *American Mineralogist*, **85**, 1275-1286.

Brigatti M.F., Galli E., Medici E., Poppi L., Cibin G., Marcelli A. & Mottana A. (2001a) Chromium-containing muscovite: crystal chemistry and XANES spectroscopy. *European Journal of Mineralogy*, **13**, 377-389.

Brigatti M.F., Kile D.E. & Poppi M. (2001b) Crystal structure and crystal chemistry of lithium-bearing muscovite-$2M_1$. *Canadian Mineralogist*, **39**, 1171-1180.

Brigatti M.F., Mottana A., Malferrari D. & Cibin G. (2007) Crystal structure and chemical composition of Li-, Fe-, and Mn-rich micas. *American Mineralogist*, **92**, 1395-1400.

Brigatti M.F., Malferrari D, Laurora A. & Elmi C. (2011) Structure and mineralogy of layer silicates: recent perspectives and new trends. *EMU Notes in Mineralogy*, **11**, 1-71.

Brigatti M. F., Galán E. & Theng B. K. G. (2013) Structure and Mineralogy of Clay Minerals. Pp. 21–81 in: *Developments in Clay Science – Volume 5A. Handbook of Clay Science,* 2nd edition. (F. Bergaya &G. Lagaly editors), Elsevier.

Brindley G. W. (1982) Chemical compositions of berthierines. *Clays and Clay Minerals*, **30,** 153-155.

https://doi.org/10.1180/clm.2023.20 Published online by Cambridge University Press

Brindley G W., Dunham K. C., Eyles V. A. & Taylor J. H. (1951) The crystal structure of chamosite minerals. *Mineralogical Magazine*, **29**, 502-525.

Brindley G. W. & Youell R. F. (1953) Ferrous chamosite and ferric chamosite. *Mineralogical Magazine*, **30**, 57-70.

Brindley G. W. & Wan H. M. (1975) Compositions, structures and thermal behavior of nickel containing minerals in the lizardite- nepouite series. *American Mineralogist*, **60**, 863-871.

Brindley G.W., Bish D.L. & Wan H-M. (1977) The nature of kerolite, its relation to talc and stevensite. *Mineralogical Magazine*, **41**, 443-452.

Brindley G. W & Kikkawa S. (1979) A crystal-chemical study of Mg,Al and Ni,Al hydroxyl-perchlorates and hydroxyl-carbonates. *American Mineralogist*, **64**, 836-841.

Brindley,G.W., Bish D.L. & Wan H-M. (1979) Compositions, structures, and properties of nickel-containing minerals in the kerolite-pimelite series. *American Mineralogist*, **64**, 615-625.

Brindley G.W. & Kao C.C. (1984) Structural and IR relations among brucite-like divalent metal hydroxides. *Physics and Chemistry of Minerals*, **10**, 187-191.

Bruce L.A., Sanders J.V. & Turney, T.W. (1986) Hydrothermal synthesis and characterization of cobalt clays. *Clays and Clay Minerals*, **34**, 25-36.

Buckley H.A., Bevan J.C., Brown K.M. & Johnson L.R. (1978) Glauconites and celadonites: two separate mineral species. *Mineralogical Magazine*, **42**, 373-382.

de la Calle C. & Suquet H. (1991) Vermiculite. Pp. 455-496 in: *Hydrous phyllosilicates (Reviews in Mineralogy, Volume 19)* (S.W. Bailey editor). Mineralogical Society of America, Washington D.C., USA.

Capitani G. & Mellini M. (2004) The modulated crystal structure of antigorite: The *m*= 17 polysome. *American Mineralogist*, **80**, 147-155.

Capitani G., Compagnoni R., Cossio R., Botta S. & Mellini M. (2021) The intracrystalline microstructure of Monte Fico lizardite, by optics, μ-Raman spectroscopy and TEM. *European Journal of Mineralogy*, **33**, 425-432.

Caruso L.J. & Chernosky J.V. (1979) The stability of lizardite. *The Canadian Mineralogist*, **17**, 757-769.

Chemtob S.M., Nickerson R.D., Morris R.V., Agresti D.G. & Catalano J. G. (2015) Synthesis and structural characterization of ferrous trioctahedral smectite: implications for clay mineral genesis and detectability on Mars. *Journal of Geophysical Research Planets*, **120,** 1119–1140.

Chernosky J. V. J_R (1975) Aggregate refractive indices and unit cell parameters of synthetic serpentine in the system MgO-Al_2O_3-SiO_2-H_2O. *American Mineralogist*, **60**, 200-208.

Choi S.J., Oh J.M. & Choy J.H. (2008) Human-related application and nanotoxicology of inorganic particles: complementary aspects. *Journal of Materials Chemistry* **18**, 615–620.

Chukhrov F.V., Zvyagin B.B., Drits V.A., Gorshkov A., Ermilova L.P., Goilo E.A. & Rudnitskaia E.S. (1979 a) The ferric analogue to pyrophyllite and related phases. Pp. 55-64 in *Proceedings of the International Clay Conference*, Oxford**.**

Chukhrov F.V., Zvyagin B.B., Drits V.A., Gorshkov A., Ermilova L.P., Goilo E.A. & Rudnitskaia E.S. (1979 b) Über ferripyrophyllit. *Chemie der Erde*, **38**, 324-330.

Coey J. M. D., Chukhrov F. V. & Zvyagin B.B. (1984) Cation distribution, Mössbauer spectra and magnetic properties of ferripyrophyllite. *Clays and Clay Minerals*, **32**, 198-204.

https://doi.org/10.1180/clm.2023.20 Published online by Cambridge University Press

Cooper M. A. & Hawthorne F. C. (1996) The crystal structure of shigaite, $[AlMn^{2+}_2(OH)_6]_3(SO_4)_2Na(H_2O)_6\{H_2O\}_6$, a hydrotalcite-group mineral. *The Canadian Mineralogist*, **34**, 91-97.

Corona J.C., Jenkins D.M. & Dyar D. (2015) The experimental incorporation of Fe into talc: a study using X-ray diffraction, Fourier transform infrared spectroscopy and Mössbauer spectroscopy. *Contributions to Mineralogy and Petrology*, **170**, 1-15.

Costantino U., Marmottini F., Nocchetti M. & Vivani R. (1998) New Synthetic Routes to Hydrotalcite-Like Compounds. Characterisation and Properties of the Obtained Materials. *European Journal of Inorganic Chemistry,* **10**, 1439-1446.

Costantino U., Nocchetti M., Sisani M. & Vivani R. (2009) Recent progress in the synthesis and application of organically modified hydrotalcites. *Zeitschrift für Kristallogr*aphie **224**, 273–281.

Dalmon J.A. & Martin G-A. (1968) Sur la préparation et la structure de silicates basiques de cobalt et de magnésium de type talc et antigorite. *Comptes Rendus de l'Académie des Sciences, Paris*, **267**, 610-614.

Decarreau A. (1980) Cristallogenèse expérimentale des smectites magnésiennes : hectorite, stévensite. *Buletin de Mineralogie,* **103**, 579-590.

Decarreau A. (1983) Etude expérimentale de la cristallogenèse des smectites. Mesures des coefficients de partage smectites trioctaèdriques-solution aqueuse pour les métaux M^{2+} de la première série de transition. *Sciences Géologiques, Mémoire n° 74,185 p*. Université Louis Pasteur, Strasbourg, France.

Decarreau A. & Petit S (2014) Fe^{3+}/Al^{3+} partitioning between tetrahedral and octahedral sites in dioctahedral smectites. *Clay Minerals*, **49**, 657-665.

Dekov V.M., Kamenov G.D., Stummeyer J., Thiry M., Savelli C., Shanks W.C., Fortin D., Kuzmann E. & Vértes A. (2007) Hydrothermal nontronite formation at Eolo Seamount (Aeolian volcanic arc, Tyrrhenian Sea). *Chemical Geology*, **245**,103–119.

D'Espinose de la Caillerie J.B., Kermarec M. & Clause O. (1995) Impregnation of gamma-Alumina with Ni(II) or Co(II) ions at neutral pH : Hydrotalcite-type coprecipitate formation and characterization. *Journal of the American Chemical Society*, **117***,* 11471-11481.

De Wall S. A. (1970) Nickel minerals from Barberton, South Africa: III. Willemseite, a nickel-rich talc. *American Mineralogist*, **55**, 31-42.

Donnay G., Morimoto N., Takeda H. & Donnay J.H.D. (1964) Trioctahedral one-layer micas: I. Crystal structure of a synthetic iron mica. *Acta Crystallographica*, **17**, 1369–1373.

Drits V.A., McCarty D.K. & Zviagina B.B. (2006) Crystal-chemical factors responsible for the distribution of octahedral cations over *trans*- and *cis*-sites in dioctahedral 2:1layer silicates. *Clays and Clay Minerals*, **54**, 131-152.

Drits V. A., Guggenheim S., Zviagina B.B. & Kogure, T. (2012) Structures of the 2:1layers of pyrophyllite and talc. *Clays and Clay Minerals*. **60**, 574-587.

Eberl D. Jones B.F. & Khoury H.N. (1982) Mixed- layer kerolite/stevensite from the Amargosa Desert, Nevada. *Clays and Clay Minerals,* **39**, 321-326.

Eggleton R.A. & Bailey S.W. (1967) Structural aspects of dioctahedral chlorite. *American Mineralogist*, **52**, 673-689.

Engelhardt W.von (1942) Die strukturen von thuryngit, bavalit, und chamosit und ihre stellung in der chloritgruppe. *Zeitschrift für Kristallographie, Kristallgeometrie, Kristallphysik, Kristallchemie*, **104**, 152-159

https://doi.org/10.1180/clm.2023.20 Published online by Cambridge University Press

Ennadi A., Legrouri A., De Roy A. & Besse J. P. (2000) X-Ray diffraction pattern simulation for thermally treated [Zn–Al–Cl] Layered Double Hydroxide. *Journal of Solid Solid State Chemistry*, **152**, 568-572.

Evans B. W. (1976) Stability of chrysotile and antigorite in the serpentinite multisystem. *Schweizer Mineralogische und Petrographische Mitteilungen*, **56**, 79-93.

Evans B.W. & Guggenheim, S. (1991) Talc, pyrophyllite, and related minerals. Pp 225-294 in: *Hydrous phyllosilicates (Reviews in Mineralogy, Volume 19)* (S.W. Bailey editor). Mineralogical Society of America, Washington, D.C.

Falini G., Foresti E., Gazzano M., Gualtieri A.F., Leoni M., Lesci I. G. & Roveri N. (2004) Tubular-shaped stoichiometric chrysotile nanocrystals. *Chemistry - A European Journal,* **10**, 3043-3049.

Faust G.T., Hataway J.C. & Millot G. (1959) A restudy of stevensite and allied minerals. *American Mineralogist*, **44**, 342-370.

Ferrage E., Lanson B., Sakharov B., Geoffroy N., Jacquot E. & Drits V. (2007) Investigation of dioctahedral smectite hydration properties by modeling of X-ray diffraction profiles: Influence of layer charge and charge location. *American Mineralogist*, **92**, 1731–1743.

Ferrage E. (2016) Investigation of the interlayer organization of water and ions in smectite from the combined use of diffraction experiments and molecular simulations: A review of methodology, applications and perspectives. *Clays and Clay Minerals*, **64**, 346–371.

Fiore S., Huertas F.J., Huertas F. & Linares J. (1995) Morphology of kaolinite crystals synthesized under hydrothermal conditions. *Clays and Clay Minerals*, **43**, 353–360.

Forbes W.C. (1969) Unit-cell parameter and optical properties of talc on the join $Mg_3Si_4O_{10}(OH)_2$ $Fe_3Si_4O_{10}(OH)_2$. *American Mineralogist*, **54**, 1399-1408.

Foord E.E., Starkey H.C., Taggart J.E. & Shawe D.R. (1987) Reassessment of the volkonskoite-chromium smectite nomenclature problem. *Clays and Clay Minerals*, **35**, 139-149.

Forano C., Costantino U., Prévôt V. & Taviot Gueho C. (2013) Layered Double Hydroxides(LDH). Pp 745–782 in: *Developments in Clay Science – Volume 5A. Handbook of Clay Science,* 2nd edition. (F. Bergaya &G. Lagaly editors), Elsevier.

Fritsch E., Balan E., Petit S. & Juillot F. (2021) Structural, textural, and chemical controls on the OH stretching vibrations in serpentine-group minerals. *European Journal of Mineralogy*, **33**, 447–462.

Frondel C. & Ito J. (1966) Hendricksite: a new species of mica. *American Mineralogist*, **51**, 1107-1123.

Frondel C. & lto J. (1975) Zinc-rich chlorites from Franklin, New Jersey with a note on chlorite nomenclature. *Neues Jahrbuch fiir Mineralogie Abhandlungen*, **123**, 111- 115.

Gastuche M.C.G., Brown G. & Mortland M. M. (1967) Mixed magnesium–aluminum hydroxides. I Preparation and characterization of compounds formed in dialyzed systems. *Clay Minerals*, **7**, 177-192.

Gates W.P., Slade P.G., Manceau A. & Lanson B. (2002) Site occupancies by iron in nontronites. *Clays and Clay Minerals*, **50**, 223-239.

Gaudin A., Petit S., Rose J., Martin F., Decarreau A., Noack Y. & Borschneck D. (2004) The accurate crystal chemistry of ferric smectites from the lateritic nickel ore of Murrin Murrin (Western Australia). II: spectroscopic (IR and EXAFS) approaches. *Clay Minerals*, **39**, 453-467.

https://doi.org/10.1180/clm.2023.20 Published online by Cambridge University Press

Geiger C. A., Henry D. L., Bailey S. W. & Maj J. J. (1983) Crystal structure of cronstedtite 2H_2. *Clays and Clay Minerals*, **31**, 97- 108.

Gerth, J. (1990) Unit-cell dimension of pure and trace metal associated goethites. *Geochimica Cosmochimica Acta*, **54**, 363-371.

Giese R.F. (1991) Kaolin minerals: structure and stabilities. Pp 29-66 in: *Hydrous phyllosilicates (Reviews in Mineralogy, Volume 19)* (S.W. Bailey editor). Mineralogical Society of America, Washington D.C., USA.

Grauby O., Petit S., Decarreau A. & Baronnet A. (1994) The nontronite-saponite series: an experimental approach**.** *European Journal of Mineralogy*, **6,** 99-112**.**

Grégoire B., Ruby C. & Carteret C. (2012) Structural cohesion of MII-MIII Layered Double Hydroxides crystals: Electrostatic forces and cationic polarizing power. *Crystal Growth & Design*, **12**, 4324-4333.

Grüner J.W. (1944) The composition and structure of minesotaite, a common iron silicate in iron formations. *American Mineralogist*, **29,** 363-372.

Guggenheim S. (1984) The brittle micas Pp 61-104 in: *Micas (Reviews in Mineralogy, Volume 13)* (S.W. Bailey editor). Mineralogical Society of America, Washington, D.C.

Guggenheim, S. & Eggleton, R. A. (1986) Structural modulations in iron-rich and magnesium-rich minnesotaite. *The Canadian Mineralogist*, **24**, 479-497.

Guggenheim S. & Eggleton R. A (1987) Modulated 2:1 layer silicates: review, systematics and predictions. *American Mineralogist*, **72**, 724- 738.

Guggenheim S. & Eggleton R. A. (1988) Crystal chemistry, classification, and identification of modulated layer silicates. Pp 675-725 in: *Hydrous Phyllosilicates (Reviews in Mineralogy, Vol. 19), (S. W. Bailey editor)*. Mineralogical Society of America, Washington, D.C.

Guggenheim S. V. & Eggleton R. A. (1998) Modulated crystal structures of greenalite and caryopilite: a system with long-range, in-plane structural disorder in the tetrahedral sheet. *The Canadian Mineralogist*, **36**, 163-179.

Guggenheim S. V. & Zhan W. (1998) Effet of temperature on the structures of lizardite-1*T* and lizardite 2H_1. *The Canadian Mineralogist*, **36**, 1587-1594.

Guggenheim S. V. & Bailey S.W. (1989) An occurrence of a modulated serpentine related to the greenalite-caryopilite series. *American Mineralogist*, **74**, 637-641.

Güven N. (1971) The crystal structures of 2M1 phengite and 2M1 muscovite. *Zeitschrift für Kristallographie*, **134**, 196-212.

Handbook of Mineralogy *(Anthony J.W., Bideaux R.A., Bladh K.W. & Nichols M.C., Eds.)*, Mineralogical Society of America, Chantilly, VA 20151-1110, USA. http://www.handbookofmineralogy.org/.

Hazen R.M. & Wones D.R. (1972) The effect of cation substitutions on the physical properties of trioctahedral micas. *American Mineralogist*, **57**, 103- 129.

Hazen R. M. & Burnham C.W. (1973) The crystal structure of one-layer phlogopite and annite. *American Mineralogist*, **58**, 889-900.

Heuser M., Andrieux P., Petit S. & Stanjek H. (2013) Iron-bearing smectites: a revised relationship between structural Fe, *b* cell edge lengths and refractive indices. *Clay Minerals*, **48**, 97-103.

https://doi.org/10.1180/clm.2023.20 Published online by Cambridge University Press

Hewitt D.A. & Wones D.R. (1975) Physical properties of some synthetic Fe-Mg-Al trioctahedral biotites. *American Mineralogist*, **60**, 854-862.

Higashi S., Miki K. & Komarneni S. (2002) Hydrothermal synthesis of Zn-smectites. *Clays and Clay Minerals*, **50**, 299-305.

Hill R.J. (1979) Crystal structure refinement and electron density distribution in diaspore. *Physics and Chemistry of Minerals*, **5**, 179-200.

Huminicki D. M. C. & Hawthorne F. C. (2003) The crystal structure of nikischerite, $NaFe^{2+}_6Al_3(SO4)_2(OH)_{18}(H_2O)_{12}$, a mineral of the shigaite group. *The Canadian Mineralogist*, **41**, 79-82.

Hybler J., Petříček, Ďurovič S. & Smrčok Ľ. (2000) Refinement of the crystal structure of cronstedtite-1*T*. *Clays and Clay Minerals*, **48**, 331-338.

Hybler J. (2016) Crystal structure of cronstedtite-6T_2, a non-MDO polytype. *European Journal of Mineralogy*, **28**, 777-788.

Hybler J., Sejkora J. & Venclík V. (2016) Polytypism of cronstedtite from Pohled, Czech Republic. *European Journal of Mineralogy*, **28**, 765-775.

Hybler J. & Sejkora J. (2017) Polytypism of cronstedtite from Chyňava, Czech Republic. *Journal of Geosciences*, **62**, 137-146.

Hybler J., Dolniček Z., Sejkora J. & Števko M. (2020) Polytypism of cronstedtite from Nagybörzsöny, Hungary. *Clays and Clay Minerals*, **68**, 632-645.

Hybler J., Dolniček Z., Sejkora J. & Števko M. (2021) Polytypism of cronstedtite from Ouedi Beht, El Hammam, Morocco. *Clays and Clay Minerals*, **69**, 702-734.

Iriarte I., Petit S., Huertas J., Fiore S., Grauby O., Decarreau A. & Linares J. (2005) Synthesis of kaolinite with a high level of Fe^{3+} for Al substitution. *Clays and Clay Minerals*, **53**, 1-10.

Jahanbagloo I. C. & Zoltai T. (1968) The crystal structure of a hexagonal Al-serpentine. *American Mineralogist*, **53**, 14-24.

Jain A., Ong S.P., Hautier G., Chen W., Richards W.D., Dacek S., Cholia S., Gunter D., Skinner D., Ceder G., Persson K.A. (2013) The Materials Project: A materials genome approach to accelerating materials innovation. *APL Materials*, **1** (1), 011002.

Jasmund K., Sylla H.M. & Freund F. (1975) Solid solution in synthetic serpentines phases. Pp. 267-274 in: *Proceedings of the International Clay Conference*, Mexico**.**

Joussein E., Petit S., Chruchman J., Theng B., Righi D. & Delvaux B. (2005) Halloysite clay minerals – a review. *Clay Minerals,* **40**, 383-426.

Kato (1963) New data on the so-called bementite. *Journal of the Mineralogical Society of Japan*, **6**, 93-103.

Khoury H.N., Mackenzie R.C., Russel J.D. & Tait J.M. (1984) An iron free volkonkoite. *Clay Minerals*, **19**, 43-57.

Kloprogge J.T. (2017) Application of vibrational spectroscopy in clay minerals synthesis. Pp.222-287 in: *Infrared and Raman spectroscopies of clay minerals* (W.P. Gates, J.T. Kloprogge, J. Madejová& F. Bergaya, editors), Developments in Clay Science, Vol. 8, Elsevier.

Kodama H., De Kimpe C.R. & Dejou J. (1988) Ferrian saponite in a gabbro saprolite at Mont Mégantic, Quebec. *Clays and Clay Minerals*, **36**, 102-110.

https://doi.org/10.1180/clm.2023.20 Published online by Cambridge University Press

Kohler T. & Armbruster T. (1997) Hydrogen bonding and Jahn-Teller distortion in groutite α-MnOOH and manganite γ- MnOOH, and their relations to the manganese dioxides ramsdellite and pyrolusite. *Journal of Solid State Chemistry*, **133***, 486-500.*

Köster H.M., Ehrlicher U., Gilg H.A., Jordan R., Murad E. & Onnich K. (1999) Mineralogical and chemical characteristics of five nontronites and Fe-rich smectites. *Clay Minerals*, **34**, 579- 599.

Knurr R.A. & Bailey S.W. (1986) Refinement of Mn-substituted muscovite and phlogopite. *Clays and Clay Minerals*, **34**, 7–16.

Lee S.S., Guggenheim S., Dyar M.D. & Guidotti C.V. (2007) Chemical composition, statistical analysis of the unit cell, and electrostatic modeling of the structure of Al-saturated chlorite from metamorphosed rocks. *American Mineralogist*, **92**, 954-965.

Lombardo G. M., Pappalardo G. C., Punzo F., Costantino F., Costantino U. & Sisani M. (2005) A novel integrated X-ray powder diffraction (XRPD) and molecular dynamics (MD) approach for modelling mixed-metal (Zn, Al) layered double hydroxides (LDHs). *European Journal of Inorganic Chemistry*, **24**, 5026-5034.

McCauley J.W. & Newnham R.E. (1971) Origin and prediction of ditrigonal distortions in micas. *American Mineralogist*, **56**, 1626-1638.

MacEwan D.M.C. (1961) Montmorillonite minerals. Pp.143-207 in: *The X-Ray Identification and crystal structures of clay minerals, 2nd Ed.* (G. Brown, editor), Mineralogical Society, London.

Maksimovic Z. (1966) Kerolite- pimelite series from Goles Mountain. Yugoslavia. Pp. 97-105 in: *Proceedings of the International Clay Conference,* Jerusalem.

Maksimovic Z. & Bish D. (1978) Brindleyite, a nickel-rich aluminous serpentine mineral analogous to berthierine. *American Minereralogist*, **63**, 484-489.

Manohara G. V. & Vishnu Kamath P. (2010) Synthesis and structure refinement of layered double hydroxides of Co, Mg and Ni with Ga. *Bulletin of Materials Science,* **33***,* 325-331.

Manohara G. V., Prasanna S. V. & Vishnu Kamath P. (2011) Structure and Composition of the Layered Double Hydroxides of Mg and Fe: Implications for Anion-Exchange Reactions. *European Journal of Inorganic Chemistry,* **16***,* 2624-2630.

Martin F., Petit S., Decarreau A., Grauby O., Hazemann J.L & Noack Y. (1992) Experimental study of (Si-Ge) tetrahedral solid solution in Ni-Co-Mg talcs. *Thin Solid Films,* **222**, 189 - 195.

Martin F., Petit S., Decarreau A., Ildefonse Ph., Grauby O., Beziat D., De Parseval Ph. & Noack Y. (1998) Ga/Al substitutions in synthetic kaolinites and smectites. *Clay Minerals*, **33**, 231-241.

Martin F., Ildefonse Ph., Hazemann J.L., Mathe P., Noack Y., Grauby O., Beziat D. & de Parseval Ph. (1997) Gallium crystal chemistry in synthetic goethites. *Proceedings of the 9th International Conference on X-Ray Absorption Fine Structure. Pp.* C2 821-822, Journal de Physique III.

Martin de Vidales J.L., Pozo M., Alia J.M., Garcia-Navaro F. & Rull F. (1991) Kerolite- stevensite mixed-layers from the Madrid basin, central Spain. *Clay Minerals*, **26**, 329-342.

Mathieson A. McL. &Walker G.F. (1954) Crystal structure of magnesium-vermiculite. *American Mineralogist*, **39**, 231-255.

Mellini M. (1982) The crystal structure of lizardite 1*T*: hydrogen bonds and polytypism. *American Mineralogist*, **67**, 587-598.

https://doi.org/10.1180/clm.2023.20 Published online by Cambridge University Press

Mellini M. & Zanazzi P.F. (1987) Crystal structures of lizardites-1*T* and lizardites-2*H1* from Coli, Italy. *American Mineralogist*, **72**, 943- 948.

Mellini M. & Viti C. (1994) Crystal structures of lizardites-1*T* from Elba, Italy. *American Mineralogist*, **79**, 1194-1198.

Mellini M. (2013) Structure and microstructure of serpentine minerals. *EMU Notes in Mineralogy 14,* **Chapter 5**, 1–27.

Merlino S. & Orlandi P. (2001) Carraraite and zaccagnaite, two new minerals from the Carrara marble quarries: their chemical compositions, physical properties, and structural features. *American Mineralogist*, **86***,* 1293-1301.

Mercier P.H.J., Rancourt D.G., Robert Jean-Louis, Berman R.G. & Redhammer G.J. (2005) Fundamental difference between synthetic powder and natural or synthetic single-crystal 1*M* micas: Geometric homo-octahedral vs. geometric meso-octahedral sheets. *American Mineralogist*, **90***,* 399-410.

Nadeau P.H., Farmer V.C., Mc Hardy W.J. & Bain D.C. (1985) Compositional variations of the Unterrupsroth beidellite. *American Mineralogist*, **70**, 1004-1010.

Nestroinaya O. V., Ryltsova I. G., Lebedeva O. E., Uralbekov B. M. & Ponomarenko O. I. (2017) Synthesis and thermal transformation of multi-component layered double MgCo/AlFe hydroxides with hydrotalcite srtucture. *Russian Journal of General Chemistry*, **87***,* 163-167.

Nagelschmidt G. (1938) On the atomic arrangement and variability of the members of the montmorillonite group. *Mineralogical Magazine*, **25**, 140.

Oberlin A. & Méring J. (1966) Observation sur l'hectorite (étude en microscopie et diffraction électroniques). *Bulletin de la Société française de Minéralogie Cristallographie*, **89**, 29-40.

Parise J.B., Leinenweber K., Weidner D.J., Tan K., von Dreele R.B. (1994) Pressure-induced H bonding: Neutron diffraction study of brucite, $Mg(OD)_2$, to 9.3 GPa. *American Mineralogist*, **79**, 193-196,

Pastor-Rodriguez J. & Taylor H. F. W. (1971) Crystal structure of coalingite. *Mineralogical Magazine,* **38***,* 286-294.

Pauling L. (1930) The structures of the chlorites. *PNAS*, **16**, 578-582.

Peacor D. R., Essene E. J., Simmons Jr, W. B. & Bigelow W. (1974) Kellyite a new Mn-Al member of the serpentine group from Bald Knob, North Carolina, and new data on grovesite. *American Mineralogist*, **59**, 1153- 1156**.**

Perdikatsis B. & Burzlaff H. (1981) Struktuverfeinerung am Talk $Mg_3[(OH)_2Si_4O_{10}]$. *Zeitschrift für Kristallographie*, **156**, 177-186.

Peterson R. C., Hill R. J.& Gibbs G. V. (1979) A molecular-orbital study of distortions in the layer structures brucite, gibbsite and serpentine. *The Canadian Mineralogist*, **17**, 703-713

Petit S. (1990) *Etude cristallochimique de kaolinites ferrifères et cuprifères de synthèse (150-250°C)*. PhD Thesis, Université de Poitiers, France.

Petit S., Decarreau A., Eymery J.P. & Thomassin J.H. (1988) Synthèse de kaolinites ferriques à 200°C. Comparaison avec des kaolinites d'altération supergène : teneur en fer, morphologie, cristallinité. *Comptes Rendus de l'Académie des Sciences*, **t.307, série II**, 1961-1966.

Petit S. & Decarreau A. (1990) Hydrothermal (200°C) synthesis and crystal chemistry of iron-rich kaolinites. *Clay Minerals*, **25**, 181-196.

https://doi.org/10.1180/clm.2023.20 Published online by Cambridge University Press

Petit S., Prot T., Decarreau A., Mosser C. & Toledo-Groke C. (1992) Crystallochemical study of a population of particles in smectites from a lateritic weathering profile. *Clays and Clay Minerals*, **40**, 436-445.

Petit S., Caillaud J., Righi D., Madejová F., Elsass F. & Köster H.M. (2002) Characterization and crystal chemistry of Fe-rich montmorillonite from Ölberg, Germany. *Clay Minerals*, **37**, 283-297.**D**

Petit S., Martin F., Wiewiora A., Parseval P. D. & Decarreau A. (2004) Crystal-chemistry of talc: A near infrared (NIR) spectroscopy study. *American Mineralogist*, **89**, 319-326.

Petit S., Righi D. & Decarreau A. (2008) Transformation of synthetic Zn-stevensite into Zn-talc induced by the Hofmann-Klemen effect. *Clays and Clay Minerals,* **56**, 645-654.

Petit S., Decarreau A., Gates W., Andrieux P. & Grauby O. (2015) Hydrothermal synthesis of dioctahedral smectites: The Al–Fe^{3+} chemical series. Part II: Crystal-chemistry. *Applied Clay Science*, **104**, 96-105.

Petit S., Baron F. & Decarreau A. (2017) Synthesis of nontronite and other iron-rich smectites: a critical review. *Clay Minerals,* **52**, 469-483.

Pollastri S., Perchiazzi N., Lezzerini M., Plaisier J.R., Cavallo A., Dalconi M.C., Gandolfi N. B. & Gualtieri A.F. (2016) The crystal structure of mineral fibres. 1. Chrysotile. *Periodico di Mineralogia*, **85**, 249-259.

Post J.L., Cupp B.L. & Madsen F.T. (1997) Beidellite and associated clays from the De Lamar mine and Florida Mountain area, Idaho. *Clays and Clay Minerals*, **45**, 240-250.

Pozo M. & Casas J. (1999) Origin of kerolite and associated Mg clays in palustrine-lacustrine environments. The Esquivas deposit (Neogene Madrid basin, Spain). *Clay Minerals*, **34**, 395-418.

Radha A. V., Vishnu Kamath P. & Shivakumara C. (2007) Order and disorder among the layered double hydroxides: combined Rietveld and DIFFaX approach. *Acta Crystallographica Section B: Structural Science,* **63**, 243-250.

Radha S., Prasanna S. V. & Vishnu Kamath P. (2011) Polytype Selection by Intercalated Anions: Design and Synthesis of the 3R2 Polytype of the Layered Double Hydroxide of Zn and Al. *Crystal Growth Design,* **11**, 2287-2293

Radoslovich E. W. (1962) The cell dimensions and symmetry of layer lattice silicates. II. Regression relations. *American Mineralogist*, **47**, 617-636.

Radoslovich E. W. & Norrish K. (1962) The cell dimensions and symmetry of layer lattice silicates. I. Some structural considerations. *American Mineralogist*, **47**, 599-616.

Radoslovich E. W. (1963) The cell dimensions and symmetry of layer lattice silicates. VI. Serpentine and kaolin morphology. *American Mineralogist*, **48**, 368-378.

Redhammer G.J. & Roth G. (2002) Single-crystal structure refinements and crystal chemistry of synthetic trioctahedral micas $KM_3(Al^{3+},Si^{4+})_4O_{10}(OH)_2$, where M = Ni^{2+}, Mg^{2+}, Co^{2+}, Fe^{2+}, or Al^{3+}. *American Mineralogist*, **87**, 1464-1476.

Rieder M. (1970) Chemical composition and physical properties of lithium-iron micas from the Krusné hory Mts. (Erzgebirge) Part A: chemical composition. *Contributions to Mineralogy and Petrology*, **27**, 131-158.

Rieder M., Pichova A., Fassova M., Fediukova E. & Cerny P. (1971) Chemical composition and physical properties of lithium-iron micas from the Krusné hory Mts. (Erzgebirge), Czechoslovakia and Germany. Part B: cell parameters and optical data. *Mineralogical Magazine*, **38**, 190-196.

Rius J. & Allmann R. (1984) The superstructure of the double layer mineral wermlandite, $[Mg_7(Al_{0.57}Fe_{0.43})_2(OH)_{18}][(Ca_{0.6}Mg_{0.4})(SO_4)_2,12H_2O]$. *Zeitschrift für Kristallographie*, **168**, 133-144.

https://doi.org/10.1180/clm.2023.20 Published online by Cambridge University Press

Robert J.L. (1976) Phlogopite solid solutions in the system K_2O-MgO-Al_2O_3-SiO_2-H_2O. *Chemical Geology*, **17**, 195-212.

Robinson G.W. & Chamberlain S.C. (1984) Famous mineral localities: the Sterling Mine Antwerp, New York. *The Mineralogical Record*, **July-August**, 199–216.

Roussel H., Briois V., Elkaim E., de Roy A. & Besse J. P. (2000) Cationic Order and Structure of [Zn−Cr−Cl] and [Cu−Cr−Cl] Layered Double Hydroxides: A XRD and EXAFS Study. Journal of Physical Chemistry B, **104***,* 5915-5923.

Rozenson I. & Heller-Kallai L. (1976) Reduction and oxidation of Fe^{3+} in dioctahedral smectites -1: Reduction with hydrazine and dithionite. *Clays and Clay Minerals*, **24**, 271-282.

Rule A.C.& Bailey S.W. (1987) Refinement of the crystal structure of a monoclinic ferroan clinochlore. *Clay and Clay Minerals*, **35**, 129-138.

Russel J.D. & Clark D.R. (1978) The effect of Fe-for-Si substitution on the *b*-dimension of nontronite. *Clay Minerals*, **13**, 133-137.

Ryan P.C. & Hillier S. (2002) Berthierine/chamosite, corrensite, and discrete chlorite from evolved verdine and evaporite-associated facies in the Jurassic Sundance Formation, Wyoming. *American Mineralogist*, **87**, 1607–1615.

Saalfeld H. &Wedde M. (1974) Refinement of the crystal structure of gibbsite, $Al(OH)_3$. *Zeitschrift für Krystallographie*, **139**, 129-135.

Sankaranarayanan, S., Sharma, A. & Srinivasan, K. (2015) Co Cu Al layered double hydroxides – efficient solid catalysts for the preparation of industrially important fatty epoxides. *Catalysis Science & Technology,* **5***,* 1187-1197.

Schulze D.G. (1984) The influence of aluminum on iron oxides. VIII. Unit-cell dimensions of Al-substituted goethites and estimation of Al from them. *Clays and Clay Minerals*, **38**, 36-44.

Schwertmann U., Gasser U. & Sticher H. (1989) Chromium for iron substitution in synthetic goethites. *Geochimica Cosmochimica Acta*, **53,** 1293-1297**.**

Shannon R.D. (1976) Revised effective ionic radii and systematic studies of interatomic distances in halides and chalcogenides. *Acta Crystallographica,* **A32**, 751-767.

Shannon R.D., Gumerman P.S. & Chenavas J. (1975) Effect of octahedral distortion on mean Mn^{3+}-O distances. *American Mineralogist*, **60**, 714-716.

Shirozu, M & Bailey, S.W. (1966) Crystal structure of a two-layer Mg-vermiculite. *American Mineralogist*, **51**,1124-1143.

Smyth J.R., Dya rM.D., May H.M., Bricker O.P. & Acler J.G. (1997) Crystal structure refinement and Mössbauer spectroscopy of an ordered, triclinic clinochlore. *Clays and Clay Minerals*, **45**, 544-550.

Środoń (2013) Identification and quantitative analysis of clay minerals. Pp. 34 in: *Developments in Clay Science – Volume 5B. Handbook of Clay Science,* 2nd edition. (F. Bergaya &G. Lagaly editors), Elsevier.

Steadman R. & Youell R. F. (1958) Mineralogy and crystal structure of greenalite. *Nature*, **181**, 45.

Stiers W. & Schwertmann U. (1985) Evidence of manganese substitution in synthetic goethite. *Geochimica Cosmochimica Acta,* **49**, 1909-1911.

Suquet H., De La Calle C. & Pezerat H. (1975) Swelling and structural organization of saponite. *Clays and Clay Minerals*, **23**, 1-9.

https://doi.org/10.1180/clm.2023.20 Published online by Cambridge University Press

Suquet H., Malard C., Copin E. & Pézerat H. (1981) Variation du paramètre b et de la distance basale (001) dans une série de de saponites à charge croissante. *Clay Minerals*, **16**, 53-67.

Taner M. F. & Laurent R. (1984) Iron-rich amesite from lake Asbestos mine, Black Lake, Quebec. *The Canadian Mineralogist*, **22**, 437- 442.

Tomisaka T. & Kato T. (1963) A study of the polymorphism of serpentine minerals. *Journal of the Mineralogical Society of Japan*, **6,** 209- 229.

Toraya H. (1981) Distortions of octahedra and octahedral sheets in 1M micas and the relation to their stability. *Zeitschrift für Kristallographie,* **157**, 173-190.

Tsipursky S.I. & Drits V.A. (1984) The distribution of octahedral cations in the 2:1layers of dioctahedral smectites studied by oblique -texture electron diffraction. *Clay Minerals*, **19**, 177-193.

Wahle M.W., Bujnowski T.J., Guggenheim S. & Kogure T. (2010) Guidottite, the Mn-analogue of cronstedtite: a new serpentine-group mineral from South Africa. *Clays and Clay Minerals*, **58**, 364-376.

Weiss A., Roch G. & Hofmann U. (1954) Zur Kenntnis von wolkonskoit. *Berichte der Deutschen Keramischen Gesellschaft*, **31**, 301-305.

Weiss Z., Rieder M., Chmielová M. & Krajíček J. (1985) Geometry of the octahedral coordination in micas: a review of refined structures. *American Mineralogist*, **70**, 747-757.

Wicks F.J. & Whittaker J.W. (1975) A reappraisal of the structures of the serpentine minerals. *The Canadian Mineralogist*, **13**, 227-243.

Wicks F.J. & Hawthorne F.C. (1986) Distance least-squares modelling of lizardite lT structure. Pp. 144 in: Program Abstracts II Joint Annual Meeting of the Geological Association of Canada and Mineralogical Association of Canada, Ottawa, Canada.

Wicks F.J. & O'Hanley D.S. (1991) Serpentine minerals: structures and petrology. Pp 91-167 in: *Hydrous phyllosilicates (Reviews in Mineralogy, Volume 19)* (S.W. Bailey, editor). Mineralogical Society of America, Washington, D.C.

Wiewiora A., Raussel-Colomb J. A. & Garcia-Gonzales T. (1991) The crystal structure of amesite from Mount Sobotka: a nonstandard polytype. *American Mineralogist*, **76**, 647-652.

Wiewiora A. & Wilamowski A. (1996) The relation between composition and *b* for chlorites. *Geologica Carpathica Clays,* **5***,* 79-87.

Wilkins R.W.T. & Ito J. (1967) Infrared spectra of some synthetic talcs. *American Mineralogist*, **52**, 1649-1661.

Wise W.S. & Eugster H.P. (1964) Celadonite: synthesis, thermal stability and occurrence. *American Mineralogist*, **49**, 1031-1083.

Wones D.R. (1963) Physical properties of synthetic biotites on the join phlogopite-annite. *American Mineralogist*, **48**, 1300-1321.

Wones D.R. & Eugste,r H.P. (1965) Stability of biotite: experiment, theory and application. *American Mineralogist*, **50**, 1228-1272.

Wunder B., & Schreyer W. (1997) Antigorite: High-pressure stability in the system MgO-SiO_2–H_2O (MSH), *Lithos*, **41***,* 213–227.

Yoder H.S. & Eugster H.P. (1955) Synthetic and natural muscovite. *Geochimica Cosmochimica Acta*, **8**, 225-280.

https://doi.org/10.1180/clm.2023.20 Published online by Cambridge University Press

Yoshimura T., Shirozu H. & Hirowabori F. (1963) Bementite and pyromanganite from the Ichinomata mine, Kunamoto prefecture. *Journal of the Mineralogical Society of Japan,* **3**, 457-467.

Zazzi A, Hirsch T.K., Leonova E., Kaikkonen A., Grins J., Annersten H. & Eden M. (2006) Structural investigations of natural and synthetic chlorite minerals by X-ray diffraction, Mössbauer spectroscopy and solid-state nuclear magnetic resonance. *Clays and Clay Minerals*, **54**, 252-265.

Zhang H., Gilbert B. & Banfield J.F. (2021) Atomic perspective on the serpentine–chlorite solid-state transformation. *Chemistry of Materials*, **33**, 6338−6345.

Zheng H. & Bailey S.W. (1989) Structure of intergrown triclinic and monoclinic II*b* chlorites from Kenya. *Clay and Clay Minerals*, **37**, 308-316.

Zheng H. & Bailey S.W. (1997a) Refinement of an amesite-$2H_1$ polytype from Postmasburg, South Africa. *Clay and Clay Minerals*, **45**, 301-310.

Zheng H. & Bailey S.W. (1997b) Refinement of the cookeite ‘‘r’’ structure. *American Mineralogist*, **82**, 1007-1013.

Zviagina B.B. & Drits V.A. (2019) Structural factors affecting the crystal-chemical variability in Al-rich K-dioctahedral 2M1 micas. *Clay Minerals*, **54**, 1-11.

https://doi.org/10.1180/clm.2023.20 Published online by Cambridge University Press

Table captions

Table 1. Ionic radii (Å) of cations and O^{2-} and their coordination from Shannon (1976).

Table 2. Data used for hydroxide, oxy-hydroxide, and layered double hydroxide structures. *R*: mean ionic radius of octahedral cations (Å); (see text) (Å). *Sample reference in the paper. *a, b, and c*: crystallographic parameters (Å).

Table 3. Data used for TO phyllosilicates. *R*: mean ionic radius of octahedral cations (see text); *b*: crystallographic parameter (in Å). *Sample reference in the paper.

Table 4. Data used for TOT phyllosilicates with a neutral structure. *R*: mean ionic radius of octahedral cations (Å) (see text); *b*: crystallographic parameter (Å). *Sample reference in the paper.

Table 5. Data used for smectites. *R*: mean ionic radius of octahedral cations (Å) (see text); *b*: crystallographic parameter (Å). *Sample reference in the paper.

Table 6. Data used for micas. *R*: mean ionic radius of octahedral cations (Å) calculated with $r(Li^+)$ = 0.76 Å (see text); *b*: crystallographic parameter (Å). *Sample reference in the paper.

Table 7. Parameters of the regressions calculated for the synthetic micas (Figs. 15 to 19).

Table 8. Data used for chlorites. *R*: mean ionic radius of octahedral cations (Å) calculated with $r(Li^+)$ = 0.76 Å (see text); *b*: crystallographic parameter (Å). *Sample reference in the paper.

Table 9. Summary of tetrahedral parameters of chlorite. Sample reference from Table 8. Tetrahedral rotation angle α_{ref}: measured by structure refinement, α_{calc}: calculated ($\alpha=\arccos(b/b_{tet.})$ (Eq. 4) – see text). [#]: from structure refinement. [£]: calculated using the following equation derived from Eq. 3: (Si-O) = ($b_{tet.}$- $\sqrt{2}.^{IV}$Al.Δ) /(4.$\sqrt{2}$) with $b_{tet.}$ obtained from Eq. 4 with α_{ref}, and Δ = 0.13 being the difference between Si-O and Al-O bond lengths.

Table 10. Regression parameters proposed for the different mineral families investigated.

Table 11. Structural details for some phyllosilicates for comparison. Sample reference from Table 6 for micas, and table 4 for talc. *R* calculated with r(Li^+)= 0.60 Å. Tetrahedral rotation angle α_{ref}: measured by structure refinement, α_{calc}: calculated ($\alpha = arccos(b/b_{tet.})$ (Eq. 4) – see text). %O enlargement compared to hydroxides; O sheet thickness measured by structure refinement and α_{ref}: from Brigatti & Guggenheim (2002) for micas, and Drits *et al*. (2012) for talc.

https://doi.org/10.1180/clm.2023.20 Published online by Cambridge University Press

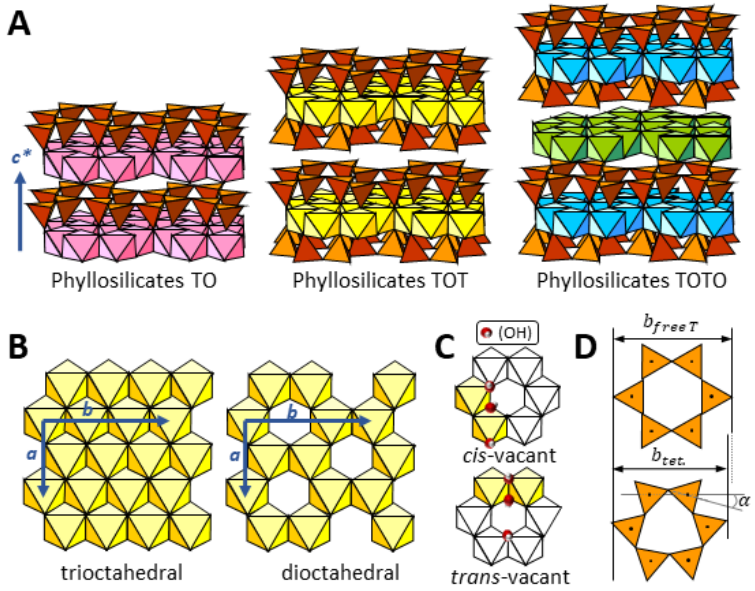

Fig. 1. Schematic representation of (A) basic structures of TO, TOT, and TOTO phyllosilicates. (B) Projection of *a* and *b* cell parameters (orthorhombic representation) on the surface of a trioctahedral and a dioctahedral sheet. (C) Distinction between *cis*- and *trans*-vacant di-octahedral sheets. (D) Tetrahedral rotation angle α.

https://doi.org/10.1180/clm.2023.20 Published online by Cambridge University Press

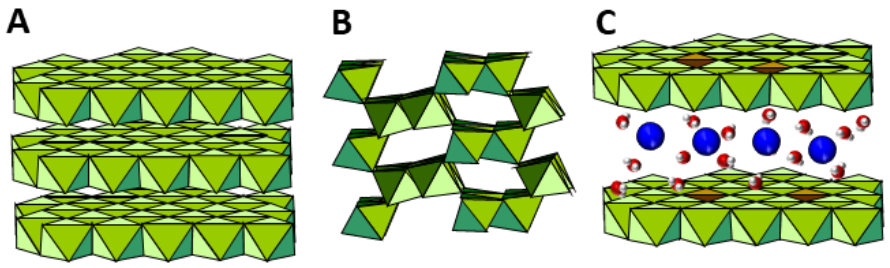

Fig. 2. Basic structure of (A) hydroxide (brucite), (B) oxyhydroxide (goethite), and (C) layered double hydroxides.

https://doi.org/10.1180/clm.2023.20 Published online by Cambridge University Press

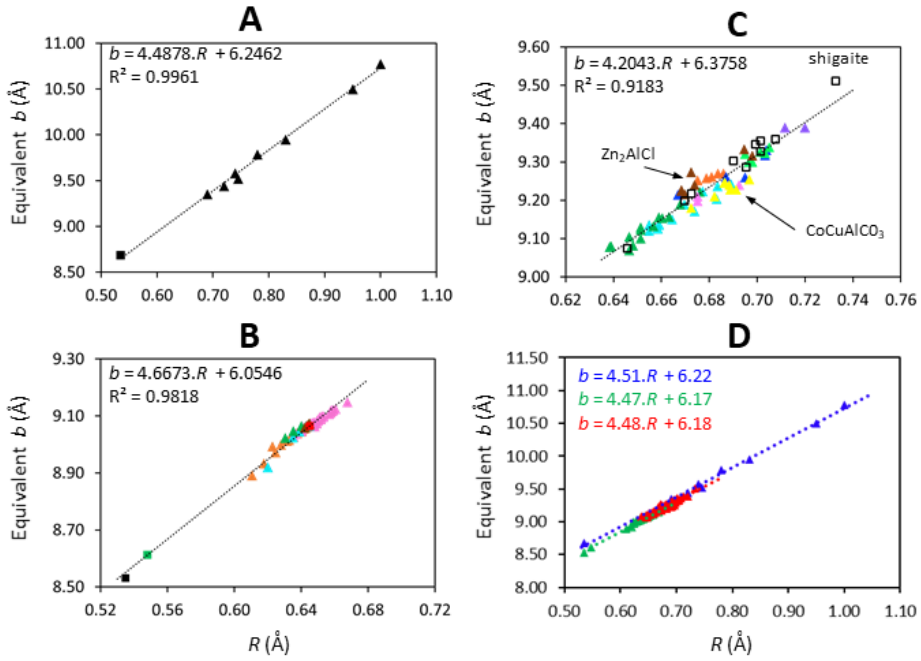

Fig. 3. Evolution of the equivalent *b* parameter (in Å) with the mean ionic radius of octahedral cations *R* (in Å) for hydroxide families (Table 2). (A) $M^{n+}(OH)_n$ hydroxides with square = natural gibbsite and triangles = M^{2+}- hydroxides synthetic series. (B) MO(OH) oxyhydroxides with squares or triangles corresponding to natural or synthetic samples, respectively. Black = diaspore, red = goethite, green = groutite, blue = GaO(OH), light blue = Ga-goethites series, orange = Co^{3+}-, Ni^{2+}-, Cu^{2+}-, Zn^{2+}-, Cd^{2+}-, and Pb^{4+}- goethites series, pink = Al-goethites series, green = Mn^{3+}-goethites series, and brown = Cr^{3+}-goethites series. (C) Layered double hydroxides with squares or triangles corresponding to natural or synthetic samples, respectively. Light blue = $MgAlCO_3$, green = $NiAlCO_3$, light green = $MgFeCO_3$, orange = $NiFeCO_3$, pink = $CoAlCO_3$, violet = $CoFeCO_3$, blue = $GaM^{2+}CO_3$, yellow = $CoCuAlCO_3$, brown = others. (D) Comparative regressions calculated from the model between the octahedral sheet dimension and *R* (see text for details). Blue dotted line = $M^{n+}(OH)_n$, green dotted line = MO(OH), and red dotted line = layered double hydroxides.

https://doi.org/10.1180/clm.2023.20 Published online by Cambridge University Press

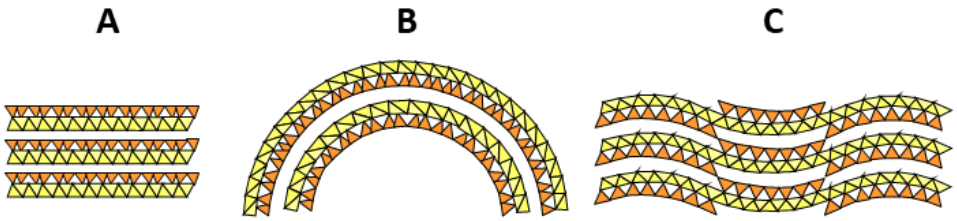

Fig. 4. Schematic representation of different structures of TO serpentines based on the crystal morphology. (A) flat morphology, (B) curved morphology, and (C) wavy corrugated morphology.

https://doi.org/10.1180/clm.2023.20 Published online by Cambridge University Press

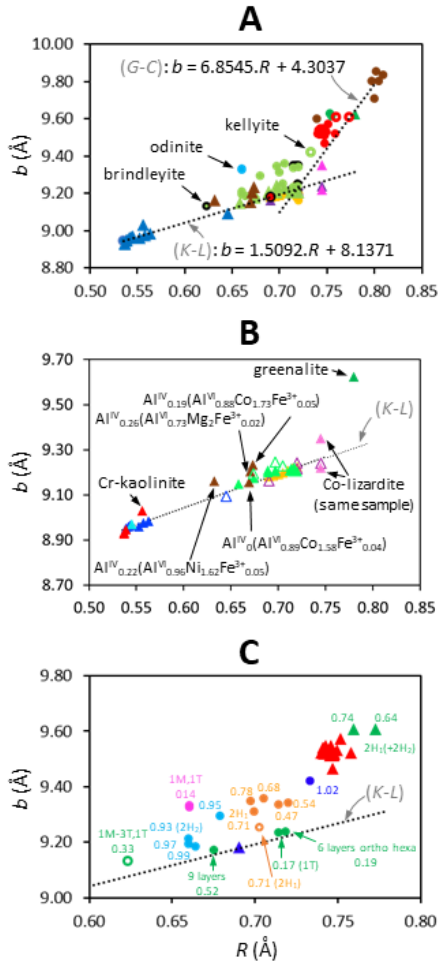

Fig. 5. *b vs.* mean ionic radius of octahedral cations *R* for TO phyllosilicates (Table 3). (A) Circles = natural samples, and triangles = synthetic samples. Blue = kaolinite, yellow = lizardite, black = antigorite, light green = Al- serpentine, with black border = brindleyite, open circle = kellyite, red = Fe^{3+}-serpentine: full circles = cronstedtite, with black border = pecoraite, open circles = guidottite, dark green = greenalite, brown circles = caryopilite, violet triangles = R^{2+}-chrysotile series, pink triangles = Co-lizardite. (K-L) and (G-C) correspond to kaolinite-lizardite and greenalite-caryopilite regression lines, respectively. (B) Focus on synthetic kaolinite-lizardite series. Blue triangles = Fe^{3+}-kaolinite series, open triangle = theoretical end-member, light blue triangle= Ga^{3+}-substituted kaolinite, red triangles= R^{3+}-kaolinite series, yellow triangles= Ni-Mg lizardite series, pink triangles= Co-lizardite, open violet triangles= R^{2+}-chrysotile, light green triangles = Mg-Al-serpentine series (Chemosky, 1975), open light green triangles = other Mg-Al- serpentines, brown triangles = R^{2+}- Al serpentine series, green triangle = greenalite. (C) Focus on natural Al-serpentines (circles) and Fe^{3+}- serpentines (triangles). Polytype (partly) and tetrahedral Al or Fe^{3+} pfu are indicated. Light blue circles = amesite, orange circles = berthierine, orange open circle = Ti-berthierine, green open circle =

https://doi.org/10.1180/clm.2023.20 Published online by Cambridge University Press

brindleyite, pink circles = odinite, dark blue circle = kellyite, green circles = other. Red triangles = cronstedtite ($2H_1$, $2H_2$, $3T$, $1T$, $6T_2$, and $3T$+$1M$ polytypes), blue triangle = pecoraite, green triangles = guidottite.

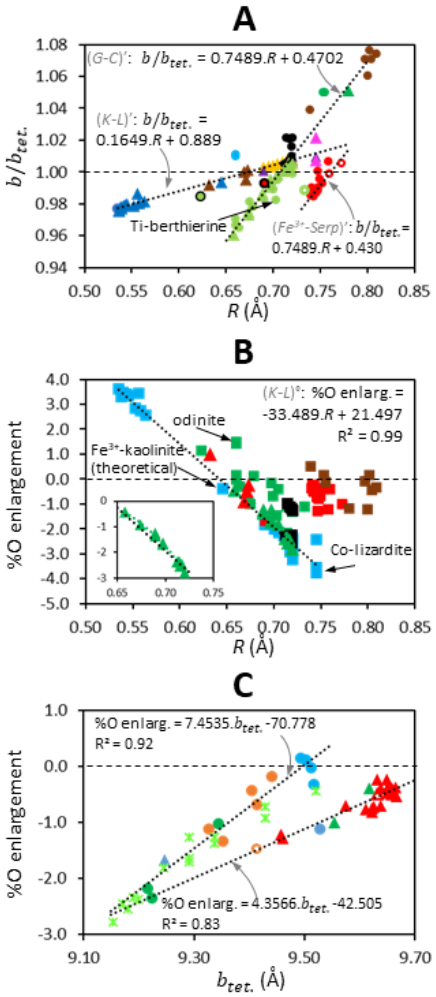

Fig. 6. (A) $b/b_{tet.}$ ratio *vs.* mean ionic radius of octahedral cations *R* for TO phyllosilicates (Table 3). Same symbols and colors as in Fig. 5A. (*K-L*)' and (*G-C*)' correspond to kaolinite-lizardite and greenalite-caryopilite regression lines. (B) Evolution of the percentage of octahedral enlargement compared to hydroxides (Eq. 6, see text for details) *vs. R*. Blue squares = kaolinites and lizardites, green squares = natural Al-serpentines, green triangles = synthetic Al-serpentines (zoom on the Chernosky (1975)'s series), red squares = Fe^{3+}-serpentines, black squares = antigorite, brown squares = caryopilites and greenalites. Blue dotted line = regression for kaolinite-lizardite series. (C) Evolution of the percentage of octahedral enlargement *vs.* $b_{tet.}$ for Al- and Fe^{3+}- serpentines. Same symbols and colors as in Fig. 5C for natural samples, light green crosses = synthetic Al-serpentines.

https://doi.org/10.1180/clm.2023.20 Published online by Cambridge University Press

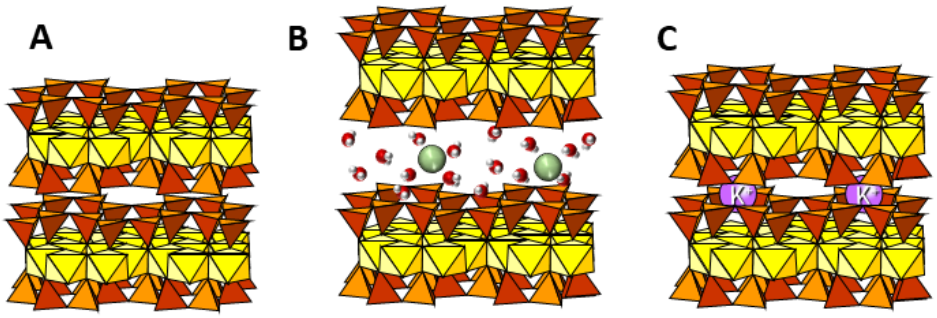

Fig. 7. Schematic representation of structures of various TOT phyllosilicates. (A) neutral TOT (e.g., pyrophyllite and talc), (B) low-charge hydrated TOT (e.g., smectite), and (C) high-charge TOT (e.g., mica).

https://doi.org/10.1180/clm.2023.20 Published online by Cambridge University Press

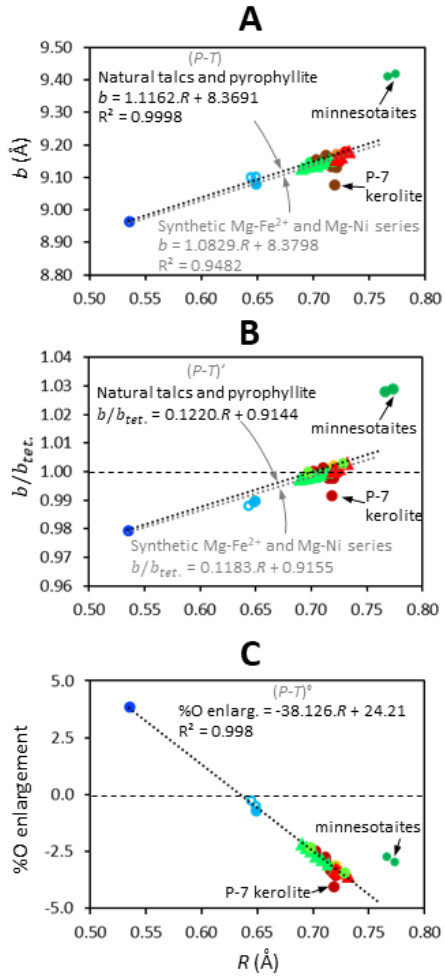

Fig. 8. (A) *b vs.* mean ionic radius of octahedral cations *R* for electro-neutral TOT phyllosilicates (Table 4). Circles = natural samples, triangles = synthetic samples. Dark blue circles = pyrophyllite, light blue circles = ferripyrophyllites, open circles = same sample, yellow circle = Mg-talc, red circle = Fe^{2+}-talc, green circle = willemseite, dark green circles = minnesotaites, brown circles = natural kerolites, light green triangles = synthetic Mg-Ni kerolite series, red triangles= Mg-Fe^{2+} synthetic talcs series. (*P-T*) corresponds to the natural pyrophyllite-talc regression line. Grey dotted line = regression calculated with Mg-Fe^{2+} and Mg-Ni synthetic series. B) $b/b_{tet.}$ ratio *vs.* the mean ionic radius of octahedral cations *R* for the same samples (and color code) as (A). (C) Evolution of the percentage of octahedral enlargement (Eq. 6, see text for details) *vs. R* for the same samples (and color code) as (A), dotted line = regression calculated excluding ferripyrophyllites, natural kerolites, and minnesotaites samples.

https://doi.org/10.1180/clm.2023.20 Published online by Cambridge University Press

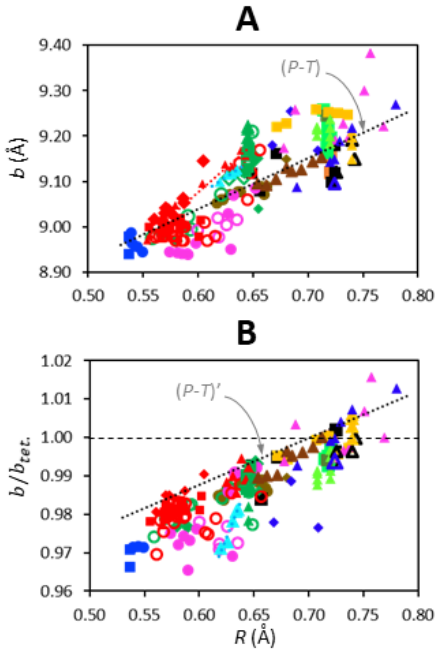

Fig. 9. (A) *b vs.* mean ionic radius of octahedral cations *R* for smectites (Table 5). (*P-T*) corresponds to the pyrophyllite-talc regression line (Fig. 8A). Triangles = synthetic smectites, red = $(Si_4)(Al_4)$ $(Fe^{3+}_{(2-x)}Al_x)$, light blue = $(Si_4)(Ga_4)$ $(Fe^{3+}_{(2-x)}Ga_x)$, green = $(Si_{4-x}Fe^{3+}_x)Fe^{3+}_2$, brown = $(Si, Fe^{3+})_4(Fe^{3+}, Mg)_y$, pink = Fe^{2+}-saponite series, light green = $(Si_{4-x}Al_x)(Mg_{(3-y)}Al_y)$, yellow = Zn-stevensite, dark blue = stevensite series, dark blue open symbol = hectorite, black open symbol = hectorite and Zn-hectorite. Other symbols = natural samples. Squares = samples from Radoslovich (1962), blue = beidellites, red = montmorillonites, green = nontronites, light green = saponites, yellow = sauconites, dark green = griffithite, black = hectorites, orange = stevensites, black = volkonskoites. Pink circles = samples from Brigatti (1983), open circles = nontronites, full circles = Al- and Fe^{3+}-montmorillonites. Green circles = dioctahedral smectites (Russell & Clark, 1978). Red open circles = dioctahedral smectites (Tsipursky & Drits, 1984) blue circles = beidellites (Post *et al.*, 1997), brown circles = intermediary smectites (Gaudin *et al.*, 2004). Red diamonds = dioctahedral smectites (Heuser *et al.*, 2013), green diamonds dioctahedral smectites (Köster *et al.*, 1999), open green diamonds = other nontronites, brown diamonds = other intermediary smectites, blue diamonds =

https://doi.org/10.1180/clm.2023.20 Published online by Cambridge University Press

vermiculites. (B) b/b_{tet} ratio *vs.* the mean ionic radius of octahedral cations *R* for the same samples (and color code) as (A). (*P-T*)' corresponds to the pyrophyllite-talc regression line derived from Fig. 8B.

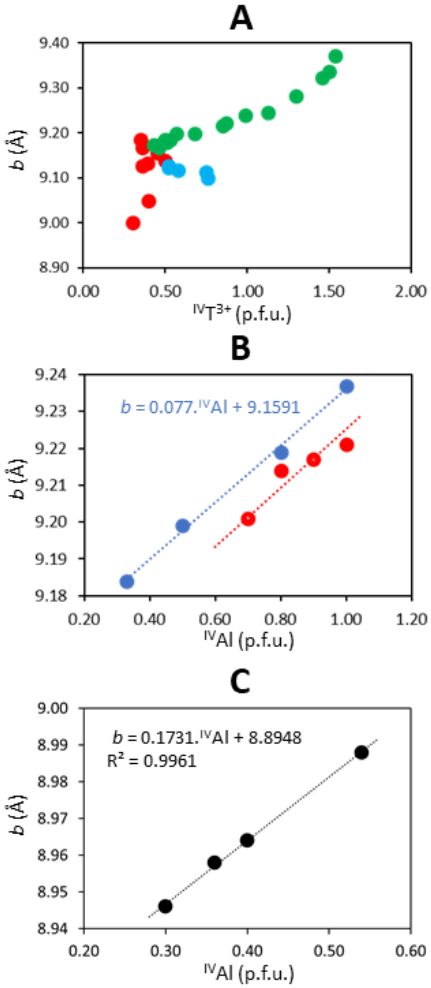

Fig. 10. *b vs.* tetrahedral substitutions rate for selected smectites (Table 5). (A) Data for synthetic dioctahedral smectites series, red = $(Si,Al)_4$ $(Fe^{3+}_{(2-x)}Al_x)$ (Petit *et al.* 2015), light blue = $(Si,Ga)_4$ $(Fe^{3+}_{(2-x)}Ga_x)$ (Petit *et al.* 2016), green = $(Si_{4-x}Fe^{3+}_x)Fe^{3+}_2$ (Baron *et al.*, 2016b). (B) Data for synthetic saponites (Suquet *et al.*, 1977) with blue circles = y=0 series, red circles = y=0.2 series (see text for details). (C) Data for natural beidellites (Post *et al.*, 1997).

https://doi.org/10.1180/clm.2023.20 Published online by Cambridge University Press

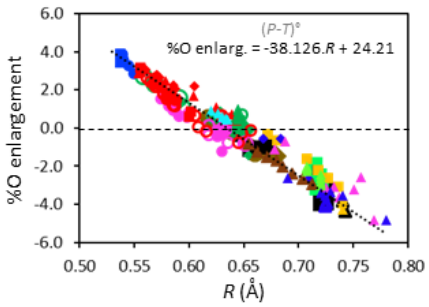

Fig. 11. Evolution of the percentage of octahedral enlargement (Eq. 6, see text for details) *vs. R* for the same smectite samples (and color code) as Fig. 9. *(P-T)°* corresponds to the pyrophyllite-talc regression (Fig. 8C).

https://doi.org/10.1180/clm.2023.20 Published online by Cambridge University Press

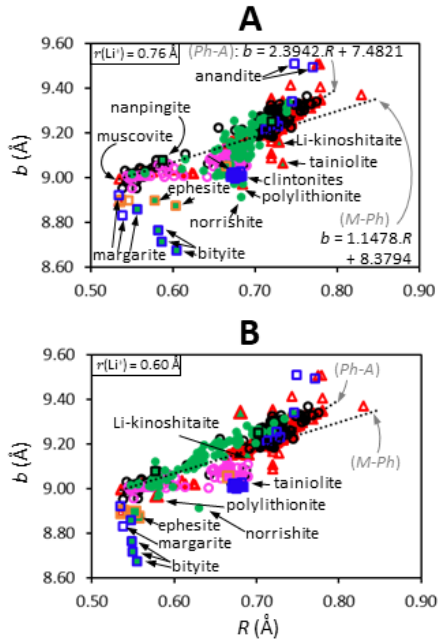

Fig. 12. *b vs.* mean ionic radius of octahedral cations *R* for for micas (Table 6). (*M-Ph*) and (*Ph-A*) correspond to muscovite-phlogopite and phlogopite-annite regression lines. Red triangles = synthetic micas (details in Figs.15), black open circles = true K-micas, pink open circles = interlayer deficient K-micaceous samples, green circles and other symbols filled in green = Li-containing micas, orange open squares = Na-micas, black open square = Cs,Rb mica, blue open squares = brittle micas. (A) *R* calculated with $r(Li^{+}) = 0.76$ Å. (B) *R* calculated with $r(Li^{+}) = 0.60$ Å (see text).

https://doi.org/10.1180/clm.2023.20 Published online by Cambridge University Press

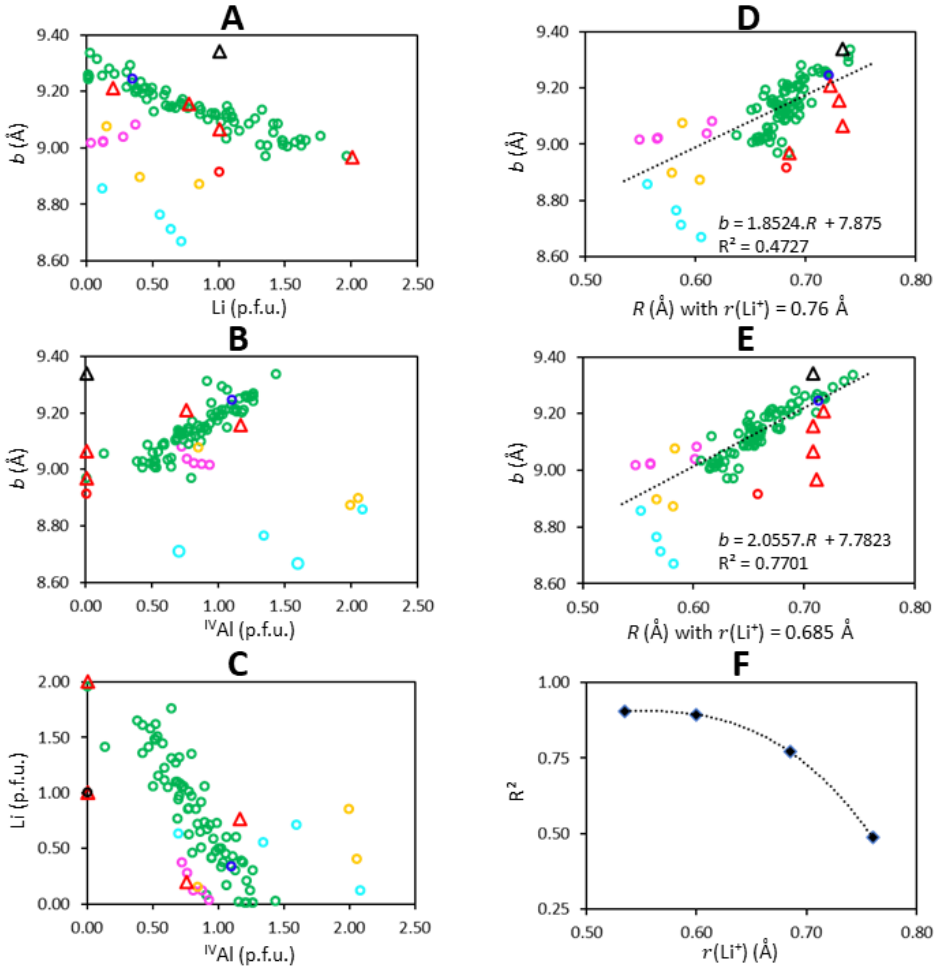

Fig. 13. Evolution of structural parameters in Li-micas (Table 6). Circles = natural samples, triangles = synthetic samples. Green circles = true K- micas; Pink circles = Li-muscovites, yellow circles = Na-micas, dark blue circle = Rb-Cs- mica, light blue circles = brittle micas, red circle = norrishite ($Si_4(LiMn^{3+}{}_2)K$ mica. Red triangles = K-Si micas, black triangle = K-Ge mica. (A) *b vs.* octahedral lithium content. (B) *b vs.* tetrahedral aluminum content. (C) Octahedral lithium *vs.* tetrahedral aluminum. (D) *b vs.* the mean ionic radius of octahedral cations *R* with $r(Li^+)$ = 0.760 Å. (F) *b vs. R* with $r(Li^+)$ = 0.685 Å. (F) Evolution of the coefficient of the linear regressions for the $r(Li^+)$ considered.

https://doi.org/10.1180/clm.2023.20 Published online by Cambridge University Press

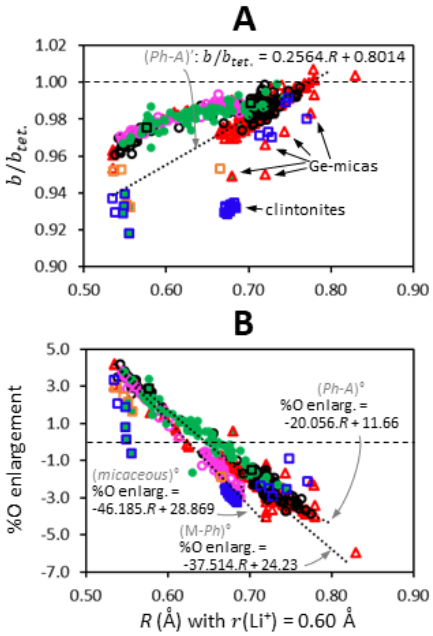

Fig. 14. (A) $b/b_{tet.}$ *vs.* the mean ionic radius of octahedral cations *R* for the same samples (and color code) as Fig.12. (*Ph-A*)' corresponds to the phlogopite-annite regression line. (B) Percentage of octahedral enlargement (Eq. 6, see text for details) *vs. R* for the same samples (and color code) as Fig.12. (*M-Ph*)° corresponds to the muscovite-phlogopite regression line, and *(micaceous)*° to the interlayer depleted micas regression line.

https://doi.org/10.1180/clm.2023.20 Published online by Cambridge University Press

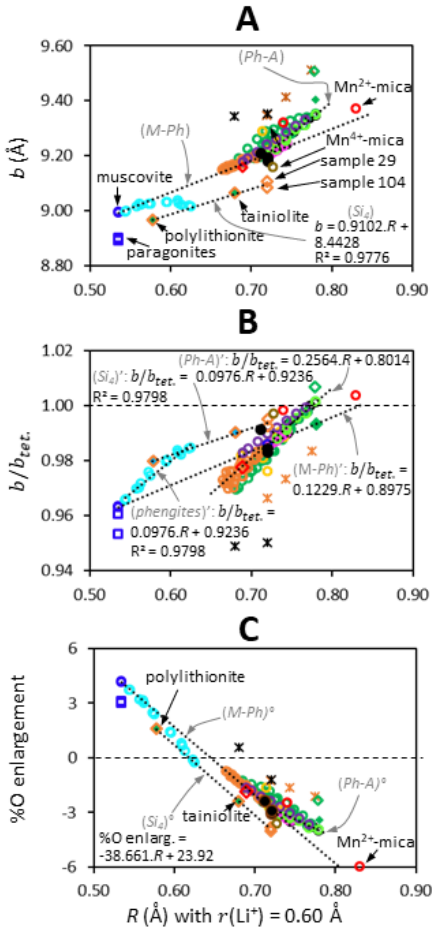

Fig. 15. (A) *b vs.* mean ionic radius of octahedral cations *R* for synthetic micas (Table 6). (*M-Ph*) and (*Ph-A*) correspond to muscovite-phlogopite and phlogopite-annite regression lines. *(Si₄)* corresponds to the tetrasilicic micas regression line. Dark blue circles = muscovite, light blue circles = $K(Si_{3+x}Al_{1-x})(Al_{2-x}Mg_x)O_{10}(OH)_2$ $2M_1$ micas series (Zviagina & Drits, 2019), orange circles = $K(Si_{3-x+2y}Al_{1+x-2y})(Mg_{3-x-y}Al_x\square_y)O_{10}(OH)_2$ series (Robert, 1976), black full circles = phlogopites, green circles = $K(Si,Al)_4(Fe^{2+},Fe^{3+},Mg)_3$ series, pink circles = JLRMgCo, light green circles = JLRMgFe, purple circles = FeNiGR, black circles = $K(Si_3Al_1)(Mg_{3-x}R^{2+}{}_x)$ series (Hazen & Wones, 1972), red circles = Zn- and Mn- micas (Frondel & Ito, 1966), brown circle = Mn^{4+}-mica (sample 110, Brigatti & Guggenheim, 2002). Orange diamonds = tetrasilicic micas, filled in green symbols = Li-rich, red diamond = Li-kinoshitaite, green diamonds = ferri-annite, full symbol = K, empty symbol = Cs. Blue squares = paragonites. Crosses = Ge-micas, black = 4Ge, orange = 3GeAl. (B) $b/b_{tet.}$ ratio *vs. R* for the same samples (and color code) as (A). (*M-Ph*)', (*Ph-A*)', and *(Si₄)'* correspond to muscovite-phlogopite, phlogopite-annite, and tetrasilicic micas regression lines. *(Phengites)'* correspond to the $2M_1$ micas in the series muscovite–phengite–aluminoceladonite regression line. (C) Percentage of

https://doi.org/10.1180/clm.2023.20 Published online by Cambridge University Press

octahedral enlargement *vs. R* for the same samples (and color code) as (A). *M-Ph*)°, (*Ph-A*)°, and *(Si$_4$)*° correspond to the muscovite-phlogopite, phlogopite-annite, and tetrasilicic micas regression lines.

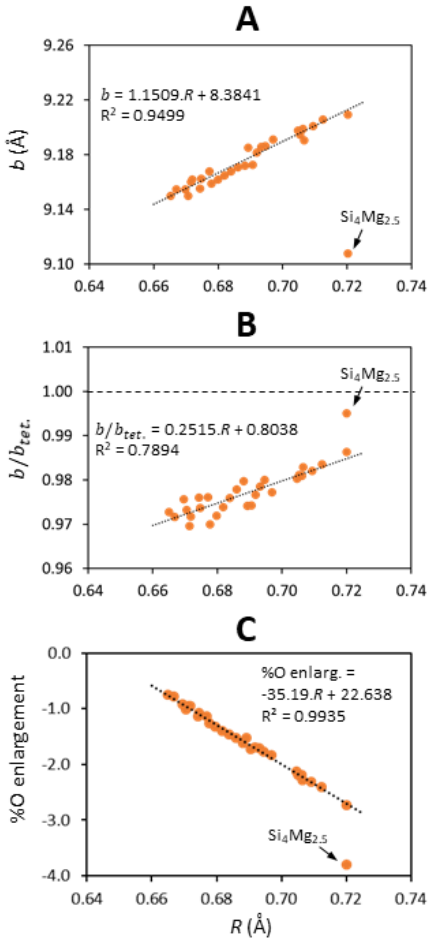

Fig. 16. Focus on the $K(Si_{3-x+2y}Al_{1+x-2y})(Mg_{3-x-y}Al_x\square_y)O_{10}(OH)_2$ synthetic series of Robert (1976) (Table 6). (A) *b vs.* mean ionic radius of octahedral cations *R*. (B) $b/b_{tet.}$ *vs. R*. (C) %O enlargement *vs. R*.

https://doi.org/10.1180/clm.2023.20 Published online by Cambridge University Press

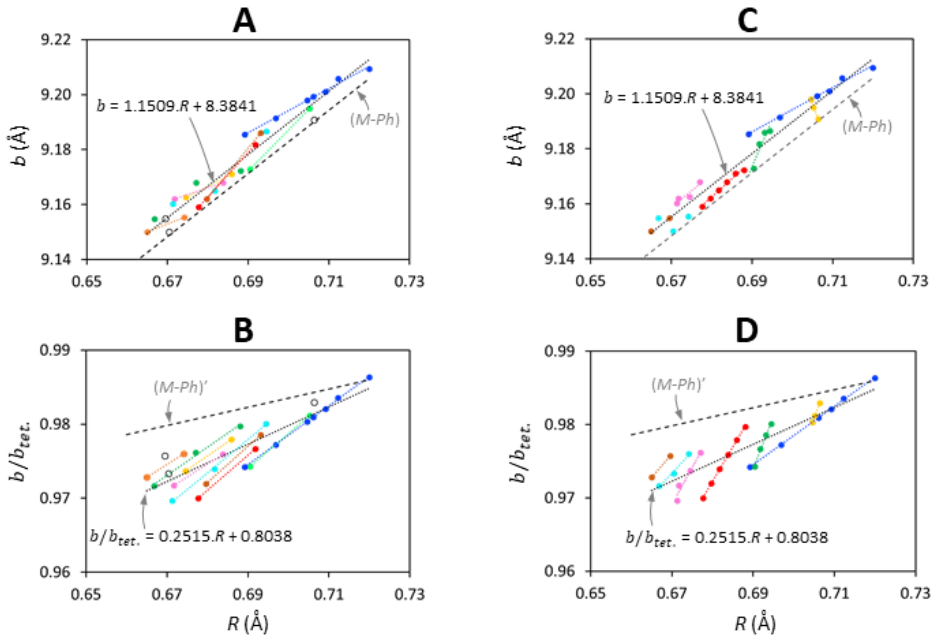

Fig. 17. Focus on the $K(Si_{3-x+2y}Al_{1+x-2y})(Mg_{3-x-y}Al_x\square_y)O_{10}(OH)_2$ synthetic series of Robert (1976) (Table 6, sample 29 is not represented). (A) b *vs*. R. (B) $b/b_{tet.}$ ratio *vs*. R. Blue: y=0; light green: y=0.025; red: y=0.05; brown: y=0.075; light blue: y=0.1; pink: y=0.125; yellow: y=0.150; green: y=0.175; orange: y= 0.225; open circles: single data. Evolution of b (C) or the $b/b_{tet.}$ ratio (D) with the mean ionic radius of octahedral cations R for blue: y=0; yellow: y=-0.5x+0.25; green: y=-x+0.5; red; y=-1.5x+0,75; pink y=-2x+1; light blue: y=-2.5x+1.25; brown: y=-3x+1.5. See Table 7 for the corresponding regressions. (*M-Ph*) and (*M-Ph*)' corresponds to the muscovite-phlogopite regression line.

https://doi.org/10.1180/clm.2023.20 Published online by Cambridge University Press

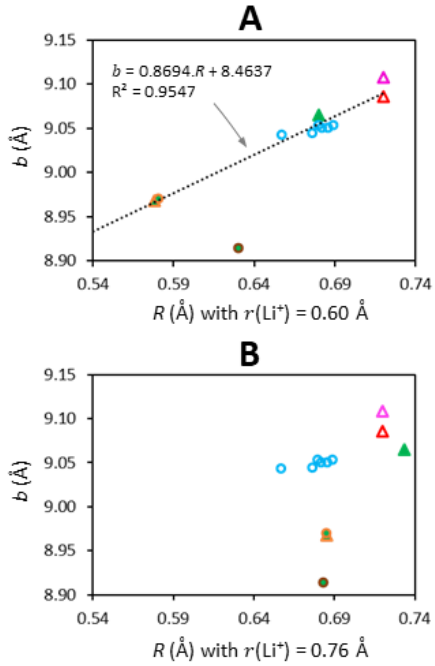

Fig. 18. *b vs*. *R* for tetrasilicic K-micas (Table 6). (A) *R* calculated with r(Li^+) = 0.6 Å. (B) *R* calculated with r(Li^+) = 0.76 Å. Triangles = synthetic samples, pink = $Mg_{2.5}(OH)_2$-mica (sample 29 (Robert, 1976)), red = $Mg_{2.5}F_2$-mica (sample 104 (Brigatti & Guggenheim, 2002)), green = Mg_2Li-mica (tainiolite, sample 105 (Brigatti & Guggenheim, 2002)), orange = $AlLi_2$–mica (polylithionite). Circles = natural sample, orange = polylithionite (sample 45 (Rieder, 1970)), blue = celadonites, brown = norrishite (($LiMn^{3+}{}_2$)-mica (sample 111 (Brigatti & Guggenheim, 2002)) . Symbols filled in green = Li-containing-micas.

https://doi.org/10.1180/clm.2023.20 Published online by Cambridge University Press

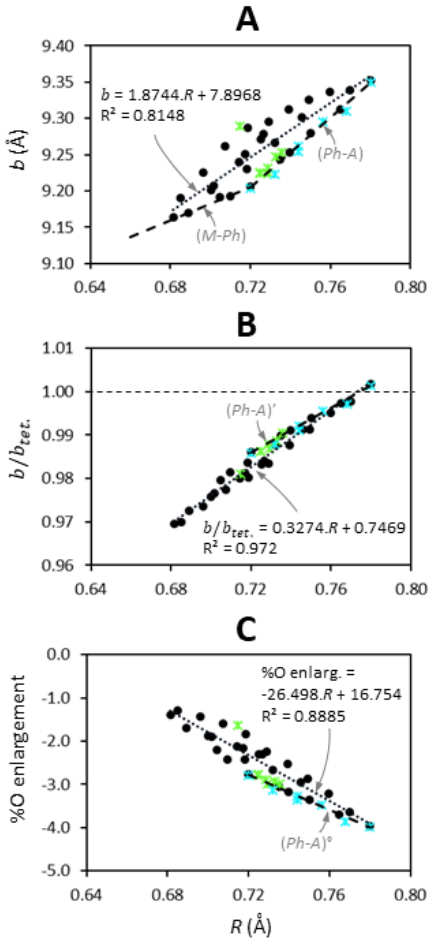

Fig. 19. Focus on the $K(Si_{3-z}Al_{1+z})(Mg_xFe^{2+}{}_yAl_z)O_{10}(OH)_2$ synthetic series. Black circles = from Hewitt & Wones (1975), green crosses = from Redhammer *et al*. (2002), blue crosses = from Mercier *et al.* (2005) (Table 6). (A) *b vs.* mean ionic radius of octahedral cations R. (B) $b/b_{tet.}$ *vs. R.* (C) %O enlargement *vs. R*. The dashed lines correspond to muscovite-phlogopite (M-Ph) and phlogopite-annite (Ph-A) regression lines. The dotted line is the regression calculated with the Hewitt & Wones (1975) data.

https://doi.org/10.1180/clm.2023.20 Published online by Cambridge University Press

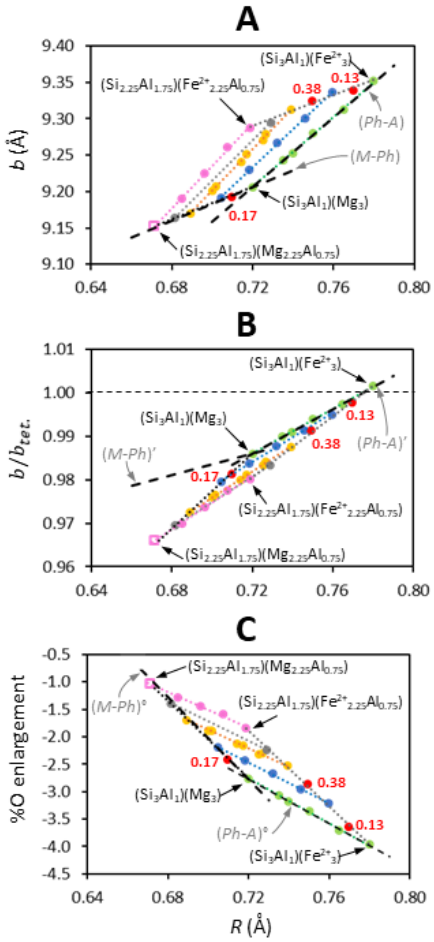

Fig. 20. Focus on the $K(Si_{3-z}Al_{1+z})(Mg_xFe^{2+}{}_yAl_z)O_{10}(OH)_2$ synthetic series of Hewitt & Wones (1975) (Table 6). Evolution of b (A), or $b/b_{tet.}$ ratio (B), or %O enlargement (C) with the mean ionic radius of octahedral cations R for green circles: z = 0, blue circles: z = 0.25, yellow circles: z = 0.50, gray circles: z = 0.63, pink circles: z = 0.75, pink open square: calculated by extrapolation, red circles: single data with the indicated z value. Dotted lines= linear regression for each z series (see Table 7 for the corresponding regressions). The dashed lines correspond to muscovite-phlogopite *(M-Ph)* and phlogopite-annite *(Ph-A)* regression lines.

https://doi.org/10.1180/clm.2023.20 Published online by Cambridge University Press

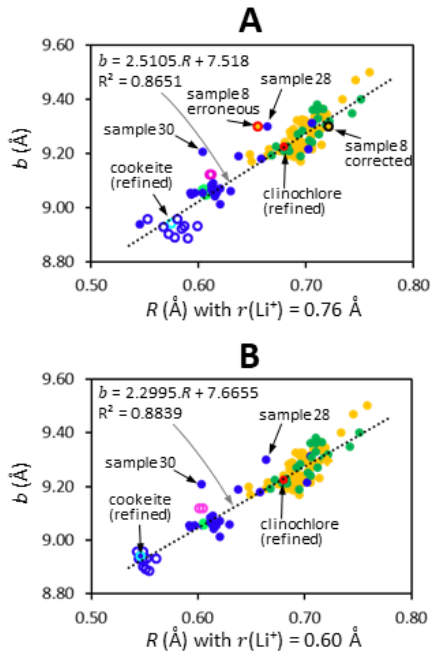

Fig. 21. *b vs*. *R* for chlorites (Table 8) Calculation of *R* performed with (A) $r(Li^{+})$ = 0.76 Å and (B) $r(Li^{+})$ = 0.60 Å.. Dark blue circles = di-tri and di-dioctahedral chlorites, yellow circles = trioctahedral chlorites, green circles = various chlorites (Radoslovich, 1962), pink circles: vanadium chlorites, light green circles = Fe^{3+}-sudoites, red circle = clinochlore (Smyth *et al*., 1997), light blue circle = cookeite (Zheng & Bailey, 1997). Open circles = Li-containing chlorites. Dotted line: regression calculated with all samples.

https://doi.org/10.1180/clm.2023.20 Published online by Cambridge University Press

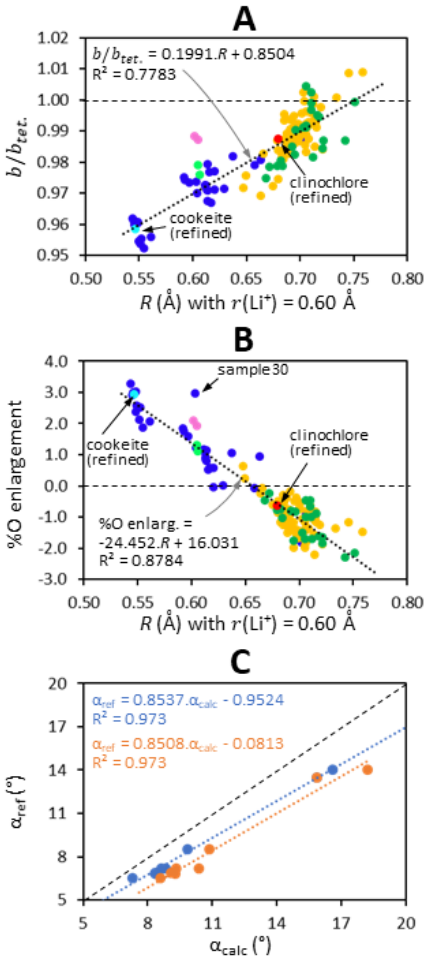

Fig. 22. $b/b_{tet.}$ (A) and %O enlargement (B) *vs.* R calculated with $r(Li^+)$ = 0.60 Å for chlorites (Table 8). Same samples and color code as in Fig. 21. (C) Tetrahedral rotation angle measured by structure refinement α_{ref}: *vs.* tetrahedral rotation angle α_{calc} calculated: in blue = using fixed Si-O and Al-O bond lengths (1.618 and 1.748 Å, respectively), and in orange, using mean T-O bond lengths obtained by structure refinement (see text and Table 9). The dashed line represents the line of isovalues.

https://doi.org/10.1180/clm.2023.20 Published online by Cambridge University Press

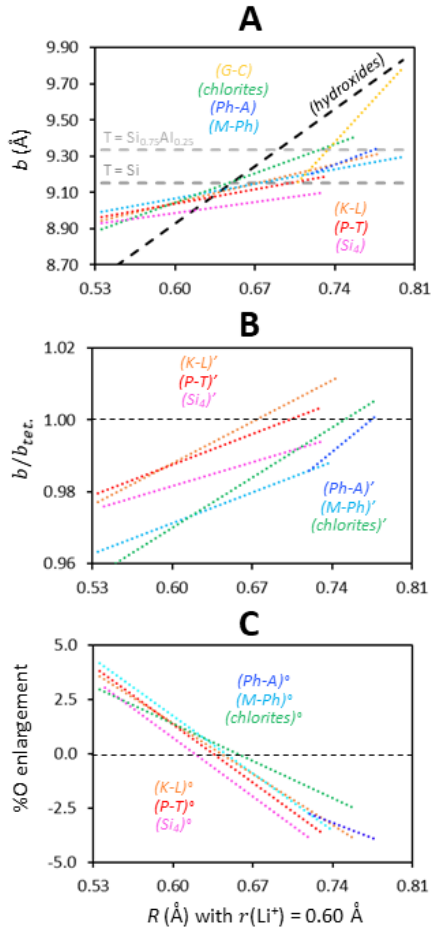

Fig. 23. (A) *b vs. R* calculated with $r(Li^+) = 0.60$ Å for the various studied phyllosilicates structures. Horizontal dashed gray lines = calculated theoretical « free » T sheet (dark gray: unsubstituted, light gray: $Si_{0.75}{}^{IV}Al_{0.25}$). Black dashed line = experimentally determined regression for hydroxides (see text for details). Colored dotted lines = regression lines determined in this study, such as kaolinite-lizardite (*K-L*), pyrophyllite-talc (*P-T*), muscovite-phlogopite (*M-Ph*), phlogopite-annite (*Ph-A*), tetrasilicic micas *(Si₄), (chlorites)*, and TO modulated phyllosilicates *(G-C)*. (B) $b/b_{tet.}$ *vs. R* for the same phyllosilicates as in (A) . (C) %O enlargement compared to hydroxides (see text for details) *vs. R* for the same phyllosilicates as in (A). The intersection between the 0%O enlargement line (black dashed line) and the colored dotted lines corresponds to *R* for which the thickness of the O sheets is the same for phyllosilicates and hydroxides. Above this 0%O enlargement line the O sheets of phyllosilicates are thinner than the hydroxides for the same *R*, while below this line they are thicker.

https://doi.org/10.1180/clm.2023.20 Published online by Cambridge University Press

Table 1. Ionic radii (r in Å) of cations and O^{2-} and their coordination from Shannon (1976).

Ion	Radius r
$^{VI}Al^{3+}$	0.535
$^{IV}Al^{3+}$	0.39
$^{IV}Be^{2+}$	0.27
$^{VI}Ca^{2+}$	1.00
$^{VI}Cd^{2+}$	0.95
$^{VI}Co^{2+}$	0.745
$^{VI}Co^{3+}$	0.545
$^{VI}Cr^{3+}$	0.615
$^{VI}Cu^{2+}$	0.73
$^{VI}Fe^{2+}$	0.78
$^{VI}Fe^{3+}$	0.645
$^{IV}Fe^{3+}$	0.49
$^{VI}Ga^{3+}$	0.62
$^{IV}Ga^{3+}$	0.47
$^{IV}Ge^{4+}$	0.39
$^{VI}Li^{+}$	0.76
$^{VI}Mg^{2+}$	0.72
$^{IV}Mn^{2+}$	0.66
$^{VI}Mn^{2+}$	0.83
$^{VI}Mn^{3+}$	0.645
$^{VI}Ni^{2+}$	0.69
$^{II}O^{2-}$	1.35
$^{III}O^{2-}$	1.36
$^{IV}O^{2-}$	1.38
$^{IV}Si^{4+}$	0.26

https://doi.org/10.1180/clm.2023.20 Published online by Cambridge University Press

$^{VI}Ti^{4+}$	0.605
$^{VI}V^{3+}$	0.64
$^{VI}Zn^{2+}$	0.74

https://doi.org/10.1180/clm.2023.20 Published online by Cambridge University Press

Table 2: Data used for hydroxide, oxi-hydroxide, and layer doubled hydroxide structures. *R*: mean ionic radius of octahedral cations (Å); (see text) (Å). *Sample reference in the paper. *a, b, and c*: crystallographic parameters (Å).

Structural formula / composition	Sample*	*R*	*parameter*	*b*	References	Comments
Hydroxides						
$Al(OH)_3$	gibbsite	0.535		8.684	Saalfeld &Wedde (1974)	
$M^{2+}(OH)_2$	synthetic series		*a*	*b = 3.a*	Brindley & Kao (1984)	*b* = 3.*a* (see text)
Ni		0.690	3.117	9.351		
Mg		0.720	3.147	9.441		
Zn		0.740	3.194	9.582		
Co		0.745	3.173	9.519		
Fe		0.780	3.262	9.786		
Mn		0.830	3.316	9.948		
Cd		0.950	3.499	10.497		
Ca		1.000	3.592	10.776		
Oxihydroxide			*c*	*b* = 3.*c*		*b* = 3.*c* (see text)
αAlO(OH)	diaspore	0.535	2.844	8.532	Hill (1979)	
FeO(OH)	goethite	0.645	3.022	9.065	Schulze (1984)	
Al-goethite $Fe^{3+}_{(1-x)}Al^{3+}_xO(OH)$ x	synthetic series mole% Al				Schulze (1984)	

This is a 'preproof' accepted article for Clay Minerals. This version may be subject to change during the production process.
DOI: 10.1180/clm.2023.20

0.005	0.5	0.644	3.021	9.063	
0.017	1.7	0.643	3.02	9.060	
0.027	2.7	0.642	3.019	9.057	
0.042	4.2	0.640	3.016	9.048	
0.067	6.7	0.638	3.013	9.039	
0.097	9.7	0.634	3.008	9.024	
0.113	11.3	0.633	3.005	9.015	
0.047	4.7	0.640	3.015	9.045	
0.09	9	0.635	3.009	9.027	
0.124	12.4	0.631	3.004	9.012	
0.157	15.7	0.628	3.000	9.000	
0.016	1.6	0.643	3.021	9.063	
0.026	2.6	0.642	3.020	9.060	
0.035	3.5	0.641	3.018	9.054	
0.314	31.4	0.610	2.964	8.892	
0.249	24.9	0.618	2.978	8.934	
0.186	18.6	0.625	2.991	8.973	
0.203	20.3	0.623	2.998	8.994	
Co-goethite	mole% Co				Gerth (1990)
$Fe^{3+}_{(1-x)}Co^{3+}_{x}O(OH)$ x					
0.0049	0.49	0.645	3.024	9.071	
0.0249	2.49	0.643	3.021	9.063	
0.451	4.51	0.640	3.018	9.055	
0.0455	4.55	0.640	3.021	9.063	
0.0487	4.87	0.640	3.016	9.048	
0.0825	8.25	0.637	3.013	9.038	
0.0971	9.71	0.635	3.010	9.030	
Ni-goethite	mole% Ni				Gerth (1990)
$Fe^{3+}_{(1-x)}Ni^{2+}_{x}O(OH)$ x					
0.0051	0.51	0.645	3.025	9.074	
0.0122	1.22	0.646	3.022	9.067	
0.0208	2.08	0.646	3.023	9.069	
0.0253	2.53	0.646	3.024	9.073	
0.0393	3.93	0.647	3.025	9.074	
0.0396	3.96	0.647	3.024	9.073	

https://doi.org/10.1180/clm.2023.20 Published online by Cambridge University Press

0.0542	5.42	0.647	3.026	9.077	
Cu-goethite	mole% Cu				Gerth (1990)
$Fe^{3+}_{(1-x)}Cu^{2+}_{x}O(OH)$ x					
0.0051	0.51	0.645	3.024	9.071	
0.0287	2.87	0.647	3.024	9.072	
0.0464	4.64	0.649	3.026	9.079	
0.0482	4.82	0.649	3.026	9.077	
0.0488	4.88	0.649	3.025	9.075	
Zn-goethite	mole% Zn				Gerth (1990)
$Fe^{3+}_{(1-x)}Zn^{2+}_{x}O(OH)$ x					
0.0056	0.56	0.646	3.024	9.071	
0.0282	2.82	0.648	3.026	9.077	
0.0436	4.36	0.650	3.028	9.084	
0.0458	4.58	0.650	3.028	9.083	
0.0477	4.77	0.650	3.029	9.086	
0.0573	5.73	0.651	3.032	9.097	
0.0686	6.86	0.652	3.033	9.099	
Cd-goethite	mole% Cd				Gerth (1990)
$Fe^{3+}_{(1-x)}Cd^{2+}_{x}O(OH)$ x					
0.0048	0.48	0.646	3.025	9.075	
0.0066	0.66	0.647	3.025	9.074	
0.0221	2.21	0.652	3.030	9.089	
0.0256	2.56	0.653	3.032	9.097	
0.0274	2.74	0.653	3.033	9.100	
0.0379	3.79	0.657	3.036	9.107	
0.0401	4.01	0.657	3.037	9.112	
0.0409	4.09	0.657	3.038	9.114	
0.0414	4.14	0.658	3.040	9.119	
0.044	4.4	0.658	3.040	9.120	
0.0442	4.42	0.658	3.039	9.117	
0.0454	4.54	0.659	3.040	9.120	
0.0506	5.06	0.660	3.042	9.125	
0.0743	7.43	0.668	3.050	9.149	

https://doi.org/10.1180/clm.2023.20 Published online by Cambridge University Press

Pb-goethite	mole% Pb					
$Fe^{3+}_{(1-x)}Pb^{4+}_{x}O(OH)$ x						
0.0039	0.38	0.645	3.023	9.070		
0.008	0.8	0.646	3.022	9.066		
0.0154	1.54	0.647	3.021	9.064		
0.0163	1.63	0.647	3.024	9.071		
0.017	1.7	0.647	3.023	9.068		
0.0216	2.16	0.648	3.022	9.066		
0.0229	2.29	0.648	3.021	9.064		
Ga-goethite	Ga/Ga+Fe (%)				Martin *et al.* (1997)	
$Fe^{3+}_{(1-x)}Ga^{3+}_{x}O(OH)$ x						
0	0	0.645	3.022	9.065		
0.1	10	0.643	3.021	9.063		
0.25	25	0.639	3.015	9.045		
0.4	40	0.635	3.008	9.024		
1	100	0.620	2.973	8.920		
Cr-goethite	Cr/Cr+Fe (%)				Schwertmann *et al.* (1989)	
$Fe^{3+}_{(1-x)}Cr^{3+}_{x}O(OH)$ x						
0	0	0.645	3.025	9.074		
0.02	2	0.644	3.023	9.070		
0.05	5	0.643	3.022	9.066		
0.1	10	0.642	3.019	9.058		
Mn^{3+}-goethite	Mn/Mn+Fe (%)				Stiers & Schwertmann (1985)	
$Fe^{3+}_{(1-x)}Mn^{3+}_{x}O(OH)$ x						
0	0	0.645	3.024	9.073		
0.05	5	0.640 #	3.022	9.065		# using r(Mn^{3+}) = 0.548 Å (see text)
0.1	10	0.635 #	3.016	9.047		
0.15	15	0.630 #	3.008	9.023		
1	groutite	0.548 #	2.870	8.613	natural sample	
Layered Double Hydroxide			*a*	*b = 3.a*#		# see text
$M^{2+}_{a}M^{3+}_{b}(OH)_{2(a+b)}[Z^{c-}]_{b/c}$						
	Natural samples					
$Mg_6Al_2(OH)_{16}[CO_3]\,4H_2O$	hydrotalcite	0.670	3.066£	9.199	Brindley & Kikawa (1979)	£ extracted from Fig. 5

https://doi.org/10.1180/clm.2023.20 Published online by Cambridge University Press

$Ni_6Al_2(OH)_{16}[CO_3]\ 4H_2O$	takovite	0.646	3.025[£]	9.075		
$Mg_6Cr_2(OH)_{16}[CO_3]\ 4H_2O$	stichite	0.695	3.096	9.287[#]	Mills *et al.* (2011)	[#]single crystal XRD
$Mg_3Fe^{3+}(OH)_8[Cl]$	iowaite	0.701	3.118	9.355[#]	Braithwaite *et al.* (1994)	measurement
$Mg_3Fe^{3+}(OH)_8[C0_3]$	pyroaurite	0.701	3.109	9.328[#]	Allman (1968)	
$Mn_2Al(OH)_6[S0_4]$	shigaite	0.733		9.512[#]	Cooper & Hawthorne (1996)	
$Fe^{2+}{}_2Al(OH)_6[S0_4]$	nikisherite	0.700		9.347[#]	Huminicki & Hawthorne (2003)	
$Zn_2Al\ (OH)_6[C0_3]$	zaccagnaite	0.672	3.073	9.218[#]	Merlino & Orlandi (2001)	
$Mg_5Fe^{3+}(OH)_{12}[C0_3]$	coalingite	0.708	3.120	9.360[#]	Pastor-Rodriguez & Taylor (1971)	
$Mg_7Al_{1.14}Fe^{3+}{}_{0.86}(OH)_{18}[S0_4]$	wermlandite	0.690		9.303[#]	Rius & Allmann (1984)	
	Synthetic series					
$Mg_{1-x}Al_x[C0_3]$ x						
	Mg^{2+}/Al^{3+}					
0.167	5	0.689	3.081	9.242	Bellotto *et al.* (1996)	
0.33	2	0.659	3.046	9.138		
0.20	4	0.683	3.068	9.204	Grégoire *et al.* (2012)	
0.25	3	0.674	3.057	9.171		
0.33	2	0.658	3.042	9.126		
0.33	2	0.659	3.045	9.136	Costantino *et al.* (1998)	
0.33	2	0.658	3.042	9.127	Radha *et al.* (2007)	
$Ni_{1-x}Al_x[C0_3]$ x					Brindley & Kikawa (1979)	
0.35	S1	0.655	3.045[#]	9.136		[#] extracted from Fig. 5
0.30	S2	0.664	3.050[#]	9.150		
0.27	S3	0.670	3.063[#]	9.189		
0.23	S4	0.677	3.074[#]	9.223		
0.35	Gast1	0.655	3.040[#]	9.121		
0.20	Gast2	0.683	3.079[#]	9.237		
$Ni_{1-x}Al_x[C0_3]$ x						
	Sample name				Brindley & Kikawa (1979)	

https://doi.org/10.1180/clm.2023.20 Published online by Cambridge University Press

0.28	S11	0.646	3.023[#]	9.069	[#] extracted from Fig. 5
0.27	S12	0.648	3.027[#]	9.081	
0.22	S13	0.657	3.044[#]	9.133	
0.19	S14	0.660	3.051[#]	9.153	
0.17	S15	0.663	3.052[#]	9.157	
	Ni^{2+}/Al^{3+}				
0.09	10	0.676	3.074	9.222	Grégoire *et al.* (2012)
0.14	6	0.668	3.063	9.189	
0.20	4	0.659	3.052	9.156	
0.25	3	0.651	3.043	9.129	
0.33	2	0.638	3.026	9.078	
0.33	2	0.639	3.027	9.081	d'Espinose de la Caillerie (1995)
0.28	2.5	0.647	3.035	9.105	
0.25	3	0.651	3.041	9.123	
0.25	3	0.651	3.034	9.101	Radha *et al.* (2007)
$Ni_{1-x}Fe^{3+}_x[CO_3]$ x	Ni^{2+}/Fe^{3+}				Grégoire *et al.* (2012)
0.09	10	0.686	3.09	9.27	
0.14	6	0.684	3.09	9.27	
0.2	4	0.681	3.087	9.261	
0.25	3	0.679	3.086	9.258	
0.333	2	0.675	3.084	9.252	
$Mg_{1-x}Fe^{3+}_x[CO_3]$ x	Mg^{2+}/Fe^{3+}				Grégoire *et al.* (2012)
0.20	4	0.705	3.113	9.339	
0.25	3	0.701	3.109	9.327	
0.33	2	0.695	3.107	9.321	
0.22	3.5	0.703	3.108	9.323	Manohara *et al.* (2011)
0.29	2.4	0.698	3.100	9.300	
0.31	2.2	0.697	3.100	9.300	
$Co^{2+}_{1-x}Al_x[CO_3]$ x	Co^{2+}/Al^{3+}				
0.25	3	0.693	3.08	9.24	Grégoire *et al.* (2012)
0.33	2	0.675	3.07	9.21	

https://doi.org/10.1180/clm.2023.20 Published online by Cambridge University Press

0.33	2	0.675	3.07	9.20	Radha *et al.* (2007)
$Co^{2+}_{1-x}Fe^{3+}_{x}[CO_3]$ x	Co^{2+}/Fe^{3+}				
0.25	3	0.720	3.13	9.39	Grégoire *et al.* (2012)
0.33	2	0.712	3.13	9.39	
$M^{2+}_{1-x}Ga^{3+}_{x}[CO_3]$ M^{2+}, x	M^{2+}/Ga^{3+}				
Ni 0.33	2	0.667	3.071	9.214	Manohara *et al.* (2010)
Co 0.33	2	0.704	3.110	9.331	
Mg 0.25	3	0.695	3.087	9.260	
Mg 0.167	5	0.703	3.106	9.318	Bellotto *et al.* (1996)
Mg 0.33	2	0.687	3.087	9.261	
$Zn^{2+}_{1-x}Al^{3+}_{x}[Z]$ x , Z	Zn^{2+}/Al^{3+}				
0.35 CO_3^{2-}	1.86	0.668	3.076	9.227	Lombardo *et al.* (2005)
0.35 Cl^-	1.86	0.668	3.075	9.225	
0.33 Cl^-	2	0.672	3.091	9.273	Ennadi *et al.* (2000)
0.32 SO_3^{2-}	2.1	0.674	3.080	9.240	Radha *et al.* (2011)
0.34 IO_3^-	1.92	0.670	3.072	9.216	
$M^{2+}_{1-x}Cr^{3+}_{x}[Cl]$ M^{2+} , x	M^{2+}/Cr^{3+}				
0.34 Zn	1.97	0.698	3.106	9.317	Roussel *et al.* (2000)
0.31 Cu	2.25	0.695	3.111	9.333	
$Co^{2+}_{x}Cu^{2+}_{y}Al^{3+}_{z}[CO_3]$ x , y , z	M^{2+}/M^{3+}				
0.66 0.09 0.25	2.91	0.691	3.076	9.228	Sankaranarayanan *et al.* (2015)
0.50 0.25 0.25	3.01	0.689	3.076	9.228	
0.34 0.42 0.24	3.21	0.688	3.080	9.240	
0.23 0.53 0.24	3.14	0.687	3.082	9.246	
0.07 0.70 0.23	3.39	0.686	3.082	9.246	
0.77 0 0.23	3.45	0.697	3.085	9.255	
$Mg^{2+}_{w}Co^{2+}_{x}Al^{3+}_{y}Fe^{3+}_{z}[CO_3]$ w , x , y , z					Nestroinaya *et al.* (2017)

https://doi.org/10.1180/clm.2023.20 Published online by Cambridge University Press

0.59	0.1	10.26	0.04	2.36	0.672	3.06	9.18
0.50	0.23	0.21	0.07	2.60	0.682	3.07	9.21

https://doi.org/10.1180/clm.2023.20 Published online by Cambridge University Press

Table 3: Data used for TO phyllosilicates. *R* : mean ionic radius of octahedral cations (see text) ; *b*: crystallographic parameter (in Å).
*Sample reference in the paper.

TO structure	Sample*	*R*	*b*	References	Comments
Natural kaolinite					
$Si_2Al_2O_5(OH)_4$	Keokuk (Iowa,USA)	0.535	8.945	Bish & Von Dreele (1989)	
Synthetic kaolinites					
Fe^{3+}-kaolinite series $Si_2(Al_{2-x}\ Fe^{3+}_x)O_5(OH)_4$ (octahedral composition)				Petit (1990)	
$Al_{1.93}Fe^{3+}_{0.07}$	a = 0.1	0.539	8.952		
$Al_{1.88}Fe^{3+}_{0.12}$	a = 0.2	0.542	8.959		
$Al_{1.85}Fe^{3+}_{0.15}$	a = 0.3	0.543	8.966		
				Iriarte *et al.* (2005)	
$Al_{1.68}Fe^{3+}_{0.32}$	KAF28	0.553	8.960		
$Al_{1.59}Fe^{3+}_{0.41}$	KAF42	0.558	8.976		
$Al_{1.49}Fe^{3+}_{0.51}$	KAF54	0.563	8.984		
Fe^{3+}_2	theoretical end-member	0.645	9.094		
R^{3+}-kaolinite series $Si_2(Al_{2-x}\ R^{3+}_x)O_5(OH)_4$ (octahedral composition)				Bentabol *et al.* (2009)	

This is a 'preproof' accepted article for Clay Minerals. This version may be subject to change during the production process.
DOI: 10.1180/clm.2023.20

$Al_{1.96}Fe_{0.04}$	Fe K100	0.537	8.928		
$Al_{1.95}Ga_{0.05}$	Ga K100	0.537	8.934		
$Al_{1.89}Fe_{0.01}Cr_{0.11}$	Cr K100 (1)	0.539	8.946		
$Al_{1.47}Fe_{0.01}Cr_{0.52}$	Cr K100 (2)	0.556	9.030		
Ga^{3+}-kaolinite					
$Si_2(Al_{1.76}Ga^{3+}_{0.24})O_5(OH)_4$		0.545	8.97	Martin *et al.* (1998)	
<u>Lizardite</u> (anhydrous composition)					
$(Si_{1.94}Al_{0.06})$ $(Mg_{2.83}Fe^{2+}_{0.07}Al_{0.09})$	Coli *1T*	0.716	9.223	Mellini & Zanazzi (1987)	
$(Si_{1.93}Al_{0.07})$ $(Mg_{2.83}Fe^{2+}_{0.05}Al_{0.1})$	Coli *2H1*	0.715	9.211		
$(Si_{1.93}Al_{0.07})$ $(Mg_{2.74}Fe^{2+}_{0.16}Al_{0.09})$	Monte Fico *1T*			Mellini & Viti (1994)	
	MFN3-1	0.718	9.232		
	MFN3-6		9.246		
$(Si_{1.996}Al_{0.004})$ $(Mg_{2.987}Fe^{2+}_{0.004}Mn_{0.005}Al_{0.004})$	Gew-graze *1T*			Mellini *et al.* (2010)	
	KG-2	0.720	9.163		
	KG-3		9.199		
Si_2 $(Mg_{2.87}Ni_{0.05}Fe^{3+}_{0.03}Al_{0.02})$	Valojoro, Madagascar	0.717	9.180	Brindley & Wan (1975)	
Synthetic lizardite series $Si_2(Mg_{3-x}Ni_x)O_5(OH)_4$				Baron *et al.* (2016)	
(octahedral composition)					
Mg_3	x = 0	0.720	9.226		
$Mg_{2.5}Ni_{0.5}$	x = 0.5	0.715	9.218		
Mg_2Ni_1	x = 1	0.710	9.209		
$Mg_{1.5}Ni_{1.5}$	x = 1.5	0.705	9.199		
Mg_1Ni_2	x = 2	0.700	9.191		
$Mg_{0.5}Ni_{2.5}$	x = 2.5	0.695	9.185		
Ni_3	x = 3	0.690	9.181		
Synthetic Co-lizardite					
$Si_2Co_3O_5(OH)_4$	Co-antigorite	0.745	9.220	Dalmon & Martin (1968)	same sample

https://doi.org/10.1180/clm.2023.20 Published online by Cambridge University Press

	$Co_3Si_2O_5(OH)_4$		9.350[#]	Bayliss (1981)	[#]recalculated value from XRD pattern
Synthetic chrysotile series $Si_2(R^{2+})_3O_5(OH)_4$				Jasmund *et al.* (1975)	
(octahedral composition)					
Mg_3	Mg-chrysotile	0.720	9.216		
Ni_3	Ni-chrysotile	0.690	9.162		
Co_3	Co-chrysotile	0.745	9.240		
Mg_3	Mg-chrysotile	0.720	9.241	Falini *et al.* (2004)	
Antigorite (anhydrous composition)					
$(Si_{1.99}Al_{0.01})(Mg_{2.67}Fe^{2+}_{0.1}Al_{0.04})$	Val Malenco, Italy	0.719	9.251	Capitani & Mellini (2004)	
$(Si_{1.87}Al_{0.13})(Mg_{2.57}Fe^{2+}_{0.195}Fe^{3+}_{0.156}Al_{0.01})$	Natural n°9	0.719	9.350	Tomisaka & Kato (1963)	
$(Si_{2.008})(Mg_{2.58}Fe^{2+}_{0.208}Fe^{3+}_{0.06}Al_{0.138})$	Natural n°14	0.714	9.350		
$(Si_{1.99}Al_{0.01})(Mg_{2.57}Fe^{2+}_{0.24}Fe^{3+}_{0.11}Al_{0.09})$	Natural n°17	0.717	9.350		
$Si_{2.00}(Mg_{2.55}Fe^{2+}_{0.25}Fe^{3+}_{0.12}Al_{0.03})$	Natural n°18	0.720	9.350		
$(Si_{1.94}Al_{0.06})(Mg_{2.58}Fe^{2+}_{0.07}Fe^{3+}_{0.35}Al_{0.01})$	Natural n°7	0.712	9.220		
$(Si_{1.95}Al_{0.01}Fe^{3+}_{0.04})(Mg_{2.87}Fe^{2+}_{0.01}Fe^{3+}_{0.06})$	Antigorite n°1	0.719	9.219	Brindley &Von Knorring (1953)	
$Si_2(Mg_{2.72}Al_{0.01}Fe^{3+}_{0.13})$	Antigorite n°2	0.716	9.219		
Al- serpentine					
(anhydrous composition)					
Berthierine					
$(Si_{1.32}Al_{0.68})(Mg_{0.23}Fe^{2+}_{1.82}Fe^{3+}_{0.01}Al_{0.83})$	chamosite[£]	0.705	9.360	Brindley & Youell (1953)	[£]actually berthierine
$(Si_{1.29}Al_{0.71})(Mg_{0.17}Fe^{2+}_{1.81}Fe^{3+}_{0.02}Al_{0.90})$[a]	n°874[£]	0.700	9.312[b]	[a] Brindley (1982)	named chamosite at this time
$(Si_{1.22}Al_{0.78})(Mg_{0.17}Fe^{2+}_{1.79}Fe^{3+}_{0.01}Al_{0.93})$[a]	Wabana[£]	0.697	9.348 [b]	[b] Brindley *et al.* (1951)	
$(Si_{1.46}Al_{0.54})(Mg_{0.4}Fe^{2+}_{1.72}Fe^{3+}_{0.32}Al_{0.45})$[c]	Frodingham[£]	0.720	9.342 [b]		[c]calculated from chemical analyses in [b]
$(Si_{1.53}Al_{0.47})(Mg_{0.38}Fe^{2+}_{1.64}Fe^{3+}_{0.29}Al_{0.52})$[c]	Schmiedefeld[£]	0.714	9.336 [b]		
$(Si_{1.29}Al_{0.71})(Mg_{0.46}Fe^{2+}_{1.13}Ti_{0.77}Al_{0.12})$	Ti-berthierine	0.703	9.252	Arima *et al.* (1985)	
Amesite					
$(Si_{1.052}Al_{0.948})(Mg_{1.15}Fe^{2+}_{0.96}Al_{0.99}Mn_{0.02})$	amesite Lake Asbestos	0.679	9.294	Taner & Laurent (1984)	

https://doi.org/10.1180/clm.2023.20 Published online by Cambridge University Press

$(Si_{1.01}Al_{0.99})(Mg_{1.63}Fe^{2+}_{0.33}Al_{0.999})$	amesite Chester	0.664	9.186		
$(Si_{1.027}Al_{0.973})(Mg_{1.94}Fe^{2+}_{0.03}Cr_{0.07}Al_{0.94})$	amesite	0.660	9.195	Anderson & Bailey (1981)	
$(Si_{1.075}Al_{0.925})(Mg_{1.9}Fe^{2+}_{0.025}Ni_{0.01}Al_{0.875}Cr_{0.145})$	amesite	0.660	9.212[d]	Wiewiora *et al.* (1991)	[d] single crystal X-ray analysis
Others					
$(Si_{1.83}Al_{0.17})(Mg_{2.79}Fe^{2+}_{0.04}Fe^{3+}_{0.1}Al_{0.07})$	lizardite Val Sissone	0.714	9.235[e]	Mellini (1982)	[e] crystal structure refinement
$(Si_{1.81}Al_{0.19})(Mg_{2.64}Fe^{2+}_{0.05}Fe^{3+}_{0.13}Al_{0.03})$	Thompson Lake	0.719	9.239	Olsen (1961)	
$(Si_{1.48}Al_{0.52})(Mg_{2.07}Fe^{2+}_{0.07}Al_{0.72})$	Al-serpentine	0.675	9.171	Jahanbagloo & Zoltai (1968)	
$(Si_{1.67}Al_{0.33})(Mg_{0.27}Fe^{2+}_{0.16}Ni_{1.36}Al_{0.92})$	brindleyite	0.623	9.133	Maksimovic & Bish (1978)	
$(Si_{179}Al_{0.21})(Mg_{0.77}Fe^{2+}_{0.28}Fe^{3+}_{0.78}Al_{0.56}\ Mn_{0.15})$	odinite	0.660	9.334 9.326	Bailey (1988)	purest sample - mixture of 1*T* et 1*M* polyptypes
$(Si_{0.98}Al_{1.02})\ (Mg_{0.245}Mn_{1.825}Fe^{3+}_{0.09}Al_{0.84})$	kellyite	0.733	9.420	Peacor *et al.* (1974)	
Fe^{3+}- serpentine					
(anhydrous composition)					
Pecoraite					
$(Si_{1.88}Fe^{3+}_{0.15})(Mg_{0.08}Ni_{2.93})$	Sterling Mine, USA	0.691	9.180	Robinson & Chamberlain (1984)	
Cronstedtite					
$(Si_{1.51}Fe^{3+}_{0.49})\ (Fe^{2+}_{1.64}Fe^{3+}_{0.49}Mg_{0.71}Mn_{0.16})$	Pribram, Czech Republik	0.747	9.467[§]	Geiger *et al*. (1983) Hybler *et al*. (2000)	[§] crystal structure refined
$(Si_{1.22}Fe^{3+}_{0.78})\ (Fe^{2+}_{2.2}\ Fe^{3+}_{0.8}\ Al_{0.02})$	Herja, Romania	0.743	9.547[§]		triangular tabular crystal
$(Si_{1.34}Fe^{3+}_{0.66})\ (Fe^{2+}_{2.32}\ Fe^{3+}_{0.68}\ Al_{0.02})$	Lostwithi, England	0.749	9.532[§]		conical crystal
	Pohled, Czech Republik			Hybler *et al*. (2016)	
$(Si_{1.249}Fe^{3+}_{0.751})\ (Fe^{2+}_{2.245}Fe^{3+}_{0.755})$	$2H_1$ (+$2H_2$)	0.746[#]	9.516[#§]		[#]average values
$(Si_{1.271}Fe^{3+}_{0.729})\ (Fe^{2+}_{2.271}Fe^{3+}_{0.729})$	$6T_2$	0.747[#]	9.516[#§]		
$(Si_{1.228}Fe^{3+}_{0.772})\ (Fe^{2+}_{2.228}Fe^{3+}_{0.772})$	3*T* + 1*M*	0.745	9.514[§]		
	Pohled, Czech Republik			Hybler (2016)	
$(Si_{1.575}Fe^{3+}_{0.485})\ (Fe^{2+}_{2.515}Fe^{3+}_{0.485})$	$6T_2$	0.758	9.522[§]		
	Nižná Slaná, Slovakia			Hybler *et al*. (2017)	
$(Si_{1.182}Fe^{3+}_{0.818})\ (Fe^{2+}_{2.182}Fe^{3+}_{0.818})$	3*T*	0.743[#]	9.521[#§]		[#]average values

https://doi.org/10.1180/clm.2023.20 Published online by Cambridge University Press

$(Si_{1.197}Fe^{3+}_{0.803})(Fe^{2+}_{2.197}Fe^{3+}_{0.803})$	$3T + 1M$	0.744[#]	9.527[#§]		
$(Si_{1.206}Fe^{3+}_{0.794})(Fe^{2+}_{2.206}Fe^{3+}_{0.794})$	$2H_1$	0.744[#]	9.532[#§]		
	Chyňava, Czech Republic			Hybler & Sejkora (2017)	
$(Si_{1.206}Fe^{3+}_{0.794})(Fe^{2+}_{2.047}Fe^{3+}_{0.794}Mg_{0.159})$	$2H_1$	0.741[#]	9.527[#§]		[#]average values
$(Si_{1.185}Fe^{3+}_{0.815})(Fe^{2+}_{2.030}Fe^{3+}_{0.815}Mg_{0.155})$	$2H_1$ $(+2H_2)$	0.740[#]	9.522[#§]		
$(Si_{1.236}Fe^{3+}_{0.764})(Fe^{2+}_{2.034}Fe^{3+}_{0.764}Mg_{0.202})$	$3T$	0.742[#]	9.518[#§]		
$(Si_{1.371}Fe^{3+}_{0.629})(Fe^{2+}_{2.148}Fe^{3+}_{0.629}Mg_{0.223})$	$1T + 3T$	0.747[#]	9.513[#§]		
$(Si_{1.387}Fe^{3+}_{0.613})(Fe^{2+}_{2.151}Fe^{3+}_{0.613}Mg_{0.236})$	$1T$	0.748[#]	9.521[#§]		
	Nagybörzsöny, Hungary			Hybler *et al*. (2020)	
$(Si_{1.19}Fe^{3+}_{0.81})(Fe^{2+}_{2.19}Fe^{3+}_{0.80}Mg_{0.002})$		0.746[#]	9.547[#§]		[#]average values
	Litošice, Czech Republic			Hybler *et al*. (2021)	
$(Si_{1.22}Fe^{3+}_{0.78})(Fe^{2+}_{1.80}Fe^{3+}_{0.78}Mg_{0.02}Mn_{0.41})$	$1T$	0.751[#]	9.572[#§]		[#]average values
$(Si_{1.24}Fe^{3+}_{0.76})(Fe^{2+}_{1.86}Fe^{3+}_{0.76}Mg_{0.31}Mn_{0.066})$	$2H_1 + 2H_2$	0.741	9.540[§]		
Guidottite					
	Republic of South Africa			Wahle *et al*. (2010)	
$(Mn_{1.86}Fe^{3+}_{0.61}Mg_{0.54})(Si_{1.36}Fe^{3+}_{0.64})$		0.773	9.608		
$(Mn_{1.70}Fe^{3+}_{0.96}Mg_{0.24})(Si_{1.26}Fe^{3+}_{0.74})$		0.760	9.608		
Synthetic serpentine series					
$(Si_{2-x}Al_x)(Mg_{3-x}Al_x)O_5(OH)_4$					
$(Si_2)(Mg_3)$	241M	0.720	9.204	Chernosky (1975)	
$(Si_{1.95}Al_{0.05})(Mg_{2.95}Al_{0.05})$	75G	0.717	9.222		
$(Si_{1.925}Al_{0.075})(Mg_{2.925}Al_{0.075})$	73G	0.715	9.204		
$(Si_{1.9}Al_{0.1})(Mg_{2.9}Al_{0.1})$	72G 87G	0.714	9.219		
$(Si_{1.875}Al_{0.125})(Mg_{2.875}Al_{0.125})$	70G	0.712	9.207		
$(Si_{1.625}Al_{0.375})(Mg_{2.625}Al_{0.375})$	349M	0.697	9.210		
$(Si_{1.625}Al_{0.375})(Mg_{2.625}Al_{0.375})$	368M	0.697	9.204		
$(Si_{1.5}Al_{0.5})(Mg_{2.5}Al_{0.5})$	366M	0.689	9.210		
$(Si_{1.5}Al_{0.5})(Mg_{2.5}Al_{0.5})$	391M	0.689	9.200		

https://doi.org/10.1180/clm.2023.20 Published online by Cambridge University Press

$(Si_{1.25}Al_{0.75})(Mg_{2.25}Al_{0.75})$	390M	0.674	9.175		
$(Si_1 Al_1)(Mg_2Al_1)$	367M	0.658	9.148		
$(Si_{1.625}Al_{0.375})(Mg_{2.625}Al_{0.375})$	1-Layer ortho serpentine	0.697	9.245	Gillery (1959)	
$(Si_{1.25}Al_{0.75})(Mg_{2.25}Al_{0.75})$	6-Layer ortho serpentine	0.674	9.193		
$(Si_{1.75}Al_{0.25})$ $(Mg_{2.75}Al_{0.25})$	Lizardite	0.705	9.229	Caruso & Chernosky (1979)	
$(Si_{2-x}Al_x)(R^{2+}_y Al_z)O_5(OH)_4$					
$(Si_{1.78}Al_{0.22})(Ni_{1.62}Fe^{3+}_{0.05}Al_{0.96})$	Al-Ni lizardite	0.633	9.162	Bentabol *et al.* (2013)	
$(Si_{1.81}Al_{0.19})(Co_{1.73}Fe^{3+}_{0.05}Al_{0.88})$	Al-Co lizardite	0.673	9.234		
$Si_{2.02}(Co_{1.58}Fe^{3+}_{0.04}Al_{0.89})$	Al-Co lizardite	0.669	9.155		
Synthetic serpentine (anhydrous composition)					
$(Si_{1.74}Al_{0.26})$ $(Mg_{2.00}Fe^{3+}_{0.02}Al_{0.73})$	Al-Mg lizardite	0.670	9.203	Bentabol *et al.* (2010)	
Fe- Mn- serpentine (anhydrous composition)					Corrugated structures
$Si_2(Fe^{2+})_3$	synthetic greenalite	0.780	9.624	Jasmund *et al.* (1975)	
Si_2 $(Fe^{2+}_{2.25}Fe^{3+}_{0.5})$	greenalite	0.755	9.612	Steadman & Youell (1958)	
$(Si_{1.51}Fe^{3+}_{0.49})$ $(Fe^{2+}_{1.64}Fe^{3+}_{0.49}Mg_{0.71}Mn_{0.16})$	greenalite	0.747	9.467	Geiger *et al.* (1983)	
$(Si_{1.95}Al_{0.05})$ $(Mg_{0.18}Fe^{2+}_{1.71}Mn_{0.49}Al_{0.27}Fe^{3+}_{0.18})$	greenalite	0.753	9.63	Bayliss (1981)	
$(Si_{1.77}Al_{0.23})$ $(Mg_{1.47}Fe^{2+}_{0.44}Mn_{0.6}Al_{0.2}Fe^{3+}_{0.03}Zn_{0.27})$	baumite	0.739[a]	9.6[b]	[a]Frondel & Ito (1975)	[b]Guggenheim & Bailey (1989)
Si_2 $(Mg_{0.35}Fe^{2+}_{0.05}Mn_{2.47}Al_{0.13})$	Mn-serpentine[#]	0.804	9.804	Yoshimura *et al.* (1958)	[#]caryopilite
Si_2 $(Mg_{0.29}Fe^{2+}_{0.16}Mn_{1.83}Zn_{0.11})$	Mn-serpentine[#]	0.809	9.834	Kato (1963)	

https://doi.org/10.1180/clm.2023.20 Published online by Cambridge University Press

Si_2 ($Mg_{0.4}Fe^{3+}_{0.06}Mn_{2.17}$)	Mn-serpentine#	0.797	9.804	Kato (1963)
Si_2 ($Mg_{0.6}Fe^{2+}_{0.27}Mn_{1.76}$)	Mn-serpentine#	0.800	9.708	Kato (1963)
Si_2 ($Mg_{0.34}Fe^{2+}_{0.18}Mn_{1.76}Al_{0.07}$)	Mn-serpentine#	0.802	9.852	Kato (1963)

Table 4: Data used for TOT phyllosilicates with neutral structure. *R*: mean ionic radius of octahedral cations (Å) (see text); *b*: crystallographic parameter (Å). *Sample reference in the paper.

TOT neutral structure (anhydrous composition)	**Sample***	***R***	***b***	**References**	**Comments**
Pyrophyllite					
Si_4 Al_2	pyrophyllite	0.535	8.966$	Drits *et al.* (2012)	$refined unit cell
($Si_{3.94}Fe^{3+}_{0.06}$)($Mg_{0.1}Fe^{3+}_{1.9}$)	ferripyrophyllite	0.649	9.080	Badaut *et al.* (1992)	
($Si_{3.80}Al_{0.13}Fe^{3+}_{0.07}$)($Fe^{3+}_{1.96}Mg_{0.11}$)$Ca_{0.05}$	ferripyrophyllite	0.649	9.100	Chukhrov *et al.* (1979)	
($Si_{3.80}Al_{0.04}Fe^{3+}_{0.16}$)($Al_{0.09}Fe^{3+}_{1.96}Mg_{0.11}$)$Ca_{0.05}$	same sample	0.644		Coey *et al.* (1984)	
Talc					
Si_4 Mg_3	talc	0.720	9.173$	Drits *et al.* (2012)	$refined unit cell
Si_4 ($Al_{0.02}Fe^{3+}_{0.26}Fe^{2+}_{0,78}Mg_{1.90}$)	Antwerp	0.728	9.180	Robinson & Chamberlain (1984)	
($Si_{3.93}Al_{0.07}$) ($Fe^{3+}_{0.1}Ni_{2.12}Mg_{0.81}$)	willemseite	0.697	9.149	De Waal (1970)	
Si_4 ($Al_{0.02}Fe^{3+}_{0.26}Fe^{2+}_{0,78}Mg_{1.90}$)					
Minnesotaite					
Si_4 ($Fe^{2+}_{2.28}Mg_{0.72}$)#	Mesabi range, Minesota, USA	0.766	9.410	Grüner (1944)	# SF calculated from chemical data
($Si_{3.88}Al_{0.17}$) ($Fe^{2+}_{2.50}Mg_{0.39}$ $Mn_{0.06}$)	Sample 1	0.773	9.419$	Guggenheim & Eggleton (1986)	$refined unit cell

https://doi.org/10.1180/clm.2023.20 Published online by Cambridge University Press

Synthetic Fe^{2+}-talc series	(magnetite-iron and			Forbes (1969)
Si_4 ($Mg_{3-x}Fe^{2+}_x$)	magnetite-wüstite buffers)			
Mg_3	Fe/Fe+Mg= 0	0.720	9.156	
$Mg_{2.97}Fe^{2+}_{0.03}$	0.01	0.721	9.157	
$Mg_{2.955}Fe^{2+}_{0.045}$	0.015	0.721	9.159	
$Mg_{2.925}Fe^{2+}_{0.075}$	0.025	0.722	9.160	
$Mg_{2.895}Fe^{2+}_{0.105}$	0.035	0.722	9.161	
$Mg_{2.775}Fe^{2+}_{0.225}$	0.075	0.725	9.165	
$Mg_{2.4}Fe^{2+}_{0.6}$	0.2	0.732	9.181	
Kerolite				
Si_4 ($Al_{0.07}Fe^{3+}_{0.02}Mg_{2.8}$)	Sample 1	0.715	9.134	Martin de Vidales *et al.* (1991)
($Si_{3.96}Al_{0.04}$) ($Al_{0.07}Fe^{3+}_{0.03}Mg_{2.72}Li_{0.09}$)	P-7	0.718	9.078	Eberl *et al.* (1982)
($Si_{3.95}Al_{0.05}$) ($Al_{0.015}Fe^{3+}_{0.015}Mg_{2.945}Ti_{0.005}$)	SAN I-1	0.718	9.133	Pozo & Casas (1999)
Kerolite-pimelite series				Brindley *et al.* (1979)
($Si_{3.94}Al_{0.01}Fe^{3+}_{0.01}$) ($Mg_{3.09}Ni_{0.01}$)	1	0.720	9.132	
($Si_{3.94}Al_{0.02}Fe^{3+}_{0.03}$) ($Mg_{2.16}Ni_{0.87}$)	6	0.711	9.150	
($Si_{3.97}Al_{0.03}$) ($Mg_{2.04}Ni_{0.91}Fe^{3+}_{0.01}$)	8	0.711	9.168	
($Si_{3.99}Al_{0.01}$) ($Mg_{1.22}Ni_{1.74}Fe^{3+}_{0.02}$)	17	0.702	9.156	
Synthetic Ni-Mg kerolite series				Baron *et al.* (2016a) (description of samples only, SF and *b* values are unpublished)
Si_4 ($Mg_{3-x}Ni_x$)				
Mg_3	x = 0	0.720	9.160	
$Mg_{2.36}Ni_{0.64}$	x = 0.5	0.714	9.154	
$Mg_{1.8}Ni_{1.2}$	x = 1	0.708	9.144	
$Mg_{1.28}Ni_{1.72}$	x = 1.5	0.703	9.138	
$Mg_{0.82}Ni_{2.18}$	x = 2	0.698	9.136	

https://doi.org/10.1180/clm.2023.20 Published online by Cambridge University Press

$Mg_{0.42}Ni_{2.58}$	x = 2.5	0.694	9.134
Ni_3	x = 3	0.690	9.130

Table 5. Data used for smectites. *R*: mean ionic radius of octahedral cations (Å) (see text); *b*: crystallographic parameter (Å). *Sample reference in the paper.

Smectites (octahedral and tetrahedral anhydrous compositions)	**Sample***	***R***	***b***	**References**	**Comments**
Natural smectites					
Dioctahedral smectites				Russel & Clark (1978)	
$(Si_{3.845}Al_{0.155})(Al_{1.565}Fe^{3+}_{0.2}Mg_{0.25})$	Wyoming montmorillonite	0.569	8.988		
$(Si_{3.665}Al_{0.335})(Al_{1.755}Mg_{0.255})$	Unterrupsroth montmorillonite	0.558	8.976		
$(Si_{3.995}Al_{0.005})(Al_{1.36}Fe^{3+}_{0.06}Mg_{0.60})$	Otay montmorillonite	0.593	8.994		
$(Si_{3.82}Al_{0.18})(Al_{1.27}Fe^{3+}_{0.42}Mg_{0.37})$	Woburn montmorillonite	0.591	9.024		
$(Si_{3.105}Al_{0.07}Fe^{3+}_{0.82})(Fe^{3+}_{2.02}Mg_{0.1})$	California nontronite	0.649	9.210		
$(Si_{3.65}Al_{0.35})(Al_{0.53}Fe^{3+}_{1.37}Mg_{0.13})$	Washington nontronite	0.621	9.072		
$(Si_{3.67}Al_{0.05}Fe^{3+}_{0.28})(Fe^{3+}_{1.95}Mg_{0.05})$	El Pao nontronite	0.647	9.162		
$(Si_{3.41}Al_{0.47}Fe^{3+}_{0.12})(Fe^{3+}_{2}Mg_{0.02})$	Pfaffenreuth nontronite	0.646	9.144		

https://doi.org/10.1180/clm.2023.20 Published online by Cambridge University Press

$(Si_{3.42}Al_{0.525}Fe^{3+}_{0.055})(Fe^{3+}_{1.98}Mg_{0.02})$	Garfield nontronite	0.646	9.138	
Dioctahedral smectites				Brigatti (1983)
$(Si_{3.98}Al_{0.02})(Al_{0.15}Fe^{3+}_{1.45}Mg_{0.39})$	1	0.651	9.085	
$Si_{4.0}(Al_{0.4}Fe^{3+}_{1.31}Mg_{0.25})$	2	0.632	9.070	
$(Si_{3.98}Al_{0.02})(Al_{0.6}Fe^{3+}_{1.06}Mg_{0.39})$	3	0.627	9.030	
$(Si_{3.65}Al_{0.35})(Al_{0.68}Fe^{3+}_{0.87}Mg_{0.48})$	4	0.626	9.005	
$(Si_{3.77}Al_{0.23})(Al_{0.99}Fe^{3+}_{0.78}Mg_{0.24})$	5	0.600	8.993	
$(Si_{3.56}Al_{0.44})(Al_{0.9}Fe^{3+}_{0.72}Mg_{0.55})$	6	0.618	8.978	
$(Si_{3.36}Al_{0.64}))(Al_{0.75}Fe^{3+}_{0.71}Mg_{0.81})$	7	0.635	9.015	
$(Si_{3.25}Al_{0.75}))(Al_{0.95}Fe^{3+}_{0.7}Mg_{0.59})$	8	0.618	9.020	
$(Si_{3.84}Al_{0.16})(Al_{1.12}Fe^{3+}_{0.57}Mg_{0.35})$	9	0.597	8.965	
$(Si_{3.55}A_{0.45})(Al_{0.87}Fe^{3+}_{0.53}Mg_{0.82})$	10	0.630	8.952	
$(Si_{3.41}Al_{0.59})(Al_{1.4}Fe^{3+}_{0.46}Mg_{0.39})$	11	0.590	8.942	
$(Si_{3.75}Al_{0.25})(Al_{1.44}Fe^{3+}_{0.35}Mg_{0.31})$	12	0.581	8.944	
$(Si_{3.82}Al_{0.18})(Al_{1.35}Fe^{3+}_{0.31}Mg_{0.45})$	13	0.591	8.940	
$(Si_{3.87}Al_{0.13})(Al_{1.38}Fe^{3+}_{0.25}Mg_{0.4})$	14	0.585	8.942	
$(Si_{3.89}Al_{0.11})(Al_{1.52}Fe^{3+}_{0.17}Mg_{0.32})$	15	0.574	8.945	
Dioctahedral smectites				Tsipursky & Drits (1984)
$(Si_{3.95}Al_{0.05})(Al_{1.38}Fe^{3+}_{0.18}Mg_{0.44})$	1 cv[#]	0.586	8.97	[#]cv, tv: cis, trans octahedral vacant site
$(Si_{3.96}Al_{0.04})(Al_{1.54}Fe^{3+}_{0.18}Mg_{0.26})$	2 tv-cv	0.569	8.98	(Drits *et al.*, 2006)
$(Si_{3.98}Al_{0.02})(Al_{1.38}Fe^{3+}_{0.14}Mg_{0.48})$	3 tv-cv	0.587	8.97	
$(Si_{3.91}Al_{0.09})(Al_{1.36}Fe^{3+}_{0.41}Mg_{0.24})$	4 tv	0.580	8.98	
$Si_4\ (Al_{1.51}Fe^{3+}_{0.10}Mg_{0.39})$	5 cv	0.577	8.98	
$Si_4\ (Al_{1.40}Fe^{3+}_{0.26}Mg_{0.34})$	6 tv	0.581	9.00	
$(Si_{3.98}Al_{0.02})(Al_{1.32}Fe^{3+}_{0.26}Mg_{0.41})$	7 tv	0.587	9.00	
$Si_4\ (Al_{1.39}Fe^{3+}_{0.31}Mg_{0.30})$	8 tv	0.580	8.97	
$(Si_{3.83}Al_{0.17})(Al_{1.47}Fe^{3+}_{0.19}Mg_{0.34})$	9 cv	0.577	8.98	
$(Si_{3.89}Al_{0.11})(Al_{0.89}Fe^{3+}_{0.62}Fe^{2+}_{0.03}Mg_{0.46})$	10 tv-cv	0.615	8.98	

https://doi.org/10.1180/clm.2023.20 Published online by Cambridge University Press

Si_4 $(Al_{0.2}Fe^{3+}_{1.51}Mg_{0.29})$	11 tv	0.645	9.06	
$(Si_{3.71}Al_{0.29})(Al_{1.64}Fe^{3+}_{0.05}Fe^{2+}_{0.01}Mg_{0.31})$	12 tv tv-cv	0.567	8.98	
$(Si_{3.73}Al_{0.27})(Al_{1.05}Fe^{3+}_{0.37}Mg_{0.57})$	13 tv-cv	0.608	8.97	
$(Si_{3.86}Al_{0.14})(Al_{1.68}Mg_{0.32})$	14 cv	0.565	8.98	
$(Si_{3.41}Al_{0.59})(Al_{1.57}Fe^{3+}_{0.37}Fe^{2+}_{0.01}Mg_{0.05})$	15 tv-cv	0.561	8.98	
$(Si_{3.53}Al_{0.47})(Al_{0.96}Fe^{3+}_{0.88}Fe^{2+}_{0.02}Mg_{0.26})$	16 tv	0.606	9.01	
$(Si_{3.45}Al_{0.55})(Al_{0.33}Fe^{3+}_{1.59}Mg_{0.08})$	17 tv	0.630	9.12	
$(Si_{3.49}Al_{0.51})(Fe^{3+}_{1.87}Fe^{2+}_{0.17})$	18 tv	0.656	9.17	
$(Si_{3.65}Al_{0.35})(Fe^{3+}_{1.92}Mg_{0.08})$	19 tv	0.648	9.12	
$(Si_{3.46}Al_{0.54})(Al_{0.16}Fe^{3+}_{1.85}Mg_{0.04})$	20 tv	0.638	9.14	
Dioctahedral smectites				Heuser *et al.* (2013)
$(Si_{3.78}Al_{0.22})(Al_{1.55}Fe^{3+}_{0.25}Mg_{0.2})$	BeC	0.567	9.010	*b* measured by Rietveld
$(Si_{3.89}Al_{0.11})(Al_{1.43}Fe^{3+}_{0.28}Mg_{0.29})$	BeD	0.577	9.026	
$(Si_{3.88}Al_{0.12})(Al_{1.40}Fe^{3+}_{0.27}Mg_{0.23})$	BeE	0.573	9.037	
$(Si_{3.60}Al_{0.40})(Al_{1.15}Fe^{3+}_{0.74}Mg_{0.11})$	BeH	0.586	9.064	
$(Si_{3.92}Al_{0.08})(Al_{1.55}Fe^{3+}_{0.19}Mg_{0.26})$	BeW	0.570	9.030	
$(Si_{3.69}Al_{0.31})(Al_{1.61}Fe^{3+}_{0.09}Mg_{0.30})$	FR 10-0382	0.568	9.013	
$(Si_{3.79}Al_{0.21})(Al_{1.68}Fe^{3+}_{0.11}Mg_{0.21})$	FR10-0532	0.560	9.017	
$(Si_{3.85}Al_{0.15})(Al_{1.24}Fe^{3+}_{0.48}Mg_{0.28})$	FR11-0229	0.587	9.053	
$(Si_{3.69}Al_{0.31})(Al_{1.47}Fe^{3+}_{0.35}Mg_{0.18})$	Cameron	0.571	9.041	
$(Si_{3.56}Al_{0.44})(Al_{0.74}Fe^{3+}_{1.25}Mg_{0.01})$	Cheney	0.605	9.145	
Iron-rich smectites				Köster *et al.* (1999)
$(Si_{3.68}Al_{0.32})(Al_{1.24}Fe^{3+}_{0.6}Fe^{2+}_{0.05}Mg_{0.19})$	Oberpullendorf	0.590	8.997	
$(Si_{3.86}Al_{0.14})(Al_{1.4}Fe^{3+}_{0.35}Fe^{2+}_{0.02}Mg_{0.26})$	Sauteloup	0.580	8.968	
$(Si_{3.67}Al_{0.26}Fe^{3+}_{0.07})(Fe^{3+}_{1.91}Fe^{2+}_{0.08}Mg_{0.03})$	Hoher Hagen nontronite	0.651	9.151	
$(Si_{3.49}Al_{0.51})(Al_{0.21}Fe^{3+}_{1.69}Fe^{2+}_{0.1}Mg_{0.05})$	Manito nontronite	0.642	9.125	
$(Si_{3.92}Al_{0.08})(Al_{0.37}Fe^{3+}_{0.98}Fe^{2+}_{0.06}Cr_{0.03}Ni_{0.02}Mg_{0.71})$	Ölberg	0.655	9.040	
Other nontronites				

https://doi.org/10.1180/clm.2023.20 Published online by Cambridge University Press

$(Si_{3.73}Al_{0.27})(Al_{0.15}Fe^{3+}_{1.68}Mg_{0.14})$	Tyrrhenian Sea	0.642	9.110	Dekov *et al.* (2007)
$(Si_{3.59}Al_{0.41})(Al_{0.39}Fe^{3+}_{1.53}Mg_{0.08}Cu_{0.02})$	Serra Dos Carajas, Brazil	0.628	9.108	Petit *et al.* (1992)
Beidellites				Post *et al.* (1997)
$(Si_{3.6}Al_{0.4})(Al_{1.96}Fe^{3+}_{0.05}Mg_{0.02})$	Idawa Mine	0.540	8.964	
$(Si_{3.7}Al_{0.3})(Al_{1.84}Fe^{3+}_{0.08}Mg_{0.11})$	DeLamar Mine	0.549	8.946	
$(Si_{3.64}Al_{0.36})(Al_{1.9}Fe^{3+}_{0.09}Mg_{0.04})$	Blain tunnel	0.544	8.958	
$(Si_{3.46}Al_{0.54})(Al_{1.96}Fe^{3+}_{0.04}Mg_{0.02})$	Black Jack Mine	0.539	8.988	
Other natural smectites				Radoslovich (1962)
Al-rich dioctahedral smectites				
$Si_4(Al_{1.46}Fe^{3+}_{0.06}Mg_{0.49})$	Santa Rita	0.583	8.993	
$(Si_{3.80}Al_{0.20})(Al_{1.55}Fe^{3+}_{0.21}Mg_{0.23})$	Belle Fourche	0.568	8.993	
$(Si_{3.78}Al_{0.22})(Al_{1.51}Fe^{3+}_{0.27}Mg_{0.23})$	Merritt	0.571	9.000	
$(Si_{3.86}Al_{0.12}Fe^{3+}_{0.02})(Al_{1.58}Fe^{3+}_{0.18}Mg_{0.25})$	Clay Spur	0.568	9.001	
$Si_4(Al_{1.47}Fe^{3+}_{0.06}Mg_{0.49})$	Polkville	0.583	9.002	
$(Si_{3.91}Al_{0.09})(Al_{1.46}Fe^{3+}_{0.18}Mg_{0.31})$	Amory	0.575	9.004	
$(Si_{3.88}Al_{0.08}Fe^{3+}_{0.04})(Al_{1.42}Fe^{3+}_{0.19}Mg_{0.41})$	Plymouth	0.583	9.011	
$Si_4(Al_{1.28}Fe^{3+}_{0.06}Mg_{0.71})$	Otay	0.602	9.014	
$(Si_{3.80}Al_{0.20})(Al_{1.51}Fe^{3+}_{0.31}Mg_{0.20})$	Little Rock	0.570	8.996	
$(Si_{3.85}Al_{0.15})(Al_{1.37}Fe^{3+}_{0.19}Mg_{0.47})$	Chambers	0.588	9.004	
$(Si_{3.90}Al_{0.10})(Al_{1.55}Fe^{3+}_{0.20}Mg_{0.25})$	Upton	0.569	8.997	
$(Si_{3.91}Al_{0.09})(Al_{1.57}Fe^{3+}_{0.18}Fe^{2+}_{0.02}Mg_{0.23})$	Belle Fourche	0.569	8.988	
$(Si_{3.89}Al_{0.11})(Al_{1.45}Fe^{3+}_{0.16}Fe^{2+}_{0.01}Mg_{0.44})$	Lemon	0.584	9.019	
$(Si_{3.97}Al_{0.03})(Al_{1.55}Fe^{3+}_{0.06}Mg_{0.39})$	Rideout	0.574	8.994	
$(Si_{3.99}Al_{0.01})(Al_{1.57}Fe^{3+}_{0.12}Mg_{0.30})$	San Antonio	0.570	8.997	
$Si_4(Al_{1.45}Mg_{0.58}Li_{0.16})$	Honeycomb	0.600	8.979	
$(Si_{3.74}Al_{0.26})(Al_{1.77}Fe^{3+}_{0.03}Mg_{0.20})$	Unter-Rupsroth	0.555	9.000	
$(Si_{3.46}Al_{0.54})(Al_{1.96}Fe^{3+}_{0.04})$	Black Jack	0.537	8.940	
$(Si_{3.48}Al_{0.52})(Al_{1.98}Fe^{3+}_{0.02}Mg_{0.01})$	Black Jack	0.537	8.978	

https://doi.org/10.1180/clm.2023.20 Published online by Cambridge University Press

Nontronites

$(Si_{3.5}Al_{0.5})(Al_{0.03}Fe^{3+}_{2.02}Mg_{0.01})$	Manito	0.644	9.155	
$(Si_{3.5}Al_{0.5})(Al_{0.05}Fe^{3+}_{1.93}Mg_{0.12})$	Garfield	0.647	9.175	
$(Si_{3.5}Al_{0.5})(Al_{0.08}Fe^{3+}_{1.84}Mg_{0.08})$	Nontron	0.644	9.12	
$(Si_{3.57}Al_{0.43})(Al_{0.08}Fe^{3+}_{1.79}Fe^{2+}_{0.04}Mg_{0.08})$	Behenjy	0.646	9.13	

Trioctahedral smectites

$(Si_{3.19}Al_{0.75}Fe^{3+}_{0.06})(Fe^{3+}_{0.45}Fe^{2+}_{0.26}Mg_{2.29})$	saponite	0.714	9.258	
$(Si_{3.70}Al_{0.30})(Al_{0.04}Fe^{3+}_{0.01}Mg_{2.85})$	saponite	0.717	9.165	
$(Si_{3.38}Al_{0.62})(Al_{0.03}Fe^{3+}_{0.02}Mg_{2.95})$	saponite	0.718	9.218	
$(Si_{3.63}Al_{0.37})(Fe^{3+}_{0.01}Mg_{2.99})$	saponite	0.720	9.198	
$(Si_{3.50}Al_{0.50})(Al_{0.15}Fe^{3+}_{0.04}Mg_{2.92}Mn_{0.01})$	saponite	0.717	9.178	
$(Si_{3.38}Al_{0.52}Fe^{3+}_{0.1})(Al_{0.05}Fe^{2+}_{0.05}Mg_{2.91})$	saponite	0.718	9.197	
$(Si_{3.19}Al_{0.81})(Al_{0.04}Fe^{3+}_{0.44}Fe^{2+}_{0.52}Mg_{1.88})$	griffithite	0.717	9.246	
$(Si_{3.30}Al_{0.70})(Al_{0.79}Fe^{3+}_{0.02}Zn_{1.85}Mg_{0.14})$	sauconite	0.680	9.228	
$(Si_{3.39}Al_{0.61})(Al_{0.78}Fe^{3+}_{0.23}Zn_{1.54}Mg_{0.15})$	sauconite	0.672	9.220	
$(Si_{3.27}Al_{0.73})(Al_{0.12}Fe^{3+}_{0.13}Zn_{2.64}Mg_{0.11})$	sauconite	0.727	9.251	
$(Si_{3.35}Al_{0.65})(Al_{0.04}Fe^{3+}_{0.02}Zn_{2.89}Mg_{0.10}Mn_{0.01})$	sauconite	0.736	9.247	
$(Si_{3.39}Al_{0.61})(Al_{0.17}Fe^{3+}_{0.58}Zn_{1.95}Mg_{0.12})$	sauconite	0.707	9.259	
$(Si_{3.47}Al_{0.53})(Al_{0.22}Fe^{3+}_{0.17}Zn_{2.40}Mg_{0.18})$	sauconite	0.718	9.252	
Si_4 $(Al_{0.01}Mg_{2.71}Li_{0.34})$	hectorite	0.724	9.119	
$(Si_{3.95}$ $Al_{0.05})(Mg_{2.73}Li_{0.33})$	hectorite	0.724	9.180	
Si_4 $(Fe^{3+}_{0.02}Mg_{2.88}Mn_{0.02})$	stevensite	0.720	9.156	
$(Si_{3.82}Al_{0.18})(Al_{0.4}Cr^{3+}_{0.35}Fe^{3+}_{0.58}Mg_{0.82})$	volkonskoite	0.648	9.119	

Other volkonskoite

$(Si_{3.7}Al_{0.3})(Cr^{3+}_{1.1}Mg_{1.26})$	Jordan	0.671	9.162	Khoury *et al.* (1984)
$(Si_{3.59}Al_{0.41})(Cr^{3+}_{1.07}Fe^{3+}_{0.35}Mg_{0.75})$	R4820	0.656	9.08	Foord *et al.* (1987)

https://doi.org/10.1180/clm.2023.20 Published online by Cambridge University Press

Other saponite				
$(Si_{3.30}Al_{0.68}Fe^{3+}_{0.02})(Mg_{2.50}Fe^{2+}_{0.26}Fe^{3+}_{0.24})$	Kosakov	0.719	9.233	Suquet *et al.* (1975)
Other trioctahedral smectites				
$Si_4\ Mg_{2.85}$	stevensite n°1	0.720	9.120	Faust (1959)
$Si_4\ (Mg_{2.66}Li_{0.3})$	hectorite	0.724	9.120	
$Si_4\ (Mg_{2.87}Li_{0.1}Fe^{2+}_{0.06}Al_{0.03})$	ghassoulite	0.721	9.100	
Smectitic series (Murin Murin. Australia)				Gaudin *et al.* (2004)
$(Si_{3.8}Al_{0.2})(Al_{0.36}Fe^{3+}_{1.19}Mg_{0.29}Cr_{0.09}Ni_{0.13})$	2-22	0.638	9.078	
$(Si_{3.79}Al_{0.21})(Al_{0.67}Fe^{3+}_{0.91}Mg_{0.19}Cr_{0.13}Ni_{0.13})$	2-21	0.617	9.054	
$(Si_{3.78}Al_{0.22})(Al_{0.47}Fe^{3+}_{1.01}Mg_{0.2}Cr_{0.17}Ni_{0.19})$	2-19	0.629	9.072	
$(Si_{3.78}Al_{0.22})(Al_{0.59}Fe^{3+}_{0.91}Mg_{0.23}Cr_{0.19}Ni_{0.12})$	2-17	0.621	9.060	
$(Si_{3.79}Al_{0.21})(Al_{0.08}Fe^{3+}_{1.3}Mg_{0.55}Cr_{0.05}Ni_{0.12})$	5-19v	0.660	9.072	
$(Si_{3.69}Al_{0.31})(Al_{0.54}Fe^{3+}_{0.99}Mg_{0.19}Cr_{0.21}Ni_{0.1})$	5-46	0.622	9.060	
$(Si_{3.8}Al_{0.2})(Al_{0.31}Fe^{3+}_{1.29}Mg_{0.2}Cr_{0.1}Ni_{0.11})$	5-43v3	0.636	9.078	
$(Si_{3.79}Al_{0.21})(Al_{0.11}Fe^{3+}_{1.41}Mg_{0.37}Cr_{0.08}Ni_{0.12})$	5-36	0.654	9.084	
$(Si_{3.79}Al_{0.21})(Al_{0.15}Fe^{3+}_{1.33}Mg_{0.5}Cr_{0.03}Ni_{0.13})$	5-25	0.657	9.090	
$(Si_{3.65}Al_{0.35})(Fe^{3+}_{1.67}Mg_{0.46}Cr_{0.05}Ni_{0.12})$	5-23	0.662	9.090	
Other intermediary smectites				
$(Si_{3.49}Al_{0.51})(Al_{0.17}Fe^{3+}_{0.85}Mg_{1.39})$	Mont Megantic, Quebec	0.680	9.150	Kodama *et al.* (1988)
Vermiculite				
$(Si_{2.86}Al_{1.14})(Al_{0.15}Fe^{3+}_{0.01}Mg_{2.83})$	Llano	0.684	9.255	Shirozu & Bailey (1966)
$(Si_{2.72}Al_{1.28})(Al_{0.16}Fe^{3+}_{0.48}Mg_{2.36})$	Kenya	0.668	9.18	Mathieson & Walker (1954)
$(Si_{2.65}Al_{1.35})(Al_{0.35}Fe^{3+}_{0.29}Fe^{2+}_{0.04}Mg_{2.68})$	Ajmer, India	0.709	9.168	http://www.handbookofmineralogy.org/

Synthetic smectites

https://doi.org/10.1180/clm.2023.20 Published online by Cambridge University Press

Dioctahedral Al-Fe^{3+} smectitic series				Petit *et al.* (2015)	
$(Si, Al)_4$ $(Fe^{3+}_{(2-x)}Al_x)$					
$(Si_{3.52}Al_{0.35}Fe^{3+}_{0.13})(Fe^{3+}_2)$	1	0.645	9.186		
$(Si_{3.64}Al_{0.36})(Fe^{3+}_{1.89}Al_{0.11})$	14	0.639	9.168		
$(Si_{3.61}Al_{0.39})(Fe^{3+}_{1.74}Al_{0.26})$	19	0.631	9.132		
	Beidellite 19		9.189	Heuser *et al.* (2013)	Italicized: same sample,
$(Si,Al)_4$ $(Fe^{3+}_{0.38}Al_{1.62})$	23	0.556	8.982		*b* measured by Rietveld
	Beidellite 23		*9.059*	Heuser *et al.* (2013)	
$(Si,Al)_4$ $(Fe^{3+}_{0.34}Al_{1.66})$	31	0.554	8.970		
	Beidellite 31		*9.019*	Heuser *et al.* (2013)	
$(Si_{3.47}Al_{0.45}Fe^{3+}_{0.07})(Fe^{3+}_{1.97}Al_{0.03})$	39	0.643	9.156		
$(Si_{3.51}Al_{0.36}Fe^{3+}_{0.13})(Fe^{3+}_{1.80}Al_{0.20})$	41	0.634	9.126		
$(Si_{3.5}Al_{0.5})(Fe^{3+}_{1.64}Al_{0.36})$	43	0.625	9.138		
$(Si,Al)_4$ $(Fe^{3+}_{1.26}Al_{0.74})$	52	0.604	9.096		
$(Si_{3.6}Al_{0.4})(Fe^{3+}_{0.8}Al_{1.2})$	53	0.579	9.048		
$(Si_{3.7}Al_{0.3})(Fe^{3+}_{0.57}Al_{1.43})$	54	0.566	9.000		
Dioctahedral Ga-Fe^{3+} smectitic series				Petit *et al.* (2016)	
$(Si, Ga)_4$ $(Fe^{3+}_{(2-x)}Ga_x)$					
$(Si_{3,24}Ga_{0.76})Ga_2)$	0.00	0.620	9.100		
$(Si_{3.25}Ga_{0.75})Fe^{3+}_{0.5}Ga_{1.5})$	0.25	0.626	9.114		
$(Si_{3.42}Ga_{0.58})Fe^{3+}_{0.86}Ga_{1.14})$	0.50	0.631	9.117		
$(Si_{3.48}Ga_{0.52})Fe^{3+}_{1.11}Ga_{0.89})$	0.75	0.634	9.123		
$(Si_{3.48}Ga_{0.52})Fe^{3+}_{1.24}Ga_{0.76})$	1.00	0.636	9.127		
Dioctahedral Fe^{3+}-nontronite series				Baron *et al.* (2016b)	
$(Si_{4-x}Fe^{3+}_x)$ (Fe^{3+}_2) (tetrahedral composition)					
$Si_{3.57}Fe^{3+}_{0.43}$		0.645	9.174		
$Si_{3.54}Fe^{3+}_{0.46}$		0.645	9.168		
$Si_{3.51}Fe^{3+}_{0.49}$		0.645	9.180		

https://doi.org/10.1180/clm.2023.20 Published online by Cambridge University Press

$Si_{3.50}\,Fe^{3+}_{0.50}$		0.645	9.186	
$Si_{3.49}Fe^{3+}_{0.51}$		0.645	9.180	
$Si_{3.47}\,Fe^{3+}_{0.53}$		0.645	9.186	
$Si_{3.43}Fe^{3+}_{0.57}$		0.645	9.198	
$Si_{3.32}Fe^{3+}_{0.68}$		0.645	9.198	
$Si_{3.15}\,Fe^{3+}_{0.85}$		0.645	9.216	
$Si_{3.13}\,Fe^{3+}_{0.87}$		0.645	9.222	
$Si_{3.01}Fe^{3+}_{0.99}$		0.645	9.240	
Di-trioctahedral Fe^{3+}-Mg smectitic series				Grauby *et al.* (1995)
$(Si,\,Fe^{3+})_4\,(Fe^{3+},\,Mg)_y$				
$(Si_{3.88}\,Fe^{3+}_{0.12})\,(Fe^{3+}_{1.73}\,Mg_{0.24})$	2	0.654	9.095	
$(Si_{3.9}\,Fe^{3+}_{0.1})\,(Fe^{3+}_{1.58}\,Mg_{0.47})$	3	0.662	9.092	
$(Si_{3.87}\,Fe^{3+}_{0.13})\,(Fe^{3+}_{1.40}\,Mg_{0.76})$	4	0.671	9.104	
$(Si_{3.97}\,Fe^{3+}_{0.03})\,(Fe^{3+}_{1.17}\,Mg_{1.02})$	5	0.680	9.129	
$(Si_{3.96}\,Fe^{3+}_{0.04})\,(Fe^{3+}_{1.08}\,Mg_{1.22})$	6	0.685	9.122	
$(Si_{3.97}\,Fe^{3+}_{0.03})\,(Fe^{3+}_{0.84}\,Mg_{1.58})$	7	0.694	9.126	
$(Si_{3.96}\,Fe^{3+}_{0.04})\,(Fe^{3+}_{0.56}\,Mg_{2.03})$	8	0.704	9.143	
$Si_4\,(Fe^{3+}_{0.30}\,Mg_{2.43})$	9	0.712	9.152	
Fe^{2+}-rich saponite series				Chemtob *et al.* (2014)
$(Si_{3.54}Al_{0.46})(Fe^{2+}_{2.66}Al_{0.27})$	A	0.757	9.384	
$(Si_{3.54}Al_{0.46})(Fe^{2+}_{2.36}Al_{0.28}\,Mg_{0.27})$	B	0.751	9.300	
$(Si_{3.42}Al_{0.58})(Fe^{2+}_{1.43}Al_{0.17}Fe^{3+}_{0.27}Mg_{0.99})$	C	0.732	9.228	
$(Si_{3.52}Al_{0.48})(Fe^{2+}_{0.82}Al_{0.17}Fe^{3+}_{0.04}Mg_{1.75})$	D	0.725	9.192	
$(Si_{3.6}Al_{0.4})(Fe^{2+}_{1.5}Al_{0.86}Fe^{3+}_{0.17})$	E	0.688	9.258	
$(Si_{3.58}Al_{0.42})(Fe^{2+}_{0.83}Al_{0.8}Fe^{3+}_{0.06}Mg_{0.78})$	F	0.678	9.174	
$(Si_{3.63}Al_{0.37})(Fe^{2+}_{2.57}Mg_{0.56})$	G	0.769	9.222	
$(Si_{3.63}Al_{0.37})(Fe^{2+}_{0.98}Fe^{3+}_{0.05}Mg_{2.15})$	H	0.737	9.198	

https://doi.org/10.1180/clm.2023.20 Published online by Cambridge University Press

Saponite series				Suquet *et al.* (1981)
Na $(Si_{4-x}Al_x)$ $(Mg_{(3-y)}Al_y)$				
$(Si_{3.67}Al_{033})(Mg_{3.0})$	1	0.720	9.184	
$(Si_{3.5}Al_{0.5})(Mg_{3.0})$	2	0.720	9.199	
$(Si_{3.3}Al_{0.7})(Mg_{2.8}Al_{0.2})$	3	0.708	9.201	
$(Si_{3.2}Al_{0.8})(Mg_{2.8}Al_{0.2})$	4	0.708	9.214	
$(Si_{3.1}Al_{0.9})(Mg_{2.8}Al_{0.2})$	5	0.708	9.217	
$(Si_{3.2}Al_{0.8})(Mg_{3.0})$	6	0.720	9.219	
$(Si_{3.0}Al_{1.0})(Mg_{2.8}Al_{0.2})$	7	0.708	9.221	
$(Si_{3.0}Al_{1.0})(Mg_{3.0})$	8	0.720	9.237	
Trioctahedral smectites				
$(Si_{3.6}Al_{0.4})$ Zn_3	sauconite	0.740	9.192	Higashi *et al.* (2002)
Si_4 $(Zn_{2.6}Li_{0.4})$	Zn-hectorite	0.743	9.150	
Si_4 $(Mg_{2.6}Li_{0.4})$	hectorite	0.725	9.120	
Hectorite				
Si_4 $(Mg_{2.67}Li_{0.33})$	hectorite	0.724	9.096	Decarreau (1980)
Zn-stenvensite series				Petit *et al.* (2008)
Si_4 Zn_x				
Si_4 $Zn_{2.77}$	Zn80	0.740	9.198	
Si_4 $Zn_{2.97}$	Zn100	0.740	9.198	
Si_4 $Zn_{2.99}$	Zn120	0.740	9.210	
Si_4 $Zn_{2.90}$	Zn150	0.740	9.180	
Si_4 $Zn_{2.97}$	Zn200	0.740	9.150	
Stenvensite series				Decarreau (1983)
Si_4 $R^{2+}{}_{3-\varepsilon}$				
Si_4 $Ni_{3-\varepsilon}$	Ni	0.690	9.087	

https://doi.org/10.1180/clm.2023.20 Published online by Cambridge University Press

$Si_4\ Mg_{3-\varepsilon}$	Mg	0.720	9.144
$Si_4\ Zn_{3-\varepsilon}$	Zn	0.740	9.219
$Si_4\ Fe^{2+}_{3-\varepsilon}$	Fe	0.780	9.270
$Si_4\ (Mg_{0.82}Zn_{0.18})_{3-\varepsilon}$	Zn 0.18	0.724	9.150
$Si_4\ (Mg_{0.43}Zn_{0.47})_{3-\varepsilon}$	Zn 0.47	0.729	9.190

https://doi.org/10.1180/clm.2023.20 Published online by Cambridge University Press

Table 6: Data used for micas. *R*: mean ionic radius of octahedral cations (Å) calculated with r(Li^+) = 0.76 Å (see text); *b*: crystallographic parameter (Å). *Sample reference in the paper.

Mica and assimilated (anhydrous composition)	Sample*	*R*	*b*	References	Comments
Synthetic mica					
$(Si_3Al_1)(Al_2)K$	2M muscovite	0.535	8.995	Yoder & Eugster (1955)	
$(Si_3Al_1)(Al_2)K$	muscovite	0.535	8.992	Guidotti *et al.* (1992)	average of 12 muscovites
				Radoslovich & Norrish (1962)	as named in the paper
$(Si_3Al_1)(Al_2)Na$	32	0.535	8.900		paragonite
$(Si_3Al_1)(Mg_3)K$	27	0.720	9.204		phlogopite
$(Si_3Al_1)(Mg_3)K$ F	28	0.720	9.195		fluorophlogopite
				Frondel & Ito (1966)	
$(Si_3Al_1)(Mn_3)K$	Mn-mica	0.830	9.37		
$(Si_3Al_1)(Zn_3)K$	Zn-mica	0.740	9.32		
Synthetic series (Si_3Al_1) $(Mg_{3-x}R^{2+}_x)$ K				Hazen & Wones (1972)	
Mg_3	M#1	0.720	9.204		
Co_3	M#114	0.745	9.240		
Cu_3	M#29	0.730	9.238		
Ni_3	M#115	0.690	9.175		
$Mg_{2.5}Fe^{2+}_{0.5}$	0.169	0.730	9.230		
$Mg_{2.25}Fe^{2+}_{0.75}$	0.250	0.735	9.242		
$Mg_{1.94}Fe^{2+}_{1.06}$	0.352	0.741	9.260		
$Mg_{1,65}Fe^{2+}_{1.35}$	0.450	0.747	9.276		
$Mg_{1,35}Fe^{2+}_{1.65}$	0.550	0.753	9.285		
$Mg_{0.7}Fe^{2+}_{2.3}$	0.765	0.766	9.312		
$Mg_{0.36}Fe^{2+}_{2.64}$	0.880	0.773	9.335		
Fe^{2+}_3	Fe^{2+}_3	0.780	9.347		
Synthetic series $(Si_{3-z}Al_{1+z})$ $(Mg_xFe^{2+}_yAl_z)$ K				Hewitt & Wones (1975)	
$(Si_3Al)(Mg_3)$	222-69	0.720	9.206		
$(Si_3Al_1)(Mg_{2.25}Fe^{2+}_{0.75})$	45-73	0.735	9.243		

https://doi.org/10.1180/clm.2023.20 Published online by Cambridge University Press

$(Si_3Al_1)(Mg_{2.01}Fe^{2+}_{0.99})$	40-73	0.740	9.253
$(Si_3Al_1)(Mg_{1.50}Fe^{2+}_{1.50})$	53-73	0.750	9.280
$(Si_3Al_1)(Mg_{0.75}Fe^{2+}_{2.25})$	68-73	0.765	9.312
$(Si_3Al_1)(Fe^{2+}_3)$	142-70	0.780	9.352
$(Si_{2.87}Al_{1.13})(Fe^{2+}_{2.87}Al_{0.13})$	67-73	0.770	9.339
$(Si_{2.83}Al_{1.17})(Mg_{2.83}Al_{0.17})$	55-73	0.710	9.193
$(Si_{2.75}Al_{1.25})(Mg_{2.75}Al_{0.25})$	189-70	0.705	9.191
$(Si_{2.75}Al_{1.25})(Mg_{2.06}Fe^{2+}_{0.69}Al_{0.25})$	28-73	0.718	9.230
$(Si_{2.75}Al_{1.25})(Mg_{1.375}Fe^{2+}_{1.375}Al_{0.25})$	29-73	0.732	9.267
$(Si_{2.75}Al_{1.25})(Mg_{0.69}Fe^{2+}_{2.06}Al_{0.25})$	11-72	0.746	9.301
$(Si_{2.75}Al_{1.25})(Fe^{2+}_{2.75}Al_{0.25})$	143-70	0.760	9.336
$(Si_{2.62}Al_{1.38})(Fe^{2+}_{2.62}Al_{0.38})$	4-72	0.749	9.325
$(Si_{2.50}Al_{1.50})(Mg_{2.50}Al_{0.50})$	224-69	0.689	9.170
$(Si_{2.50}Al_{1.50})(Mg_{1.95}Fe^{2+}_{0.55}Al_{0.50})$	153-70	0.700	9.201
$(Si_{2.50}Al_{1.50})(Mg_{1.88}Fe^{2+}_{0.62}Al_{0.50})$	26634	0.702	9.207
$(Si_{2.50}Al_{1.50})(Mg_{1.25}Fe^{2+}_{1.25}Al_{0.50})$	13-72	0.714	9.240
$(Si_{2.50}Al_{1.50})(Mg_{1.10}Fe^{2+}_{1.40}Al_{0.50})$	193-70	0.717	9.251
$(Si_{2.50}Al_{1.50})(Mg_{0.70}Fe^{2+}_{1.80}Al_{0.50})$	152-70	0.725	9.271
$(Si_{2.50}Al_{1.50})(Mg_{0.625}Fe^{2+}_{1.875}Al_{0.50})$	14-72	0.727	9.279
$(Si_{2.50}Al_{1.50})(Fe^{2+}_{2.50}Al_{0.50})$	38-73	0.739	9.312
$(Si_{2.37}Al_{1.63})(Fe^{2+}_{2.37}Al_{0.63})$	6-72	0.729	9.295
$(Si_{2.37}Al_{1.63})(Mg_{2.37}Al_{0.63})$	179-70	0.681	9.164
$(Si_{2.25}Al_{1.75})(Mg_{1.69}Fe^{2+}_{0.56}Al_{0.75})$	15-72	0.685	9.190
$(Si_{2.25}Al_{1.75})(Mg_{1.125}Fe^{2+}_{1.125}Al_{0.75})$	16-72	0.696	9.225
$(Si_{2.25}Al_{1.75})(Mg_{0.56}Fe^{2+}_{1.69}Al_{0.75})$	17-72	0.708	9.261
$(Si_{2.25}Al_{1.75})(Fe^{2+}_{2.25}Al_{0.75})$	7-72	0.719	9.287
Synthetic series $(Si,Al)_4$ $(Fe^{2+},Fe^{3+},Mg)_3$ K	P (bar); T (°C)		Wones & Eugster (1965)
$Mg_{2.1}Fe^{2+}_{0.48}Fe^{3+}_{0.42}$	1035; 850	0.719	9.238
$Mg_{1.95}Fe^{2+}_{0.60}Fe^{3+}_{0.45}$	1035; 750	0.721	9.238
$Mg_{2.19}Fe^{2+}_{0.42}Fe^{3+}_{0.39}$	2070; 900	0.719	9.233
$Mg_{1.95}Fe^{2+}_{0.60}Fe^{3+}_{0.45}$	2070; 800	0.721	9.238
$Mg_{1.59}Fe^{2+}_{1.26}Fe^{3+}_{0.15}$	1035; 800	0.741	9.262
$Mg_{0.93}Fe^{2+}_{1.86}Fe^{3+}_{0.21}$	1035; 700	0.752	9.296
$Mg_{1.32}Fe^{2+}_{1.50}Fe^{3+}_{0.18}$	2070; 800	0.746	9.281
Synthetic series $(Si_{4-x}Al_x)$ (Mg_yAl_z) K			Robert (1976)

https://doi.org/10.1180/clm.2023.20 Published online by Cambridge University Press

$(Si_3Al)Mg_3$	1	0.720	9.209	
$(Si_{2.875}Al_{1.125})(Mg_{2.875}Al_{0.125})$	2	0.712	9.206	
$(Si_{2.825}Al_{1.175})(Mg_{2.825}Al_{0.175})$	3	0.709	9.201	
$(Si_{2.775}Al_{1.225})(Mg_{2.775}Al_{0.225})$	4	0.706	9.199	
$(Si_{2.750}Al_{1.250})(Mg_{2.750}Al_{0.250})$	5	0.705	9.198	
$(Si_{2.625}Al_{1.375})(Mg_{2.625}Al_{0.375})$	6	0.697	9.191	
$(Si_{2.500}Al_{1.500})(Mg_{2.500}Al_{0.500})$	7	0.689	9.185	
$(Si_{2.812}Al_{1.188})(Mg_{2.738}Al_{0.238})$	8	0.705	9.195	
$(Si_{2.925}Al_{1.075})(Mg_{2.715}Al_{0.215})$	9	0.706	9.191	
$(Si_{2.575}Al_{1.425})(Mg_{2.500}Al_{0.475})$	10	0.690	9.173	
$(Si_{2.650}Al_{1.350})(Mg_{2.500}Al_{0.450})$	11	0.692	9.182	
$(Si_{2.725}Al_{1.275})(Mg_{2.500}Al_{0.425})$	12	0.693	9.186	
$(Si_{2.800}Al_{1.200})(Mg_{2.500}Al_{0.400})$	13	0.694	9.187	
$(Si_{2.775}Al_{1.225})(Mg_{2.325}Al_{0.525})$	14	0.686	9.171	
$(Si_{2.862}Al_{1.138})(Mg_{2.338}Al_{0.488})$	15	0.688	9.172	
$(Si_{2.687}Al_{1.313})(Mg_{2.313}Al_{0.563})$	16	0.684	9.168	
$(Si_{2.600}Al_{1.400})(Mg_{2.300}Al_{0.600})$	17	0.682	9.165	
$(Si_{2.512}Al_{1.488})(Mg_{2.288}Al_{0.638})$	18	0.680	9.162	
$(Si_{2.425}Al_{1.575})(Mg_{2.275}Al_{0.675})$	19	0.678	9.159	
$(Si_{2.400}Al_{1.600})(Mg_{2.100}Al_{0.800})$	20	0.671	9.160	
$(Si_{2.500}Al_{1.500})(Mg_{2.125}Al_{0.750})^{\#}$	21	0.672	9.162	#typographical error: original ($Mg_{2.12}$
$(Si_{2.600}Al_{1.400})(Mg_{2.150}Al_{0.700})$	22	0.675	9.163	
$(Si_{2.700}Al_{1.300})(Mg_{2.175}Al_{0.650})$	23	0.677	9.168	
$(Si_{2.537}Al_{1.463})(Mg_{2.013}Al_{0.813})$	24	0.667	9.155	
$(Si_{2.650}Al_{1.350})(Mg_{2.050}Al_{0.750})$	25	0.670	9.150	
$(Si_{2.762}Al_{1.238})(Mg_{2.088}Al_{0.688})$	26	0.674	9.155	
$(Si_{2.625}Al_{1.375})(Mg_{1.950}Al_{0.825})$	27	0.665	9.150	
$(Si_{2.750}Al_{1.250})(Mg_{2.000}Al_{0.750})$	28	0.670	9.155	
$(Si_4)(Mg_{2.5})$	29	0.720	9.108	
				Redhammer & Roth (2002)
Synthetic K-micas				
$(Si_{2.92}Al_{1.08})(Ni_3Al_{0.04})$	NiPhl	0.688	9.180	
$(Si_{2.92}Al_{1.08})(Mg_{2.98}Al_{0.03})$	Phl	0.718	9.204	
$(Si_3Ga)(Mg_3)$	GaPhl	0.720	9.214	
$(Si_{2.91}Al_{1.09})(Co_{2.94}Al_{0.06})$	CoAn	0.741	9.247	
$(Si_{2.91}Al_{1.09})(Mg_{2.68}Fe^{2+}_{0.33}Al_{0.03})$	A20#2	0.725	9.225	
$(Si_{2.91}Al_{1.09})(Mg_{2.68}Fe^{2+}_{0.33}Al_{0.03})$	A20#4	0.725	9.225	

https://doi.org/10.1180/clm.2023.20 Published online by Cambridge University Press

$(Si_{2.96}Al_{1.04})(Mg_{2.45}Fe^{2+}_{0.53}Al_{0.03})$	A40	0.729	9.231		
$(Si_{2.91}Al_{1.09})(Mg_{2.35}Fe^{2+}_{0.68}Al_{0.01})$	A60	0.733	9.247		
$(Si_{2.97}Al_{1.03})(Mg_{2.19}Fe^{2+}_{0.82}Al_{0.01})$	Mga1.2	0.736	9.254		
$(Si_{2.94}Al_{1.06})(Mg_{2.51}Fe^{2+}_{0.50}Al_{0.01})$	Mga1.6	0.729	9.224		
$(Si_{2.91}Al_{1.09})(Co_{1.67}Ni_{1.32}Al_{0.04})$	CoNi1.8	0.718	9.220		
$(Si_{2.28}Al_{1.72})(Al_{0.79}Fe^{2+}_{2.18})$	Sd87	0.715	9.289		
Synthetic K-(Si_3Al_1)-micas				Mercier *et al.* (2005)	Structure refined
(octahedral composition)	JLRMgCo				
$(Co_{0.3}Mg_{2.7})$	0.3	0.723	9.206		
$(Co_{0.6}Mg_{2.4})$	0.60	0.725	9.205		
$(Co_{0.6}Mg_{2.4})$	0.60	0.725	9.211		
$(Co_{0.9}Mg_{2.1})$	0.90	0.728	9.212		
$(Co_{1.2}Mg_{1.8})$	1.2	0.730	9.216		
$(Co_{1.5}Mg_{1.5})$	1.5	0.733	9.218		
$(Co_{1.8}Mg_{1.2})$	1.8	0.735	9.227		
$(Co_{2.1}Mg_{0.9})$	2.1	0.738	9.237		
$(Co_{2.4}Mg_{0.6})$	2.4	0.740	9.234		
$(Co_{2.4}Mg_{0.6})$	2.4	0.740	9.238		
$(Co_{2.7}Mg_{0.3})$	2.7	0.743	9.244		
(Co_3)	3	0.745	9.247		
	JLRMgFe				
(Mg_3)	0	0.720	9.204		
$(Fe_{0.6}Mg_{2.4})$	0.6	0.732	9.223		
$(Fe_{1.2}Mg_{1.8})$	1.2	0.744	9.254		
$(Fe_{1.2}Mg_{1.8})$	1.2	0.744	9.262		
$(Fe_{1.8}Mg_{1.2})$	1.8	0.756	9.295		
$(Fe_{2.4}Mg_{0.6})$	2.4	0.768	9.310		
(Fe_3)	3	0.780	9.350		
	FeNiGR				
(Ni_3)	3	0.690	9.177		
$(Fe_{0.2}Ni_{2.8})$	2.8	0.696	9.191		
$(Fe_{0.6}Ni_{2.4})$	2.4	0.708	9.213		
(Fe_1Ni_2)	2	0.720	9.242		
$(Fe_{1.4}Ni_{1.6})$	1.6	0.732	9.261		
$(Fe_{1.8}Ni_{1.2})$	1.2	0.744	9.285		
$(Fe_{2.2}Ni_{0.8})$	0.8	0.756	9.308		

https://doi.org/10.1180/clm.2023.20 Published online by Cambridge University Press

$(Fe_{2.6}Ni_{0.4})$	0.4	0.768	9.329		
Synthetic $2M_1$ K-micas series				Zviagina & Drits (2019)	selected data from
$(Si_{3.987}Al_{0.013})$ $(Al_{1.021}Mg_{0.974})$	P13-1	0.625	9.016		Schmidt *et al.* (2001)
$(Si_{3.947}Al_{0.053})$ $(Al_{1.053}Mg_{0.957})$	P17	0.623	9.019		
$(Si_{3.823}Al_{0.177})$ $(Al_{1.135}Mg_{0.838})$	P11-2	0.614	9.021		
$(Si_{3.817}Al_{0.183})$ $(Al_{1.187}Mg_{0.809})$	P18-2	0.610	9.028		
$(Si_{3.662}Al_{0.338})$ $(Al_{1.341}Mg_{0.662})$	P12-1	0.596	9.032		
$(Si_{3.642}Al_{0.358})$ $(Al_{1.352}Mg_{0.654})$	P15	0.595	9.031		
$(Si_{3.478}Al_{0.522})$ $(Al_{1.574}Mg_{0.416})$	P28	0.574	9.024		
$(Si_{3.401}Al_{0.599})$ $(Al_{1.578}Mg_{0.442})$	P25	0.575	9.026		
$(Si_{3.288}Al_{0.712})$ $(Al_{1.708}Mg_{0.308})$	P33	0.563	9.022		
$(Si_{3.219}Al_{0.781})$ $(Al_{1.770}Mg_{0.249})$	P30	0.558	9.015		
$(Si_{3.176}Al_{0.824})$ $(Al_{1.773}Mg_{0.292})$	P26	0.561	9.025		
$(Si_{3.124}Al_{0.876})$ $(Al_{1.918}Mg_{0.108})$	P31	0.545	8.998		
$(Si_{3.113}Al_{0.887})$ $(Al_{1.908}Mg_{0.097})$	P29	0.544	8.997		
$(Si_{3.81}Al_{0.19})$ $(Al_{1.21}Mg_{0.75}Fe^{2+}_{0.04})$	2M1 Al-celadonite	0.609	9.037		
Various synthetic micas (collected data) – K as the main interlayer cation if not specified				Brigatti & Guggenheim (2002)	Structure refined as named in the paper
$(Si_{3.45}Al_{0.55})$ $(Al_{1.88})$ $Na_{0.91}$	2	0.535	8.890		paragonite
$(Si_{2.84}Al_{1.16})$ $(Li_{0.77}Mg_{2.23})$ $Ba_{0.97}$, $F_{2.08}$	15	0.730	9.157		lithian kinoshitaite
$(Si_{3.07}Al_{0.03}$ $Fe^{3+}_{0.90})$ $(Fe^{2+}_{2.97}$ $Fe^{3+}_{0.03})$ $Cs_{0.89}$	60	0.779	9.506		cesium tetra-ferri-annite
$(Si_{3.0}$ $Fe^{3+}_{1.0})$ $(Fe^{2+}_{3.0})$	61	0.780	9.404		tetra-ferri-annite
$(Si_{2.98}Al_{1.02})$ $(Mg_{2.97})$ $F_{2.08}$	72	0.720	9.183		fluoro phlogopite
$(Si_{4.0})$ $(Li_{2.0}$ $Al_{1.0})$ $F_{2.0}$	96	0.685	8.968		polylithionite
$(Si_{3.25}$ $Al_{0.75})$ $(Mg_{2.80}Li_{0.20})$ $F_{2.0}$	97	0.723	9.210		Li-containing phlogopite
$(Si_{2.98}$ $Al_{1.02})$ $(Mg_{2.97})$ $F_{1.94}$	98	0.720	9.195		fluoro phlogopite
$(Ge_{3.0}$ $Al_{1.0})$ $(Mg_{1.04}Mn_{1.946})$ $F_{2.0}$	102	0.775	9.509		tetra Ge-Mn-F phlogopite
$(Ge_{3.0}$ $Al_{1.0})$ $(Mg_{2.36}Mn_{0.64}$ $Al_{1.0})$ $F_{2.0}$	103	0.743	9.413		tetra Ge-Mn-F phlogopite
$(Si_{4.0})$ $(Mg_{2.50})$ $F_{2.0}$	104	0.720	9.086		tetra-silicic-F phlogopite
$(Si_{4.0})$ $(Mg_{2.0}$ $Li_{1.0})$ $F_{2.0}$	105	0.733	9.065		tainiolite
$(Ge_{4.0})$ $(Mg_{2.5})$ $F_{2.0}$	106	0.720	9.353		tetra-Ge-F phlogopite
$(Ge_{4.0})$ $(Mg_{2.0}$ $Li_{1.0})$ $F_{2.0}$	107	0.733	9.341		tetra-Ge tainiolite
$(Si_{3.50}$ $Al_{0.50})$ $(Mg_{2.75})$ $F_{2.0}$	108	0.720	9.164		fluoro phlogopite
$(Ge_{3.0}$ $Al_{1.0})$ $(Mg_{3.0})$ $F_{2.0}$	109	0.720	9.345		tetra-Ge-F phlogopite

https://doi.org/10.1180/clm.2023.20 Published online by Cambridge University Press

$(Si_{2.82}\ Mn_{0.18})\ (Mg_{2.44}Mn_{0.24})\ F_{2.0}$	110	0.728	9.157		fluoro phlogopite
Natural micas (anhydrous composition – K as the main interlayer cation if not specified)					
Muscovites and phengites				Zviagina & Drits (2019)	
$(Si_{3.12}Al_{0.88})(Al_{1.88}Fe^{2+}_{0.14}Mg_{0.01})$	1 - Muscovite 2M_1	0.553	9.016		
$(Si_{3.06}Al_{0.94})(Al_{1.72}Fe^{3+}_{0.15}Mg_{0.10}Ti_{0.02}Mn^{3+}_{0.02})$	2 - Muscovite 2M_1	0.548	9.018		
$(Si_{3.16}Al_{0.84})(Al_{1.84}Fe^{3+}_{0.06}\ Fe^{2+}_{0.01}Mg_{0.10})$	3 - Muscovite 2M_1	0.548	9.000		
$(Si_{3.102}Al_{0.98})(Al_{1.90}Fe^{3+}_{0.02}Fe^{2+}_{0.05}Mg_{0.06}Ti_{0.01})$	4 - Muscovite 2M_1	0.548	9.008		
$(Si_{3.10}Al_{0.90})(Al_{1.83}Fe^{2+}_{0.16}Mg_{0.01})$	5 - Muscovite 2M_1	0.556	9.021		
$(Si_{3.11}Al_{0.89})(Al_{1.86}Fe^{2+}_{0.04}Mg_{0.08}Cr_{0.06})$	6 - Muscovite 2M_1	0.549	9.011		
$(Si_{3.09}Al_{0.91})(Al_{1.83}Fe^{2+}_{0.07}Mg_{0.06})$	7 - Muscovite 2M_1	0.552	9.004		
$(Si_{3.07}Al_{0.93})(Al_{1.88}Fe^{2+}_{0.07}Mg_{0.06}Ti_{0.03})$	8 - Muscovite 2M_1	0.550	8.996		
$(Si_{3.03}Al_{0.97})(Al_{1.86}Fe^{3+}_{0.01}Fe^{2+}_{0.06}Mg_{0.07}Ti_{0.02})$	9 - Muscovite 2M_1	0.550	9.013		
$(Si_{3.09}Al_{0.91})(Al_{1.71}Fe^{3+}_{0.16}Fe^{2+}_{0.13}Mn^{2+}_{0.01})$	10 - Muscovite 2M_1	0.561	9.035		
$(Si_{3.2.92}Al_{1.08})(Al_{1.88}Fe^{3+}_{0.09}Mg_{0.05}Ti_{0.02})$	11 - Muscovite 2M_1	0.545	8.991		
$(Si_{3.18}Al_{0.82})(Al_{1.64}Fe^{3+}_{0.08}Fe^{2+}_{0.08}Mg_{0.16}Ti_{0.02})$	12 - Muscovite 2M_1	0.565	9.022		
$(Si_{3.018}Al_{0.82})(Al_{1.78}Fe^{2+}_{0.12}Mg_{0.06}Ti_{0.04})$	13 - Muscovite 2M_1	0.557	8.982		
$(Si_{3.30}Al_{0.70})(Al_{1.65}Fe^{2+}_{0.29}Ti_{0.01}Mn^{2+}_{0.07})$	14 - Fe-rich Muscovite 2M_1	0.581	9.074		
$(Si_{3.26}Al_{0.74})(Al_{1.67}Fe^{2+}_{0.34}Mg_{0.04})$	15 - Fe-rich Muscovite 2M_1	0.579	9.052		
$(Si_{3.25}Al_{0.75})(Al_{1.51}Fe^{2+}_{0.15}Mg_{0.27}Ti_{0.01}Cr_{0.09})$	16 - Mg-rich Muscovite 2M_1	0.582	9.043		
$(Si_{3.38}Al_{0.62})(Al_{1.55}Fe^{2+}_{0.21}Mg_{0.24}Ti_{0.02})$	17 - Phengite 2M_1	0.583	9.051		
$(Si_{3.45}Al_{0.55})(Al_{1.42}Fe^{2+}_{0.24}Mg_{0.33}Ti_{0.04})$	18 - Phengite 2M_1	0.595	9.057		
Dioctahedral true micas (collected data)				Brigatti & Guggenheim (2002)	Single crystal refinement structure as named in the paper
$(Si_{3.51}Al_{0.49})\ (Al_{1.83}Fe^{3+}_{0.03}Fe^{2+}_{0.04}Mg_{0.10}Mn_{0.04})$	1M space group $C2$ 1	0.556	8.952		muscovite
$(Si_{3.11}Al_{0.89})\ (Al_{1.83}Fe^{3+}_{0.12}Fe^{2+}_{0.36}Mg_{0.06})$	1M space group $C2/c$ 4	0.547	8.996		muscovite
$(Si_{3.30}Al_{0.70})\ (Al_{1.65}Fe^{2+}_{0.29}Mn_{0.07}Ti_{0.01})\ F_{0.22}$	5	0.581	9.074		muscovite
$(Si_{3.18}Al_{0.82})\ (Al_{1.78}Fe^{2+}_{0.12}Mg_{0.06}Ti_{0.04})$	6	0.557	8.982		muscovite
$(Si_{2.92}Al_{1.08})\ (Al_{1.88}Fe^{3+}_{0.09}Mg_{0.03}Ti_{0.02})\ F_{0.11}$	7	0.545	8.991		muscovite
$(Si_{3.03}Al_{0.97})\ (Al_{1.86}Fe^{3+}_{0.01}Fe^{2+}_{0.06}Mg_{0.07}Ti_{0.02})$	8	0.550	9.013		muscovite
$(Si_{3.09}Al_{0.91})\ (Al_{1.71}Fe^{3+}_{0.16}Fe^{2+}_{0.13}Mn_{0.01})\ F_{0.22}$	9	0.561	9.035		muscovite
$(Si_{3.18}Al_{0.82})\ (Al_{1.83}Fe^{2+}_{0.07}Mg_{0.07}Ti_{0.06})$	10	0.552	9.005		muscovite
$(Si_{3.07}Al_{0.93})\ (Al_{1.88}Fe^{2+}_{0.07}Mg_{0.06}Ti_{0.03})\ F_{0.19}$	11	0.550	8.996		muscovite
$(Si_{3.09}Al_{0.91})\ (Al_{1.83}Fe^{2+}_{0.07}Mg_{0.07}Ti_{0.06})\ F_{0.23}$	12	0.552	9.004		muscovite
$(Si_{3.17}Al_{0.83})\ (Al_{1.78}Fe^{2+}_{0.13}Mg_{0.15}Ti_{0.04})\ F_{0.19}$	13	0.565	9.003		muscovite

https://doi.org/10.1180/clm.2023.20 Published online by Cambridge University Press

$(Si_{2.87}Al_{1.13})$ $(Al_{1.80}Fe^{2+}_{0.07}Mg_{0.15}Ti_{0.05})$ $F_{0.41}$	14	0.558	8.997	muscovite
$(Si_{3.18}Al_{0.82})$ $(Al_{1.64}Fe^{3+}_{0.08}Fe^{2+}_{0.08}Mg_{0.16}Ti_{0.04})$	15	0.565	9.022	muscovite
$(Si_{3.11}Al_{0.89})$ $(Al_{1.86}Cr_{0.06}Fe^{2+}_{0.04}Mg_{0.08}Ti_{0.04})$	16	0.550	9.011	Cr-containing muscovite
$(Si_{3.07}Al_{0.93})$ $(Al_{1.84}Cr_{0.10}Fe^{2+}_{0.02}Mg_{0.02}Ti_{0.02})$	17	0.544	8.979	Cr-containing muscovite
$(Si_{3.14}Al_{0.86})$ $(Al_{1.83}Cr_{0.11}Fe^{2+}_{0.10}Mg_{0.11}Ti_{0.03})$	18	0.561	9.040	Cr-containing muscovite
$(Si_{3.02}Al_{0.98})$ $(Al_{0.27}Cr_{1.42}Fe^{2+}_{0.01}Mg_{0.18}V_{0.13})$ $F_{0.30}$	30	0.616	9.103	chromphyllite
$(Si_{3.09}Al_{0.91})$ $(Al_{1.93}Fe^{2+}_{0.01}Mg_{0.01}Mn_{0.01})$ $F_{0.12}$	33	0.539	8.950	muscovite
$(Si_{3.02}Al_{0.98})$ $(Al_{1.90}Fe^{3+}_{0.02}Fe^{2+}_{0.05}Mg_{0.06}Ti_{0.02})$	36	0.548	9.008	muscovite
$(Si_{3.39}Al_{0.61})$ $(Al_{1.45}Fe^{3+}_{0.05}Fe^{2+}_{0.09}Mg_{0.50}Ti_{0.01})$	37	0.593	9.038	magnesian muscovite
$(Si_{2.94}Al_{1.06})$ $(Al_{1.99}Fe_{0.03}Mg_{0.01}Ti_{0.003})$ $(K_{0.04}Na_{0.92}Ca_{0.02})$	39	0.538	8.898	paragonite
$(Si_{3.01}Al_{0.68}Fe^{3+}_{0.14})$ $(Al_{1.87}Mn^{3+}_{0.03}Mg_{0.06}Ti_{0.01})$ $F_{0.14}$	45	0.542	9.027	muscovite
$(Si_{3.09}Al_{0.91})$ $(Al_{1.81}Fe^{2+}_{0.14}Mg_{0.12})$ $F_{0.19}$	46	0.562	9.015	muscovite
$(Si_{2.98}Al_{1.02})$ $(Al_{1.93}Fe^{2+}_{0.02}Mg_{0.10})$ $(K_{0.10}Na_{0.60}Ca_{0.03})$	48	0.546	8.894	paragonite
	$2M_2$ space group $C2/c$			
$(Si_{3.16}Al_{0.84})$ $(Al_{1.64}Fe^{2+}_{0.17}Mg_{0.22}Li_{0.15})(K_{0.06}Cs_{0.88}Rb_{0.01})F_{0.21}$	49	0.588	9.076	nanpingite
	$3T$ space group $P3_112$			
$(Si_{3.34}Al_{0.56})$ $(Al_{1.54}Fe_{0.25}Mg_{0.21}Ti_{0.04})$	51	0.563	9.028	muscovite
$(Si_{3.54}Al_{0.46})$ $(Al_{1.41}Mg_{0.60}Ti_{0.02})$	52	0.590	9.033	magnesian muscovite
$(Si_{3.11}Al_{0.89})$ $(Al_{1.c04}Fe^{2+}_{0.04}Mg_{0.09}Ti_{0.01})$	53	0.551	9.000	muscovite
$(Si_{2.96}Al_{1.04})$ $(Al_{2.02}Fe^{3+}_{0.01}Mg_{0.01})$ $(K_{0.16}Na_{0.71}Ca_{0.03})$	54	0.536	8.889	paragonite
Dioctahedral brittle micas (collected data)				
	$2M_1$ space group Cc			
$(Si_{2.11}Al_{1.89})$ $(Al_{1.99}Fe^{2+}_{0.01}Mg_{0.03})$ $Ca_{0.81}Na_{0.19}$	19	0.539	8.828	margarite
$(Si_{1.92}Al_{2.08})$ $(Al_{1.96}Fe_{0.03}Mg_{0.10}Li_{0.12})$ $Ca_{0.73}Na_{0.23}$	21	0.557	8.857	margarite
Trioctahedral true micas (collected data)				
	$1M$ space group $C2/m$			
$(Si_{2.74}Al_{1.26})$ $(Al_{0.24}$ $Fe^{3+}_{0.009}Fe^{2+}_{0.12}$ $Mg_{2.48}Mn_{0.01}$ $Ti_{0.02})$	1	0.705	9.195	phlogopite
$(Si_{2.65}Al_{1.35})$ $(Al_{0.24}$ $Fe^{3+}_{0.007}Fe^{2+}_{0.11}$ $Mg_{2.55}Mn_{0.01}$ $Ti_{0.02})$	2	0.705	9.180	phlogopite
$(Si_{2.60}Al_{1.40})$ $(Al_{0.18}$ $Fe^{3+}_{0.15}Fe^{2+}_{0.03}$ $Mg_{2.63}$ $Ti_{0.01})$	3	0.705	9.189	phlogopite
$(Si_{2.50}Al_{1.50})$ $(Al_{0.47}Fe^{3+}_{0.15}Fe^{2+}_{0.07}$ $Mg_{2.23}Mn_{0.04}$ $Ti_{0.01})$	4	0.692	8.179	Al-phlogopite
$(Si_{2.60}Al_{1.40})$ $(Al_{0.20}$ $Fe^{3+}_{0.11}Fe^{2+}_{0.04}$ $Mg_{2.64}Mn_{0.01})$	5	0.706	9.199	phlogopite
$(Si_{2.81}Al_{1.39})$ $(Al_{0.05}$ $Fe^{3+}_{0.50}Fe^{2+}_{0.70}$ $Mg_{1.54}Mn_{0.02}$ $Ti_{0.20})$	6	0.712	9.244	ferroan phlogopite
$(Si_{2.50}Al_{1.37}$ $Fe^{3+}_{0.13})$ $(Fe^{2+}_{1.05}$ $Mg_{0.92}Mn_{0.01}$ $Ti_{0.67})$	7	0.715	9.244	magnesian annite
$(Si_{2.78}Al_{1.19}$ $Fe^{3+}_{0.03})$ $(Fe^{3+}_{0.45}Fe^{2+}_{0.79}$ $Mg_{1.43}Mn_{0.01}$ $Ti_{0.23}Li_{0.01})$	8	0.717	9.258	ferroan phlogopite
$(Si_{2.80}Al_{1.20})$ $(Al_{0.01}Fe^{3+}_{0.46}Fe^{2+}_{0.71}$ $Mg_{1.50}Mn_{0.03}$ $Ti_{0.15}Li_{0.01})$	9	0.719	9.353	ferroan phlogopite

https://doi.org/10.1180/clm.2023.20 Published online by Cambridge University Press

$(Si_{2.79}Al_{1.21})$ $(Al_{0.05}Fe^{3+}_{0.39}Fe^{2+}_{0.95}$ $Mg_{1.35}Mn_{0.03}$ $Ti_{0.20}Li_{0.01})$	10	0.695	9.242	ferroan phlogopite
$(Si_{2.74}Al_{1.26})$ $(Al_{0.02}Fe^{3+}_{0.36}Fe^{2+}_{0.86}$ $Mg_{1.39}Mn_{0.02}$ $Ti_{0.25}Li_{0.01})$	11	0.718	9.258	ferroan phlogopite
$(Si_{2.85}Al_{1.15})$ $(Al_{0.05}Fe^{3+}_{0.34}Fe^{2+}_{0.91}$ $Mg_{1.35}Mn_{0.03}$ $Ti_{0.23}Li_{0.02})$	12	0.718	9.251	ferroan phlogopite
$(Si_{2.94}Al_{1.06})$ $(Al_{0.01}Fe^{3+}_{0.18}Fe^{2+}_{0.06}$ $Mg_{2.33}Mn_{0.01}$ $Ti_{0.41})$ $F_{0.79}$	13	0.700	9.207	titanian phlogopite
$(Si_{2.68}Al_{1.32})$ $(Al_{0.93}Fe^{3+}_{0.41}Fe^{2+}_{0.39}$ $Mg_{1.10}Mn_{0.03}$ $Ti_{0.14})$	14	0.656	9.219	Al-phlogopite
$(Si_{2.68}Al_{1.32})$ $(Al_{0.14}Fe^{3+}_{0.38}Fe^{2+}_{0.31}$ $Mg_{2.00}Mn_{0.01}$ $Ti_{0.17})$	15	0.702	9.222	ferrian phlogopite
$(Si_{3.25}Al_{0.75})$ $(Fe^{2+}_{0.74}$ $Mg_{1.70}Mn_{0.01}$ $Ti_{0.49})$ $F_{0.31}$	16	0.716	9.245	ferroan phlogopite
$(Si_{2.75}Al_{1.25})$ $(Al_{0.02}Fe^{3+}_{0.39}Fe^{2+}_{0.60}$ $Mg_{1.61}Mn_{0.01}$ $Ti_{0.37})$ $F_{0.23}$	17	0.707	9.230	ferroan phlogopite
$(Si_{2.65}Al_{1.35})$ $(Al_{0.12}Fe^{3+}_{0.47}Fe^{2+}_{0.42}$ $Mg_{1.85}Mn_{0.01}$ $Ti_{0.14})$	18	0.704	9.219	ferrian phlogopite
$(Si_{2.62}Al_{1.38})$ $(Al_{0.13}Fe^{3+}_{0.72}Fe^{2+}_{0.30}$ $Mg_{1.67}Mn_{0.01}$ $Ti_{0.18})$	19	0.701	9.224	ferrian phlogopite
$(Si_{2.59}Al_{1.41})$ $(Al_{0.24}Fe^{3+}_{0.23}Fe^{2+}_{0.76}$ $Mg_{1.58}Ti_{0.17})$	20	0.708	9.241	ferroan phlogopite
$(Si_{2.86}Al_{1.14})$ $(Al_{0.22}Cr_{0.05}Fe^{2+}_{0.39}$ $Mg_{2.17}Mn_{0.02}$ $Ti_{0.14})$ $F_{0.20}$	21	0.708	9.207	ferroan phlogopite
$(Si_{2.91}Al_{1.09})$ $(Cr_{0.03}Fe^{2+}_{0.28}$ $Mg_{2.42}Mn_{0.01}$ $Ti_{0.1})$ $F_{0.72}$	22	0.718	9.190	phlogopite
$(Si_{2.93}Al_{1.07})$ $(Al_{0.09}Cr_{0.05}Fe^{2+}_{0.59}$ $Mg_{1.60}Mn_{0.03}$ $Ti_{0.52})$ $F_{0.57}$	23	0.706	9.228	ferroan phlogopite
$(Si_{2.87}Al_{1.13})$ $(Al_{0.15}Cr_{0.07}Fe^{2+}_{0.50}$ $Mg_{1.90}Mn_{0.03}$ $Ti_{0.33})$ $F_{0.30}$	24	0.707	9.204	ferroan phlogopite
$(Si_{2.90}Al_{1.10})$ $(Al_{0.04}Cr_{0.05}Fe^{2+}_{0.50}$ $Mg_{2.09}Mn_{0.02}$ $Ti_{0.27})$ $F_{0.44}$	25	0.717	9.190	ferroan phlogopite
$(Si_{2.73}Al_{1.27})$ $(Al_{0.01}Cr_{0.01}Fe^{2+}_{0.94}$ $Mg_{1.48}Mn_{0.02}$ $Ti_{0.39})$	26	0.724	9.235	ferroan phlogopite
$(Si_{2.81}Al_{1.19})$ $(Al_{0.08}Cr_{0.01}Fe^{2+}_{1.24}$ $Mg_{1.40}Mn_{0.02}$ $Ti_{0.23})$ $F_{0.31}$	27	0.731	9.256	ferroan phlogopite
$(Si_{2.76}Al_{1.24})$ $(Al_{0.19}Cr_{0.01}Fe^{2+}_{1.30}$ $Mg_{1.24}Mn_{0.01}$ $Ti_{0.20})$	28	0.727	9.215	magnesian annite
$(Si_{2.84}Al_{1.04}$ $Fe^{3+}_{0.12})$ $(Fe^{3+}_{0.16}Fe^{2+}_{0.09}$ $Mg_{2.65}$ $Ti_{0.08})$	29	0.715	9.211	phlogopite
$(Si_{2.82}Al_{1.13}$ $Fe^{3+}_{0.05})$ $(Fe^{3+}_{0.22}Fe^{2+}_{0.09}$ $Mg_{2.60}$ $Ti_{0.09})$	30	0.713	9.230	phlogopite
$(Si_{2.81}Al_{1.14}$ $Fe^{3+}_{0.05})$ $(Fe^{3+}_{0.23}Fe^{2+}_{0.09}$ $Mg_{2.57}$ $Ti_{0.10})$	31	0.712	9.219	phlogopite
$(Si_{2.71}Al_{1.20}$ $Fe^{3+}_{0.24})$ $(Fe^{3+}_{0.24}Fe^{2+}_{0.62}$ $Mg_{1.90}$ $Mn_{0.02}$ $Ti_{0.18})$	32	0.720	9.244	ferroan phlogopite
$(Si_{3.11}Fe^{3+}_{0.89})$ $(Fe^{3+}_{0.05}Fe^{2+}_{0.17}Mg_{2.70}$ $Ti_{0.01})$ $F_{0.14}$	33	0.722	9.270	tetra-ferriphlogopite
$(Si_{3.07}Fe^{3+}_{0.93})$ $(Fe^{3+}_{0.06}Fe^{2+}_{0.17}Mg_{2.75}Mn_{0.01}$ $Ti_{0.01})$	34	0.723	9.277	tetra-ferriphlogopite
$(Si_{2.82}Al_{1.11}$ $Fe^{3+}_{0.07})$ $(Fe^{3+}_{0.15}Fe^{2+}_{0.08}$ $Mg_{2.68}$ $Mn_{0.01}$ $Ti_{0.08})$ $F_{0.11}$	35	0.715	9.239	phlogopite
$(Si_{2.85}Al_{1.07}$ $Fe^{3+}_{0.08})$ $(Fe^{3+}_{0.19}Fe^{2+}_{0.07}$ $Mg_{2.68}$ $Ti_{0.05})$	36	0.715	9.214	phlogopite
$(Si_{2.85}Al_{1.10}$ $Fe^{3+}_{0.05})$ $(Fe^{3+}_{0.21}Fe^{2+}_{0.07}$ $Mg_{2.64}$ $Mn_{0.01}$ $Ti_{0.06})$	37	0.714	9.235	phlogopite
$(Si_{2.76}Al_{1.19}$ $Fe^{3+}_{0.05})$ $(Fe^{3+}_{0.30}Fe^{2+}_{0.38}$ $Mg_{2.17}$ $Mn_{0.01}$ $Ti_{0.13})$	38	0.715	9.238	ferroan phlogopite
$(Si_{2.74}Al_{1.15}$ $Fe^{3+}_{0.11})$ $(Fe^{3+}_{0.25}Fe^{2+}_{0.34}$ $Mg_{2.19}$ $Mn_{0.01}$ $Ti_{0.13})$	39	0.716	9.228	ferroan phlogopite
$(Si_{2.91}Al_{0.71}$ $Fe^{3+}_{0.38})$ $(Fe^{3+}_{0.10}Fe^{2+}_{0.22}Mg_{2.64}$ $Mn_{0.01}$ $Ti_{0.03})$	40	0.721	9.247	tetra-ferriphlogopite
$(Si_{3.15}Al_{0.04}$ $Fe^{3+}_{0.81})$ $(Fe^{3+}_{0.23}Fe^{2+}_{0.20}Mg_{2.54}$ $Ti_{0.02})$	41	0.717	9.284	tetra-ferriphlogopite
$(Si_{3.05}$ $Fe^{3+}_{0.95})$ $(Fe^{3+}_{0.08}Fe^{2+}_{0.17}Mg_{2.73}$ $Ti_{0.01})$	42	0.721	9.288	tetra-ferriphlogopite
$(Si_{3.05}$ $Fe^{3+}_{0.95})$ $(Fe^{3+}_{0.11}Fe^{2+}_{0.20}Mg_{2.68}$ $Mn_{0.01})$	43	0.722	9.292	tetra-ferriphlogopite
$(Si_{2.77}Al_{1.23})$ $(Al_{0.18}Fe^{3+}_{0.18}Fe^{2+}_{1.01}$ $Mg_{1.26}$ $Mn_{0.02}Ti_{0.28})$	44	0.714	9.252	ferroan phlogopite
$(Si_{2.85}Al_{1.5})$ $(Al_{0.21}Fe^{2+}_{1.37}$ $Mg_{1.15}$ $Mn_{0.03}Ti_{0.25})$ $F_{0.16}$	45	0.726	9.263	magnesian annite
$(Si_{2.82}Al_{1.18})$ $(Al_{0.18}$ $Fe^{3+}_{0.13}Fe^{2+}_{1.20}$ $Mg_{1.19}$ $Mn_{0.02}Ti_{0.29})$ $F_{0.14}$	46	0.719	9.258	magnesian annite

https://doi.org/10.1180/clm.2023.20 Published online by Cambridge University Press

$(Si_{2.77}Al_{1.23})$ $(Al_{0.31}$ $Fe^{3+}_{0.16}Fe^{2+}_{1.10}$ $Mg_{1.23}$ $Mn_{0.01}Ti_{0.19})$ $F_{0.12}$	47	0.712	9.260	ferroan phlogopite
$(Si_{2.76}Al_{1.17}$ $Fe^{3+}_{0.07})$ $(Fe^{3+}_{0.23}Fe^{2+}_{0.38}Mg_{2.25}$ $Mn_{0.01}$ $Ti_{0.13})$	48	0.717	9.230	ferroan phlogopite
$(Si_{2.90}Al_{1.06}$ $Fe^{3+}_{0.04})$ $(Fe^{3+}_{0.20}Fe^{2+}_{0.11}Mg_{2.59}$ $Mn_{0.01}$ $Ti_{0.05})$	49	0.716	9.219	phlogopite
$(Si_{3.01}Al_{0.13}$ $Fe^{3+}_{0.86})$ $(Fe^{3+}_{0.30}Fe^{2+}_{0.54}Mg_{1.99}$ $Mn_{0.02}$ $Ti_{0.01})$	50	0.724	9.306	ferroan tetra-ferriphlogop
$(Si_{2.71}Al_{1.29})$ $(Al_{0.35}Fe^{3+}_{0.01}Fe^{2+}_{1.45}$ $Mg_{0.77}Mn_{0.04}$ $Ti_{0.21})$	51	0.721	9.268	magnesian annite
$(Si_{2.62}Al_{1.38})$ $(Al_{0.54}Fe^{3+}_{0.01}Fe^{2+}_{1.41}$ $Mg_{0.83}Mn_{0.03}$ $Ti_{0.17})$	52	0.709	9.239	magnesian annite
$(Si_{2.63}Al_{1.37})$ $(Al_{0.48}Fe^{2+}_{1.48}$ $Mg_{0.70}Mn_{0.06}$ $Ti_{0.20})$	53	0.714	9.257	magnesian annite
$(Si_{2.68}Al_{1.32})$ $(Al_{0.64}Fe^{2+}_{1.33}$ $Mg_{0.73}Mn_{0.04}$ $Ti_{0.17})$	54	0.702	9.222	magnesian annite
$(Si_{2.69}Al_{1.31})$ $(Al_{0.60}Fe^{2+}_{1.36}$ $Mg_{0.73}Mn_{0.02}$ $Ti_{0.14})$ $_{0.12}$	55	0.705	9.232	magnesian annite
$(Si_{2.72}Al_{1.28})$ $(Al_{0.50}Fe^{2+}_{1.46}$ $Mg_{0.70}Mn_{0.03}$ $Ti_{0.16})$ $F_{0.15}$	56	0.713	9.256	magnesian annite
$(Si_{3.49}Al_{0.51})$ $(Li_{1.48}Fe^{2+}_{0.02}Fe^{3+}_{0.008}$ $Mg_{0.05}Mn_{0.03}$ $Al_{1.30})$	62	0.659	9.011	trilithionte
$(Si_{2.75}Al_{1.15}$ $Fe^{3+}_{0.07}$ $Ti_{0.03})$ $(Fe^{3+}_{0.06}Fe^{2+}_{0.20}Mg_{1.74}$ $Mn^{2+}_{0.95}$ $Mn^{3+}_{0.18})$	63	0.756	9.295	manganoan phlogopite
$(Si_{2.91}Al_{1.09})$ $(Al_{0.38}Fe^{2+}_{1.00}Mg_{1.90}$ $Li_{0.34}Mn_{0.04}Ti_{0.05})(K_{0.46}Cs_{0.23}Rb_{0.28})F_{0.45}$	65	0.721	9.247	Rb,Cs,phlogopite
$(Si_{2.81}Al_{1.19})$ $(Al_{0.09}Fe^{3+}_{0.19}$ $Mg_{0.12}Mn_{0.05}$ $Ti_{0.22})$	66	0.749	9.324	annite
$(Si_{2.95}$ $Fe^{3+}_{1.05})$ $(Mg_{3.0})$ $F_{1.30}$	67	0.720	9.199	phlogopite
$(Si_{2.91}Al_{1.09})$ $(Al_{0.07}Fe^{2+}_{0.16}$ $Mg_{2.70}$ $Ti_{0.03})$ $F_{1.13}$	70	0.718	9.202	phlogopite
$(Si_{2.86}Al_{1.07}$ $Fe^{3+}_{0.02}Ti_{0.03})$ $(Fe^{3+}_{0.03}Mg_{2.27}$ $Mn^{2+}_{0.49})$	71	0.739	9.241	manganoan phlogopite
$(Si_{2.82}Al_{1.04}$ $Fe^{3+}_{0.14})$ $(Fe^{3+}_{0.08}Fe^{2+}_{0.13}$ $Mg_{2.73}$ $Ti_{0.06})$ $F_{0.11}$	73	0.718	9.239	phlogopite
$(Si_{3.03}Al_{0.07}$ $Fe^{3+}_{0.90})$ $(Fe^{3+}_{0.01}Fe^{2+}_{0.60}$ $Mg_{2.36}$ $Mn_{0.01}$ $Ti_{0.01})$	74	0.732	9.293	octa ferroan tetra ferriphl
$(Si_{3.02}Al_{0.06}$ $Fe^{3+}_{0.92})$ $(Fe^{2+}_{0.60}$ $Mg_{2.38}$ $Mn_{0.01}Ti_{0.01})$	75	0.732	9.290	octa ferroan tetra ferriphl
$(Si_{2.94}Al_{0.78}$ $Fe^{3+}_{0.28})$ $(Fe^{3+}_{0.04}Fe^{2+}_{0.43}$ $Mg_{2.39}$ $Mn_{0.01}Ti_{0.08})$	76	0.725	9.267	ferroan phlogopite
$(Si_{2.82}Al_{1.10}$ $Fe^{3+}_{0.08})$ $(Fe^{3+}_{0.10}Fe^{2+}_{0.44}$ $Mg_{2.36}$ $Mn_{0.01}Ti_{0.09})$	77	0.723	9.246	ferroan phlogopite
$(Si_{2.84}Al_{1.14}$ $Fe^{3+}_{0.02})$ $(Fe^{3+}_{0.06}Fe^{2+}_{0.60}$ $Mg_{2.23}$ $Mn_{0.01}Ti_{0.10})$	78	0.727	9.244	ferroan phlogopite
$(Si_{3.00}Al_{0.90}$ $Fe^{3+}_{0.10})$ $(Fe^{2+}_{1.14}$ $Mg_{1.73}$ $Mn_{0.04}Ti_{0.09})$	79	0.741	9.259	ferroan phlogopite
$(Si_{3.01}Al_{0.92}$ $Fe^{3+}_{0.07})$ $(Fe^{2+}_{0.44}$ $Mg_{2.51}Ti_{0.05})$ $F_{0.18}$	80	0.727	9.227	ferroan phlogopite
$(Si_{2.94}Al_{1.06})$ $(Fe^{3+}_{0.03}Fe^{2+}_{0.35}$ $Mg_{2.07}Ti_{0.33})$ $F_{0.93}$	81	0.713	9.208	phlogopite
$(Si_{2.12}Al_{1.88})$ $(Al_{0.93}Fe_{0.17}Mg_{1.20}$ $Cr_{0.01})(K_{0.02}Na_{0.83})$	83	0.666	9.050	preiswerkite
$(Si_{2.84}Al_{1.16})$ $(Al_{0.16}Fe^{3+}_{0.86}Fe^{2+}_{0.01}$ $Mg_{1.67}$ $Mn_{0.01}Ti_{0.34})$ $F_{0.17}$	85	0.677	9.210	ferrian phlogopite
$(Si_{2.88}Al_{1.12})$ $(Fe^{2+}_{0.10}$ $Mg_{2.77}Ti_{0.11})$ $F_{0.51}$	86	0.718	9.206	phlogopite
$(Si_{2.97}Al_{1.06})$ $(Fe^{2+}_{1.07}$ $Mg_{1.57}$ $Mn_{0.06}Ti_{0.10})$ $F_{0.94}$	91	0.738	9.241	ferroan phlogopite
$(Si_{3.36}Al_{0.64})$ $(Al_{1.13}Li_{1.3})$ $F_{1.53}$	93	0.656	9.010	trilithionite
$(Si_{2.98}Al_{0.08}Fe^{3+}_{0.85}Ti_{0.03})$ $(Fe^{2+}_{0.16}$ $Mg_{2.89}$ $Mn_{0.01})$	94	0.723	9.297	tetra ferri phlogopite
$(Si_{3.00}$ $Fe^{3+}_{1.00})$ $(Mg_{3.00})$	95	0.720	9.292	tetra ferri phlogopite
$(Si_{2.86}Al_{1.14})$ $(Al_{0.19}Fe^{2+}_{0.71}Fe^{3+}_{0.19}$ $Mg_{1.68}Mn_{0.01}Ti_{0.34})$ $F_{0.17}$	99	0.706	9.231	ferroan phlogopite
$(Si_{2.71}Al_{1.29})$ $(Al_{0.18}$ $Fe^{3+}_{0.01}Fe^{2+}_{2.31}$ $Mg_{0.28}$ $Li_{0.04}Mn_{0.02}Ti_{0.10})$ $_{0.14}$	101	0.758	9.311	annite
$(Si_{4.00})$ $(Li_{1.00}$ $Mn^{3+}_{2.00})$	111	0.683	8.914	norrishite
$(Si_{2.98}Al_{1.02})$ $(Al_{0.47}Fe^{2+}_{2.02}$ $Mg_{0.03}$ $Li_{0.33}Mn_{0.07})$ $F_{0.99}$	112	0.739	9.293	Al-fluoro annite

https://doi.org/10.1180/clm.2023.20 Published online by Cambridge University Press

	1*M* space group *C*2			
$(Si_{3.48}Al_{0.53})$ $(Al_{1.10}$ $Fe^{3+}_{0.03}Fe^{2+}_{0.15}$ $Mg_{0.16}$ $Li_{1.51}Mn_{0.16})$ $F_{1.67}$	113	0.679	9.005	polylithionite
$(Si_{3.87}Al_{0.13})$ $(Al_{1.13}Fe^{2+}_{0.07}$ $Mg_{0.16}$ $Li_{1.41}Mn_{0.05})$ F_x	128	0.666	9.055	polylithionite
$(Si_{3.09}Al_{0.91})$ $(Al_{1.05}Fe^{2+}_{0.77}$ $Fe^{3+}_{0.16}Mg_{0.01}$ $Li_{0.67}Mn_{0.050}Ti_{0.01})$ $F_{1.21}$	129	0.673	9.14	polylithionite-siderophylit
$(Si_{3.33}Al_{0.67})$ $(Al_{0.98}Fe^{2+}_{0.09}$ $Fe^{3+}_{0.03}Mg_{0.01}$ $Li_{1.27}Mn_{0.50}Ti_{0.005})$ $F_{1.58}$	130	0.695	9.102	masutomilite
	2M_1 space group *C*2/*c*			
$(Si_{2.78}Al_{1.22})$ $(Fe^{2+}_{0.70}Fe^{3+}_{0.52}$ $Mg_{1.53}Mn_{0.02}Ti_{0.22})$	131	0.713	9.249	ferroan phlogopite
$(Si_{2.84}Al_{1.16})$ $(Al_{0.40}Fe^{3+}_{0.17}Fe^{2+}_{1.36}Mg_{0.80}$ $Mn_{0.01}Ti_{0.26})$	132	0.709	9.242	magnesian annite
$(Si_{2.79}Al_{1.21})$ $(Al_{0.23}Fe^{2+}_{0.81}Mg_{1.63}$ $Mn_{0.02}Ti_{0.33})$ $F_{0.31}$	133	0.709	9.220	ferroan phlogopite
$(Si_{2.87}Al_{1.13})$ $(Al_{0.34}Fe^{2+}_{0.79}Mg_{1.57}$ $Mn_{0.002}Ti_{0.30})$ $F_{0.26}$	134	0.703	9.222	ferroan phlogopite
$(Si_{2.79}Al_{1.21})$ $(Al_{0.12}Fe^{2+}_{1.39}Mg_{1.16}$ $Mn_{0.007}Ti_{0.32})$ $Cl_{0.14}$	135	0.728	9.245	magnesian annite
$(Si_{2.71}Al_{1.29})$ $(Al_{0.60}Fe^{2+}_{1.36}Mg_{0.71}$ $Mn_{0.04}Ti_{0.16})$	136	0.705	9.242	magnesian annite
$(Si_{2.84}Al_{1.16})$ $(Al_{0.16}Fe^{3+}_{0.01}Fe^{2+}_{1.36}Mg_{1.67}$ $Mn_{0.01}Ti_{0.34})$	137	0.685	9.212	ferrian phlogopite
$(Si_{3.62}Al_{0.38})$ $(Al_{1.26}Fe^{2+}_{0.002}Mg_{0.002}$ $Li_{1.65}Mn_{0.04}Ti_{0.001})$ $F_{1.52}$	138	0.666	9.026	polylithionite
$(Si_{2.86}Al_{1.14})$ $(Al_{0.19}$ $Fe^{3+}_{0.19}Fe^{2+}_{0.71}Mg_{1.68}$ $Mn_{0.01}Ti_{0.34})$ $F_{0.17}$	139	0.706	9.234	hydrogenated ferroan phlogopite
	2M_1 space group *Cc*			
$(Si_{3.00}Al_{1.00})$ $(Al_{0.97}Fe^{3+}_{0.14}Mg_{0.02}$ $Li_{0.50}Mn_{0.03})$ $F_{0.91}$	140	0.682	9.187	lithian siderophyllite
	2M_1 space group *C*1			
$(Si_{2.01}Al_{1.99})$ $(Al_{2.01}Fe^{3+}_{0.01}Li_{0.85}Mg_{0.03}Mn_{0.005}Cr_{0.01})(K_{0.001}Na_{0.94}Ca_{0.03})$	141	0.604	8.872	ephesite
	2M_2 space group *C*2/*c*			
$(Si_{3.49}Al_{0.51})$ $(Al_{1.30}Fe^{3+}_{0.008}Fe^{2+}_{0.002}Mg_{0.05}$ $Li_{1.48}Mn_{0.03})$ F_x	142	0.656	9.023	trilithionite
$(Si_{3.36}Al_{0.64})$ $(Al_{1.26}Fe^{3+}_{0.003}Mg_{0.007}$ $Li_{1.76}Mn_{0.03})$ $F_{1.53}$	143	0.666	9.040	polylithionite
$(Si_{3.39}Al_{0.61})$ $(Al_{1.40}Fe^{2+}_{0.07}Mg_{0.03}$ $Li_{1.03}Mn_{0.03})$ $F_{1.20}$	144	0.637	9.032	trilithionite
	3*T* space group $P3_112$			
$(Si_{3.48}Al_{0.52})$ $(Al_{1.25}Fe_{0.015}Mg_{0.01}$ $Li_{1.62}Mn_{0.09})$ $F_{1.54}$	145	0.668	9.007	polylithionite
$(Si_{2.97}Al_{1.03})$ $(Al_{0.68}$ $Al_{0.19}$ $Fe^{3+}_{0.34}Fe^{2+}_{1.25}Zn_{0.02}Li_{0.37}Mn_{0.04})$ $F_{1.06}$	146	0.699	9.195	lithian siderophyllite
Trioctahedral brittle micas (collected data)				
	1*M* space group *C2/m*			
$(Si_{1.20}Al_{2.76})$ $(Al_{0.68}Fe^{3+}_{0.04}Fe^{2+}_{0.11}Mg_{2.21})$ Ca, $F_{0.14}$	1	0.680	9.005	clintonite
$(Si_{1.19}Al_{2.79})$ $(Al_{0.64}Fe^{2+}_{0.22}Mg_{2.14})$ Ca, $F_{0.11}$	2	0.685	9.006	clintonite
$(Si_{1.25}Al_{2.75})$ $(Al_{0.76}Fe^{2+}_{0.13}Mg_{2.09})$ Ca	3	0.676	8.995	clintonite
$(Si_{1.24}Al_{2.76})$ $(Al_{0.65}Fe^{2+}_{0.13}Mg_{2.22})$ Ca, $F_{0.17}$	4	0.683	9.026	clintonite
$(Si_{1.19}Al_{2.78}Fe^{3+}_{0.03})$ $(Al_{0.67}Fe^{2+}_{0.16}Mg_{2.17}Ti_{0.01})$ Ca, $F_{0.19}$	5	0.682	9.003	clintonite
$(Si_{1.28}Al_{2.70}Fe^{3+}_{0.02})$ $(Al_{0.63}Fe^{2+}_{0.16}Mg_{2.20}Ti_{0.01})$ Ca, $F_{0.18}$	6	0.684	9.005	clintonite
$(Si_{2.17}Al_{1.83})$ $(Al_{0.17}Fe^{2+}_{0.27}Mg_{2.53}Ti_{0.03})$ $(K_{0.41}Ba_{0.54})$ $F_{0.71}$	7	0.714	9.214	potasium kinoshitaite
$(Si_{2.03}Al_{1.97})$ $(Al_{0.04}Fe^{2+}_{0.27}Mg_{2.64}Mn_{0.31})$ Ba, $F_{0.37}$	8	0.729	9.230	kinoshitaite

https://doi.org/10.1180/clm.2023.20 Published online by Cambridge University Press

$(Si_{2.44}Al_{1.56})$ $(Fe^{3+}_{0.15}Fe^{2+}_{1.72}Mg_{0.74}Ti_{0.17})$ $(K_{0.33}Ba_{0.47})$ $F_{0.65}$	9	0.746	9.337	ferrokinoshitaite
$(Si_{1.20}Al_{2.69}Fe^{3+}_{0.11})$ $(Al_{0.70}Fe^{2+}_{0.05}Mg_{2.29}Ti_{0.006})$ *Ca*	10	0.678	9.013	clintonite
$(Si_{2.05}Al_{1.95})$ $(Al_{0.22}Fe^{3+}_{0.05}Mg_{2.07}Mn^{2+}_{0.52}Mn^{3+}_{0.21})$$(K_{0.35}Na_{0.11}$ $Ba_{0.58})$	11	0.724	9.250	magnesian kinoshitaite
$(Si_{1.10}Al_{2.90})$ $(Al_{0.74}Fe^{2+}_{0.18}Mg_{2.08})$ *Ca*	12	0.678	9.005	clintonite
$(Si_{1.32}Al_{2.68})$ $(Al_{0.70}Fe^{2+}_{0.11}Mg_{2.18})$ *Ca*	13	0.679	9.005	clintonite
$(Si_{1.08}Al_{2.92})$ $(Al_{0.82}Fe^{2+}_{0.07}Mg_{2.11})$ *Ca*	14	0.671	9.002	clintonite
	2M_1 space group *Cc*			
$(Si_{2.02}Al_{1.34}Be_{0.64})$ $(Al_{2.04}Fe^{3+}_{0.007}Li_{0.55})$ *Ca*	16	0.583	8.763	bityite
	2*Or* space group *Pnmn*			
$(Si_{2.64}Al_{0.08}$ $Fe^{3+}_{0.70}Fe^{2+}_{0.58})$ $(Mg_{0.48}Fe^{2+}_{2.46}Mn_{0.06}Ti_{0.01})$ $Ba_{0.87}$ $S_{0.85}$ $Cl_{0.15}$	17	0.771	9.492	anandite
$(Si_{2.60}Fe^{3+}_{1.40})$ $(Al_{0.10}Mg_{0.46}Fe^{2+}_{2.46}Mn^{2+}_{0.04}Mn^{3+}_{0.04})$ $Ba_{0.96}$ $S_{0.84}$ $Cl_{0.16}$	18	0.749	9.509	anandite
Li- and Fe rich 1*M* micas			Brigatti *et al.* (2000)	Pikes Peak batholith, central Colorado, USA
$(Si_{3.536}Al_{0.464})(Al_{1.055}Ti_{0.001}Fe^{3+}_{0.047}Fe^{2+}_{0.403}Mg_{0.002}Mn_{0.038}Zn_{0.002}Li_{1.411})$	114	0.681	9.085	$(OH_{0.143}F_{1.746})$
$(Si_{3.413}Al_{0.587})(Al_{1.115}Ti_{0.008}Fe^{3+}_{0.052}Fe^{2+}_{0.533}Mg_{0.010}Mn_{0.039}Zn_{0.003}Li_{1.111})$	55a	0.675	9.092	$(OH_{0.206}F_{1.627})$
$(Si_{3.412}Al_{0.588})(Al_{1.064}Ti_{0.006}Fe^{3+}_{0.059}Fe^{2+}_{0.546}Mg_{0.006}Mn_{0.046}Zn_{0.008}Li_{1.223})$	55b	0.681	9.085	$(OH_{0.241}F_{1.529})$
$(Si_{3.295}Al_{0.705})(Al_{1.007}Ti_{0.002}Fe^{3+}_{0.092}Fe^{2+}_{0.705}Mg_{0.022}Mn_{0.062}Zn_{0.005}Li_{1.082})$	130-1	0.686	9.128	$(OH_{0.187}F_{1.553})$
$(Si_{3.328}Al_{0.672})(Al_{1.020}Ti_{0.005}Fe^{3+}_{0.059}Fe^{2+}_{0.712}Mg_{0.022}Mn_{0.063}Zn_{0.005}Li_{1.095})$	130-2	0.686	9.105	$(OH_{0.186}F_{1.545})$
$(Si_{3.210}Al_{0.790})(Al_{1.050}Ti_{0.005}Fe^{3+}_{0.072}Fe^{2+}_{0.675}Mg_{0.012}Mn_{0.074}Zn_{0.006}Li_{0.974})$	137	0.681	9.114	$(OH_{0.244}F_{1.739})$
$(Si_{3.303}Al_{0.697})(Al_{1.032}Ti_{0.011}Fe^{3+}_{0.141}Fe^{2+}_{0.639}Mg_{0.013}Mn_{0.011}Zn_{0.006}Li_{0.969})$	104	0.676	9.122	$(OH_{0.244}F_{1.606})$
$(Si_{3.308}Al_{0.692})(Al_{1.035}Ti_{0.006}Fe^{3+}_{0.118}Fe^{2+}_{0.610}Mg_{0.063}Mn_{0.002}Zn_{0.006}Li_{0.941})$	54b	0.677	9.123	$(OH_{0.244}F_{1.654})$
$(Si_{3.229}Al_{0.771})(Al_{0.882}Ti_{0.005}Fe^{3+}_{0.242}Fe^{2+}_{0.648}Mg_{0.009}Mn_{0.065}Zn_{0.012}Li_{0.862})$	177	0.683	9.133	$(OH_{0.149}F_{1.921})$
$(Si_{3.175}Al_{0.825})(Al_{1.019}Ti_{0.026}Fe^{3+}_{0.039}Fe^{2+}_{0.808}Mg_{0.052}Mn_{0.059}Zn_{0.011}Li_{0.855})$	140-1	0.683	9.118	$(OH_{0.248}F_{1.622})$
$(Si_{3.235}Al_{0.765})(Al_{0.981}Ti_{0.025}Fe^{3+}_{0.053}Fe^{2+}_{0.805}Mg_{0.053}Mn_{0.060}Zn_{0.011}$ $Li_{0.852})$	140-2	0.685	9.146	$(OH_{0.248}F_{1.640})$
$(Si_{3.312}Al_{0.688})(Al_{1.109}Ti_{0.006}Fe^{3+}_{0.046}Fe^{2+}_{0.779}Mg_{0.004}Mn_{0.080}Zn_{0.002}$ $Li_{0.765})$	24	0.676	9.139	$(OH_{0.174}F_{1.591})$
$(Si_{3.057}Al_{0.943})(Al_{0.811}Ti_{0.102}Fe^{3+}_{0.094}Fe^{2+}_{1.396}Mg_{0.036}Mn_{0.079}Zn_{0.017}$ $Li_{0.409})$	47	0.700	9.233	$(OH_{0.284}F_{1.080})$
$(Si_{3.225}Al_{0.775})(Al_{0.905}Ti_{0.032}Fe^{3+}_{0.094}Fe^{2+}_{1.192}Mg_{0.023}Mn_{0.053}Zn_{0.013}$ $Li_{0.624})$	103	0.694	9.144	$(OH_{0.154}F_{1.294})$
Li-poor micas				
$(Si_{2.943}Al_{1.057})(Al_{0.835}Ti_{0.024}Fe^{3+}_{0.242}Fe^{2+}_{1.627}Mg_{0.097}Mn_{0.004}Zn_{0.007}$ $Li_{0.169})$	26	0.675	9.092	$(OH_{0.167}F_{0.903})$
$(Si_{3.0.94}Al_{0.906})(Al_{0.349}Ti_{0.108}Fe^{3+}_{0.159}Fe^{2+}_{2.222}Mg_{0.002}Mn_{0.079}Li_{0.082})$	33	0.681	9.085	$(OH_{0.119}F_{1.087})$
Li-, Fe-, and Mn- rich *1M* micas			Brigatti *et al.* (2007)	
$(Si_{3.43}Al_{0.57})(Al_{1.0}Fe^{2+}_{0.38}Mg_{0.01}Mn_{0.17}Li_{1.44})$	Hirukawa Mine	0.691	9.086	$(OH_{0.12}$ $F_{1.88})$
$(Si_{3.30}Al_{0.70})(Al_{1.0}Fe^{2+}_{0.36}Mg_{0.01}Mn_{0.31}Li_{1.32})$	Mokrusha Mine	0.695	9.133	$(OH_{0.09}$ $F_{1.91})$
$(Si_{3.11}Al_{0.89})(Al_{0.91}$ $Ti_{0.02}Fe^{2+}_{0.46}Mg_{0.03}Mn_{0.52}Li_{1.06})$	Boise County	0.706	9.146	$(OH_{0.11}$ $F_{1.89})$
Fe-Li micas[#]			Rieder *et al.* (1970)	

https://doi.org/10.1180/clm.2023.20 Published online by Cambridge University Press

$(Si_{2.975}Al_{1.025})(Fe^{2+}_{1,32}Mg_{0.05}Mn_{0.02}Fe^{3+}_{0.045}Al_{1.00}Ti_{0.02})$	44	0.675	9.253	$(OH_{1.43}\ F_{0.49})$
$(Si_{2.57}Al_{1.43})(Fe^{2+}_{1.835}Mg_{0.60}Li_{0.025}Mn_{0.01}Fe^{3+}_{0.305}Ti_{0.15})$	12	0.741	9.336	$(OH_{1.63}\ F_{0.24})$
$(Si_{2.76}Al_{1.24})(Fe^{2+}_{1.61}Mg_{0.21}Li_{0.12}Mn_{0.04}Fe^{3+}_{0.18}Al_{0.575}Ti_{0.02})$	8	0.714	9.255	$(OH_{1.62}\ F_{0.38})$
$(Si_{2.785}Al_{1.215})(Fe^{2+}_{1.485}Mg_{0.12}Li_{0.21}Mn_{0.035}Fe^{3+}_{0.23}Al_{0.64}Ti_{0.01})$	7	0.707	9.260	$(OH_{1.0}\ F_{1.01})$
$(Si_{2.74}Al_{1.26})(Fe^{2+}_{1.47}Mg_{0.06}Li_{0.305}Mn_{0.055}Fe^{3+}_{0.32}Al_{0.52}Cr_{0.025}\ Ti_{0.04})$	18	0.711	9.267	$(OH_{1.01}\ F_{0.99})$
$(Si_{2.91}Al_{1.09})(Fe^{2+}_{1.345}Mg_{0.025}Li_{0.345}Mn_{0.045}Fe^{3+}_{0.135}Al_{0.815}Ti_{0.01})$	13	0.697	9.229	$(OH_{0.98}\ F_{1.02})$
$(Si_{2.875}Al_{1.125})(Fe^{2+}_{1.185}Li_{0.30}Mn_{0.02}Fe^{3+}_{0.15}Al_{0.955}\ Ti_{0.02})$	31	0.680	9.214	$(OH_{1.42}\ F_{0.58})$
$(Si_{2.87}Al_{1.13})(Fe^{2+}_{1.035}Mg_{0.025}Li_{0.60}Mn_{0.02}Fe^{3+}_{0.155}Al_{0.94}Ti_{0.02})$	29	0.684	9.203	$(OH_{0.77}\ F_{1.23})$
$(Si_{3.04}Al_{0.96})(Fe^{2+}_{0.955}Mg_{0.01}Li_{0.585}Mn_{0.035}Fe^{3+}_{0.14}Al_{0.965}Ti_{0.01})$	9	0.681	9.186	$(OH_{1.17}\ F_{0.82})$
$(Si_{3.015}Al_{0.985})(Fe^{2+}_{1.06}Mg_{0.01}Li_{0.725}Mn_{0.05}Fe^{3+}_{0.08}Al_{0.77}Cr_{0.135}\ Ti_{0.02})$	35	0.696	9.172	$(OH_{0.44}\ F_{1.56})$
$(Si_{3.135}Al_{0.865})(Fe^{2+}_{0.65}Mg_{0.02}Li_{0.505}Mn_{0.035}Fe^{3+}_{0.155}Al_{1.155}Ti_{0.01})$	38	0.656	9.129	$(OH_{1.10}\ F_{0.91})$
$(Si_{3.14}Al_{0.86})(Fe^{2+}_{0.725}Li_{0.645}Mn_{0.045}Fe^{3+}_{0.155}Al_{1.035}Ti_{0.02})$	40	0.670	9.146	$(OH_{0.79}\ F_{1.21})$
$(Si_{3.16}Al_{0.84})(Fe^{2+}_{0.8}Mg_{0.08}Li_{0.715}Fe^{3+}_{0.105}Al_{0.99}Ti_{0.02})$	5	0.677	9.155	$(OH_{0.86}\ F_{1.14})$
$(Si_{3.07}Al_{0.93})(Fe^{2+}_{0.715}Li_{0.71}Mn_{0.03}Fe^{3+}_{0.16}Al_{1.05}Ti_{0.01})$	37	0.670	9.160	
$(Si_{3.105}Al_{0.895})(Fe^{2+}_{0.66}Mg_{0.025}Li_{0.735}Mn_{0.025}Fe^{3+}_{0.235}Al_{0.985})$	15	0.672	9.150	$(OH_{0.88}\ F_{1.13})$
$(Si_{2.815}Al_{1.185})(Fe^{2+}_{1.195}Mg_{0.26}Li_{0.375}Mn_{0.035}Fe^{3+}_{0.16}Al_{0.78}Ti_{0.08})$	2	0.692	9.209	$(OH_{1.27}\ F_{0.38})$
$(Si_{2.825}Al_{1.175})(Fe^{2+}_{1.085}Mg_{0.16}Li_{0.39}Mn_{0.035}Fe^{3+}_{0.305}Al_{0.701}Ti_{0.14})$	23	0.694	9.201	$(OH_{0.99}\ F_{1.02})$
$(Si_{2.895}Al_{1.105})(Fe^{2+}_{1.14}Mg_{0.23}Li_{0.43}Mn_{0.04}Fe^{3+}_{0.13}Al_{0.80}Ti_{0.05})$	3	0.695	9.209	$(OH_{0.87}\ F_{1.13})$
$(Si_{2.98}Al_{1.02})(Fe^{2+}_{1.065}Mg_{0.015}Li_{0.495}Mn_{0.035}Fe^{3+}_{0.14}Al_{0.94}Ti_{0.01})$	4	0.683	9.211	$(OH_{1.10}\ F_{0.91})$
$(Si_{3.02}Al_{0.98})(Fe^{2+}_{1.00}Mg_{0.235}Li_{0.475}Mn_{0.03}Fe^{3+}_{0.09}Al_{0.83}Ti_{0.05})$	6	0.688	9.200	$(OH_{1.14}\ F_{0.86})$
$(Si_{3.055}Al_{0.945})(Fe^{2+}_{0.765}Mg_{0.01}Li_{0.42}Mn_{0.02}Fe^{3+}_{0.305}Al_{0.99})$	33	0.664	9.194	
$(Si_{2.94}Al_{1.06})(Fe^{2+}_{1.085}Mg_{0.125}Li_{0.60}Mn_{0.025}Fe^{3+}_{0.105}Al_{0.875}Ti_{0.01})$	10	0.692	9.148	$(OH_{0.83}\ F_{1.17})$
$(Si_{3.20}Al_{0.80})(Fe^{2+}_{0.815}Mg_{0.025}Li_{0.455}Mn_{0.02}Fe^{3+}_{0.085}Al_{1.125}Ti_{0.01})$	14	0.662	9.170	$(OH_{1.17}\ F_{0.72})$
$(Si_{3.135}Al_{0.865})\ (Fe^{2+}_{0.685}Mg_{0.015}Li_{0.915}Mn_{0.035}Fe^{3+}_{0.11}Al_{1.00}Ti_{0.02})$	16	0.678	9.099	$(OH_{0.63}\ F_{1.38})$
$(Si_{3.315}Al_{0.685})\ (Fe^{2+}_{0.62}Li_{1.10}Mn_{0.07}Fe^{3+}_{0.06}Al_{0.98}Ti_{0.01})$	1	0.685	9.110	$(OH_{0.80}\ F_{1.21})$
$(Si_{3.27}Al_{0.73})(Fe^{2+}_{0.555}Mg_{0.03}Li_{1.06}Mn_{0.03}Fe^{3+}_{0.08}Al_{1.02}Ti_{0.03})$	22	0.677	9.105	$(OH_{0.30}\ F_{1.70})$
$(Si_{3.5}Al_{0.5})(Fe^{2+}_{0.26}Li_{1.27}Mn_{0.04}Fe^{3+}_{0.135}Al_{1.05}Ti_{0.01})$	17	0.671	9.058	$(OH_{0.34}\ F_{1.66})$
$(Si_{3.58}Al_{0.42})(Fe^{2+}_{0.005}Mg_{0.065}Li_{1.61}Mn_{0.05}Fe^{3+}_{0.02}Al_{1.17})$	41	0.669	9.028	$(OH_{0.49}\ F_{1.52})$
$(Si_{3.48}Al_{0.52})(Mg_{0.055}Li_{1.475}Mn_{0.03}Fe^{3+}_{0.01}Al_{1.28})$	43	0.659	9.026	$(OH_{0.42}\ F_{1.58})$
$(Si_{3.52}Al_{0.48})\ (Mg_{0.06}Li_{1.575}Mn_{0.01}Fe^{3+}_{0.005}Al_{1.24})$	42	0.663	9.020	$(OH_{0.47}\ F_{1.54})$
$Si_4\ (Mg_{0.035}Li_{1.96}Fe^{3+}_{0.005}Al_{0.955}Ti_{0.05})$	45	0.685	8.970	$(OH_{0.36}\ F_{1.64})$
Various micas				Radoslovich & Norrish (1962) as named in the paper
$(Si_{2.80}Al_{1.20})(Fe^{2+}_{1.30}Mg_{1.03}Mn_{0.03}Fe^{3+}_{0.15}Ti_{0.10}Al_{0.33})$	1	0.719	9.265	biotite
$(Si_{2.82}Al_{1.18})(Fe^{2+}_{1.33}Mg_{0.84}Li_{0.10}Mn_{0.03}Fe^{3+}_{0.20}Ti_{0.10}Al_{0.27})$	3	0.724	9.268	biotite
$(Si_{2.94}Al_{1.06})(Fe^{2+}_{0.37}Mg_{2.37}Li_{0.04}Fe^{3+}_{0.02}Ti_{0.15}Al_{0.07})$	4	0.717	9.251	biotite
$(Si_{2.79}Al_{1.21})(Fe^{2+}_{1.13}Mg_{1.11}Li_{0.03}Fe^{3+}_{0.18}Ti_{0.15}Al_{0.25})$	5	0.717	9.261	biotite

https://doi.org/10.1180/clm.2023.20 Published online by Cambridge University Press

$(Si_{3.00}Al_{1.00})(Fe^{2+}_{1.06}Mg_{1.54}Li_{0.07}Mn_{0.06}Fe^{3+}_{0.11}Ti_{0.13}Al_{0.01})$	6	0.736	9.251	biotite
$(Si_{2.66}Al_{1.34})(Fe^{2+}_{1.33}Mg_{0.68}Li_{0.02}Mn_{0.02}Fe^{3+}_{0.08}Ti_{0.17}Al_{0.50})$	9	0.707	9.254	biotite
$(Si_{2.78}Al_{1.22})(Fe^{2+}_{1.34}Mg_{0.94}Li_{0.01}Mn_{0.02}Fe^{3+}_{0.18}Ti_{0.16}Al_{0.26})$	11	0.721	9.262	biotite
$(Si_{2.54}Al_{1.43})(Fe^{2+}_{1.42}Mg_{0.51}Mn_{0.14}Fe^{3+}_{0.76}Ti_{0.06})$	13	0.733	9.308	biotite
$(Si_{2.74}Al_{1.26})(Fe^{2+}_{1.27}Mg_{0.88}Li_{0.03}Mn_{0.02}Fe^{3+}_{0.16}Ti_{0.12}Al_{0.38})$	14	0.714	9.246	biotite
$(Si_{2.73}Al_{1.27})(Fe^{2+}_{1.19}Mg_{1.24}Li_{0.01}Mn_{0.01}Fe^{3+}_{0.09}Ti_{0.14}Al_{0.24})$	16	0.722	9.253	biotite
$(Si_{2.78}Al_{1.22})(Fe^{2+}_{1.72}Mg_{0.28}Li_{0.04}Mn_{0.03}Fe^{3+}_{0.44}Ti_{0.18}Al_{0.13})$	18	0.731	9.328	biotite
$(Si_{2.81}Al_{1.19})(Fe^{2+}_{1.05}Mg_{1.05}Fe^{3+}_{0.26}Ti_{0.19}Al_{0.36})$	19	0.705	9.266	biotite
$(Si_{2.99}Al_{1.01})(Fe^{2+}_{1.82}Mg_{0.69}Fe^{3+}_{0.09}Ti_{0.33}Al_{0.40})$	20	0.717	9.300	biotite
$(Si_{2.99}Al_{1.01})(Fe^{2+}_{1.80}Mg_{0.51}Fe^{3+}_{0.23}Ti_{0.19}Al_{0.37})$	21	0.720	9.323	biotite
$(Si_{2.88}Al_{1.12})(Fe^{2+}_{1.00}Mg_{1.18}Fe^{3+}_{0.26}Ti_{0.31})$	22	0.722	9.260	biotite
$(Si_{2.88}Al_{1.12})(Fe^{2+}_{1.09}Mg_{1.27}Fe^{3+}_{0.19}Ti_{0.17}Al_{0.38})$	23	0.708	9.271	biotite
$(Si_{3.01}Al_{0.99})(Fe^{2+}_{1.33}Mg_{0.93}Mn_{0.01}Fe^{3+}_{0.23}Ti_{0.21}Al_{0.30})$	24	0.715	9.265	biotite
$(Si_{2.99}Al_{0.95})(Fe^{2+}_{0.23}Mg_{2.15}Fe^{3+}_{0.12}Ti_{0.48})$	25	0.703	9.241	phlogopite
$(Si_{3.02}Al_{0.98})(Fe^{2+}_{0.04}Mg_{2.98}Fe^{3+}_{0.02}Al_{0.16})$	26	0.711	9.220	phlogopite
$(Si_{3.01}Al_{1.01})(Mg_3)$	29	0.720	9.188	fluorophlogopite
$(Si_{3.11}Al_{0.89})(Al_{1.84}Fe^{3+}_{0.12}Mg_{0.06})$	30	0.547	8.995	muscovite
$(Si_{3.27}Al_{0.73})(Al_{1.27}Fe^{3+}_{0.42}Fe^{2+}_{0.15}Mg_{0.19})$	31	0.593	9.060	iron-muscovite
$(Si_{3.58}Al_{0.42})(Fe^{2+}_{0.01}Mg_{0.02}Li_{1.36}Mn_{0.03}Al_{1.32})$	33	0.652	9.006	lepidolite
$(Si_{3.21}Al_{0.79})(Fe^{2+}_{0.02}Mg_{0.02}Li_{1.35}Fe^{3+}_{0.09}Al_{0.82})$	34	0.675	8.970	lepidolite
$(Si_{3.6}Al_{0.4})(Fe^{3+}_{1.4}Mg_{0.7})$	35	0.670	9.020	celadonite
$Si_4(Al_{0.07}Fe^{3+}_{0.93}Fe^{2+}_{0.24}Mg_{0.77})$	36	0.686	9.050	celadonite
$(Si_{3.86}Al_{0.14})(Al_{0.75}Fe^{3+}_{0.36}Fe^{2+}_{0.2}Mg_{0.68})$	37	0.643	9.060	celadonite
$(Si_{3.74}Al_{0.26})(Al_{0.18}Fe^{3+}_{1}Fe^{2+}_{0.57}Mg_{0.57})$	38	0.688	9.080	celadonite
$(Si_{3.28}Al_{0.72})(Fe^{2+}_{0.60}Li_{1.05}Mn_{0.02}Fe^{3+}_{0.06}Al_{1.08})$	39	0.651	9.120	zinwaldite
$(Si_{3.46}Al_{0.54})(Fe^{2+}_{0.33}Mg_{0.02}Li_{1.15}Mn_{0.03}Fe^{3+}_{0.05}Ti_{0.02}Al_{1.16})$	40	0.665	9.060	zinwaldite
$(Si_{2.95}Al_{1.05})(Fe^{2+}_{1.19}Mg_{0.06}Li_{0.45}Mn_{0.02}Fe^{3+}_{0.03}Ti_{0.02}Al_{0.95})$	41	0.692	9.210	lithium biotite
$(Si_{3.23}Al_{0.77})(Fe^{2+}_{0.60}Mg_{0.02}Li_{1.01}Mn_{0.08}Fe^{3+}_{0.03}Al_{1.00})$	42	0.683	9.090	lithium biotite
$(Si_{3.19}Al_{0.77})(Mg_{0.40}Ti_{0.04}Al_{1.48})$	43	0.575	9.040	gümbelite
$(Si_{2.57}Al_{1.43})(Fe^{2+}_{1.46}Mg_{0.68}Fe^{3+}_{0.35}Ti_{0.23}Al_{0.07})$	44	0.728	9.290	lepidomelane
$(Si_2Al_2)(Al_2)$ *Ca*	45	0.535	8.920	margarite
$(Si_{1.95}Al_{2.05})(Fe^{2+}_{0.02}Mg_{0.04}Li_{0.40}Al_{1.90}Fe^{2+}_{0.03})$ *Na*	46	0.572	8.896	ephesite
$(Si_{1.05}Al_{2.95})(Mg_{2.18}Al_{0.72})$ *Ca*	47	0.674	9.000	xanthophyllite
$(Si_{1.17}Al_{2.83})(Fe^{2+}_{0.02}Mg_{2.09}Fe^{3+}_{0.15}Al_{0.70})$ *Ca*	48	0.673	9.010	xanthophyllite
$(Si_{1.22}Al_{2.78})(Fe^{2+}_{0.06}Mg_{2.23}Fe^{3+}_{0.04}Al_{0.72})$ *Ca*	49	0.677	9.000	xanthophyllite
$(Si_{1.16}Al_{2.84})(Fe^{2+}_{0.04}Mg_{2.14}Fe^{3+}_{0.08}Al_{0.76})$ *Ca*	50	0.672	9.020	xanthophyllite
$(Si_{2.17}Al_{0.69}Be_{1.14})(Li_{0.63}Al_{2.09})$ *Ca*	51	0.587	8.713	bityite

https://doi.org/10.1180/clm.2023.20 Published online by Cambridge University Press

$(Si_{2.06}Al_{1.59}Be_{0.35})(Mg_{0.01}Li_{0.71}Al_{1.58})$ *Ca*	52	0.605	8.670		bityite
Hendricksites				Frondel & Ito (1966)	
(available composition)					
$Mg_{0.25}Fe^{2+}_{0.03}Mn_{1.22}Zn_{1.50}$	1	0.775	9.338		
$Mg_{0.45}Fe^{2+}_{0.02}Mn_{1.05}Zn_{1.48}$	2	0.769	9.328		
$(Si_{2.664}Al_{1.336})(Al_{0.02}Mg_{0.46}Ti_{0.04}Fe^{3+}_{0.14}Fe^{2+}_{0.02}Zn_{1.43}Mn_{0.88})$	3	0.756	9.324		
$(Si_{2.727}Al_{1.266})(Mg_{0.23}Ti_{0.01}Fe^{3+}_{0.31}Fe^{2+}_{0.05}Zn_{1.36}Mn_{1.01})$	4	0.759	9.324		
$Mg_{0.42}Fe^{3+}_{0.3}Fe^{2+}_{0.08}Mn_{0.81}Zn_{1.39}$	5	0.753	9.332		
$Mg_{0.94}Fe^{2+}_{0.02}Mn_{0.88}Zn_{1.17}$	6	0.760	9.301		
$Mg_{1.66}Fe^{2+}_{0.25}Mn_{0.34}Zn_{0.75}$	7	0.742	9.257		
$Mg_{1.60}Fe^{2+}_{0.34}Mn_{0.36}Zn_{0.70}$	8	0.745	9.222		
$Mg_{2.91}Fe^{2+}_{0.08}Mn_{0.001}Zn_{0.01}$	9	0.722	9.180		
Manganophyllite				Knurr & Bailey (1986)	
$(Si_{2.79}Al_{1.21})(Al_{0.11}Ti_{0.01}\ Fe^{3+}_{0.17}Mg_{2.51}\ Mn_{0.13})$	manganophyllite	0.713	9.221		
Celadonites					
				Brigatti & Guggenheim (2002)	
$(Si_{3.94}Al_{0.06})\ (Al_{0.05}Fe^{3+}_{1.15}Fe^{2+}_{0.36}Mg_{0.41}Ti_{0.01})$	3	0.682	9.050		true mica-1*M* space group
				Wise & Eugster (1965)	
$(Si_{3.88}Al_{0.12})(Al_{0.62}Fe^{3+}_{0.64}Fe^{2+}_{0.13}Mg_{0.61})$	11	0.643	9.000		
$(Si_{3.78}Al_{0.22})(Al_{0.20}Fe^{3+}_{1.01}Fe^{2+}_{0.28}Mg_{0.57})$	13	0.673	9.042		
$(Si_{3.73}Al_{0.27})(Al_{0.30}Fe^{3+}_{1.07}Fe^{2+}_{0.20}Mg_{0.66})$	14	0.665	9.102		
$(Si_{3.90}Al_{0.10})(Al_{0.36}Fe^{3+}_{0.77}Fe^{2+}_{0.21}Mg_{0.68})$	15	0.665	9.054		
$(Si_{3.88}Al_{0.12})(Al_{1.33}Fe^{3+}_{0.01}Fe^{2+}_{0.02}Mg_{0.54})$	16	0.591	9.000		
				Radoslovich & Norrish (1962)	
$(Si_{3.6}Al_{0.4})(Fe^{3+}_{1.4}Mg_{0.7})$	35	0.670	9.020		
$Si_{4.}(Al_{0.07}Fe^{3+}_{0.93}Fe^{2+}_{0.24}Mg_{0.77})$	36	0.686	9.050		
$(Si_{3.86}Al_{0.14})(Al_{0.75}Fe^{3+}_{0.36}Fe^{2+}_{0.2}Mg_{0.68})$	37	0.643	9.060		
$(Si_{3.74}Al_{0.26})(Al_{0.18}Fe^{3+}_{1}Fe^{2+}_{0.57}Mg_{0.57})$	38	0.688	9.080		
				Buckley *et al.* (1978)	
$Si_{4.01}(Al_{0.15}Fe^{3+}_{0.81}Fe^{2+}_{0.39}Mg_{0.75})$	A	0.689	9.053#		#extracted from Fig. 3
$Si_{4.09}(Al_{0.38}Fe^{3+}_{0.49}Fe^{2+}_{0.37}Mg_{0.71})$	B	0.676	9.044#		
$(Si_{3.83}Al_{0.17})(Al_{0.28}Fe^{3+}_{0.78}Fe^{2+}_{0.22}Mg_{0.69}Ti_{0.01})$	C	0.670	9.052#		
$(Si_{3.96}Al_{0.04})(Al_{0.18}Fe^{3+}_{0.87}Fe^{2+}_{0.24}Mg_{0.71})$	D	0.678	9.050#		

https://doi.org/10.1180/clm.2023.20 Published online by Cambridge University Press

$Si_{4.01}(Al_{0.58}Fe^{3+}_{0.56}Fe^{2+}_{0.24}Mg_{0.53})$	E	0.649	9.047#	
$Si_{4.01}(Al_{0.13}Fe^{3+}_{0.95}Fe^{2+}_{0.26}Mg_{0.64})$	F	0.680	9.053#	
$(Si_{3.95}Al_{0.05})(Al_{0.02}Fe^{3+}_{1.08}Fe^{2+}_{0.19}Mg_{0.71})$	G	0.683	9.061#	
$(Si_{3.99}Al_{0.01})(Al_{0.41}Fe^{3+}_{0.75}Fe^{2+}_{0.25}Mg_{0.45})$	H	0.657	9.043#	
$(Si_{3.83}Al_{0.17})(Al_{0.1}Fe^{3+}_{0.77}Fe^{2+}_{0.19}Mg_{1.08})$	I	0.690	9.051#	
$(Si_{3.91}Al_{0.09})(Al_{0.39}Fe^{3+}_{0.66}Fe^{2+}_{0.2}Mg_{0.72}Ti_{0.01})$	Q	0.664	9.048#	
$(Si_{3.95}Al_{0.05})(Al_{0.15}Fe^{3+}_{1.24}Fe^{2+}_{0.13}Mg_{0.37}Ti_{0.01})$	BM32709	0.660	9.069#	
Glauconites				Buckley *et al.* (1978)
$(Si_{3.57}Al_{0.43})(Al_{0.21}Fe^{3+}_{1.02}Fe^{2+}_{0.64}Mg_{0.26})$	1L	0.684	9.091#	#extracted from Fig. 3
$(Si_{3.62}Al_{0.38})(Al_{0.42}Fe^{3+}_{0.96}Fe^{2+}_{0.43}Mg_{0.28})$	5D	0.661	9.088#	
$(Si_{3.77}Al_{0.23})(Al_{0.31}Fe^{3+}_{0.95}Fe^{2+}_{0.37}Mg_{0.42})$	9D	0.668	9.069#	
$(Si_{3.81}Al_{0.19})(Al_{0.44}Fe^{3+}_{0.82}Fe^{2+}_{0.51}Mg_{0.30})$	11D	0.666	9.081#	
$(Si_{3.77}Al_{0.23})(Al_{0.36}Fe^{3+}_{0.98}Fe^{2+}_{0.21}Mg_{0.46})$	12D	0.657	9.073#	
$(Si_{3.77}Al_{0.23})(Al_{0.35}Fe^{3+}_{0.99}Fe^{2+}_{0.21}Mg_{0.45})$	13D	0.657	9.072#	
$(Si_{3.76}Al_{0.24})(Al_{0.42}Fe^{3+}_{0.92}Fe^{2+}_{0.21}Mg_{0.49})$	14D	0.654	9.072#	
$(Si_{3.75}Al_{0.25})(Al_{0.36}Fe^{3+}_{0.98}Fe^{2+}_{0.24}Mg_{0.45})$	15D	0.658	9.073#	
$(Si_{3.79}Al_{0.21})(Al_{0.33}Fe^{3+}_{0.99}Fe^{2+}_{0.26}Mg_{0.45})$	16D	0.661	9.070#	
$(Si_{3.77}Al_{0.23})(Al_{0.32}Fe^{3+}_{0.97}Fe^{2+}_{0.23}Mg_{0.39})$	16L	0.658	9.077#	
$(Si_{3.65}Al_{0.35})(Al_{0.45}Fe^{3+}_{0.91}Fe^{2+}_{0.15}Mg_{0.40})$	18B	0.645	9.079#	
$(Si_{3.69}Al_{0.31})(Al_{0.40}Fe^{3+}_{1.05}Fe^{2+}_{0.15}Mg_{0.41})$	19	0.648	9.078#	
$(Si_{3.57}Al_{0.43})(Al_{0.37}Fe^{3+}_{1.15}Fe^{2+}_{0.17}Mg_{0.33})$	21	0.648	9.089#	
$(Si_{3.34}Al_{0.66})(Fe_{3}{}^{+}_{1.42}Fe^{2+}_{0.60}Mg_{0.29})$	23L	0.689	9.108#	
$(Si_{3.69}Al_{0.31})(Al_{0.08}Fe^{3+}_{1.26}Fe^{2+}_{0.12}Mg_{0.55})$	27L	0.669	9.100#	
$(Si_{3.83}Al_{0.17})(Al_{0.04}Fe^{3+}_{1.17}Fe^{2+}_{0.13}Mg_{0.72})$	29D	0.678	9.093#	
$(Si_{3.82}Al_{0.1})(Al_{0.13}Fe^{3+}_{1.16}Fe^{2+}_{0.13}Mg_{0.60})$	34D	0.669	9.088#	
$(Si_{3.81}Al_{0.19})(Fe^{3+}_{1.78}Fe^{2+}_{0.09}Mg_{0.43})$	35L	0.664	9.125#	
Al-rich illite and phengite				Drits *et al.* (2006)
$(Si_{3.40}Al_{0.60})$ $(Al_{1.75}Fe^{3+}_{0.08}Fe^{2+}_{0.01}Mg_{0.15})$	3	0.555	9.000	
$(Si_{3.41}Al_{0.59})$ $(Al_{1.66}Fe^{3+}_{0.06}Fe^{2+}_{0.02}Mg_{0.28})$	6	0.566	9.005	
$(Si_{3.63}Al_{0.37})$ $(Al_{1.41}Fe^{3+}_{0.10}Fe^{2+}_{0.07}Mg_{0.42})$	7	0.588	9.018	
$(Si_{3.51}Al_{0.49})$ $(Al_{1.83}Fe^{3+}_{0.03}Fe^{2+}_{0.04}Mg_{0.10})$	8	0.551	8.952	
$(Si_{3.25}Al_{0.75})$ $(Al_{1.84}Fe^{3+}_{0.09}Mg_{0.08})$	9	0.547	8.998	
$(Si_{3.45}Al_{0.55})$ $(Al_{1.57}Fe^{3+}_{0.13}Mg_{0.28})$	10	0.568	9.012	
$(Si_{3.44}Al_{0.56})$ $(Al_{1.27}Fe^{3+}_{0.40}Fe^{2+}_{0.13}Mg_{0.24})$	11	0.594	9.046	
$(Si_{3.54}Al_{0.46})$ $(Al_{1.24}Fe^{3+}_{0.24}Fe^{2+}_{0.12}Mg_{0.44})$	12	0.602	9.042	

https://doi.org/10.1180/clm.2023.20 Published online by Cambridge University Press

$(Si_{3.80}Al_{0.20})$ $(Al_{1.16}Fe^{3+}_{0.09}Fe^{2+}_{0.17}Mg_{0.57})$	13	0.614	9.006
$(Si_{3.80}Al_{0.20})$ $(Al_{1.18}Fe^{3+}_{0.25}Fe^{2+}_{0.01}Mg_{0.56})$	14	0.602	9.007
$(Si_{3.40}Al_{0.60})$ $(Al_{1.68}Fe^{3+}_{0.14}Mg_{0.20})$	15	0.561	9.006
$(Si_{3.27}Al_{0.73})$ $(Al_{1.85}Fe^{3+}_{0.04}Mg_{0.15})$	16a	0.551	9.000
$(Si_{3.28}Al_{0.72})$ $(Al_{1.87}Fe^{3+}_{0.04}Mg_{0.11})$	17a	0.547	8.994
$(Si_{3.47}Al_{0.53})$ $(Al_{1.76}Fe^{3+}_{0.04}Mg_{0.26}Ti_{0.01})$	19	0.561	9.006
$(Si_{3.39}Al_{0.61})$ $(Al_{1.60}Fe^{3+}_{0.20}Mg_{0.24}Ti_{0.01})$	21	0.568	9.005
$(Si_{3.39}Al_{0.61})$ $(Al_{1.54}Fe^{3+}_{0.14}Mg_{0.335}Ti_{0.02})$	22	0.574	9.005
$(Si_{3.42}Al_{0.58})$ $(Al_{1.58}Fe^{3+}_{0.11}Mg_{0.29}Ti_{0.01})$	23	0.568	9.005
$(Si_{3.48}Al_{0.52})$ $(Al_{1.73}Fe^{3+}_{0.06}Mg_{0.20}Ti_{0.01})$	24	0.557	9.005
$(Si_{3.30}Al_{0.70})$ $(Al_{1.90}Fe^{3+}_{0.02}Mg_{0.08}Ti_{0.04})$	25	0.545	9.005

[#]original compositions were with Ti in tetrahedra (except sample 45).Ti was reallocated to octahedral sites, and the corresponding amount of octahedral Al was moved to tetrahedral sites. XRD data were available in a Table which has been kindly provided to us by the author M. Rieder

Table 7. Parameters of the regressions calculated for the synthetic micas (Figs. 15 to 19).

Regression type	$b = R.A+B$	R^2	Number of points	$b/b_{tet} = R.C+D$	R^2	%O enlargement = $R.E+F$	R^2
(*M-Ph*)	$K(Si_3Al)(Mg_{3x/2}\ Al_{2-x}\square_{1-x/2})O_{10}(OH)_2$ $b = R*1.1478 + 8.3794$			$b/b_{tet} = R*0.1229 + 0.8975$		%O enlargement = -37.514.R + 24.23	
(*Ph-A*)	$K(Si_3Al_1)(Mg_xFe^{2+}_{3-x})O_{10}(OH)_2$ $b = R*2.3942 + 7.4821$			$b/b_{tet} = R*0.2564 + 0.8014$		%O enlargement = -20.056.R + 11.66	
Dioctahedral Schmidt *et al.* (2001)	$K(Si_{3+x}Al_{1-x})(Al_{2-x}Mg_x)O_{10}(OH)_2$		16	$b/b_{tet} = R*0.2553 + 0.827$	0.9805		
Trioctahedral Robert (1976)	$K(Si_{3-x+2y}Al_{1+x-2y})(Mg_{3-x-y}Al_x\square_y)O_{10}(OH)_2$						

https://doi.org/10.1180/clm.2023.20 Published online by Cambridge University Press

All except 29	$b = R^*1.1509 + 8.3841$	0.9499	28 (y ≠ 0)	$b/b_{tet} = R^*0.2515 + 0.8038$	0.7894	%O enlargement = -35.19.R + 22.638	0.9935
y							
0	$b = R^*0.8049 + 8.6308$	0.9895	7	$b/b_{tet} = R^*0.3972 + 0.7005$	0.9995		
0.025	$b = R^*1.5032 + 8.1349$	-	2	$b/b_{tet} = R^*0.4671 + 0.6518$	-		
0.05	$b = R^*1.6159 + 8.064$	-	2	$b/b_{tet} = R^*0.4744 + 0.6485$	-		
0.075	$b = R^*1.7865 + 7.9483$	-	2	$b/b_{tet} = R^*0.4919 + 0.6376$	-		
0.1	-	-	3	$b/b_{tet} = R^*0.4511 + 0.6667$	0.9982		
0.125	$b = R^*0.4973 + 8.8279$	-	2	$b/b_{tet} = R^*0.3477 + 0.7382$	-		
0.15	$b = R^*0.7395 + 8.6638$	-	2	$b/b_{tet} = R^*0.3729 + 0.7221$	-		
0.175	-	-	3	$b/b_{tet} = R^*0.378 + 0.7198$	0.9922		
0.225	$b = R^*0.5891 + 8.7583$	-	2	$b/b_{tet} = R^*0.3478 + 0.7416$	-		
y = 0.25 - 0.5x	$b = R^*-3.8609 + 11.918$	0.9946	3	$b/b_{tet} = R^*1.418 + 0.0188$	0.9997		
y = 0.5 - x	-	-	4 (x, y ≠ 0)	$b/b_{tet} = R^*1.4313 - 0.0137$	0.9879		
y = 0.75 - 1.5x	$b = R^*1.3164+ 8.2673$	0.9861	6 (y ≠ 0)	$b/b_{tet} = R^*0.9411 + 0.3323$	0.9994		
y = 1 - 2x	$b = R^*1.1666+ 8.3777$	0.8644	4 (y ≠ 0)	$b/b_{tet} = R^*1.0084+ 0.2935$	0.9409		
y = 1.25 - 2.5x	-	-	3 (y ≠ 0)	$b/b_{tet} = R^*0.6029 + 0.5694$	0.9853		
y = 1.5 - 3x	$b = R^*1.1509+ 8.33841$	-	2 (y ≠ 0)	$b/b_{tet} = R^*0.6368 + 0.5494$	-		
Hewitt & Wones (1975)	$K(Si_{3-z}Al_{1+z})(Mg_xFe^{2+}_{3-x-z}Al_z)O_{10}(OH)_2$						
All	$b = R^*1.8744 + 7.8968$	0.8148	28	$b/b_{tet} = R^*0.3274+ 0.7469$	0.972	%O enlargement = -26.498.R + 16.754	0.8885
z							
0	$b = R^*2.4105 + 7.4706$	0.9991	6	$b/b_{tet} = R^*0.2582 + 0.8001$		%O enlargement = -20.271.R + 11.833	0.9985
0.25	$b = R^*2.6255 + 7.3529$	0.9992	5	$b/b_{tet} = R^*0.2798 + 0.7826$		%O enlargement = -18.512.R + 10.86	0.9988
0.5	$b = R^*2.8435 + 7.2106$	0.9992	8	$b/b_{tet} = R^*0.3016 + 0.7648$		%O enlargement = -16.649.R + 9.7787	0.9975
0.63	$b = R^*2.7579 + 7.2846$	-	2	$b/b_{tet} = R^*0.2582 + 0.8001$		%O enlargement = -17.768.R + 10.716	
0.75	$b = R^*2.9067 + 7.2006$	0.9951	4	$b/b_{tet} = R^*0.2918 + 0.7707$		%O enlargement = -16.334.R + 9.9239	0.9838
	$K(Si_{3-z}Al_{1+z})(Fe^{2+}_{3-z}Al_z)O_{10}(OH)_2$						
	$b = R^*1.0552 + 8.5304$	0.9662	7	$b/b_{tet} = R^*0.3513 + 0.7277$		%O enlargement = -34.453.R + 22.921	0.997
	$K(Si_{3-z}Al_{1+z})(Mg_{3-z}Al_z)O_{10}(OH)_2$						
	$b = R^*1.1096 + 8.407$	0.9912	5	$b/b_{tet} = R^*0.4166 + 0.6859$		%O enlargement = -35.267.R + 22.629	0.999

https://doi.org/10.1180/clm.2023.20 Published online by Cambridge University Press

Table 8. Data used for chlorites. *R*: mean ionic radius of octahedral cations (Å) calculated with $r(Li^{+})$ = 0.760 Å (see text). *b*: crystallographic parameter (Å). *Sample reference in the paper.

Natural chlorites (Anhydrous composition)	**Sample***	***R***	***b***	**References**	**Comments**
Trioctahedral chlorites				Wiewiora & Wilamowski (1996)	
$(Si_{2.57}Al_{1.43})(Al_{1.16}Mg_{0.14}Fe^{3+}_{0.36}Mn^{2+}_{4.3})$	1	0.759	9.500		
$(Si_{2.7}Al_{1.3})(Al_{1.3}Mg_{0.6}Fe^{2+}_{0.2}Mn^{2+}_{2.6}Zn_{1.3})$	2	0.734	9.400		
$(Si_{2.72}Al_{1.28})(Al_{1.36}Mg_{0.26}Fe^{3+}_{0.39}Mn^{2+}_{3.95})$	3	0.746	9.470		
$(Si_{3.4}Al_{0.6})(Al_{0.84}Mg_{4.6}Fe^{2+}_{0.28}Fe^{3+}_{0.11}Cr_{0.02}Ni_{0.07})$	4	0.694	9.216		
$(Si_{3}Al_{1})(Al_{0.2}Mg_{5}Fe^{2+}_{0.1}Cr_{0.7})$	5	0.703	9.242		
$(Si_{2.8}Al_{1.2})(Al_{1.2}Mg_{2.6}Fe^{2+}_{2.2})$	6	0.705	9.290		
$(Si_{3.3}Al_{0.7})(Al_{0.87}Mg_{3.13}Fe^{2+}_{2})$	7	0.713	9.290		
$(Si_{2.4}Al_{1.6})(Al_{0.85}Mg_{0.7}Fe^{2+}_{3.7}Fe^{3+}_{0.75})^{\#}$	8	0.721	9.297		#typographical error original value : $Al_{0.85}Mg_{0.7}Fe^{2+}_{0.75}Fe^{3+}_{3.7}$
$(Si_{2.62}Al_{1.38})(Al_{1.17}Mg_{2.82}Fe^{2+}_{1.24}Fe^{3+}_{0.52})$	9	0.689	9.290		
$(Si_{2.8}Al_{1.2})(Al_{1.28}Mg_{4.3}Fe^{2+}_{0.3}Fe^{3+}_{0.06})$	10	0.682	9.220		
$(Si_{2.67}Al_{1.33})(Al_{2.1}Mg_{3.35}Fe^{2+}_{0.03}Fe^{3+}_{0.09})$	11	0.649	9.170		
$(Si_{2.87}Al_{1.13})(Al_{1.45}Mg_{0.79}Fe2^{+}_{2.82}Fe^{3+}_{0.12}Mn^{2+}_{0.59})$	12	0.712	9.350		
$(Si_{2.55}Al_{1.45})(Al_{1.41}Mg_{0.78}Fe^{2+}_{3,88})$	13	0.716	9.336		
$(Si_{2.85}Al_{1.15})(Al_{0.97}Mg_{4.54}Fe^{2+}_{0.28}Fe^{3+}_{0.18}Mn^{2+}_{0.01})$	14	0.691	9.234		
$(Si_{3.16}Al_{0.84})(Al_{0.82}Mg_{4.9}Fe^{2+}_{0.29}Mn^{2+}_{0.005})$	15	0.698	9.232		structure refinement parameters: Bailey (1991c)
$(Si_{3.22}Al_{0.78})(Al_{0.65}Mg_{5.04}Fe^{2+}_{0.1}Fe^{3+}_{0.17}Mn^{2+}_{0.01})$	16	0.699	9.216		
$(Si_{3.01}Al_{0.99})(Al_{0.92}Mg_{4.75}Fe^{2+}_{0.13}Fe^{3+}_{0.14})$	17	0.691	9.216		
$(Si_{2.64}Al_{1.36})(Al_{1.17}Mg_{4.02}Fe^{2+}_{0.65}Fe^{3+}_{0.13}Mn^{2+}_{0.02})$	18	0.689	9.240		
$(Si_{2.69}Al_{1.31})(Al_{1.42}Mg_{2.36}Fe^{2+}_{1.72}Fe^{3+}_{0.26}Mn^{2+}_{0.05})$	19	0.690	9.258		

https://doi.org/10.1180/clm.2023.20 Published online by Cambridge University Press

$(Si_{2.6}Al_{1.4})(Al_{1.23}Mg_{2.16}Fe^{2+}_{2.11}Fe^{3+}_{0.3}Mn^{2+}_{0.04})$	20	0.700	9.306	
$(Si_{2.51}Al_{1.49})(Al_{1.04}Mg_{0.37}Fe^{2+}_{3.57}Fe^{3+}_{0.79}Mn^{2+}_{0.01})$	21	0.714	9.354	
$(Si_{2.96}Al_{1.04})(Al_{0.95}Mg_{4.62}Fe^{2+}_{0.14}Fe^{3+}_{0.14}Cr_{0.09}Ni_{0.007})$	22	0.689	9.207	
$(Si_{3.07}Al_{0.93})(Al_{0.63}Mg_{4.95}Fe^{2+}_{0.11}Fe^{3+}_{0.03}Cr_{0.26}Ni_{0.007})$	23	0.697	9.220	
$(Si_{3.19}Al_{0.81})(Al_{0.2}Mg_{5.18}Fe^{2+}_{0.11}Fe^{3+}_{0.04}Cr_{0.51})$	24	0.706	9.231	
$(Si_{3.11}Al_{0.89})(Al_{0.19}Mg_{5.1}Fe^{2+}_{0.16}Cr_{0.60})$	25	0.705	9.215	
$(Si_{2.91}Al_{1.09})(Al_{0.36}Mg_{5.03}Fe^{2+}_{0.23}Fe^{3+}_{0.11}Cr_{0.27}Ni_{0.02})$	26	0.705	9.219	
$(Si_{2.83}Al_{1.17})(Al_{1.26}Mg_{4.06}Fe^{2+}_{0.42}Fe^{3+}_{0.15})$	27	0.683	9.192	
$(Si_{2.88}Al_{1.12})(Al_{1.0}Mg_{4.56}Fe^{2+}_{0.16}Fe^{3+}_{0.22}Ni_{0.01})$	28	0.688	9.222	
$(Si_{3.55}Al_{0.45})(Al_{0.97}Mg_{4.2}Fe^{2+}_{0.06}Fe^{3+}_{0.2}Ni_{0.22})$	29	0.685	9.192	
$(Si3_{.0}Al_{1.0})(Al_{0.2}Mg_{5.0}Fe^{2+}_{0.1}Cr_{0.7})$	30	0.703	9.240	
$(Si_{3.21}Al_{0.79})(Al_{0.56}Mg_{4.72}Fe^{2+}_{0.10}Cr_{0.47}Mn^{2+}_{0,001}Ni_{0.03})$	31	0.695	9.170	
$(Si_{3.0}Al_{1.0})(Al_{1.0}Mg_{5.0})$	32	0.689	9.187	
$(Si_{3.17}Al_{0.83})(Al_{0.83}Mg_{4.28}Fe^{2+}_{0.20}Fe^{3+}_{0.28}Cr_{0.023}Ni_{0.25})$	33	0.691	9.246	
$(Si_{2.72}Al_{1.28})(Al_{1.35}Mg_{0.41}Fe^{2+}_{3.42}Fe^{3+}_{0.46}Mn^{2+}_{0.015})$	34	0.706	9.306	
$(Si_{2.54}Al_{1.46})(Al_{0.84}Mg_{0.7}Fe^{2+}_{2.51}Fe^{3+}_{1.15}Mn^{2+}_{0.53})$	35	0.714	9.350	
$(Si_{3.28}Al_{0.98})(Al_{0.72}Mg_{4.95}Fe^{2+}_{0.04}Fe^{3+}_{0.04,}Cr_{0.23}Ni_{0.02})$	36	0.694	9.227	structure refinement parameters: Bailey (1991c)
$(Si_{2.99}Al_{1.01})(Al_{0.71}Mg_{4.92}Fe^{2+}_{0.06}Fe^{3+}_{0.06}Cr_{0.25})$	37	0.694	9.228	structure refinement parameters: Bailey (1991c)
$(Si_{3.17}Al_{0.83})(Al_{0.77}Mg_{4.82}Fe^{2+}_{0.17}Fe^{3+}_{0.18})$	38	0.695	9.230	
$(Si_{2.64}Al_{1.36})(Al_{0.85}Mg_{3.1}Fe^{2+}_{1.82}Fe^{3+}_{0.32})$	39	0.708	9.286	
$(Si_{2.69}Al_{1.31})(Al_{1.55}Mg_{3.47}Fe^{2+}_{0.86})$	40	0.680	9.241	
$(Si_{2.87}Al_{1.13})(Al_{0.79}Mg_{4.6}Fe^{2+}_{0.48}Fe^{3+}_{0.21})$	41	0.698	9.236	
$(Si_{2.62}Al_{1.38})(Al_{1.32}Mg_{2.85}Fe^{2+}_{1.53}Fe^{3+}_{0.22}Cr_{0.002})$	42	0.692	9.267	structure refinement: Rule & Bailey (1987)
$(Si_{3.55}Al_{0.45})(Al_{1.17}Mg_{0.76}Fe^{2+}_{1.2}Mn^{2+}_{0.01})$	43	0.703	9.257	
$(Si_{2.84}Al_{1.16})(Al_{0.95}Mg_{0.79}Fe^{2+}_{3.05}Fe^{3+}_{0.65}Mn^{2+}_{0.33})$	44	0.719	9.344	
$(Si_{2.73}Al_{1.27})(Al_{1.16}Mg_{4.74}Fe^{3+}_{0.07}Mn^{2+}_{0.054})$	45	0.685	9.210	
$(Si_{3.1}Al_{0.9})(Al_{0.79}Mg_{4.54}Fe^{2+}_{0.55}Fe^{3+}_{0.11}Mn^{2+}_{0.01})$	46	0.700	9.240	
$(Si_{2.69}Al_{1.31})(Al_{1.13}Mg_{2.86}Fe^{2+}_{1.85}Fe^{3+}_{0.14}Mn^{2+}_{0.04})$	47	0.703	9.290	
$(Si_{2.56}Al_{1.44})(Al_{1.25}Mg_{1.02}Fe^{2+}_{3.49}Fe^{3+}_{0.19}Mn^{2+}_{0.05})$	48	0.715	9.350	
$(Si_{2.43}Al_{1.57})(Al_{1.54}Mg_{0.2}Fe^{2+}_{4.17}Fe^{3+}_{0.03}Mn^{2+}_{0.06})$	49	0.715	9.365	

https://doi.org/10.1180/clm.2023.20 Published online by Cambridge University Press

$(Si_{2.54}Al_{1.46})(Al_{1.20}Mg_{1.01}Fe^{2+}_{3.24}Fe^{3+}_{0.41}Mn^{2+}_{0.053})$	50	0.711	9.348
$(Si_{2.73}Al_{1.27})(Al_{1.15}Mg_{4.74}Fe^{3+}_{0.074}Mn^{2+}_{0.055})$	51	0.685	9.208
$(Si_{2.54}Al_{1.46})(Al_{1.20}Mg_{1.01}Fe^{2+}_{3.24}Fe^{3+}_{0.41}Mn^{2+}_{0.053})$	52	0.711	9.354
$(Si_{2.97}Al_{1.03})(Al_{1.35}Mg_{2.24}Fe^{2+}_{1.44}Fe^{3+}_{0.45}Mn^{2+}_{0.031})$	53	0.685	9.282
$(Si_{3.17}Al_{0.83})(Al_{0.89}Mg_{3.16}Fe^{2+}_{1.58}Fe^{3+}_{0.20}Mn^{2+}_{0.009})$	54	0.706	9.270
$(Si_{2.78}Al_{1.22})(Al_{1.24}Mg_{4.27}Fe^{2+}_{0.29}Fe^{3+}_{0.06})$	55	0.683	9.216
$(Si_{2.3}Al_{1.7})(Al_{2.14}Mg_{3.21}Fe^{2+}_{0.06}Fe^{3+}_{0.2})$	56	0.647	9.198
$(Si_{2.77}Al_{1.23})(Al_{1.76}Mg_{3.58}Fe^{2+}_{0.29}Fe^{3+}_{0.03}Mn^{2+}_{0.02})$	57	0.666	9.216
$(Si_{2.7}Al_{1.3})(Al_{1.3}Mg_{1.3}Fe^{2+}_{3.4})$	58	0.714	9.336
$(Si_{2.91}Al_{1.09})(Al_{1.56}Mg_{1.11}Fe^{2+}_{3.04})$	59	0.701	9.314
$(Si_{2.64}Al_{1.36})(Al_{1.76}Mg_{0.82}Fe^{2+}_{3.19})$	60	0.697	9.326
$(Si_{2.59}Al_{1.41})(Al_{1.84}Mg_{0.83}Fe^{2+}_{3.006})$	61	0.692	9.324
$(Si_{2.67}Al_{1.33})(Al_{1.73}Mg_{0.79}Fe^{2+}_{3.26})$	62	0.698	9.324
$(Si_{2.62}Al_{1.38})(Al_{1.68}Mg_{0.93}Fe^{2+}_{3.23})$	63	0.700	9.319
$(Si_{2.61}Al_{1.39})(Al_{1.72}Mg_{1.19}Fe^{2+}_{2.9}Mn^{2+}_{0.02})$	64	0.696	9.311
$(Si_{2.5}Al_{1.5})(Al_{0.6}Mg_{5}Fe^{2+}_{0.4})$	65	0.706	9.270
$(Si_{3.01}Al_{0.99})(Al_{0.99}Mg_{1.67}Fe^{2+}_{0.5}Fe^{3+}_{0.14}Mn^{2+}_{0.005}Ni_{2.62})$	66	0.679	9.214
$(Si_{2.26}Al_{1.74})(Al_{1.33}Mg_{4.42}Fe3^{+}_{0.03}Cr_{0.19})$	67	0.675	9.209
$(Si_{3.11}Al_{0.89})(Al_{0.69}Mg_{4.44}Fe^{2+}_{0.2}Fe^{3+}_{0.4}Mn^{2+}_{0.01}Ni_{0.01})$	68	0.695	9.245
$(Si_{2.88}Al_{1.12})(Al_{0.75}Mg_{4.47}Fe^{3+}_{0.57})$	69	0.689	9.256
$(Si_{2.54}Al_{1.46})(Al_{0.81}Mg_{2.38}Fe^{2+}_{0.9}Fe^{3+}_{1.41}Mn^{2+}_{0.09}Ni_{0.01})$	70	0.686	9.264
$(Si_{3.01}Al_{0.99})(Al_{1.0}Mg_{4.12}Fe^{2+}_{0.34}Fe^{3+}_{0.3}Mn^{2+}_{0.01})$	71	0.688	9.233
$(Si_{2.65}Al_{1.35})(Al_{1.18}Mg_{0.63}Fe^{2+}_{3.19}Fe^{3+}_{0.52}Mn^{2+}_{0.09})$	72	0.710	9.362
$(Si_{2.4}Al_{1.6})(Al_{1.14}Mg_{4.59}Fe3^{+}_{0.08}Cr_{0.25})$	73	0.680	9.206
$(Si_{2.2}Al_{1.8})(Al_{1.67}Mg_{3.97}Fe3^{+}_{0.17}Cr_{0.12})$	74	0.664	9.192
$(Si_{3.53}Al_{0.47})(Al_{0.47}Mg_{4.74}Fe^{2+}_{0.28}Fe^{3+}_{0.29}Mn^{2+}_{0,01}Ni_{0.02})$	75	0.704	9.237
$(Si_{2.81}Al_{1.19})(Al_{1.39}Mg_{0.82}Fe^{2+}_{3.69})$	76	0.714	9.231
$(Si_{3}Al_{1})(Al_{0.96}Mg_{3.93}Fe^{2+}_{0.95}Fe^{3+}_{0.1}Mn^{2+}_{0.02})$	77	0.699	9.222
$(Si_{3.13}Al_{0.87})(Al_{0.65}Mg_{4.38}Fe^{3+}_{0.54}Mn^{2+}_{0.01})$	78	0.691	9.224
$(Si_{2.97}Al_{1.03})(Al_{0.98}Mg_{4.43}Fe^{2+}_{0.17}Fe^{3+}_{0.25}Ni_{0.07})$	79	0.687	9.215

https://doi.org/10.1180/clm.2023.20 Published online by Cambridge University Press

$(Si_{2.95}Al_{1.05})(Al_{1.05}Mg_{4.51}Fe^{2+}_{0.14}Fe^{3+}_{0.17}Ni_{0.02})$	80	0.686	9.228	
$(Si_{2.64}Al_{1.36})(Al_{1.45}Mg_{1.30}Fe^{2+}_{3.12}Mn^{2+}_{0.084})$	81	0.708	9.336	
$(Si_{3.06}Al_{0.94})(Al_{0.694}Mg_{4.715}$#$Fe^{2+}_{0.109}Fe^{3+}_{0.269}Cr_{0.128}Ni_{0.011})$	82	0.694	9.228	# instead of $Mg_{4.175}$ - corrected from the source paper (Zheng & Bailey, 1989)
Di-tri and di-dioctahedral chlorites				Wiewiora & Wilamowski (1996)
$(Si_{2.86}Al_{1.14})(Al_{2.98}Mg_{1.95}Fe^{2+}_{0.14}Fe^{3+}_{0.08})$	1	0.613	9.058	
$(Si_{3.14}Al_{0.86})(Al_{4.1}Mg_{0.08}Fe^{2+}_{0.01}Fe^{3+}_{0.04}Li_{0.26})$	2	0.553	8.956	structure refinement parameters: Bailey (1991c)
$(Si_{3.06}Al_{0.94})(Al_{2.45}Mg_{2.54}Fe^{2+}_{0.01}Fe^{3+}_{0.03})$	3	0.630	9.060	
$(Si_{3.3}Al_{0.7})(Al_{2.7}Mg_{2.3})$	4	0.620	9.014	
$(Si_{3.06}Al_{0.94})(Al_{0.28}Mg_{4.56}Fe^{2+}_{0.06}Fe^{3+}_{0.013}Cr_{0.46}Mn^{2+}_{0,001}Ni_{0.03})$	5	0.702	9.216	
$(Si_{2.48}Al_{1.52})(Al_{1.52}Mg_{0.32}Fe^{2+}_{3.46}Fe^{3+}_{0.04})$	6	0.706	9.314	
$(Si_{2.86}Al_{1.14})(Al_{2.9}Mg_{1.96}Fe^{2+}_{0.22})$	7	0.617	9.054	
$(Si_{3.12}Al_{0.88})(Al_{4.0}Mg_{0.24})$	8	0.545	8.940	
$(Si_{3.08}Al_{0.92})(Al_{3.9}Mg_{0.11}Fe^{3+}_{0.015}Cr_{0.02}Mn^{2+}_{0,005}Li_{0.82})$	9	0.578	8.890	
$(Si_{3.04}Al_{0.96})(Al_{3.8}Mg_{0.14}Fe^{3+}_{0.015}Ni_{0.005}Li_{1.13})$	10	0.590	8.885	
$(Si_{3.3}Al_{0.7})(Al_{2.7}Mg_{2.3})$	11	0.620	9.070	
$(Si_{3.01}Al_{0.99})(Al_{2.84}Mg_{1.91}Fe^{2+}_{0.02}Fe^{3+}_{0.19}Mn^{2+}_{0.02})$	12	0.612	9.080	
$(Si_{2.99}Al_{1.01})(Al_{2.88}Mg_{1.94}Fe^{3+}_{0.17}Mn^{2+}_{0.02})$	13	0.612	9.083	
$(Si_{3.43}Al_{0.57})(Al_{2.7}Mg_{1.97}Fe^{2+}_{0.04}Fe^{3+}_{0.09})$	14	0.615	9.042	
$(Si_{2.95}Al_{1.05})(Al_{3.89}Mg_{0.02}Fe^{2+}_{0.05}Li_{1.11})$	15	0.587	8.930	
$(Si_{3.26}Al_{0.74})(Al_{3.02}Mg_{1.18}Fe^{2+}_{0.033}Fe^{3+}_{0.35}Mn^{2+}_{0.004})$	16	0.593	9.050	
$(Si_{2.88}Al_{1.12})(Al_{2.35}Mg_{2.91}Fe^{3+}_{0,012})$	17	0.637	9.190	
$(Si_{2.79}Al_{1.21})(Al_{1.34}Mg_{2.23}Fe^{2+}_{0.29}Fe^{3+}_{0.69})$	18	0.658	9.180	
$(Si_{3.01}Al_{0.99})(Al_{2.92}Mg_{1.89}Fe^{2+}_{0.12}Fe^{3+}_{0.076}Mn^{2+}_{0.024})$	19	0.613	9.063	
$(Si_{3.0}Al_{1.0})(Al_{2.83}Mg_{2.0}Fe^{3+}_{0.18}Li_{0.015})$	20	0.613	9.067	
$(Si_{3.3}Al_{0.7})(Al_{2.86}Mg_{1.92}Fe^{2+}_{0.13})$	21	0.614	9.090	
$(Si_{3.27}Al_{0.73})(Al_{4.02}Mg_{0.013}Fe^{3+}_{0.003}Li_{0.66})$	22	0.567	8.929	
$(Si_{2.96}Al_{1.04})(Al_{3.97}Li_{1.11})$	23	0.584	8.920	

https://doi.org/10.1180/clm.2023.20 Published online by Cambridge University Press

$(Si_{3.08}Al_{0.92})(Al_{3.96}Mg_{0.017}Fe^{3+}_{0.007}Li_{0.98})$	24	0.580	8.957	
$(Si_{3.2}Al_{0.8})(Al_{3.2}Mg_{1.6})$	25	0.597	9.054	
$(Si_{3.02}Al_{0.98})(Al_{3.05}Mg_{1.79}Fe^{3+}_{0.06}Mn^{2+}_{0.004})$	26	0.604	9.054	
$(Si_{3.28}Al_{0.72})(Al_{3.08}Mg_{1.19}Fe^{2+}_{0.033}Fe^{3+}_{0.35})$	27	0.592	9.054	
$(Si_{2.2}Al_{1.8})(Al_{1.2}Mg_{2.6}Fe^{2+}_{0.3}Fe^{3+}_{1.5})$	28	0.663	9.300	problem redox suspected (Steinfink, 1958)
$(Si_{3.38}Al_{0.62})(Al_{3.96}Fe^{2+}_{0.04}Fe^{3+}_{0.09}Li_{0.7})$	29	0.572	8.900	
$(Si_{2.36}Al_{1.64})(Al_{3.14}Mg_{1.8}Fe^{3+}_{0.1}Cr_{0.12})$	30	0.604	9.207	
$(Si_{2.98}Al_{1.02})(Al_{3.77}Mg_{0.06}Fe^{2+}_{0.12}Fe^{3+}_{0.15}Li_{1.27})$	31	0.599	8.930	
Other chlorites				Radoslovich (1962)
$(Si_{2.8}Al_{1.2})(Al_{1.3}Mg_{2.8}Fe^{2+}_{1.7})$	ripidolite	0.696	9.283	
$(Si_{2.6}Al_{1.4})(Al_{1.5}Mg_{0.4}Fe^{2+}_{4.2})$	bavalite	0.716	9.365	
$(Si_{2.5}Al_{1.5})(Al_{1.2}Mg_{2.2}Fe^{2+}_{0.7}Fe^{3+}_{1.4})$	thuringite	0.668	9.192	
$(Si_{2.6}Al_{1.4})(Al_{1.22}Mg_{4.2}Fe^{2+}_{0.22})$	grochanite	0.682	9.227	
$(Si_{2.9}Al_{1.1})(Al_{0.7}Mg_{2.9}Fe^{2+}_{2.2}Fe^{3+}_{10.2})$	diabantite	0.718	9.305	
$(Si_{3.1}Al_{0.9})(Al_{0.2}Mg_{5.1}Fe^{2+}_{0.2}Cr_{0.6})$	kammererite	0.706	9.242	
$(Si_{2.5}Al_{1.5})(Al_{1.6}Mg_{4.3}Fe^{2+}_{0.1})$	sheridanite	0.672	9.226	
$(Si_{2.88}Al_{1.12})(Al_{1.21}Mg_{1.84}Fe^{2+}_{2.82})$	Mg-chamosite	0.711	9.33	
$(Si_{2.62}Al_{1.38})(Al_{1.18}Mg_{0.25}Fe^{3+}_{0.37}Mn_{3.82})$	pennantite	0.751	9.40	
$(Si_{2.4}Al_{1.6})(Al_{0.85}Mg_{0.7}Fe^{2+}_{3.7}Fe^{3+}_{0.75})$	thuringite	0.721	9.30	
$(Si_{2.7}Al_{1.3})(Al_{1.4}Fe^{2+}_{3.85}Fe^{3+}_{0.75})$	thuringite	0.706	9.31	
$(Si_{2.25}Al_{1.75})(Al_{0.8}Mg_{0.35}Fe^{2+}_{4.75}Fe^{3+}_{0.05})$	bavalite	0.742	9.35	
$(Si_{2.71}Al_{1.29})(Al_{1.35}Mg_{0.92}Fe^{2+}_{3.37}Fe^{3+}_{0.18}Mn_{0.04})$	daphnite	0.710	9.38	
$(Si_{2.99}Al_{1.01})(Al_{1.12}Mg_{0.75}Fe^{2+}_{3.23}Fe^{3+}_{0.56})$	chamosite	0.710	9.36	
$(Si_{2.42}Al_{1.58})(Al_{0.83}Mg_{0.72}Fe^{2+}_{3.68}Fe^{3+}_{0.76})$	thuringite	0.722	9.32	
$(Si_{2.6}Al_{1.4})(Al_{0.75}Mg_{4.9}Fe^{2+}_{0.07}Fe^{3+}_{0.17}Cr_{0.18})$	corundophillite	0.693	9.27	
$(Si_{3.1}Al_{0.9})(Al_{1.3}Mg_{0.75}Fe^{2+}_{3.35}Fe^{3+}_{0.6})$	chamosite	0.706	9.36	
$(Si_{2.9}Al_{1.1})(Al_{0.82}Mg_{5.20})$	leuchtenbergite	0.695	9.19	

https://doi.org/10.1180/clm.2023.20 Published online by Cambridge University Press

$(Si_{2.6}Al_{1.4})(Al_{1.30}Mg_{4.6}Fe^{2+}_{0.02}Fe^{3+}_{0.10})$	sheridanite	0.679	9.21		
$(Si_{2.6}Al_{1.4})(Al_{1.40}Mg_{3.9}Fe^{2+}_{0.70})$	chlorite	0.684	9.21		
$(Si_{2.42}Al_{1.58})(Al_{1.01}Mg_{2.7}Fe^{2+}_{2.3})$	prochlorite	0.712	9.21		
$(Si_{3.03}Al_{0.97})(Al_{0.17}Mg_{5.05}Fe^{2+}_{0.11}Fe^{3+}_{0.04}Cr_{0.71})$	Chrome chlorite	0.703	9.25		
IIb-4 triclinic clinochlore				Smyth *et al*. (1997)	
$(Si_{2.96}Al_{1.04})(Al_{0.841}Mg_{2.924}Fe^{2+}_{0.076}Fe^{3+}_{0.102}Cr_{0.004}Ti_{0.004})$	NMNH #R4513	0.680	9.226		
Cookeite				Zheng & Bailey (1997)	
$(Si_{3.042}Al_{0.958})(Al_{4.017}Mg_{0.007}Fe_{0.009}Cr_{0.005}Li_{0.852})$	Little Rock	0.575	8.940		two-layer «r » structure
Vanadium chlorite				Whitney & Northrop (1986)	
$(Si_{3.54}Al_{0.46})(Al_{2.02}Mg_{1,14}Fe^{3+}_{0.48}V_{0.4}Li_{0.04})$	TM05	0.612	9.120		
$(Si_{3.59}Al_{0.41})(Al_{1.96}Mg_{1,01}Fe^{3+}_{0.5}V_{0.48}Li_{0.05})$	TM6	0.611	9.120		
Fe^{3+}-sudoites				Billault *et al.* (2002)	
$(Si_{3.32}Al_{0.68})(Al_{2.93}Mg_{1.58}Fe^{2+}_{0.13}Fe^{3+}_{0.15})$	MR2	0,606	9.054		
$(Si_{3.42}Al_{0.58})(Al_{2.87}Mg_{1.24}Fe^{2+}_{0.24}Fe^{3+}_{0.33}Mn_{0.01})$	MR11	0,605	9.066		

https://doi.org/10.1180/clm.2023.20 Published online by Cambridge University Press

Table 9. Summary of tetrahedral parameters of chlorite. *Sample reference from Table 8. Tetrahedral rotation angle α_{ref}: measured by structure refinement, α_{calc}: calculated ($\alpha = arccos(b/b_{tet.})$ (Eq. 4) – see text). #: from structure refinement. £: calculated using the following equation derived from Eq. 3: (Si-O) = ($b_{tet.}$- √2.^{IV}Al.Δ)/(4.√2) with $b_{tet.}$ value obtained from Eq. 4 with the α_{ref} value, and Δ = 0.13 being the difference between Si-O and Al-O bond lengths.

Sample*		α_{ref}	α_{calc}	Mean bond length (Å)		
Trioctahedral	^{IV}Al	(°)	(°)	T-O#	Si-O£	Al-O£
42 - clinochlore II*b*-2	1.378	8.5	9.9	1.668	1.612	1.742
37 - clinochlore II*b*-4	1.010	7.2	8.8	1.659	1.611	1.741
36 - clinochlore II*b*-4	0.980	7.2	8.6	1.653	1.612	1.742
82 - clinochlore II*b*-4	0.944	6.9	8.3	1.652	1.613	1.743
82 - clinochlore II*b*-2	0.944	6.8	8.3	1.653	1.612	1.742
15 - clinochlore II*b*-4	0.840	6.5	7.3	1.651	1.615	1.745
Dioctahedral						
Cookeite - I*aa*	0.958	14	16.6	1.657 (x3) 1.685	1.598	1.728
2 - donbassite I*a*-2	0.860	13.5	15.9	1.675 1.617	1.600	1.730

https://doi.org/10.1180/clm.2023.20 Published online by Cambridge University Press

Table 10. Regression parameters proposed for the different mineral families investigated. *R* calculated with r(Li^+) = 0.6 Å

Regression type	b = A.R + B	$b/b_{tet.}$ = C.R + D	%O enlargement[#] = E.R + F
Hydroxides	b = 4.51.R + 6.22		
MO(OH) oxyhydroxides	b = 4.6673.R + 6.0546		
Layered double hydroxides	b = 4.2043.R + 6.3758		
TO phyllosilicates			
kaolinite-lizardite (*K-L*)	b = 1.5092.R + 8.1371	$b/b_{tet.}$ = 0.1649.R + 0.889	%O enlargement = -33.489.R + 21.497
greenalite-caryopilite (*G-C*)	b = 6.8545.R + 4.3037	$b/b_{tet.}$ = 0.7489.R + 0.47	
Al-serpentines *(G-C)'*		$b/b_{tet.}$ = 0.7489.R + 0.47	
Fe^{3+}-serpentines *(Fe^{3+}-Serp)'*		$b/b_{tet.}$ = 0.7489.R + 0.43	
Neutral TOT phyllosilicates			
Pyrophyllite-talc (*P-T*)	b = 1.1162.R + 8.3691	$b/b_{tet.}$ = 0.122.R + 0.9144	%O enlargement = -38.126.R + 24.21
Mica TOT phyllosilicates*			
muscovite-phlogopite (*M-Ph*)	b = 1.1479.R + 8.3794	$b/b_{tet.}$ = 0.1229.R + 0.8975	%O enlargement = -37.514.R + 24.23
phlogopite-annite (*Ph-A*)	b = 2.3942.R + 7.4821	$b/b_{tet.}$ = 0.2564.R + 0.8014	%O enlargement = -20.056.R + 11.66
Tetrasilicic micas	b = 0.8694.R + 8.4637	$b/b_{tet.}$ = 0.0944.R + 0.925	%O enlargement = -39.421.R + 24.328
Phengites[$] – micaceous samples[£]		$b/b_{tet.}$ = 0.2373.R + 0.8376[$]	%O enlargement = -46.185.R + 28.869[£]
Chlorite TOTO phyllosilicates	b = 2.2995.R + 7.6655	$b/b_{tet.}$ = 0.1991.R + 0.8504	%O enlargement = -24.452.R + 16.031

*See Table 7 for details on sub-relationships [#]compared to hydroxides

https://doi.org/10.1180/clm.2023.20 Published online by Cambridge University Press

Table 11. Structural details for some phyllosilicates for comparison. Sample reference from Table 6 for micas, and table 4 for talc. *R* calculated with r(Li^+)= 0.60 Å. Tetrahedral rotation angle α_{ref}: measured by structure refinement, α_{calc}: calculated ($\alpha = arccos(b/b_{tet.})$ (Eq. 4) – see text). %O enlargement compared to hydroxides; O sheet thickness measured by structure refinement and α_{ref}: from Brigatti & Guggenheim (2002) for micas, and Drits *et al*. (2012) for talc.

	sample	*R* (Å)	*b* (Å)	α_{ref} (°)	α_{calc} (°)	%O enlargement	O sheet thickness (Å)
Si_3Al K-mica	5 - muscovite	0.581	9.074	7.7	12.1	2.7	2.107
Si_3Al Cs-mica	49 - nanpingite	0.577	9.076	5.7	12.8	2.9	2.079
Si_4 K-mica	96 - polylithionite	0.578	8.968	3.0	11.5	1.6	2.095
Si_3Al K-mica	85 - ferrian phlogopite	0.677	9.210	7.3	10.5	-0.7	2.112
Si_3Al K-mica	137 - ferrian phlogopite	0.685	9.212	7.4	10.4	-1.0	2.113
Si_3Al K-mica	146 - lithian siderophyllite	0.677	9.195	4.1	10.2	-0.8	2.109
Si_4 K-mica	105 - tainiolite	0.680	9.065	1.1	7.9	-2.4	2.192
Si_4 K-mica	3 - celadonite	0.682	9.050	1.3	9.0	-2.6	2.249
Si_3Al K-mica	98 - fluoro phlogopite	0.720	9.238	7.6	10.1	-2.9	2.138
Si_4 K-mica	104 - tetra-silicic-F phlogopite	0.720	9.086	1.4	6,9	-4.0	2.186
Talc		0.720	9.173	3.6	0	-3.1	2.168

https://doi.org/10.1180/clm.2023.20 Published online by Cambridge University Press